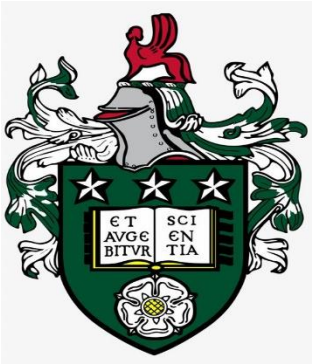

University of Leeds

School of Mechanical Engineering

Experimental and Numerical Investigation of Spherical Flame Propagation for Hydrogen-Methane-Air Mixtures

By

Marwaan Awad Hamad Al-khafaji

B.Eng., M.Sc. (Eng.)

Submitted in accordance with the requirements for the degree of Doctor of Philosophy

December, 2024

Intellectual Property and Publication Statements

The candidate confirms that the work submitted is his own, except where work which has formed part of jointly-authored publications has been included. The contribution of the candidate and the other authors to this work has been explicitly indicated below. The candidate confirms that appropriate credit has been given within the thesis where reference has been made to the work of others.

- Sections 1.2 and 2.1 and Chapter 4 of this thesis are based on a jointly-authored journal paper: *M. Al-Khafaji, J. Yang, A. S. Tomlin, H. M. Thompson, G. de Boer, K. Liu, M. E. Morsy (2023)"Laminar burning velocities and Markstein numbers for pure hydrogen and methane/hydrogen/air mixtures at elevated pressures" Fuel, vol. 354, p. 129331.* The candidate performed major tasks, including experimental work and analysing and presenting the results. The other authors, J. Yang, A. S. Tomlin, H. M. Thompson, G. de Boer, K. Liu, and M. E. Morsy, helped the candidate by providing valuable technical discussions, comments and guidance.
- Sections 1.3 and 2.2 and Chapter 5 of this thesis are based on a jointly-authored journal paper: *M. Al-Khafaji, J. Yang, A. S. Tomlin, H. M. Thompson, G. de Boer, K. Liu, (2025) "The Measurement of Turbulent Burning Velocities of Methane-Hydrogen-Air Mixtures at Elevated Pressures in a Spherical Vessel," Combustion and Flame, vol. 272, p. 113907*. The candidate performed major tasks, including experimental work and analysing and presenting the results. The other authors, J. Yang, A. S. Tomlin, H. M. Thompson, G. de Boer, and K. Liu, helped the candidate by providing valuable technical discussions, comments and guidance.
- Sections 1.4 and 2.3 and Chapter 6 of this thesis are based on a jointly-authored journal paper: *M. Al-Khafaji, J. Yang, A. S. Tomlin, H. M. Thompson, G. de Boer, "Testing an Empirical correlation for Turbulent Hydrogen-Air Flame,"* prepared to be submitted to a journal. The candidate performed major tasks, including experimental work and analysing and presenting the results. The other authors, J. Yang, A. S. Tomlin, Hrvoje Jasak, H. M. Thompson, and G. de Boer, helped the candidate by providing valuable technical discussions, comments and guidance.

Acknowledgements

In the first place, I would like to express my sincere gratitude to my supervisors, Dr Junfeng Yang, Prof. Alison S. Tomlin, Prof. Harvey M. Thompson, Dr Gregory de Boer, and Dr Kexin Liu, for their continuous support, patience, and motivation. It has been a pleasure to work alongside them. Special thanks go to Dr Mohamed E. Morsy for his valuable discussion and comments on this work. Acknowledgement must also be given to Prof. Derek Bradley, Prof. Malcolm Lawes, and Dr Christian Michelbach for the valuable discussions in the laminar burning velocity sections. Thanks to Prof. Hrvoje Jasak for his comments on the CFD code.

Thanks to the State Company of Electricity Production- North Region/ Ministry of Electricity/ Republic of Iraq for giving me the opportunity and sponsoring the PhD study.

My thanks also go to all of the staff in the Thermodynamics Laboratory. Thanks to Peter Grieve and Sam Flint for their lab technical assistance.

A massive thank you must go to my brothers and sisters for their continuous support and encouragement. Also, special thanks go to my lovely Kids, Sadane, Mohammed, Yaman, and Alhassan. Finally, my deepest gratitude is to my wife, Eman.

Abstract

The addition of hydrogen to natural gas offers several advantages: (i) reducing carbon emissions, (ii) extending the flammability limit by enhancing the flame resistance to strain-induced extinction, thereby increasing flame stability, and (iii) increasing the gas turbine's ability to operate at low loads, which expands the feasible load profile. Few previous experimental studies have focused on premixed spherical flame propagation for hydrogen/air and methane/hydrogen/air mixtures, especially at the high-pressure conditions most relevant to a hydrogen-fuelled spark-ignition car engine or an industrial gas turbine. This work employed a Schlieren technique to measure flame speeds for such mixtures in a spherical stainless steel combustion vessel, from which turbulent and laminar burning velocities were derived. The hydrogen volume fractions in methane were 30, 50, 70 and 100%. The initial pressures were 0.1, 0.5 and 1.0 MPa, and the initial temperatures were 303 and 360 K. The equivalence ratio (ϕ) was varied between 0.5 to 2 for pure hydrogen and from 0.8 to 1.2 for methane/hydrogen mixtures. The root mean square (rms) turbulent velocity (u') for turbulent measurements varied from 2.0 to 10.0 ms^{-1}.

The unstretched laminar burning velocities, u_l, are derived and presented. The Markstein length, L_b, Markstein number, Ma_b, and strain rate Markstein number, Ma_{sr}, have also been derived. The results show that the maximum u_l occurs on the rich side of stoichiometric conditions. For example, for 30% and 50% H_2, it occurs at ϕ = 1.1. However, it shifts to ϕ = 1.2 for 70% H_2 and to ϕ = 1.7 for a pure H_2 explosion. The u_l increased with hydrogen fraction and temperature and decreased with pressure. Unexpected behaviour was recorded for pure H_2 explosions at low temperatures and ϕ=1.5, 1.7, wherein u_l did not decrease when the pressure increased from 0.1 to 0.5 MPa.

Simulations of methane-hydrogen-air freely-propagating premixed laminar 1D flame using three recent chemical kinetic mechanisms were compared against the experimentally derived laminar burning velocities. There was generally good agreement with experimentally derived laminar burning velocities; however, for explosions of rich-pure hydrogen at high initial pressures, the level of agreement decreased but remained within the limits of experimental uncertainty.

Following the laminar measurements, turbulent flame investigations were conducted with the following aims: (a) to present an extensive experimental database of turbulent burning velocities for these mixtures over a wide range of conditions, (b) to establish a new correlation for turbulent burning velocity (u_t) for a flame with Lewis numbers, *Le*, not equal to unity, and (c) to quantify the dependence of u_t on pressure, temperature, stretch rate, laminar flame instability and rms velocity. As the pressure increased, the Taylor length scales decreased, increasing flame wrinkling and u_t. The u_t also increased as the temperature and *u'* increased. The fuel/air mixture with high laminar flame instability ($Le<1$) has higher u_t than those with higher *Le*. However, the u_t/u_l peaked in the high laminar burning velocity region. The turbulent flame investigation concluded that the increase in u_t resulting from flame reactivity (laminar burning velocity) is more significant than positive stretch (negative Ma_b) and flame instability.

A numerical study followed the experimental investigation using OpenFOAM software. The turbulent flame wrinkling combustion model associated with the *k-ε* and dynamic-k-equation LES turbulence models are used in the present work. The empirical correlations from the current measurements are used instead of the Gulder correlation to calculate the wrinkling factor (Ξ) and solve the transport equation for the density-weighted mean reaction regress variable (b). The results showed that the *k-ε* and LES models agreed well with the experimental result, but LES provides more information about flame surface wrinkling.

The LES simulation with the combustion model that uses the transport equation for laminar burning velocity exhibits better agreement with the experiments than for the use of a constant laminar burning velocity. In addition, The maximum velocity magnitude is within the flame at the point where the mixture starts burning (b =0.8-0.95). This velocity wave was associated with the pressure wave in the flame propagation. The peak value of pressure was more significant for higher turbulent kinetic energy.

Table of Contents

INTELLECTUAL PROPERTY AND PUBLICATION STATEMENTS I

ACKNOWLEDGEMENTS II

ABSTRACT III

LIST OF FIGURES IX

NOMENCLATURE XVIII

GREEK SYMBOLS XIX

CHAPTER 1: INTRODUCTION 1

1.1 Overview and Motivations 1

1.2 The Unstretched Laminar Burning Velocity u_l 4

1.3 Turbulent Flame and Burning Velocity 5
1.3.1 Turbulent Combustion Regimes 7

1.4 Numerical Modeling of Premixed Turbulent Hydrogen Flame 9

1.5 Aims and Objectives 10

1.6 Thesis outline 12

CHAPTER 2: THE LITERATURE REVIEW 13

2.1 Laminar Flame Propagation 13
2.1.1 The Structure of Laminar Premixed Flames 13
2.1.2 Flame Thickness 15
2.1.3 Flame Stretch Rate 16
2.1.4 Unstretched Laminar Burning Velocity 17
2.1.5 Flame Instabilities 19
2.1.6 Measurement Uncertainty and Limitations of Experimental Procedures 24
2.1.7 The Numerical 1-D Laminar Burning Velocity 27
2.1.8 Research Gaps in the Study of Laminar Flame Propagation 29

2.2 Turbulent Burning Velocity 30
2.2.1 The Effective Root Mean Square Velocity $u'k$ 35
2.2.2 Turbulent Flow and Flame Characteristic/Field Definitions 37
2.2.3 Turbulent Burning Velocity Correlations 39
2.2.4 Research Gaps for Turbulent Flame Studies 41

2.3 Numerical Investigations **41**
2.3.1 Flow Field Characteristics 42
2.3.2 Flame surface wrinkling 43
2.3.3 The Flame Wrinkling Turbulent Combustion Model 44
2.3.4 Research Gaps for Numerical Flame Studies 45

CHAPTER 3: RESEARCH METHODOLOGY 46

3.1 Introduction **46**

3.2 Experimental Apparatus **46**
3.2.1 Combustion vessel 47
3.2.2 Auxiliary systems 48

3.3 Experimental Procedure for Laminar Flame Propagation **53**
3.3.1 Unstretched Laminar Burning Velocity and Markstein Length 56

3.4 Experimental Procedure for Turbulent Flame Propagation **60**
3.4.1 Turbulent Burning Velocity 61

3.5 Numerical Modelling of Turbulent Flame Propagation **63**
3.5.1 The Governing Equations for Large Eddy Simulation (LES) 64
3.5.2 The Turbulent Governing Equations for RANS model (k-ε) 66
3.5.3 The Ξ Combustion Model 68
3.5.4 Case Setting and Boundary Conditions 71

CHAPTER 4: LAMINAR BURNING VELOCITIES AND MARKSTEIN NUMBERS 75

4.1 Introduction **75**

4.2 Flame Instabilities Observation **77**

4.3 Flame Speeds and Stretch Rate **81**

4.4 Unstretched Laminar Burning Velocities **87**

4.5 Markstein number and Markstein length **91**

4.6 Comparisons between the experimental laminar burning velocities and kinetic mechanisms for methane/hydrogen/air mixtures **100**

4.7 Conclusions **106**

CHAPTER 5: TURBULENT BURNING VELOCITIES 108

5.1 Introduction **108**

5.2 Turbulence regimes **108**

5.3 Turbulent flame radius and flame images **112**

5.4 Turbulent Burning Velocity u_t 116

5.5 Effect of Flame Stretch Rate and Flame Instabilities on Turbulent Burning Velocity 127

5.6 Turbulent burning velocity correlation 130

5.7 Chapter Conclusions 135

CHAPTER 6: SIMULATION OF TURBULENT HYDROGEN/AIR FLAME PROPAGATION 138

6.1 Introduction 138

6.2 The original Ξ combustion model 138

6.3 Mesh Dependency in the k-ε Turbulence Model 140

6.4 Model Validation 140
6.4.1 Laminar Burning Velocity Validation 141
6.4.2 Combustion and Turbulence Model Validation 143
6.4.3 Turbulent burning velocity correlations 144

6.5 Velocity and Temperature Field 147

6.6 Flame Wrinkling 158

6.7 Model Demonstration in a Simplified Gas Turbine-Like Configuration 160

6.8 Chapter Conclusion 165

CHAPTER 7: CONCLUSION 167

7.1 Future work and recommendations 171
7.1.1 Experimental work 171
7.1.2 Numerical work 172

REFERENCES 173

List of Figures

Figure 1.1: The turbulent regime diagram [40, 43, 44]. 8

Figure 2.1: Temperature, Heat Release Rate (HRR), and species profile for 1-D adiabatic premixed laminar flame of a stoichiometric methane/air mixture at 0.1 MPa and 300 K [59]. 14

Figure 2.2: Illustration of flame thickness $\delta l = \Delta x$ [61]. 16

Figure 2.3: Structure of a wrinkled flame front showing the hydrodynamic streamlines and the diffusive fluxes of heat and mass [90]. 20

Figure 2.4: The effective Lewis number plotted against hydrogen fraction at 0.1, 0.5 and 1.0 MPa [94]. 21

Figure 2.5: Flame images for 30% hydrogen in methane with initial temperature 303 K, equivalence ratio 0.8, and 40 mm flame radius (a) the smooth flame 0.1 MPa, (b) the cellular flame structure 0.5MPa. 23

Figure 2.6: The turbulent flame brushes and the associated flame radius, where T_u is the initial mixture temperature, T_b is the adiabatic flame temperature, u_e is the engulfment velocity, r_t is the flame radius at the tip of the brush, r_r is the flame radius at the root of the brush, and r_v is the volumetric flame radius. 34

Figure 3.1: Schematic view of the vessel and auxiliary system for Schlieren optical configuration. 47

Figure 3.2: The internal view of Leeds MK-II vessel. 48

Figure 3.3: Leeds Spark plug [108]. 50

Figure 3.4: Schlieren and processed images for 70% hydrogen, 30% methane laminar flame at 0.1 MPa, 360 K and 0.9 equivalence ratio, A) after 2.5 ms of ignition, and B) after 5 ms of ignition. 55

Figure 3.5: Flame speed vs. flame stretch rate for 30% H_2 in CH_4 by volume at 0.5 MPa, 360 K, ϕ=1..... 57

Figure 3.6: Schlieren and processed images for pure hydrogen turbulent flame at 0.5 MPa, 360 K, $u' = 2\ ms^{-1}$ and 0.8 equivalence ratio. 62

Figure 3.7: The geometry and mesh structure 74

Figure 4.1: The flame visualisation and pressure as a function of time, a) 30 % H_2, 0.5 MPa, 360 K, b) 70% H_2, 0.1 MPa, 303 K and c) 100% H_2, 0.1 MPa, 303 K. 76

Figure 4.2: Flame images for 50% H_2, ϕ =0.9 at 360 K with different initial pressures. 78

Figure 4.3: Flame images for an initial pressure of 0.1 MPa, ϕ =0.8 at 303 K with different H_2 volume fractions. 79

Figure 4.4: Critical flame radius (mm) vs. volumetric hydrogen fractions at 360 K and ϕ= 1. ... 81

Figure 4.5: Flame speed (ms^{-1}) vs flame radius (mm) with different equivalence ratios. a) 30% H_2, 0.5 MPa, b) 70% H_2, 0.5 MPa, c) 100% H_2, 0.1 MPa, and d) 100% H_2, 1 MPa. 82

Figure 4.6: Flame speed (ms^{-1}) vs. stretch rate (s^{-1}) at 360 K for 30, 50, 70, and 100% volumetric fraction of hydrogen for different initial pressures and equivalence ratios..... 83

Figure 4.7: Flame speed (ms^{-1}) vs. stretch rate (s^{-1}) at 303 K for 30, 50, 70, and 100% volumetric fraction of hydrogen for different initial pressures and equivalence ratios..... 84

Figure 4.8: Possible instability onsets for the case with 50% H_2, 0.5 MPa, 360K and ϕ=1, image with label 1 at 3.75 ms after ignition, the time step is 0.25 ms. 86

Figure 4.9: The measurement uncertainty in the laminar burning velocity due to the choice of the onset of instability condition. 88

Figure 4.10: Unstretched laminar burning velocity vs. equivalence ratio for 30, 50 and 70% hydrogen fractions at different initial pressures and temperatures (a) at 360 K and different initial pressure, (b) at 0.5 MPa and different initial temperatures..... 89

Figure 4.11: Unstretched laminar burning velocity with equivalence ratio for 100% hydrogen at different initial pressures and temperatures, (a) 303 K and (b) 360 K. 90

Figure 4.12: Unstretched laminar burning velocity with equivalence ratio for present and previous studies at 0.1 MPa and 303K, (a) H_2/CH_4 and (b) pure H_2. 90

Figure 4.13: Markstein length vs. hydrogen fraction for lean, stoichiometric and rich mixtures at different initial pressures and temperatures, (a) ϕ= 0.8, (b) ϕ= 1 and (c) ϕ= 1.2. 93

Figure 4.14: The impact of pressure and temperature on the Markstein length at different equivalence ratios for pure hydrogen. 94

Figure 4.15: Markstein number vs. hydrogen fraction at ϕ = 0.8 and 1.2 and different initial pressures, (a) Ma_b and (b) Ma_{sr}. 94

Figure 4.16: Total Markstein number and strain rate Markstein number vs. equivalence ratio for pure hydrogen at different initial pressures, (a) Ma_b and (b) Ma_{sr}. 94

Figure 4.17: Comparison between the experimentally derived laminar burning velocities for pure hydrogen with numerical predictions using different mechanisms at 0.1 MPa, (a) 303 K and (b) 360K. 101

Figure 4.18: Comparison between the experimentally derived laminar burning velocities for pure hydrogen with numerical predictions using different mechanisms at 0.5 MPa, (a) 303 K and (b) 360K. 102

Figure 4.19: Comparison between experimentally derived laminar burning velocities for methane/hydrogen mixtures with different mechanisms at 0.1 MPa and 303 K, (a) 30% H_2 and (b) 50% H_2. 102

Figure 4.20: Comparison between experimentally derived laminar burning velocities for methane/hydrogen mixtures with different mechanisms at 0.5, 1.0 MPa and 360 K, (a) 50% H_2 and (b) 70% H_2. 103

Figure 4.21: Numerical predictions of laminar burning velocities vs. equivalence ratio for pure hydrogen at two different pressures and 303 K. 103

Figure 4.22: Active radical concentrations for pure H_2 at 303K and ϕ = 1.7, from (a) Konnov and (b) San Diego mechanism. 103

Figure 4.23: Net rate of key pressure-dependent reactions for a pure H_2/air flame at 303 K and ϕ = 1.7, from simulations using the San Diego and Konnov reaction mechanisms (a) $H+O_2$ (+M) = HO_2 (+M), (b) $OH+OH(+M)=H_2O_2(+M)$ and (c) $H+OH+M=H_2O+M$ 105

Figure 5.1: Modified Peters-Borghi's diagram [42-44], with the present experimental conditions, with laminar burning velocity and flame thickness taken from [12]. The legends for the present experimental conditions and turbulence parameters represent (a) 30, 70% H_2 and (b) 50, 100% H_2. ϕ ϵ[0.8 1.2] for mixtures with 30% ,50% and 70% H2; [0.5 2] for pure H2. 111

Figure 5.2: The equivalent flame radius vs. time for stoichiometric mixtures at 0.5 MPa and 360 K. 113

Figure 5.3: Flame images, Pu = 0.5 MPa, Tu= 360 K and ϕ =0.8, (a) 50% H_2, u'= 2 ms^{-1}, (b) 50% H_2, u'= 8.5 ms^{-1} and (c) 100% H_2, u'= 9.5 ms^{-1}..... 113

Figure 5.4: Flame images at r_v= 45 mm, 0.1 MPa, 360 K, u'= 2 ms^{-1} and ϕ= 1, (a) 30% H_2, Ma_b= 4.1, (b) 50% H_2, Ma_b= 5.4, (c) 70% H_2, Ma_b= 9.65 and (d) 100% H_2, Ma_b= 25.2. 115

Figure 5.5: Flame images for 100% H_2 at T_u= 360K, r_v= 40 mm, and u'= 2 ms^{-1} (a) P_u= 0.1 MPa, Ma_b= 25.6, ϕ= 1.5, u_l= 3.68 ms^{-1}, (b) P_u= 0.1 MPa, Ma_b= 19.6, ϕ= 2 u_l= 3.55 ms^{-1}, (c) P_u= 0.5 MPa, Ma_b= -22.7, ϕ= 1, u_l= 2.35 ms^{-1}, (d) P_u= 0.5 MPa, Ma_b= -10.5, ϕ= 2.5, u_l= 2.75 ms^{-1}. 116

Figure 5.6: The variation of turbulent burning velocity with the flame radius for CH_4/H_2/air mixtures at different pressures and initial rms velocities, (a) 30% H_2, ϕ=0.9, (b) 30% H_2, ϕ= 1.1, (c) 50% H_2, ϕ= 1, (d) 70% H_2, ϕ= 0.8, (e) 70% H_2, ϕ= 1, and (e) 70% H_2, ϕ= 1.2. 118

Figure 5.7: The variation of turbulent burning velocity with the flame radius for H_2/air mixtures at different pressures and initial rms velocities, (a) ϕ=0.5, (b) ϕ= 0.8, (c) ϕ= 1, and (d) ϕ= 1.5. 119

Figure 5.8: Variation of turbulent burning velocity u_t with the effective rms velocity u'_k for different mixtures, pressures and initial rms velocities u' with ϕ = 1 and T=360, (a) 30% H_2, (b) 50% H_2, (c) 70% H_2 and (d) 100% H_2. 120

Figure 5.9: Variation of turbulent burning velocity with the flame radius for H_2/air mixtures at 360 K, 0.5 MPa and initial rms velocities. For ϕ= 1, Ma_b= -22.7 and u_l= 2.35 ms^{-1}. For ϕ= 2.5, Ma_b= -10.5, u_l= 2.75 ms^{-1}. 121

Figure 5.10: Variation of turbulent burning velocity at r_v= 30 mm with equivalence ratio for different fuel mixtures, pressures, temperatures and initial rms velocities 124

Figure 5.11: Variation of turbulent burning velocity at r_v= 30 mm with equivalence ratio for hydrogen flame at different pressures, temperatures and initial rms velocities. 125

Figure 5.12: Variation of turbulent burning velocity u_t with u' for stoichiometric mixture with different H_2 volume fractions and pressures. 126

Figure 5.13: Variation of normalised turbulent burning velocity with Markstein number Ma_b at 0.5 MPa and 360K (a) 50% H_2, ϕ = 0.8-1.2 and (b) 100% H_2, ϕ = 0.5-2. 128

Figure 5.14: The present experimental measurements in the *U-K* diagram. 129

Figure 5.15: Correlation of u_t/u'_k with *Ka1* for different fuel mixtures and Ma_b, (a) pure H_2, Ma_b from -25 to 20, (b) H_2/CH_4, positive Ma_b and (c) H_2/CH_4, negative Ma_b 134

Figure 5.16: Normalised turbulent flame speed $u_t/u_l/K_{a1}$ as a function of *Da /Le* for present data and literature correlation [123] 135

Figure 6.1: Evolution of the flame radius with time from the experiment and the original Xifoam simulation methods. 139

Figure 6.2: Flame radius with time for stoichiometric hydrogen/air at 360K and 0.5 MPa with three mesh sizes. 140

Figure 6.3: The comparison between u_l from the present experiment and correlation in [163], (a) 0.1 MPa and (b) 0.5 MPa. 141

Figure 6.4: Experimental and numerical hydrogen flame (LES simulation), 1 ms after ignition, at 0.1 MPa, 360 K and u'= 6 m/s. 142

Figure 6.5: Flame radius vs time for experimental and LES simulation with two combustion models (S_u constant and transport equation) for stoichiometric hydrogen flame at 360 K, and u'= 6 ms^{-1}, (a) 0.1 MPa and (b) 0.5 MPa. 142

Figure 6.6: Flame radius vs time for experimental and k-ε simulation with two combustion models (S_u constant and transport equation) for stoichiometric hydrogen flame at 360 K, 0.5 MPa, and u'= 6 ms^{-1}. 142

Figure 6.7: Flame isotherm-surface at 2000 K after 2.5 ms of ignition for stoichiometric hydrogen flame at 360 K, 0.5 MPa, and u'= 6 ms^{-1}, (a) k-ε and (b) LES simulation. 144

Figure 6.8: The flame radius vs time for experimental and LES simulation with two Ξ calculations (equations 3.39 and 3.41) for stoichiometric hydrogen flame at 360 K, 0.5 MPa, and u'= 6 ms^{-1}. 145

Figure 6.9: Flame radius vs. time for experimental and LES simulation for stoichiometric hydrogen flame at 360 K, (a) 0.1 MPa u'= 2 ms^{-1}, (b) 0.5 MPa u'= 2 ms^{-1} (c) 1 MPa u'= 2 $ms^{-1}$and (c) 1 MPa u'= 6 ms^{-1} 147

Figure 6.10: Temperature (K) contour and flow velocity vector ms^{-1} after 3 ms of ignition for different pressures and rms velocities. 149

Figure 6.11: Velocity magnitude U ms^{-1} after 3 ms with 0.5 MPa and different rms velocity. 149

Figure 6.12: Velocity magnitude (left axes) for a radial line at steps 1.5 and 2.5 ms with 0.1 MPa and u' = 2 ms^{-1}; the right axes represent the regress variable (b = 0 burned gases, b=1 unburned gases). 151

Figure 6.13: Velocity magnitude (left axes) for a radial line at steps 1.5 and 2.5 ms with 1 MPa and u' = 6 ms^{-1}; the right axes represent the regress variable (b = 0 burned gases, b=1 unburned gases). 152

Figure 6.14: Velocity magnitude (left axes) for a radial line at steps 1.5 and 2.5 ms with 0.5 MPa and u' = 6ms^{-1}; the right axes represent the regress variable (b = 0 burned gases, b=1 unburned gases). 153

Figure 6.15: Pressure wave for a radial line at steps 1.5 and 2.5 ms (P=1 Mpa, T=360 K, ϕ=1 and u'= 2 ms^{-1}). 154

Figure 6.16: Pressure wave for a radial line at steps 1.5 and 2.5 ms (P=1 Mpa, T=360 K, ϕ=1 and u'= 6 ms^{-1}). 155

Figure 6.17: Pressure wave for a radial line at steps 1.5 and 2.5 ms (P=0.5 Mpa, T=360 K, ϕ=1 and u'= 6 ms^{-1}). 156

Figure 6.18: Temperature distribution for a radial line at steps 1.5 and 2.5 ms (P=0.5 Mpa, T=360 K, ϕ=1 and u'= 6 ms^{-1}). 157

Figure 6.19: Flame isotherm-surface at 2000 K after 3ms of ignition for different pressures and rms velocities (ϕ=1). 160

Figure 6.20: Flame isotherm-surface at 2000 K after 3ms of ignition for different pressures and rms velocities (ϕ=0.5). 160

Figure 6.21: Siemens Energy SGT 100, DLE combustor [187], a) 3D combustor, and b) cross section combustor. 161

Figure 6.22: The modelled flame zone. 162

Figure 6.23: The temperature contours at different time steps for the stoichiometric hydrogen flame at 0.5 MPa, 360 K and u'= 2 ms^{-1}. 165

Figure 6.24: The velocity at 2 ms for the vertical line shown in Figure 6.23 at ms 165

List of Tables

Table 2-1: Compares the experimental conditions (equivalence ratio, unburned gas pressure and temperature) and previous outward flame propagation studies. 30

Table 3-1: The initial experimental conditions. 63

Table 3-2: The initial and boundary conditions in the numerical simulation 72

Table 4-1: Laminar burning velocity, Markstein length, critical flame radius, flame thickness, burned gas and strain Markstein number for 30% hydrogen fraction 96

Table 4-2: Laminar burning velocity, Markstein length, critical flame radius, flame thickness, burned gas and strain Markstein number for 50% hydrogen fraction 97

Table 4-3: Laminar burning velocity, Markstein length, critical flame radius flame, thickness, burned gas and strain Markstein number for 70% hydrogen fraction 98

Table 4-4: Laminar burning velocity, Markstein length, critical flame radius, flame thickness, burned gas and strain Markstein number for pure hydrogen explosions 99

Table 5-1: Taylor (λ) and Kolmogorov (η) length scales for 50% H_2 with ϕ=1 at various experimental pressures, temperatures and rms turbulent velocities. 109

Table 5-2: Taylor (λ) and Kolmogorov (η) length scales for 100% H_2 with ϕ=1.5 at various experimental pressures, temperatures and rms turbulent velocities. 110

Table 5-3: The effective rms fluctuation velocity *u'k* at r_v= 30 mm for all experimental *u'*. 122

Table 6-1: The initial and boundary conditions of the numerical simulation 163

Nomenclature

$\mathcal{A}$	Flame surface area (m^2)
C_p	Specific heat (KJ/Kg.K)
$\mathcal{D}$	Thermal diffusivity (m^2s^{-1})
L_b	Flame speed Markstein length (mm)
Le	Lewis number
L	Turbulent integral length scale
Ma_b	Flame speed Markstein number
Ma_{sr}	Strain Markstein number
P_u	Initial pressure (MPa)
P_r	Prandtl number
r_{cl}	Critical flame radius (mm)
r_{sch}	Flame radius from Schlieren images (mm)
r_v	Volumetric flame radius (mm)
S_n	Stretched flame speed (m/s)
S_s	Unstretched flame speed (m/s)
U_f	The uncertainty weight factor
u_l	Unstretched laminar burning velocity (ms^{-1})
T_b	Adiabatic equilibrium burned gas temperature (K)
T_u	Unburned gas temperature (K)
K_{a1}	Karlovitz stretch factor $\left(\frac{\delta_l/u_l}{\lambda/u'}\right)$
K_a	Karlovitz number $\left(\frac{\delta_l/u_l}{\eta/u_\eta}\right)$
D_a	Damköhler number
u'	Root Mean Square (rms) velocity (ms^{-1})
u_k'	The effective root mean square (rms) turbulent velocity (ms^{-1})
u_t	The turbulent burning velocity (ms^{-1})
u_η	The turnover velocity on the Kolmogorov scale, $u_n = u' 15^{0.25} Re_\lambda{}^{-0.5}$

Greek symbols

α	Flame stretch rate (1/s)
δ_l	Flame thickness (mm)
γ	Thermal conductivity (kJ/m.K.s)
μ	Dynamic viscosity (kg/m.s)
ν	Kinematic viscosity (m^2s^{-1})
φ	Equivalence ratio
ρ_b	Burned gas density (kg/m^3)
ρ_u	Un-burned gas density (kg/m^3)
λ	Turbulent Taylor length scale (mm)
η	Turbulent Kolmogorov length scale (mm)
Re_λ	Reynolds number based on Taylor length scale
Re_L	Reynolds number based on integral length scale

Chapter 1: Introduction

1.1 Overview and Motivations

Achieving net-zero greenhouse gas emissions has been set as a goal for many nations, and they have noticeably increased their investment in low-carbon emission technologies, such as renewable energy [1]. The hydrogen from clean sources, “green hydrogen”, is essential to achieve net-zero greenhouse gas emissions. The UK government established a plan for a "green industrial revolution", producing 5 GW of hydrogen from renewable sources and £500 million in the North East of England to produce hydrogen using offshore wind energy [2]. Hydrogen is used to integrate renewable energy systems [3]. The major drawback of wind and solar energy is that they are non-continuous sources [4, 5]. Two choices are suggested to overcome this issue and continually supply clean energy: (a) using batteries and (b) using green hydrogen. The batteries are costly, harmful to the environment [3], and can only be used for short-term storage [6]. In addition to its long-term storage, green hydrogen can be used for (i) electricity production, (ii) industry, (iii) public transport, and (vi) domestic heating [6]. The Photovoltaic (PV)-hydrogen hybrid power plant is an example of an integrated power production system [7]; the electricity is produced from the PV unit during the day, and the hydrogen is produced and stored in a tank during excess radiation. The stored hydrogen is then used to fuel the gas turbine unit during the night or low solar time. Hydrogen can also be produced during excess energy or low energy prices (H_2-energy storage) and potentially used in gas turbines during higher energy prices [8]. In addition, replacing conventional fuels with green hydrogen can slow down the global warming process [9]. A significant reduction in CO_2 emission is achieved when hydrogen is used in gas turbines instead of natural gas. When the natural gas is replaced by hydrogen in a 50 MW gas turbine unit, the amount of CO_2 emissions cut is between 46.37 and 71.15 tones-CO_2/hour [5].

The history of hydrogen as an alternative fuel dates back to its inception in the aerospace industry in 1943, when the US Air Force initiated a research program at Ohio State University. This research was followed by several studies sponsored by NASA after the energy crisis in 1973. These studies used liquid hydrogen and liquid oxygen in the US space program [10]. In electricity production, burning natural gas in gas turbine engines remains common [11, 12]. Hydrogen can be used solely to power the gas turbine engine. Alternatively, it can be blended with natural gas when clean hydrogen production is insufficient to fuel the entire power production unit. Adding hydrogen to natural gas reduces carbon emissions and stabilises the lean premixed flame in gas turbine combustors [13].

Moreover, hydrogen addition reduces ignition energy and enhances flame speed, as natural gas typically possesses a high ignition energy and low flame propagation speed [14]. Overall, the addition of hydrogen to natural gas offers several advantages: (i) reducing carbon emissions, (ii) extending the flammability limit by enhancing the flame resistance to strain-induced extinction [15-17], thereby increasing flame stability and (iii) increasing the gas turbine ability to operate at low loads, which expands the feasible load profile [8, 18]. However, several challenges emerge in designing combustion equipment for hydrogen blends or pure hydrogen. While hydrogen has a high specific energy (120 MJ/kg), it suffers from low energy density (9.6 MJ/m^3) at atmospheric conditions. Consequently, to achieve equivalent power output from a gas turbine, the hydrogen volume flow rate must be three times higher than that of natural gas [19]. Hydrogen also has a high adiabatic flame temperature of 2390 K at ambient and stoichiometric conditions, potentially resulting in elevated NO_X emissions [13, 19].

In addition, hydrogen increases the risk of flashback, wherein the flame drifts toward the burner and the premixed section due to its short auto-ignition time and high burning velocity [20]. Moreover, the hydrogen can lead to thermo-acoustic instabilities, enthalpy reduction, and heat transfer coefficient variations [13, 21]. Therefore, modifications are required in the storage, piping unit, and combustor to use hydrogen or a hydrogen-based blended fuel. These factors (NOx, flashback, thermo-acoustic instabilities, enthalpy reduction, heat transfer coefficient variation, etc.) motivate the need for comprehensive analysis of the combustion characteristics of pure hydrogen and hydrogen blends under high-pressure conditions close to those encountered at power plants to facilitate the design of multi-fuel combustors.

The present study investigates laminar and turbulent premixed combustion of methane-hydrogen-air mixtures at elevated initial pressures up to 1.0 MPa, at initial temperatures (303 K and 360 K), and over a wide range of equivalence ratios. Since methane (CH_4) occupies around 80 to 95% of natural gas components by volume, it is commonly used to demonstrate the combustion behaviour of natural gas [11, 14]. Methane is the main component of natural gas, the primary fuel of industrial gas turbines [22]. Moreover, studying methane-hydrogen (CH_4-H_2) blends for gas turbine applications is preferred over natural gas-hydrogen blends because CH_4-H_2 blends only two components, making their combustion chemistry and kinetics easier to be understood and modelled, compared to the complex mixture of hydrocarbons in natural gas. Therefore, CH_4 has been chosen to represent natural gas in this study. Experimental data from this research will serve as a valuable resource for kinetics researchers since the laminar burning velocity at high initial pressure is used to evaluate kinetic reaction mechanisms, which could be subsequently employed in the simulation of potential hydrogen combustors.

This data will also be valuable for gas turbine and engine designers; they can use the turbulent flame propagation data to validate the numerical models. In addition, the turbulent and laminar burning velocity can be used as input to the combustion model [23-25]. Measurements are conducted in the Leeds fan-stirred spherical combustion vessel (MK-II). The laminar and turbulent measurements are fed into a numerical model to simulate the turbulent flame propagation. Further details are provided in the subsequent sections.

Few previous experimental studies have focused on premixed spherical flame propagation for hydrogen/air and methane/hydrogen/air mixtures, especially at the high-pressure conditions most relevant to a hydrogen-fuelled spark-ignition car engine or an industrial gas turbine. In the present study, the hydrogen volume fractions in methane are 30, 50, 70 and 100%. The initial pressures are 0.1, 0.5 and 1.0 MPa, and the initial temperatures are 303 and 360 K. The equivalence ratio (ϕ) is varied between 0.5 to 2 for pure hydrogen and from 0.8 to 1.2 for methane/hydrogen mixtures. Both lean and rich mixtures are essential to understanding flame behaviour and safety and emission considerations across different conditions. The root mean square (rms) turbulent velocity (u') for turbulent measurements varied from 2.0 to 10.0 ms^{-1}.

1.2 The Unstretched Laminar Burning Velocity u_l

The unstretched laminar burning velocity, u_l, is the steady one-dimensional adiabatic free flame propagation velocity in the doubly infinite domain [26]. The flame propagates in an idealized, unbounded space without physical boundaries effects. This type of flame cannot be achieved experimentally. Thus, the laminar burning velocity is not directly measurable and is derived from experimental data using different assumptions.

The u_l is described as a physicochemical property of a fuel/oxidiser resulting from exothermicity, diffusivity and reactivity [27]. It indicates the overall mixture reactivity and is used to determine the heat release rate and evaluate kinetic reaction mechanisms. Based on the recent review of Konnov et al. [26], the first experimental investigation of a spherical flame in a combined chamber with central spark ignition was conducted in 1906 by Hopkinson [28]. Flamm and Mache [29] proposed a relationship between pressure and burning rate in the constant volume chamber. The first photograph of a spherical flame taken simultaneously with pressure data was reported in 1927 by Ellis and Wheeler [30]. Bernard L. and Guenther V.E. [31] derived the laminar burning velocity from time-pressure records. Researchers then reported that laminar spherical flame propagation is affected by the flame stretch, which changes the flame surface area over time due to aerodynamic boundary conditions [26].

The stretch effect must be removed to obtain the unstretched laminar burning velocity. Markstein [32] proposed a relationship between flame curvature and propagation velocity. Using Markstein's theory in the 1980s, the unstretched laminar burning velocity was derived from the stretched flame in various burner, counter-flow, and spherical flames [33-36]. In the present work, the unstretched laminar burning velocity for the hydrogen/methane/air mixture is derived from the spherical expanding flame at various conditions, as will be explained in the following chapters.

1.3 Turbulent Flame and Burning Velocity

Turbulent flame propagation plays a crucial role in numerous practical applications, such as gas turbines and internal combustion engines, making its investigation vital for advancing hydrogen combustors. Understanding this phenomenon requires experimentation in simplified turbulent flow configurations such as burners and combustion vessels, which are essential for developing robust numerical models that can address more complex industrial scenarios [37].

In the turbulent spherical expanding flame in combustion vessels, the mean features of the flow, such as turbulence intensity and initial and boundary conditions, are well controlled. Therefore, the input parameters such as Reynolds number, pressure, temperature, chemical, and turbulent time scales can be varied to investigate the turbulent flame propagation over a wide range of conditions.

It was reported early in 1883 by Mallard and Le Chatelier that turbulence enhanced the burning rate of the premixed flame [38]. In 1940, Damköhler reported that the turbulent eddies (i) wrinkle the flame surface and increase the flame surface area, (ii) increase molecular transfer within the flame, and (iii) increase the burning velocity [38]. In turbulent premixed combustion, the flow in front of the flame moves, and the flame is wrinkled. The flame is distorted and folded due to the interaction with the turbulent eddies. The turbulent burning velocity is the most critical parameter, measured in the spherical turbulent flame propagation. The turbulent burning velocity is the unburned gas velocity normal to a selected surface on the flame brushes. It calculates the mass burning and the supplied heat release rates [39].

In this study, experiments were conducted in a large spherical vessel equipped with stirring fans and optical access, which enabled the detection of flame fronts using the Schlieren technique. This setup allowed for comprehensive investigations across a broad range of initial turbulence levels, pressures, and temperatures, providing valuable insights into the behaviour of turbulent combustion. To enhance the analysis of the experimental results, the turbulent combustion regime was first characterised. This identification was crucial for understanding the dynamics of the flame propagation and for ensuring that the subsequent data analysis accurately reflected the underlying physical processes.

1.3.1 Turbulent Combustion Regimes

To gain insight into premixed turbulent flames, Borghi introduced a diagram [40] that classifies various combustion regimes by comparing the chemical and turbulent flow scales (Figure 1.1). The chemical length scale is the flame thickness, the region between the cold and hot gases where chemical reactions and heat diffusion occur. The turbulent length scales describe the range of eddy size that existed in the turbulent flow. They are classified in three sizes: (i) the integral length scale (L), which represents the average of the largest eddies and contains the most turbulent kinetic energy; (ii) the Taylor length scale (λ), which represents the intermediate eddies and the turbulent viscus forces, and (iii) the Kolmogorov length scale (η), represents the smallest turbulent eddies after which the turbulent kinetic energy is dissipated to heat.

This diagram aims to determine the turbulent flame characteristics used to identify the turbulent combustion model. For example, rapid chemistry (compared to transport processes) occurs within the flamelet regime in fragile layers, known as flamelets, which are immersed within the turbulent flow field [41]. The flamelet regime exists when the Kolmogorov length scale (η) exceeds the flame thickness. However, the boundaries of the flamelet regime were expanded through a DNS study by Poinsot et al. [42], who proposed that the premixed turbulent flame belongs to the flamelet regime as long as the thin flame interface separates the reactant and burned gases. They clarified that the classical regime diagram [40] was based on the Klimov-Williams criteria (Da >1) while overlooking the flame front resistance to turbulent eddies, particularly viscous, transient and curvature effects, which become significant within the Kolmogorov scale range [42]. The small eddies may be dissipated before interacting with the flame as they have minimal kinetic energy and short lifetimes.

Pope [43] introduced the smallest turbulent scale ($l_s=13\eta$), which modifies the flame surface. This characteristic length scale, l_s, is at the centroid of the dissipation spectrum [44]. The flamelet regime expands as l_s defines the smallest affected turbulent length scales. According to Pope [43], the flamelet regime's limit is reached when l_s becomes approximately the order of the flame thickness. The broken reaction or flame extinction regime occurs if the flame thickness is less than $l_{s,}$ which is 13 times the Kolmogorov turbulent scale [42, 43]. Consequently, the premixed flamelet exists in most practical combustion cases, such as in reciprocating engines and gas turbines. The turbulent flamelet combustion models can be applied in this regime. The following chapters will present an analysis of the turbulent hydrogen/methane/air flame. This analysis is essential for practical engineering applications such as gas turbines, furnaces and internal combustion engines. An extensive database of turbulent burning velocities for this mixture will be presented to quantify the dependency on pressure, temperature, stretch rate and root mean square turbulence velocity (rms).

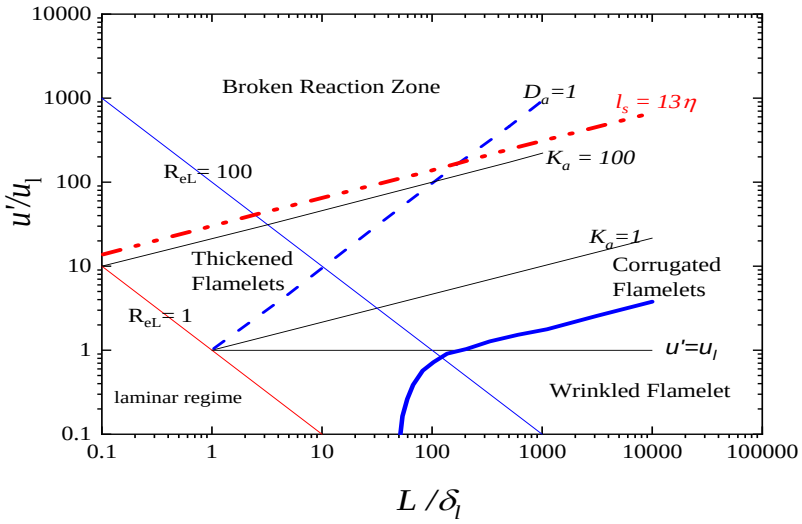

Figure 1.1: The turbulent regime diagram [40, 43, 44].

1.4 Numerical Modeling of Premixed Turbulent Hydrogen Flame

Computational Fluid Dynamic (CFD) tools can provide important information about turbulent flames that is difficult to obtain experimentally [45]. The design of new hydrogen combustors or any practical applications can be aided by using CFD tools [46]. CFD has been used to obtain spherically-expanding flames' flow velocity, temperature and pressure [45, 47, 48]. The present study focused on premixed flame propagation in which a strong interaction between chemistry and fluid dynamics is involved. Combustion models are applied along with turbulence models to simulate turbulent flame propagation. There are two main directions in combustion modelling research: (a) solving detailed or reduced chemistry [46] and (b) modelling the reacting flow using a range of different assumptions [23-25, 49]. As combustion chemistry models are computationally expensive, most traditional combustion models aim to reduce the computational cost by simplifying the detailed chemical kinetics [24]. The turbulent premixed flame is modelled in different ways to avoid solving the expensive chemistry, such as (i) Eddy Break-Up models (EBU) [50], (ii) Bray-Moss-Libby model [46], and (iii) models based on the flame surface area estimation (flamelet models) [24, 25]. The primary assumption in flamelet models is that the reactions are fast and occur in a very thin layer separating the burned and unburned mixture. The flamelet concept applies when the relevant chemical time scale is significantly shorter than the convection and diffusion time scales ($Da > 1$). The premixed turbulent flame in the present study is modelled using the flame wrinkling model (Ξ), which is a flamelet model, as it balances computational speed and accuracy [48]. This model was chosen because it links the experimental work to the numerical simulation.

In addition to combustion models, different turbulence models have been applied in previous work to simulate the turbulent flow, such as Direct Numerical Simulation (DNS), Large Eddy Simulation (LES) and Reynolds Averaged Navier-Stokes equation (RANS) [51]. DNS is the most accurate method, but it is computationally expensive and requires extremely fine meshes. DNS resolves all the scales of turbulence down to the smallest eddies (Kolmogorov scales), and it is very challenging, therefore, to simulate flow in complex geometries of practical combustion chambers at high Reynolds numbers. DNS has been used to investigate flames in simple geometries with reduced chemical mechanisms [52, 53]. In contrast, the RANS approach solves the time-averaged Navier-Stokes equations and accounts for the effect of turbulence on the mean flow field. It is much less expensive and has been used to simulate flames in large, complex geometries [47]. LES simulation is the central method, as it directly solves the large turbulent eddies and models the small eddies using one of the sub-grids methods [54]. The mesh size is smaller than for DNS and larger than for RANS. LES is the most promising model for studying practical combustion dynamics [45, 51]. Therefore, the present study combines dynamic-k-equation LES and Launder-Sharma k-ε turbulence models with the Ξ combustion model.

1.5 Aims and Objectives

The present study experimentally and numerically analyses laminar and turbulent flames of hydrogen/air and methane/hydrogen/air mixtures. The objectives of the present study are as follows:

1- ***Experimental Investigation:*** Conduct investigations to determine laminar burning velocities and Markstein numbers for a wide range of methane-hydrogen-air mixtures at elevated initial pressures up to 1.0 MPa.

2- ***Simulation and Comparison***: Perform CFD simulations using recent chemical kinetic mechanisms, compare the simulation results against the experimentally derived laminar burning velocities, and conduct sensitivity analysis to understand species behaviour within the mixture.

3- ***Turbulent Burning Velocity Database***: Provide an extensive experimental database for the turbulent burning velocity of methane/hydrogen/air and hydrogen/air mixtures under elevated pressure conditions.

4- ***Development of a New Correlation***: Develop a new correlation for turbulent burning velocities for flames with non-unity Lewis numbers, including all parameters that affect the turbulent burning velocity. This correlation is implemented in the present combustion model.

5- ***Quantification of Dependencies***: Quantify the dependencies of turbulent burning velocity on various parameters, including pressure, temperature, stretch rate, laminar flame instability and turbulent fluctuating velocity.

6- ***Model Evaluation***: Evaluate a numerical model by simulating the spherical turbulent flame propagation using a combustion flamelet model (the flame wrinkling (Ξ) model).

7- ***Prediction of Difficult-to-Measure Parameter***s: Utilise this model to predict challenging-to-measure parameters, such as flow velocity, pressure wave, and temperature.

8- ***Investigation of Turbulent Flame Wrinkling***: Investigate the effects of pressure, turbulent fluctuation velocity and Lewis number on the turbulent flame wrinkling using the developed model.

1.6 Thesis outline

This thesis comprises seven chapters. Chapter 1 presents an introduction to the background and motivation of the study, outlining its main aspects. Chapter 2 is the literature review. The review focuses on laminar and turbulent spherical flame propagation. It includes a discussion of both experimental and numerical studies. Chapter 3 presents this study's experimental apparatus, techniques, and procedures. The methods include the measurement of flame radii and the associated image processing. The experiments were initiated with laminar flames and followed by turbulent flame measurements. The numerical methods for turbulent flame modelling are also given in this chapter. The methods focus on the flame wrinkling combustion model along with RANS and LES turbulence modelling. Chapter 4 presents the experimental results for laminar flame propagation. The discussion includes the derivation of laminar burning velocities, flame stretch rates, Markstein lengths, and flame instabilities. The turbulent measurements and discussion are given in Chapter 5. It discusses the effect of (i) stretch rate on turbulent flame speed, (ii) turbulent length scales on flame wrinkling, and (iii) Lewis number (flame instability) on turbulent burning velocity. This chapter presents and discusses empirical correlations for the turbulent burning velocity. Chapter 6 presents numerical results. The results are compared for turbulent and combustion models. The turbulence models are RANS (k-ε) and LES. The laminar burning velocity is implemented in different ways in the flame wrinkling combustion model. The outcomes of these combustion models are compared and discussed in this chapter. Conclusions and recommendations are drawn in Chapter 7.

Chapter 2: The Literature Review

2.1 Laminar Flame Propagation

The present study delves into the practical applications of premixed spherical flame propagation of hydrogen/air and methane/hydrogen/air mixtures. These mixtures, thoroughly mixed before ignition, form the basis of premixed flames found in gas turbines, internal combustion engines, and various engineering applications. This section includes a comprehensive literature review on laminar premixed flames, flame thickness, laminar burning velocity, stretch rate, flame instabilities, and related dimensionless numbers, all directly relevant to these practical applications.

2.1.1 The Structure of Laminar Premixed Flames

The laminar premixed flame can be defined as a smooth flame free from the influence of flow. The flame is a thin reaction layer moved in the fuel/air mixture with great complexity [38]. The premixed laminar flame structure was first described by Mallard and Le Chatelier [55], reporting that the flame propagation is controlled by the conduction of heat from the burned to the unburned mixture. The effect of molecular transport processes on the laminar burning velocity and the dependency of the reaction rate on the flame temperature was introduced by Zel'dovich and Frank-Kamenetskii in 1938 [38]. The importance of laminar flame chemistry was highlighted by Semenov and Hinshelwood [56, 57], reporting the complex chain reaction mechanism with the understanding of the formation and consumption of intermediate radical species. The computation of the hydrogen laminar flame structure was initiated by Dixon-Lewis and Williams [58] using a theoretical estimation of diffusion and transport properties of the mixture. As a result of these studies, the structure of the premixed flame can be computed numerically nowadays.

The structure of the laminar premixed flame, a complex interplay of temperature and species concentration profiles, can be computed using a detailed chemical kinetic mechanism with appropriate thermodynamic and molecular transport properties. This flame structure, consisting of four zones: the cold zone (unburned gas mixture), the preheat zone (heat conduction and mass diffusion), the reaction zone (chemical reaction and mass diffusion), and the product zone[59], presents a significant intellectual challenge. An example of the flame structure for a stoichiometric CH_4/air flame at an initial temperature of 300 K and pressure of 0.1 MPa is presented in Figure 2.1 [59]. The nonlinear heat release rate, increasing the temperature until it reaches the adiabatic temperature in the product zone, and the involvement of many chemical species in different reactions in the reaction zone underscore the need for advanced computational methods.

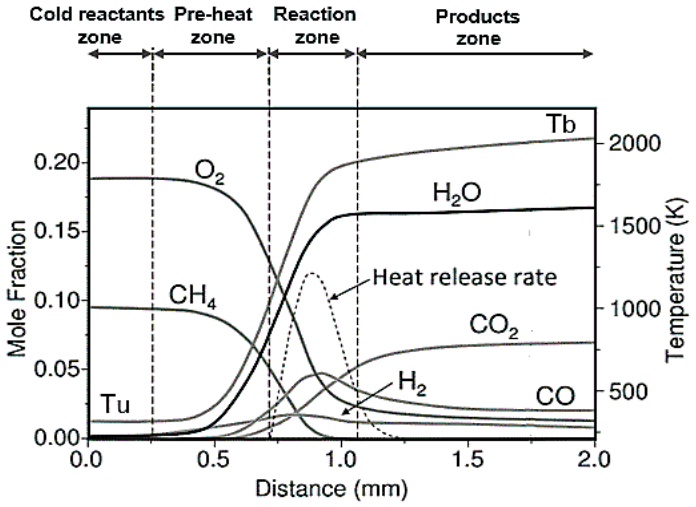

Figure 2.1: Temperature, Heat Release Rate (HRR), and species profile for 1-D adiabatic premixed laminar flame of a stoichiometric methane/air mixture at 0.1 MPa and 300 K [59].

2.1.2 Flame Thickness

Flame thickness, δ_l, is defined as the distance between the end of the cold reactant zone and the product zone's beginning [60] (Figures 2.1 and 2.2). The flame thickness includes the preheat and reaction zone thickness (Figure 2.1). The preheat zone presents the largest proportion of the flame thickness. Determining δ_l is challenging as these zones have rapid heat and mass transfer. This problem is critical in hydrogen flames, as H radicals in the reaction layer diffuse upstream and recombine there. Consequently, the preheat zone is not chemically inert [61]. Different methods have been adopted in the literature to calculate the flame thickness. The thermal flame thickness [62] is commonly derived from the temperature profile of the flame structure:

$$\delta_l = {(T_b - T_u)}\Big/{\left(\frac{dT}{dx}\right)_{max}} \tag{2.1}$$

where T_b and T_u are the adiabatic and unburned gas temperatures, respectively. $\left(\frac{dT}{dx}\right)_{max}$ is the maximum temperature gradient within the flame. The dimensional (or diffusive) laminar flame thickness [63] is the thermal diffusivity ratio to laminar burning velocity, D/u_l. Substituting the thermal diffusivity (D) with the viscosity and Prandtl number, *Pr*, the above equation can be re-written as:

$$\delta_l = {\frac{\nu}{u_l}}\Big/{Pr} \tag{2.2}$$

where ν is the cold mixture kinematic viscosity. The flame thickness is the ratio of kinematic viscosity to laminar burning velocity for the mixture with a unity Prandtl number.

Göttgens et al. [61] have evaluated the flame thickness for hydrogen and hydrocarbon fuels by solving the governing equations using detailed chemistry for 1-dimensional planar steady premixed flames and proposed the following expression for the flame thickness:

$$\delta_l = \frac{\left(\gamma/C_p\right)_{T^o}}{\rho_u u_l} \tag{2.3}$$

where γ is thermal conductivity, C_p is mixture-specific heat at constant pressure, ρ_u is the unburned gas density, and T^o is the critical temperature at which the reaction starts [61]. Following previous works [64-66], Equation 2.3 has been chosen to calculate the flame thickness in the present study.

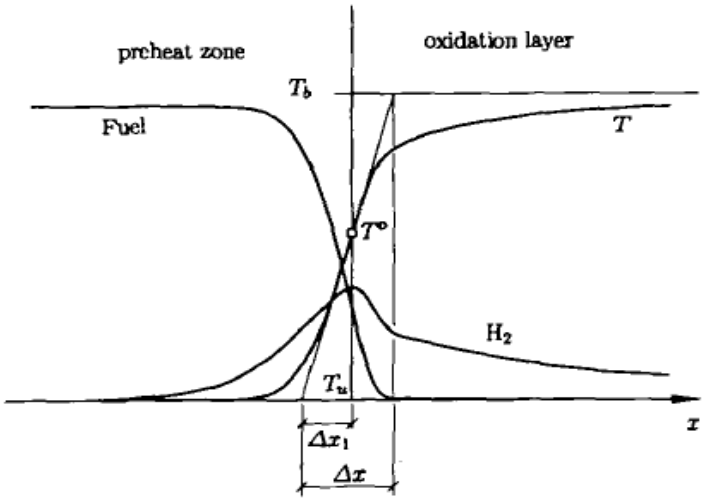

Figure 2.2: Illustration of flame thickness $\delta_l = \Delta x$ [61].

2.1.3 Flame Stretch Rate

Flame stretch rate (α) strongly affects spherical laminar flame propagation and extinction, changing the species concentrations and temperature gradients in the preheat and reaction zones [34, 67, 68]. Stretch results from transverse and tangential velocity components and flame curvature [60, 69]. The effect of stretch rate on flame extinction was first investigated by Karlovitz et al. [70], followed by a study on the relationship between stretch and flame curvature by Markstein in 1964 [60]. Williams expressed the overall stretch rate as the change in flame surface area by the original area (Equation 2.5) [62, 71].

$$\alpha = \frac{1}{A}\frac{dA}{dt} = \frac{1}{\pi r_{sch}^2}\frac{2\pi r_{sch} dr_{sch}}{dt} = \frac{2}{r_{sch}}\frac{dr_{sch}}{dt} = \frac{2}{r_{sch}}S_n \quad (2.5)$$

where r_{sch} is the flame radius from the Schlieren image, and S_n is the stretched flame speed.

The stretch rate and flame instability (explained in the next section) must be reported with the associated Markstein number in spherical laminar flame propagation. The stretch rate and the onset of instability determine the unstretched laminar burning velocities and Markstein numbers (Ma_b) [71]. Ma_b is a dimensionless number that quantifies the flame stretch rate effect upon the laminar flame speed [71]. A small value of Ma_b indicates that the flame stretch rate has only a minor impact on the flame speed. For positive Ma_b, the flame speed decreases with increasing flame stretch rate. In contrast, a negative Ma_b value is accompanied by the early onset of cellularity and flame speeds that increase with increasing stretch rate [72, 73]. To present complete quantitative studies on laminar flame characteristics, Markstein numbers, flame instabilities and stretch rates must be reported alongside the laminar burning velocities.

2.1.4 Unstretched Laminar Burning Velocity

The unstretched laminar burning velocity (u_l) is critical in designing and optimising practical combustion systems, including gas turbines, IC engines, furnaces, and rocket engines [74]. Despite the turbulent nature of these systems, u_l remains a fundamental parameter, particularly in the design and optimisation of gas turbine burners [63, 75, 76]. It is derived experimentally to provide reliable data for validating kinetics models, and it can be used as a thermo-physical parameter in combustion modelling. Therefore, an accurate experimental and computational determination of the laminar burning velocity is crucial in the field of combustion [74].

Many experimental setups have been designed to derive the laminar burning velocity, such as the flat-burner flame, the counter flow/stagnation flame, and outwardly propagating spherical flames. The latter is the most effective method to derive the laminar burning velocities at elevated pressures relevant to gas turbine conditions [76]. Moreover, the spherical outward flame propagation provides a well-defined stretch rate and controlled experimentation, and the flame configuration is straightforward [74, 75]. The present study uses the Leeds spherical explosion vessel (MK-II) to derive the laminar burning velocity for hydrogen/air and methane/hydrogen/air mixtures. The laminar burning velocity of a fuel/air mixture is affected by many parameters, such as fuel/air/diluent mixture, pressure, temperature, and other higher-order effects, such as Soret and Dufour effects [26]. Equation 2.4 can be used to identify the overall dependency of laminar burning velocity on mixture temperature and pressure.

$$u_l/u_{lo} = \left(T_u/T_{uo}\right)^{\alpha} \left(P_u/P_{uo}\right)^{\beta} \tag{2.4}$$

where T_u and P_u are the initial mixture temperature and pressure, the subscription 'o' means the reference value of u_l, T and P, α is the temperature exponent, and β is the pressure exponent [26, 77, 78]. The increased initial temperature always results in increased u_l, and the temperature exponent is a function of several parameters such as fuel type, oxidiser type, pressure, temperature and equivalence ratio [27]. However, the increased pressure results in lower u_l and the value of β is negative for hydrocarbon fuel/air mixtures [26, 79].

In hydrogen/methane/air mixtures, the unstretched laminar burning velocities increase when the hydrogen volume fraction increases, as hydrogen has significant thermal and chemical effects [75, 80, 81]. Firstly, hydrogen increases the adiabatic flame temperature for the fuel. The hydrogen supplies free active radicals (H, O, OH) to the reaction [17, 82, 83].

Mandilas et al. [84], Hu et al. [73] and Okafor et al. [85] used Schlieren photography to determine the laminar burning velocities of methane/hydrogen/air mixtures in a cylindrical combustion chamber at various hydrogen volume fractions. They concluded that the unstretched laminar burning velocities increase significantly as the hydrogen fraction increases. The same conclusion was made by Wang et al. [86], who conducted an experimental study to derive the laminar burning velocities of methane/hydrogen/air mixtures in a flat flame burner at constant fuel/air mass flow rates. Hu et al. [73] researched hydrogen volume fractions varying from 0 to 100%. They concluded that the laminar burning velocity increased linearly with temperature but decreased as the initial pressure was increased. In addition, the u_l is varied with the equivalence ratio. The peak value of the u_l was found in rich methane/air mixtures (ϕ=1.1) and shifted to the richer mixture side with the increase of the hydrogen fraction [75].

2.1.5 Flame Instabilities

Flame instability is one of the most important phenomena that must be highlighted in the experimental study of premixed outward laminar flame propagation, especially at high initial pressure with a non-unity Lewis number fuel mixture (*Le*). Flame instabilities and cell structure formation on the laminar spherical flame surface have been well studied [87]. In the spherical explosion with central ignition, the flame propagates smoothly in the early stage. Suddenly, with flame kernel growth, the flame becomes unstable with the formation of different-size cells in dynamic equilibrium [87]. The cellularity increases the surface area and accelerates the laminar flame propagation. If the allowance is made for the fireball to become large enough, the flame propagation might become turbulent and eventually detonate [88].

The interaction between the flame and the hydrodynamic disturbances leads to flame front wrinkling (instability). A hot product expands at the line interface between the burned and unburned gases, generating vorticity (Figure 2.3). As a result, the cold gases entering the flame converge and diverge, creating localised pressure changes, which lead to flame wrinkling [89]. The instability can also develop due to the competition between the energy and mass diffusion (thermo-diffusive effect). The heat flux from the burned to unburned gases is indicated by the full arrowed lines in Figure 2.3, while the broken arrowed lines indicate the species diffusion flux from the cold to the hot gasses. The molecular transport of energy and species diffusion (thermo-diffusive) can stabilise or further destabilise the flame [38].

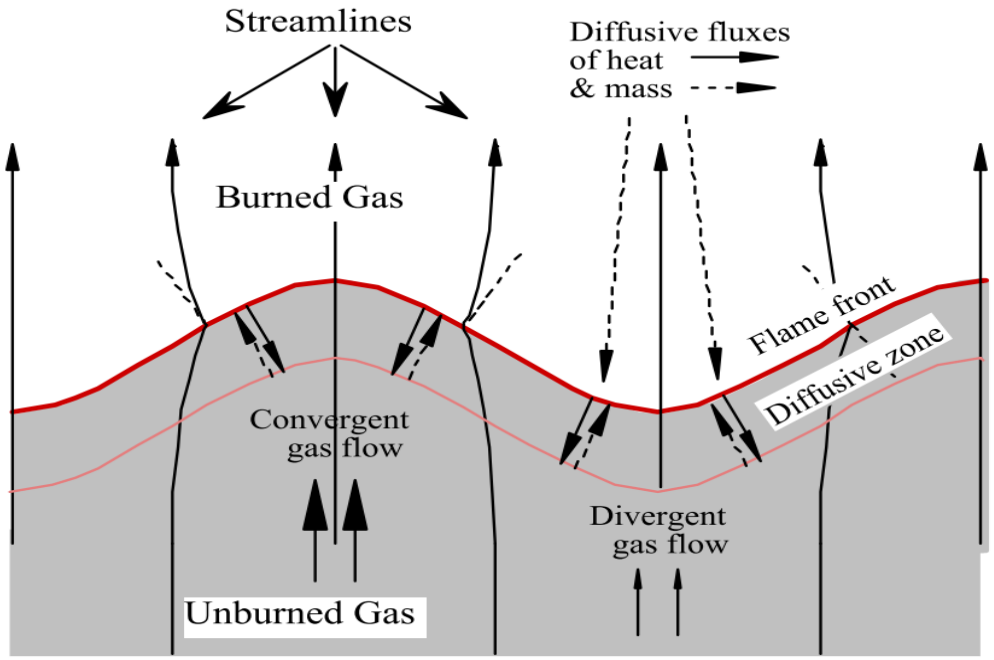

Figure 2.3: Structure of a wrinkled flame front showing the hydrodynamic streamlines and the diffusive fluxes of heat and mass [90].

There are two main types of instability. First, the hydrodynamic instability is called the Darrieus-Landau (D-L) instability, as they first reported in 1938 and 1944 [91, 92]. This instability develops due to the density differences across the flame. D-L instability also appears when the flame thickness is much thinner than the hydrodynamic scale of the flow. For example, the reaction rate can increase in high-pressure combustion, and flame thickness decreases, resulting in D-L instability [93]. The second type of instability is the diffusional–thermal (D-T) instability. The D-T instability develops when the Lewis number is lower than one. The mixture's Lewis number is a ratio of thermal diffusivity to mass diffusivity. The D-T instability is enhanced with mixtures of Lewis numbers below unity [38, 93]. The effective Lewise number is used in the present study [94]; $\left(Le_{eff} = 1 + \frac{q_{CH_4}(Le_{CH_4}-1)+ q_{H_2}(Le_{H_2}-1)}{q}\right)$; where qCH_4 and qH_2 are the non-dimensional heat release associated with the consumption of methane and hydrogen, respectively, and q is the total heat release. The method of calculating the heat release rate and the Lewise number are presented in [95] and the Lewise number of the current mixtures at different pressure is given in Figure 2.4.

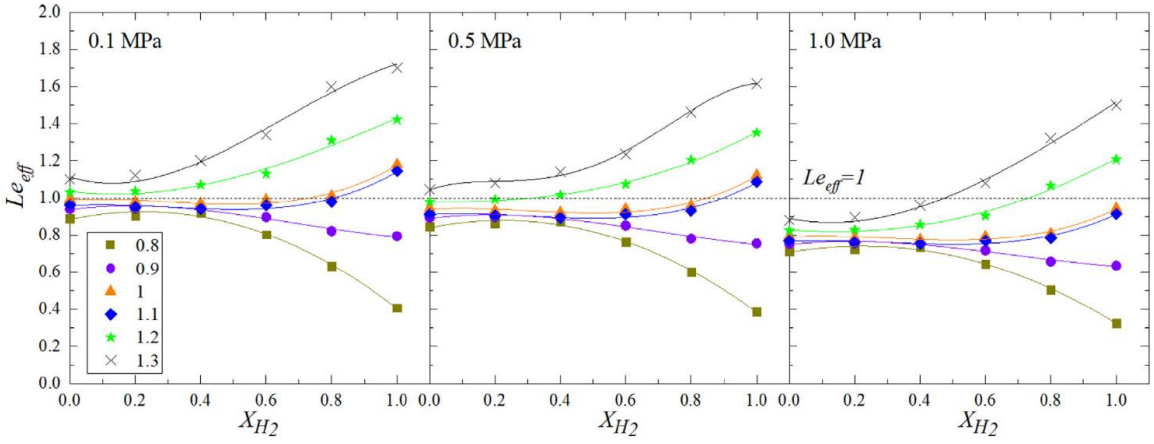

Figure 2.4: The effective Lewis number plotted against hydrogen fraction at 0.1, 0.5 and 1.0 MPa [94].

When the thermal diffusivity is lower than the mass diffusivity, the gas flow is convergent and divergent, resulting in flame instability (Figure 2.3). The flame is more stable for fuel with a Lewis number higher than one. The phenomena of D-L and T-D instabilities are well reported in the literature [12, 72, 75, 96, 97]. In addition to these two instabilities, gravity induces buoyancy instability [98]. Still, it can be neglected in the fast flame propagation due to the small effect of gravity compared to the D-L and T-D instabilities [96].

Other studies have reported the interactions between the D-L and T-D instabilities in spherical flame propagations [96, 98]. In hydrogen/methane/air mixtures, the increased hydrogen volume fraction enhances the T-D instability as *Le* decreases due to the substantial mass diffusion of hydrogen [99]. Egolfopoulos et al. [100] reported that the Lewis number for the mixture was modified by replacing the nitrogen with an inert gas to suppress the T-D instabilities. Helium is commonly used as it reduces the burning rate and increases flame thickness, suppressing the D-L instabilities. However, the ignition energy of the mixtures increased, and the burning rate decreased, especially at high pressures [100]. Inert gases such as argon and helium have also been used in other studies to suppress flame instability [101, 102].

The spherical flame initially propagates with a smooth surface. Cracks resulting from ignition effects were shown in [72] within the stable flame front. The cellular surface appears as the flame grows due to D-L and T-D instabilities at the critical flame radius, r_{cl}. The size of r_{cl} depends on flame characteristics such as fuel type, equivalence ratio, pressure and temperature; these effects will be expanded in Chapter 4, section 4.2. The onset of flame instability is the transition from the stable to the unstable region. The onset of instability has been extensively studied in the literature by identifying the critical Peclet number, $Pe_{cl,}$ defined as r_{cl}/δ_l [88, 96, 103].

Pe_{cl}, or the transition point of the flame propagation, is affected by hydrogen fraction, equivalence ratio, initial pressure and temperature. The onset of instability is also quantified by the critical laminar Karlovitz number, K_{cl}, defined as the critical flame stretch rate multiplied by the chemical time scale (δ_l / u_l) [64].

Stretch smooths the surface and stabilises the flame. The cellularity only appears once the flame radius reaches the critical radius (r_{cl}) when the stretch rate is insufficient to flatten the cellular structure [104, 105]. After r_{cl}, the flame propagates with increased speed because of cellularity, which increases the flame surface area [88]. Figure 2.5 presents a Schlieren image to show the smooth and cellular flame structure for 30% hydrogen in methane with initial pressures of 0.1 MPa, 0.5 MPa, temperature 303 K and equivalence ratio 0.8 [12]. The flame in the image (a) is stable, with only a few cracks resulting from the ignition effect [72]. However, the flame in the image (b) is unstable.

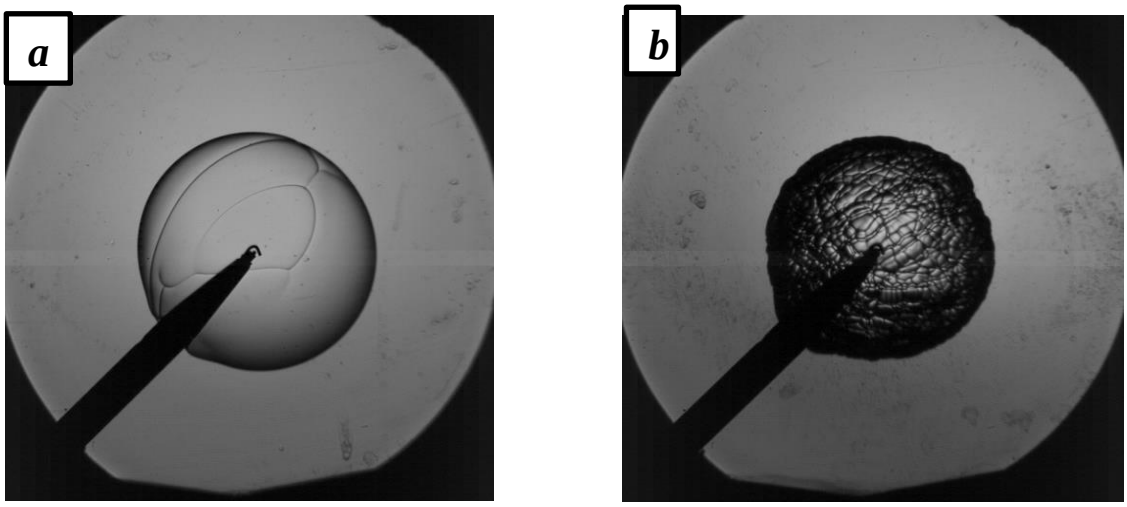

Figure 2.5: Flame images for 30% hydrogen in methane with initial temperature 303 K, equivalence ratio 0.8, and 40 mm flame radius (a) the smooth flame 0.1 MPa, (b) the cellular flame structure 0.5MPa.

2.1.6 Measurement Uncertainty and Limitations of Experimental Procedures

Egolfopoulos et al. [100] have presented a review that closely analysed the challenges in laminar flame experiments. In the spherical flame experiments, the adopted assumptions to derive the unstretched laminar burning velocity are:

a- The flame is adiabatic.

b- The burned gases are under thermodynamic equilibrium and stagnant.

c- The flame surface is smooth (free from cellularity).

d- The ignition energy is low. The ignition effect should not be included in the data used to derive the laminar burning velocity.

e- The radiation heat transfer is negligible.

f- The combustion vessel wall does not affect flame propagation (negligible wall confinement).

In the present study, the ignition energy is kept to a minimum (1 mJ) [106], and the ignition-affected data in the early flame propagation is not included in the derivation of the laminar burning velocity [71]. Equilibrium in the hot gases can be assumed as the radiation heat transfer is negligible. The current fuel mixtures (hydrogen/methane/air) have a high burning rate and minimum radiation heat loss [100]. Moreover, in the present study, the maximum flame radius used is less than 30% of the inner radius of a large spherical vessel (internal radius =190 mm) to avoid any effect of wall confinement on the measurement of flame speed. The flame speed measurements with wall confinement effects are 15-20 % less than those for large vessels without wall confinement [107]. Therefore, the error due to the ignition energy and radiative heat transfer is negligible.

Other sources of error in the experimentally derived laminar burning velocities have been evaluated elsewhere. These include the equivalence ratio [80, 108] and the adiabatic flame temperature assumption [105]. In the experimental procedure, the combustion vessel is evacuated first, and then the fuel is injected into the vessel based on its pressure fraction, followed by air injection. The change in the temperature during the fuel/air injection can affect the accuracy of the equivalence ratio ϕ, which was estimated to be ± 0.04 in the value of ϕ [80]. Another well-known source of error is the stretch correction approach (extrapolation method). Dowdy et al. [109] used linear extrapolation (equation 2.6) to obtain the unstretched flame speed and Markstein length.

$$S_s - S_n = \alpha L_b \tag{2.6}$$

where S_s is the unstretched flame speed, S_n is the stretched flame speed, α is the stretch rate, and L_b is the burned gas Markstein length. Kelley and Law [110] introduced the nonlinear extrapolation method as in the following equation:

$$\left(S_n/S_s\right)^2 \ln\left(S_n/S_s\right)^2 = -\frac{2\alpha L_b}{S_s} \tag{2.7}$$

Many other nonlinear equations are presented in the literature and summarised in [26]. The uncertainty due to the extrapolation method could be as high as 10% of the laminar burning velocity [26, 100]. Thus, this point is considered in the present study and will be discussed in Chapter 3.

The Darrieus-Landau and thermo-diffusive instabilities limit the derivation of laminar burning velocity. Research on laminar burning velocities for pure hydrogen is well known [111-114]; however, the experimental derivations of the unstretched laminar burning velocity at high initial pressures ($P_u \geq 0.3$ MPa) are very challenging due to the presence of flame cellularity in the early stages of flame propagation, which results from the Darrieus-Landau and thermo-diffusive instabilities [97]. At these conditions, there is a lack of data that can be extrapolated to obtain the laminar burning velocity. Consequently, many methods have been introduced in the literature to derive the laminar burning velocity at these conditions. Firstly, Bradley et al. [97] used the linear instability theory of Bechtold and Matalon [88] and the fractal theory of Bradley [98] to expand the stable regime and extrapolate it to zero stretch rate to obtain the unstretched laminar burning velocities for lean hydrogen at high initial pressure. Bradley et al. [97] proposed the flame speed enhancement factor, *F*, the ratio of flame speeds with and without instabilities. The theoretical stable flame speed, *S*, can be calculated from *F*. Then, *S* can be plotted as a function of the flame stretch rate, α, and extrapolated to zero to obtain the unstretched flame speed. This method [97] has been recently adopted to obtain the laminar burning velocities and examine pure hydrogen's flame cellularity at high pressures [96]. However, the calculation of *F* includes an empirical constant, which has been taken as 1/3 in [97]. It may not be suitable for the wide range of initial conditions and equivalence ratios needed to explore the laminar burning velocity.

Secondly, inert gases were used to dilute the explosive mixture [102] to suppress the flame instability. Helium and Argon are used to dilute rich and lean hydrogen-oxygen mixtures to obtain the laminar burning velocity at high initial pressure [101]. However, the present experiments focus on a hydrogen/methane/air mixture.

Thirdly, the laminar burning velocity at these conditions can be obtained if accurate kinetics become available. Thus, the precise prediction of laminar burning velocity at these conditions was the aim of kinetic researchers [26, 115, 116]. Three H_2/CH_4 combustion mechanisms were compared in this work with the experimentally derived laminar burning velocities. The most accurate mechanism has been used to determine the laminar burning velocity of hydrogen/air at high initial pressure. A review of the kinetics is presented below.

2.1.7 The Numerical 1-D Laminar Burning Velocity

An essential reason for measuring the unstretched laminar burning velocity is to provide reliable data for validating kinetics models used in the design of practical applications. However, there is uncertainty in both the experimental measurements (as discussed above) and numerical predictions [26]. The present study calculated the premixed laminar burning velocity using the one-dimensional steady freely propagating planar flame code, Chemkin-Pro [117]. The "Premixed Laminar Flame-speed Calculation" model was used. It can also be used to estimate the mole fraction and the chemical production rate of species in the flame.

In the present modelling, the reaction rate is computed using the Law of Mass Action [118]. The reaction rate constant is calculated using the Arrhenius form. The 1D planar flame is modelled by solving the governing continuity, energy and species conservation equations using detailed chemical kinetics. The system of equations is quasi-1-dimensional and isobaric. These differential equations are solved by implicit finite difference methods and a combination of time-dependent and steady-state methods [116]. The reader is referred to Chemkin help for more detail. Thermal diffusion (the Soret effect) and a multi-component diffusion model were used in the present study. The Soret and diffusional effect drives lighter molecules toward burned gases (hot region) and heavy molecules toward fresh gas (colder regions) [26].

Different combustion mechanisms for methane and hydrogen fuel are presented and reviewed in Konnov et al. [26] at initial pressures ranging from 1 to 70 atm and the cold gas temperature from 300 to 443 K: (i) the San Diego mechanism [116, 119], (ii) the Konnov reduced mechanism [26, 115], (iii) the USC mech. II [120], and (iv) GRI Mech 3.0 [121]. Zhang et al. [115] tested the following mechanisms at initial pressures ranging from 1 to 70 atm and cold gas temperatures from 300 to 443 K: (i) FFCM-I-2016, (ii) SanDiego2014, (iii) NUIG1.1-2021, (iv) Aramco-II-2016, (v) Konnov-2009, (vi) Caltech-2015, and (vii) Glarborg-2018

According to the most recent study [115, 116], the following mechanisms have satisfactory performance for both the ignition delay time and laminar burning velocity measurements for methane/hydrogen/air mixtures.

1- The latest version of the San Diego mechanism, which has 58 species and 270 elementary reactions,

2- The Konnov reduced mechanism with 27 species and 177 elementary reactions

3- The Aramco 2 reduced mechanism with 25 species and 105 elementary reactions.

Therefore, they were selected to compare the experimentally derived laminar burning velocity and the 1D numerical simulation in the present study, as they were previously validated using experimental data [26, 115, 116] and cover a range of mechanism sizes with respect to the numbers of species, the lowest having 25 species and the highest 58.

2.1.8 Research Gaps in the Study of Laminar Flame Propagation

As shown in Table 2.1, a few previous experimental studies have focused on laminar burning velocities for methane/hydrogen/air mixtures at high pressures, which are crucial for hydrogen-fuelled ICEs and industrial gas turbines [26]. Previous studies have determined laminar burning velocities in small-volume vessels, with volumes of 5 L [73, 75] and 3.5 L [85], which could have wall-confinement effects and limited field of view. Therefore, researchers in [73, 75, 85] had to extrapolate the data of the flame radius up to 25 mm to reduce the pressure increase and wall confinement effect on the measurements. To avoid the disadvantages of small combustion vessels, a large spherical vessel (30 L) is used in the present study to investigate hydrogen/methane/air flame propagation at constant pressure (pre-pressure measurements) to provide experimental data (laminar burning velocities and Markstein numbers). In this large vessel, the flame propagation was recorded at up to a 75 mm flame radius while pressure fluctuations remained small (this will be given later in section 4.1).

Hu et al. [75] derived laminar burning velocities for hydrogen/air and methane/hydrogen/air mixtures using spherical outward flame propagation, but only for atmospheric conditions. Following their initial study, Hu et al. [73] explored methane/hydrogen mixtures at pressures up to 0.75 MPa, but the equivalence ratio (ϕ) was only 0.8, limiting its applicability since the air-fuel ratio varies over a wide range in practical combustors, such as gas turbine combustors, industrial furnaces and aviation engines [122]. Therefore, the current study aims to fill the research gap by providing experimental laminar burning velocities and Markstein numbers for lean, rich hydrogen/air and methane/hydrogen/air mixtures at high pressures.

Table 2-1: Compares the experimental conditions (equivalence ratio, unburned gas pressure and temperature) and previous outward flame propagation studies.

References	% H_2 by volume	P_u (MPa)	T_u (K)	ϕ
Hu et al. [75]	0, 10, 20, 30, 40, 50, 60, 70, 80, 90, 100	0.1	303	*for H_2/CH_4/air 0.6-1.4 **for pure H_2/air 0.6-4.5
Hu et al. [73]	0, 20, 40, 60, 80, 100	0.1, 5, 7.5	303, 373, 443	0.8
Okafor et al. [85]	0, 10, 30, 50, 70, 90, 100	0.1	350	0.8, 1, 1.2
Bradley et al. [97]	100	0.1, 0.5, 1.0	365	0.4, 0.5, 0.6, 0.7, 0.8, 0.9, 1
Present study	30, 50, 70, 100	0.1, 0.5, 1.0	303, 360	*for H_2/CH_4/air 0.8, 0.9, 1, 1.1, 1.2 **for pure H_2/air 0.5, 0.8, 1, 1.5, 1.7, 2, 2.5

2.2 Turbulent Burning Velocity

Early research by Mallard and Le Chatelier [55] provided a basic understanding of flame propagation in turbulent flow, namely that turbulent fluctuation enhances the burning rate of premixed flames. However, the effect of turbulent flow on the flame is far more complicated [123]. The burning rate is affected by turbulence characteristics, laminar flame speed, flame stretch, molecular diffusion and the molecular heat diffusivity of the mixture [123]. Damköhler [124] improved the understanding of premixed turbulent flames by introducing the Damköhler number (*Da*), a key dimensionless parameter representing the ratio of turbulent time scale to chemical time scale. Damköhler's work highlighted two mechanisms through which turbulent flow increases the burning rate: (a) large turbulent scales extend the flame surface by wrinkling the flame sheet, and (b) small turbulent scales enhance transport processes within the combustion wave [38]. Further advancements by Karlovitz et al. [70] underscored the role of local stretch in turbulent flames, driven by increased velocity gradients within the flame, leading to an augmented turbulent burning velocity.

The impact of turbulent flow on the burning velocity of hydrogen/air and hydrogen/methane/air flames is critical in designing practical engineering devices for hydrogen fuel operation. The power output in these devices is controlled by the burning mass rate determined by the turbulent burning velocity (u_t). The u_t increases as the fluctuating velocity (u') increases; however, the growth rate in u_t decreases as u' rises further. Eventually, a maximum u_t is achieved, followed by a significant decline in u_t as u' continues to increase, ultimately leading to flame quenching due to high aerodynamic strain rate and heat loss [66, 125]. The turbulent scales have different effects on turbulent flame. The integral scales primarily govern flame convection and can only induce significant wrinkling in large flame kernels [125, 126]. In contrast, the Kolmogorov scales may lack the energy for effective flame wrinkling [43]. Therefore, the Taylor scales are central to flame wrinkling due to their responsibility for shear forces.

The literature provides different definitions of turbulent burning velocity [37, 127, 128], making it necessary to define this parameter in each study. The turbulent burning velocity for any fuel under specific operating conditions is a critical determinant in calculating the mass rate of burning. The mass rate of burning equals the product of turbulent burning velocity, cold reactant density, and surface area. Any change in one of these parameters necessitates a corresponding change in at least one other to determine the burning rate of premixed combustion [129]. The turbulent burning velocity is the unburned gas velocity normal to a selected surface on the flame brushes [127]. This velocity yields the mass rate of burning [127]. It has been given different terms in the literature: mass burning velocity [125], consumption speed, turbulent burning velocity [128], global turbulent burning and velocity global consumption speed [130]. In the present study and following Bradley et al. [127, 129], it is called the turbulent burning velocity (u_t).

Other burning velocities have been measured in the literature, depending on the measurement method and the reference surface from which the turbulent velocity is derived. The burning velocity measured at the leading edge of the mean flame brush is higher than this at the root of the flame [131]. The turbulent burning velocity can be measured from the cold gas velocity or flame velocity, but the location of the measurement surface should be described [127]. Initially, the engulfment velocity (u_e) represents the reactant velocity from the external zone towards the leading flame edge [129] (Figure 2.6b). However, this velocity (u_e) cannot be directly used to calculate the mass rate of burning because a significant amount of unburned gas remains behind this surface. The reactant must be converted into products after passing the reference surface [127, 129]. Secondly, the displacement velocity (u_d) indicates the flame's movement along its normal with respect to the fresh gases. It is also defined as the cold reactant velocity towards the flame, measured at its leading edge, typically in the context of a low-swirl burner using the Particle Image Velocimetry (PIV) technique [132]. This velocity is suitable for determining the mass rate of burning in the case of a flat flame, which is mainly a theoretical or numerical concept [127]. Thirdly, the turbulent burning velocity derived from pressure increases in a constant volume explosion is associated with forming combustion products [129, 133]. In the context of the present study, the turbulent burning velocity determined using the Schlieren technique is linked to the consumption rate of unburned gases, as Schlieren images rely on changes in mixture density. The Schlieren image provides a surface ahead of the flame tip in the preheat zone. The Schlieren system detects the density gradient which results from temperature gradient rather than chemical reaction as shown in Figure 2.6a.

Bradley et al. [129] showed that the reference flame radius for a spherical turbulent flame propagation can be identified from high-speed Schlieren images. This reference radius can be used to determine the mass turbulent burning velocity. They used Mie scattering from a thin planar sheet to describe the radial distribution of the flame brush (Figure 2.6b). Bradley et al. [129] assumed that the thickness of the turbulent flame brush is constant as the flame grows [134]. The mass conservation law is then applied to identify the reference radius for the turbulent burning velocity [129]. They concluded that the mass turbulent burning velocity could be obtained at the reference radius, r_v, which falls between r_r and r_t, such that the volume of burned gases inside the sphere matches the volume of unburned gases outside the sphere (Figure 2.6b). At this reference (r_v), the turbulent burning velocity gives the burning mass rate when multiplied by the cold reactant density and surface area. Bradley et al. [129] compared $u_t(r_v)$ with turbulent burning velocity from Schlieren measurement ($u_{t(r_{Sch})} = \frac{\rho_b}{\rho_u}\frac{dr_{Sch}}{dt}$). They showed that the turbulent burning velocity from Schlieren measurements must be divided by a factor of 1.11 ($u_t = \frac{1}{1.11}\frac{\rho_b}{\rho_u}\frac{dr_{Sch}}{dt}$) to obtain the mass rate of burning velocity. The present study assumed that the thickness of the turbulent flame brush is constant as the flame grows and is not affected by changing the fuel/air mixture, rms velocity, pressure and temperature. Therefore, the factor of 1.11 from Bradley et al. [129] study is used to determine the turbulent burning velocity (u_t).

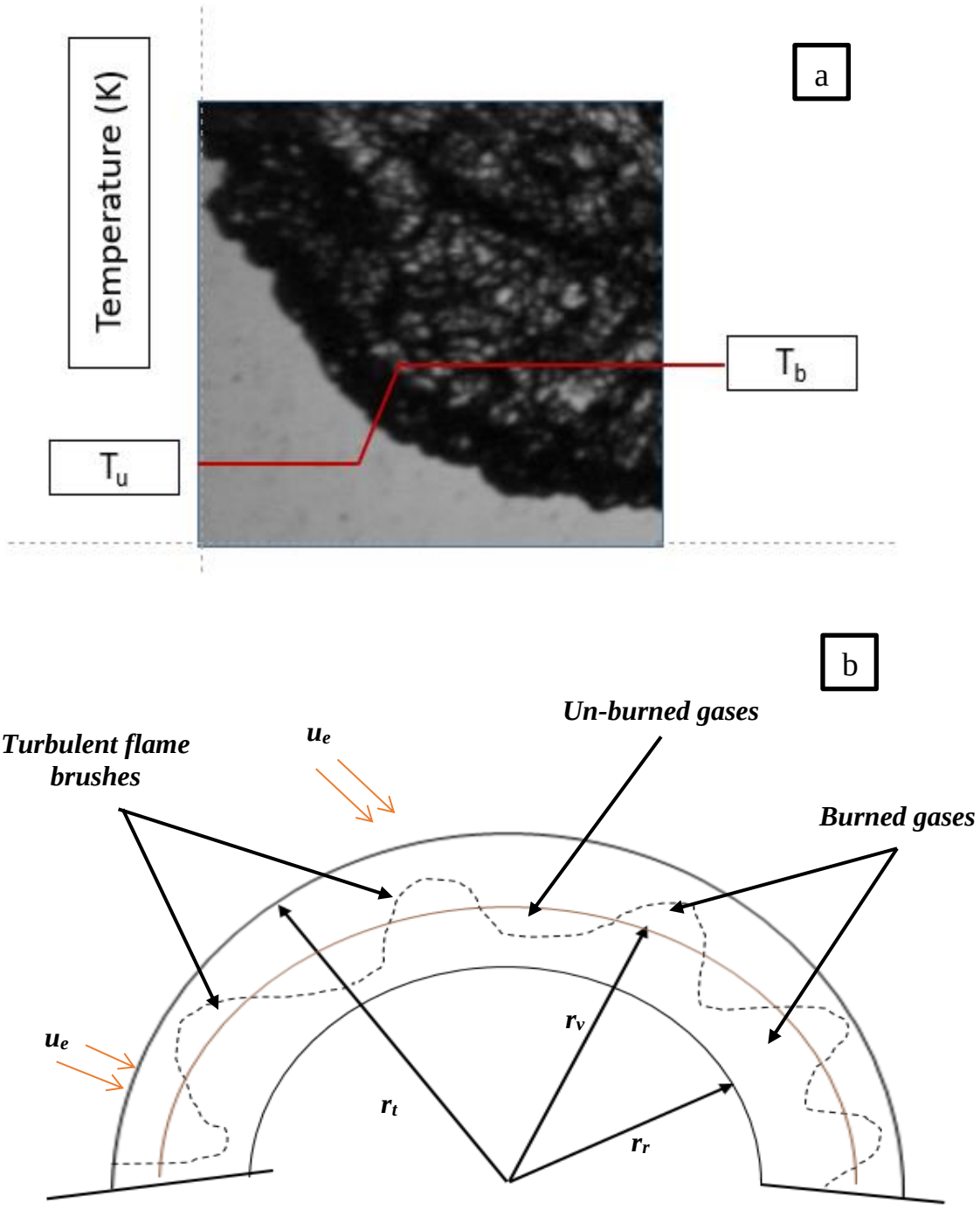

Figure 2.6: The turbulent flame brushes and the associated flame radius, where T_u is the initial mixture temperature, T_b is the adiabatic flame temperature, u_e is the engulfment velocity, r_t is the flame radius at the tip of the brush, r_r is the flame radius at the root of the brush, and r_v is the volumetric flame radius.

2.2.1 The Effective Root Mean Square Velocity u'_k

In the spherical turbulent premixed flame propagation, the flame front of the initial small flame kernel is affected only by small eddies with high wave numbers that wrinkle the flame surface. In contrast, the large eddies with lower turbulent frequencies drift the flame kernel without wrinkling the flame front. Over time, as the flame kernel grows, the flame front becomes increasingly affected by eddies with lower turbulent frequencies, resulting in a continuous increase in turbulent burning velocity [125, 127]. Therefore, it is essential to consider the relevant frequency range of the turbulent power spectrum when measuring the turbulent burning velocity of spherical flames. To address this effect, the effective root mean square (rms) velocity u'_k, which represents the local rms turbulent velocity at the flame surface, has been proposed [125]. In the present study, and following Bradley et al. [66, 125, 127, 135], u' is replaced by u'_k in the analysis of turbulent burning velocity for the spherical expanding flame.

The effective rms velocity u'_k, defined as the local rms turbulence velocity adjacent to the flame front, increases with flame propagation until it approaches the u' value [136]. Bradley et al. [136] derived the ratio $\left({u'_k}/{u'}\right)$ by integrating the non-dimensional power spectral density, $\bar{S}\left(\overline{K_\eta}\right)$ (Figure 2.7), over the range of relevant wavelengths.

$$\frac{u'_k}{u'} = \left[\frac{15^{0.5}}{R_\lambda}\int_{\overline{k_{\eta K}}}^{\overline{k_{\eta G}}} \bar{S}\left(\overline{K_\eta}\right) d\overline{k_\eta}\right]^{1/2} \tag{2.8}$$

where $\overline{k_\eta}$ is the dimensionless wave number, R_λ is Reynolds number based on the Taylor length scale λ, and $k_{\eta K}$and $k_{\eta G}$ are the smallest and largest wavelengths, respectively.

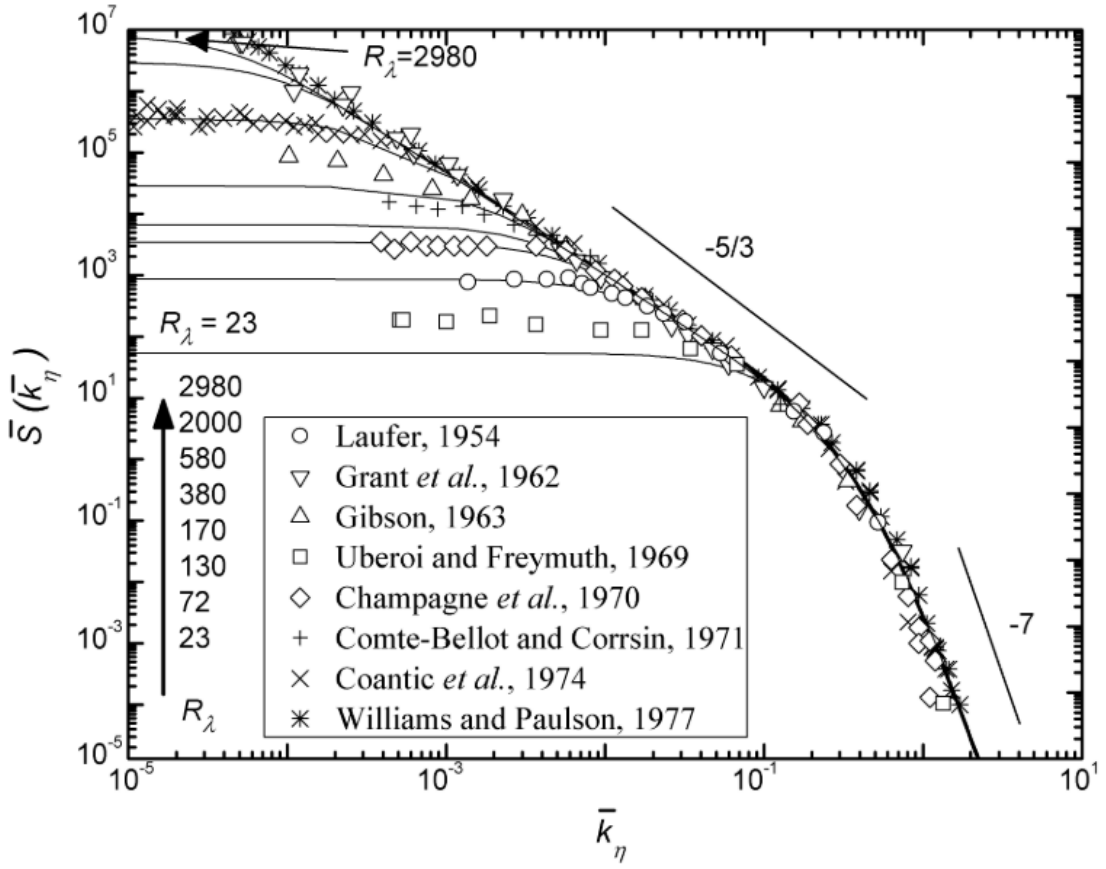

Figure 2.7: The shape of power spectral density from different researchers [38]

The upper limit $k_{\eta k}$ was assumed to be the flame diameter and the lower limit $\boldsymbol{k_{\eta G}}$ depends on the size of the smallest eddy that can have a chemical effect on the flame during its lifetime, which is taken as the Kolmogorov scale (η) [65].

$$\bar{k}_{\eta k} = \frac{2\pi\eta}{n_k L} = \left(\frac{32\pi}{15^{0.25}\, nk}\right) R_\lambda^{-1.5} \tag{2.9}$$

$$nk = \frac{2\, r_u}{L} \tag{2.10}$$

$$\bar{k}_{\eta G} = \frac{2\pi\eta}{l_G} \tag{2.11}$$

where l_G is the Gibson scale and calculated from:

$$\frac{l_G}{L} = 0.133\left(\frac{u'}{u_l}\right)^{-3} \tag{2.12}$$

$$\bar{S}\left(\overline{K_n}\right) = \frac{0.01668R_\lambda^{2.5} + 3.74R_\lambda^{0.9} - 70R_\lambda^{-0.1}}{1 + \left(0.127R_\lambda^{1.5}\,\overline{k_\eta}\right)^{5/3} + \left(1.15R_\lambda^{0.622}\,\overline{k_\eta}\right)^{4} + \left(1.27R_\lambda^{0.357}\,\overline{k_\eta}\right)^{7}} \tag{2.13}$$

During the propagation of the turbulent spherical expanding flame, the effective rms velocity continuously increases, increasing the burning velocity. Therefore, there is no single $u_{t,}$ which varies with the flame radius. However, Bradley et al. [129] and Lawes et al. [126] have taken u_t at a flame radius of 30 mm as a reference value in the analysis of turbulent flame propagation. There are many reasons for choosing this reference value. Firstly, positioning the flame at this radius extends beyond the spark plasma's influence, as the spark effect typically extends up to 10 mm [80]. Secondly, the flame at 30 mm is exposed to the full range of turbulent scales, as the flame kernel exceeds the vessel's integral length scale (L = 20 mm) [135, 137, 138], and the turbulent flow in this region is homogenous and isentropic [137].

2.2.2 Turbulent Flow and Flame Characteristic/Field Definitions

For investigating the turbulent flame propagation, the rotating speed of four stirred-fans, *f*, was adjusted for the desired *u'*, using the following equation described in [137]:

$$u' = 0.00124\,f \;\; ms^{-1} \tag{2.14}$$

where f is the fan speed in rpm. The values of u' in Leeds MK-II vessel have been studied comprehensively using a range of flow measurement techniques, including Hotwire Anemometry (HWA) [135], Laser Doppler Velocimetry (LDV) and Particle Image Velocimetry (PIV) [126, 135, 137]. Throughout the experiments, the fans operated at a constant speed. It is assumed that u' and the integral length scale are independent of pressure and temperature. The validity of this assumption has been demonstrated previously [127, 129, 137]. These studies showed that the effect of changing the initial pressure and temperature on u' is negligible. As u' with $f = 6000$ rpm decreased by 5% with increasing the temperature from 300 to 400 K, it increased by 4% with increasing pressure from 0.1 to 1.0 MPa [137]. The longitudinal integral length scale, L, was 20 mm and is unaffected by changing the fan speed [137, 139].

The Taylor- and Kolmogorov- length scales, λ and η, were derived using respectively [126]:

$$\frac{\lambda}{L} = \frac{A}{Re_\lambda} \tag{2.15}$$

$$\eta = \frac{\lambda}{15^{0.25} Re_\lambda^{0.5}} \tag{2.16}$$

where Re_λ is Reynolds number based on the Taylor length scale.

$$Re_\lambda = \frac{u'\lambda}{\upsilon} \tag{2.17}$$

where υ is the unburned kinematic viscosity and A is a constant (A= 16 ±1.5 [126, 140]).

The turbulent time scale is the ratio of the turbulent length scale to rms turbulent velocity ($^{L}/_{u'}$). The chemical time scale is the ratio of the flame thickness to the laminar burning velocity ($^{\delta_l}/_{u_l}$) [40, 41]. The Karlovitz stretch factor K_{a1}, which is the ratio of the chemical time scale to the turbulent time scale (based on λ) [141], is calculated in [127]:

$$K_{a1} = \left(\frac{u'}{\lambda}\right) \Big/ \left(\frac{u_l}{\delta_l}\right) \tag{2.18}$$

where u'/λ is the rms strain rate, with $Re_\lambda = 4(Re_L)^{0.5}$, $\delta_l = \left(\frac{\upsilon}{u_l}\right) \Big/ P_r$, and $Re_L = \frac{L\,u\prime}{\upsilon}$. Thus, the Karlovitz stretch factor K_{a1} can be calculated as:

$$K_{a1} = 0.25\left(\frac{1}{P_r}\right)\left(u'/u_l\right)^2 (Re_L)^{-0.5} \tag{2.19}$$

In [127], the assumption of a Prandtl number (*Pr)* of 1 was made, though it is not practical when dealing with high hydrogen volume fractions. As the hydrogen fraction increases, the thermal diffusivity also increases, leading to a decrease in *Pr*. *Pr* decreases with increasing ϕ when the hydrogen content in the fuel/air mixture rises. In the present study, the Prandtl number is calculated as the ratio of kinematic viscosity to thermal diffusivity (μ/α).

2.2.3 Turbulent Burning Velocity Correlations

The turbulent burning velocity is a crucial physical parameter in turbulent combustion, often serving as an input parameter for combustion modelling [23-25, 49]. Consequently, numerous studies have aimed to establish a general correlation for u_t [44, 123, 126, 127, 138, 142]. These correlations have linked the turbulent burning velocity to turbulent fluctuation [124] and laminar burning velocity [38, 143].

A review of five different u_t correlations was conducted and presented in [126]. The parameters considered in these correlations typically include the laminar burning velocity u_l, flame thickness δ_l, rms velocity u', and integral length scale, L. However, it is worth noting that the predicted values of u_t from these correlations are often inconsistent within themselves and with experimental results, primarily due to the omission of thermo-diffusive effects [126]. In alignment with Damköhler's theory, the turbulent transport of heat and mass within mixtures and the total surface area of wrinkled flamelets stand out as the primary factors governing the turbulent burning velocity [142]. Hence, Bradley et al. [66, 127, 135] introduced the *U-K* correlation $\left(U = \alpha {K_{a1}}^{\beta}\right)$, where U is the ratio of the turbulent burning velocity to the effective rms turbulence velocity and K_{a1} is the Karlovitz stretch factor.

The *U-K* correlation considers the influence of chemistry, turbulent length scales, flame thickness, flame stretch rate, and rms turbulence velocity. The constants (α and β) are functions of $Ma_{sr,}$ which incorporates the effect of strain rate on the turbulent burning velocity [66, 127, 135]. Recently, Wang et al. [123] correlated u_t with differential-diffusion and stretch effects. They used the general scaling law based on the Damköhler hypothesis: $u_t/u_l = f\left(\left(u'/u_l\right)^x, \left(L/\delta_l\right)^y, Le^{\gamma}\right)$, where L is the turbulent integral length scale, δ_l the laminar flame thickness, and Le the Lewis number. The constants x ~ 0.5-1 and y ~ 0-0.5 [144], the power exponent (γ) for Le have a negligible effect on the correlation for u_t/u_l due to the small absolute value of Le in comparison to Reynolds number [123]. The present study investigates the scaling parameters of previous studies [66, 123, 127, 135] to correlate the turbulent burning velocity for pure hydrogen/air and methane/hydrogen/air mixtures at high initial pressure and rms turbulent flow velocity.

2.2.4 Research Gaps for Turbulent Flame Studies

Previous experimental studies have shown limited focus on turbulent flame propagation for hydrogen/air and methane/hydrogen/air mixtures, particularly at high pressures, which are most relevant to gas turbine applications. Goulier et al. [138] and Morones et al. [145] conducted experimental investigations of turbulent expanding flames of lean hydrogen/air mixtures at atmospheric pressure, with rms velocities ranging from 1.0 to 2.8 m/s. The turbulent burning velocities of methane/hydrogen/air mixtures have been studied over a broad range of initial root mean square velocities (u') in [80], but solely at low pressure (0.1 MPa) and with a hydrogen volume fraction of up to only 50%. Other studies that explored turbulent flames of H_2/CH_4/air mixtures [14, 146-148] focused only on a specific range of hydrogen fractions, pressures and equivalence ratios. In contrast, the present study investigates turbulent burning velocities for methane/hydrogen/air mixtures with hydrogen volume fractions of 30%, 50%, 70%, and 100% across a broader spectrum of pressures, including 0.1, 0.5, and 1.0 MPa. Equivalence ratios varied between 0.8 and 1.2 for H_2/CH_4 mixtures and 0.5 and 2 for pure H_2. Additionally, u' is adjusted within the 2 to 10 m/s range.

2.3 Numerical Investigations

Following the experimental work, this study focuses on numerical simulation. Open Source Field Operation and Manipulation (OpenFOAM) software is used in the CFD simulation. The OpenFOAM is an open-source CFD solver using a finite volumes approach. It has a range of models including compressible and incompressible fluid mechanics, heat and mass transfer, reactive flows, etc. Several solvers are already included in OpenFoam and can be selected based on the application, conservation equation, and physical phenomena [47].

CFD tools can provide important information about spherical flame propagation that is difficult to obtain experimentally [45]**.** A literature review of the numerical and related experimental studies is presented in this section.

2.3.1 Flow Field Characteristics

The Schlieren technique used in the present experiment is limited to flame surface images. The flow velocity and temperature are difficult to measure. This information is essential for engineering designers. Flame propagation with strong pressure waves and high temperatures can damage the combustion equipment [73, 149]. CFD has recently been used to get pressure, temperature and velocity during the propagation of spherically expanding flames [45, 47, 48]. The effect of initial pressure and turbulent kinetic energy on pressure wave distribution for spherically expanding flames has been studied numerically in [45]. They used the LES turbulence model to simulate the hydrogen/air expanding flame in a 14L spherical vessel. These authors concluded that (i) the model successfully captures the propagation of pressure waves towards the wall, (ii) the peak pressure value is situated inside the flame during flame propagation, and (iii) the peak pressure value increases with higher turbulent kinetic energy. In addition, the pressure field influences the velocity field in spherical flame propagation. The pressure gradient within the flame leads to a velocity gradient. Dramatic velocity fluctuations have been found within the flame next to the peak value of the pressure wave [45]. The velocity field has been also investigated by Bradley et al. [65]. They studied the interaction between turbulent flow and flame propagation in the spherical vessel using the PIV technique. They concluded that a strong outwards velocity pulse ahead of the flame is generated due to the combined influences of a high burning rate and high volumetric expansion [65].

2.3.2 Flame surface wrinkling

Both chemical scales (such as u_l and δ_l) and turbulent scales (including L, λ, η, and u') affect flame wrinkling. These scales have been used to describe turbulent premixed flames [41-43]. The integral scales (L) primarily govern flame convection and can only induce significant wrinkling in large flame kernels [125, 126]. In contrast, the Kolmogorov scales (η) may lack the energy for effective flame wrinkling [43]. Therefore, the Taylor scales are central to flame wrinkling due to their responsibility for shear forces. The λ scale increases as the temperature rises and decreases as the pressure and fan speeds (u') increase [150]. The increase in initial pressure results in the following:

a- positive flame stretch,

b- a reduction in Taylor length scales,

c- a decrease in the flame reactivity, i.e., the laminar burning velocity (u_l)

d- enhancement in the DL instability due to the sharp density gradient across the flame front [123].

These effects collectively lead to a finer, more wrinkled flame structure, increasing the turbulent burning velocity [126].

The Lewis number can also influence flame wrinkling. Previous research showed that the mixture with high laminar flame cellularity (lower Le) has more turbulent flame wrinkling than the mixture with low laminar flame cellularity (higher Le) [123]. This can be attributed to the diffusive-thermal (DT) instability, as a mixture with $Le < 1$ has more DT instability than those with $Le \geq 1$ [94].

2.3.3 The Flame Wrinkling Turbulent Combustion Model

As mentioned in Chapter 1, the premixed turbulent flame in the present study is modelled using the flame wrinkling model (Ξ) because it balances computational speed and accuracy [48]. The present study uses the LES and RANS models for the turbulence models. LES models provide more flow details but are computationally expensive [45]. RANS models can capture the temperature, pressure and averaged velocity profiles in large and complex geometry cases [48]. In premixed combustion, the flame can be described as a reactive wave moving toward the unburned mixture [151]. As the flame wave moves, there is a great production of thermal energy inside the flame and rapid density change behind the flame, resulting in a velocity increase in the burned side (20 times the unburned side) [151]. The flamelet model was developed [152] to simulate the turbulent flow considering the laminar flames. This model solves a transport equation for the progress variable flame area density (Σ) given per unit of volume [48]. The flame wrinkling models (Ξ) were developed by [24] as an alternative for Σ models. The wrinkle density factor Ξ, the laminar flame wrinkled area per unit area, is solved on the flow direction. The turbulent flow effect on the flame is handled through a modelled transport equation for the perturbed laminar flame speed [25].

The Ξ model has been used with the Shear Stress Transport (SST) k-ω turbulent model to simulate the turbulent flame in the ORACLES combustion Chamber [48]. The chamber is a channel with two parallel inlets, and the Reynolds number ranges from 4050 to 41777. They concluded that the Ξ model is valid for the reactive flow in the ORACLES combustion chamber using the SST k-ω model and Euler and backward schemes compensation. The performance of the Ξ model in OpenFoam and FLUENT has been investigated in the high-pressure Bunsen burner [23]. Both solvers agreed well with Siewert's experimental results [153].

The spherical turbulent flame propagation through numerous obstacles has been studied using the Ξ combustion model associated with the SST-k-ω turbulent model in OpenFoam software [47]. The turbulent burning velocity in the Ξ factor has been modelled using the available correlations (Gulder, FLACS and Zimont). The findings of this study confirm that these models provide an identical free flame velocity without the obstacles. However, a significant variation was observed when the flame passed through the obstacle, as these correlations are developed for free flame propagation [47]. Moreover, these correlations are not valid for fuel/air mixtures with non-unity Lewis numbers. Therefore, the present study updated the turbulent burning velocity correlation in the Ξ combustion model.

2.3.4 Research Gaps for Numerical Flame Studies

The present study links the experiments to the numerical work. The results from the laminar and turbulent experiments are input into a numerical model. The turbulent burning velocity correlation is one outcome of the turbulent flame investigations [44, 123, 126, 127, 138, 142]. Many of these correlations have never been tested in the numerical models. Gulder, FLACS, and Zimont correlations were used in the Ξ and FLUENT solvers [47]. However, these correlations are applicable to a mixture with a unity Lewis number. The present study provides new correlations for mixtures with non-unity Lewis number (hydrogen/methane/air) at high initial pressure and rms velocity. The Gulder and FLACS correlations in the Ξ combustion model are used to calculate the wrinkling factor [47]. This work will utilise the empirical correlation from the present experiments instead of the Gulder correlation in the Ξ combustion model. This will be given in the next chapter.

Chapter 3: Research Methodology

3.1 *Introduction*

The measurements of laminar and turbulent burning velocities, stretch rate, Markstein length, and Karlovitz stretch factor for hydrogen/air and methane/hydrogen/air mixtures have been carried out using the Leeds MK-II combustion vessel equipped with high-speed Schlieren ciné photography [71]. The spherical flame measurements have become a common technique for studying laminar and turbulent combustion due to the following reasons [108, 126, 129, 154]:

1- The range of flame fundamentals can be studied in a wide range of fuel/air mixtures, temperatures, pressures, and rms turbulent velocities.

2- The experimentations are straightforward.

3- The flame front is not affected by the wall in a large vessel.

4- The measurement at constant pressure allows for adiabatic and isobaric assumptions of all thermodynamic properties.

5- The operation is not limited by flashbacks and blow-offs, as in the case of burner measurements.

6- The turbulent flow in the vessel's core is homogeneous and isotropic.

3.2 Experimental Apparatus

Figure 3.1 presents a schematic of the apparatus used in the present work. The Leeds MK-II spherical combustion vessel has been extensively used to acquire laminar and turbulent burning velocities [65, 97, 108, 126, 129, 135, 154]. The present work is based on the previous experimental setup for Schlieren measurements, except a faster camera is used to capture fast hydrogen flame propagation.

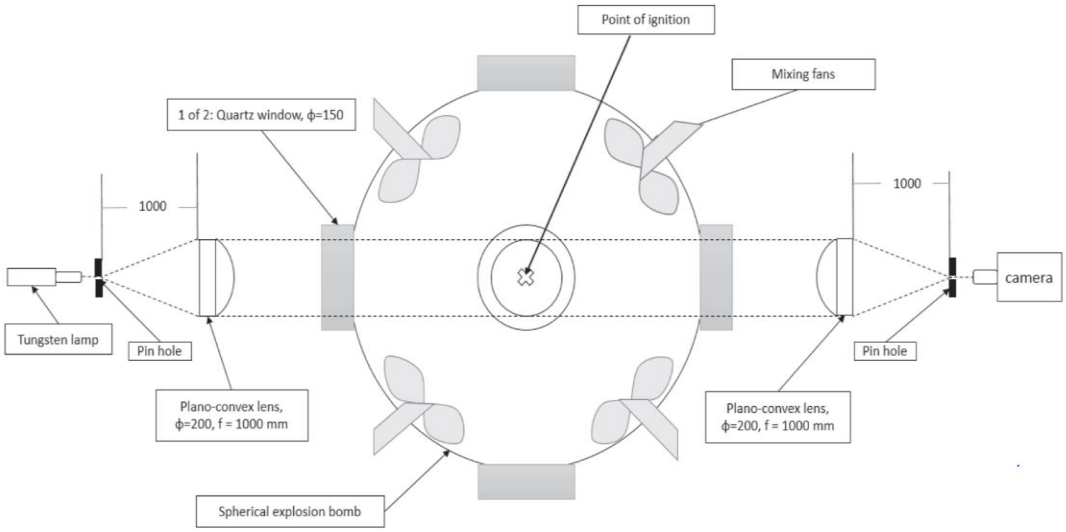

Figure 3.1: Schematic view of the vessel and auxiliary system for Schlieren optical configuration.

3.2.1 Combustion vessel

The internal view of the vessel is shown in Figure 3.2, with the main access port removed [71]. The spherical vessel, made from stainless steel, has an internal volume of 30 L with an internal diameter of 380 mm and a wall thickness of 100 mm. It is designed to withstand initial pressures up to 1.5 MPa and temperatures up to 600 K. It is equipped with three-pair orthogonal quartz windows (diameter of 150 mm) for optical access. The windows allow various imaging techniques, including Schlieren, PIV and 3D swinging-sheet laser [129]. The air and fuel are mixed by four fans, which are directly coupled to 8 KW three-phase electric motors with separate speed controllers. The fans are used to generate homogenous and isotropic turbulent flow in the vessel's core region [137]. Semenov [155] reported that four equal, eight-bladed fans rotating at the same speed in a closed volume could create uniform isotropic turbulence. As discussed in Chapter 2, Bradley et al. [137] employed the PIV technique to ensure the isotropy and homogeneity of the flow in the Leeds spherical combustion vessel.

3.2.2 Auxiliary systems

The auxiliary systems in the present work include a pressure measurement system, heating and temperature measurement and control system, ignition system, fast Schlieren imaging system, and triggering and synchronization system. The following subsection discusses these systems.

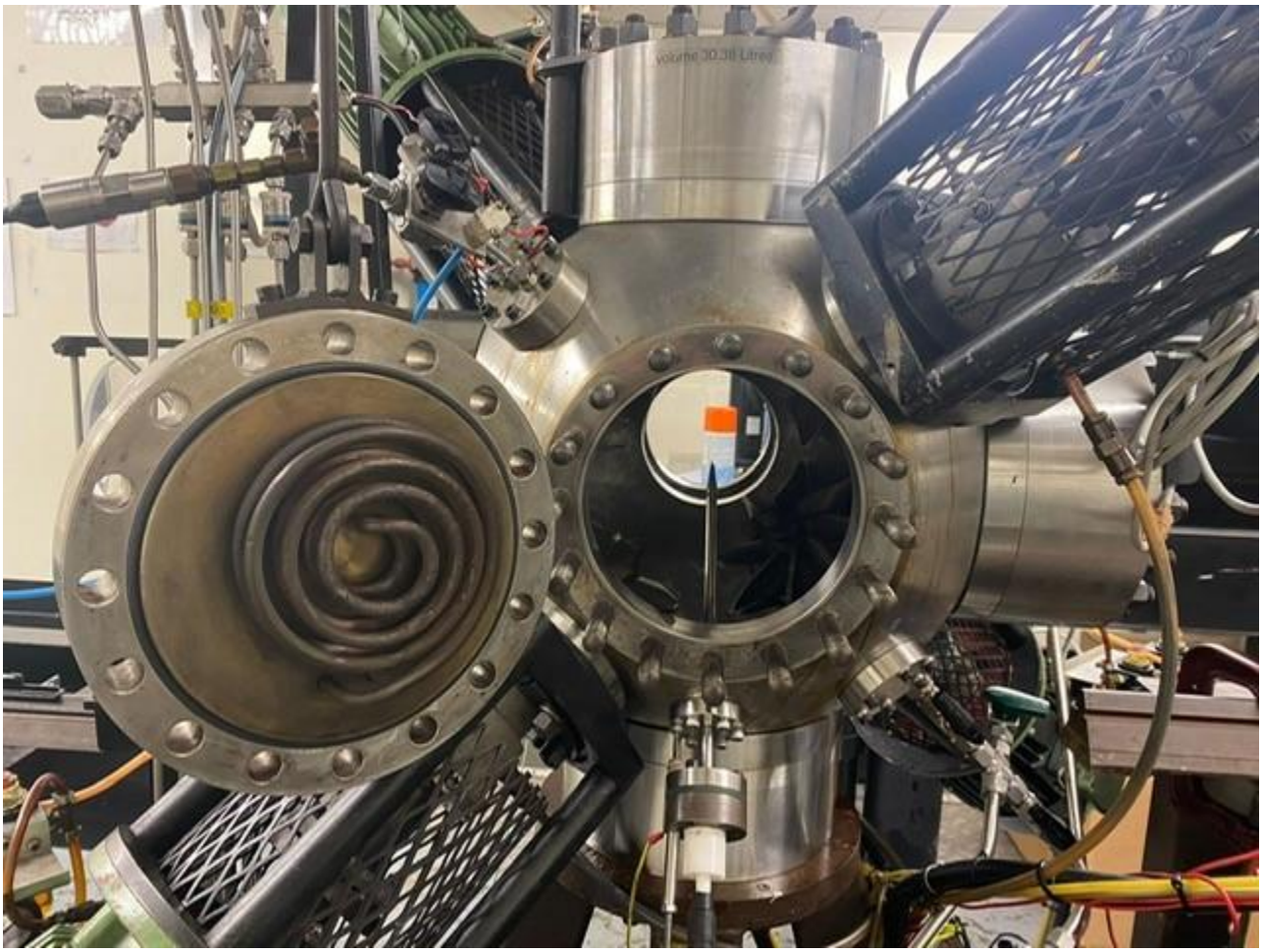

Figure 3.2: The internal view of Leeds MK-II vessel.

3.2.2.1 Pressure Measurement System

During the mixture preparation, the static pressure is measured by a Druck PDCR 911 pressure transducer. It measures the absolute pressure and is used to monitor the vacuum in the vessel before ignition. Calibration of the transducer was performed by taking readings from a mercury barometer because variations in atmospheric pressure can strongly influence the mixture equivalence ratio. A swage lock ball valve isolates the static pressure transducer before igniting for protection. After the ignition, a Kistler 701A pressure transducer is used to measure the pressure rise (dynamic pressure). This transducer is fixed to the vessel's inner wall and ranges from 0-25 MPa. LabVIEW software is used to graphically display and record the rise of pressure during flame propagation at a sampling frequency of 50kHz. The charge amplifier volts/pressure range was adjusted to 10v/bar to optimise the voltage range for the associated pressure increase during combustion.

3.2.2.2 Heating System and Temperature Measurement

The vessel is heated to the required initial operating temperature by two 2 KW heaters. The heaters are attached to the inside of the access cover and the opposing cover. The temperature is measured by a K-type thermocouple sheathed by a 1.5 mm stainless steel casing [108]. It is positioned 75 mm away from the vessel's inner wall surface. The fans were kept running during heating to maintain a uniform temperature and avoid overheating the elements. The uniform temperature can minimize the risk of hot spot development and pre-combustion [108]. The vessel is heated to a considerably high temperature in the initial heating. The heaters are turned off for 15-30 minutes to achieve the desired initial temperature. This procedure allows for a more significant rate of heat transfer to reduce the heat-up time [108].

After running some experiments, the vessel needs heating or cooling, depending on the heat of the reaction. Cooling is achieved by flushing the vessel with fresh air.

3.2.2.3 Ignition system

The spark plug is centred in the vessel to ignite the mixture. A variable arc discharged system is used to supply the required ignition energy efficiently. The spark plug was assembled at Leeds combustion lab (Figure 3.3). The plug includes three layers: an anode with a 1.5 mm diameter of high carbon steel, ceramic insulation, and a stainless steel tube with a protuberance serving as a cathode. The plug is inserted into a 6.35 mm stainless steel tube mounted through the vessel wall. This tube connects the outer section (cathode) to the earth through the vessel's wall. The anode rod is attached to 12V coil windings with a standard male (high tension) cable [108]. The spark effect on the flame is kept to a minimum for all explosions ($\leq$ 23 mJ [139]) and is achieved by reducing the spark gap. As the gap is small, the spark dissipation is minimal. The spark gap is reduced as the hydrogen volume fraction and pressure increase. The gap was 0.8, 0.6 and 0.4 mm for 0.1, 0.5 and 1 MPa, respectively.

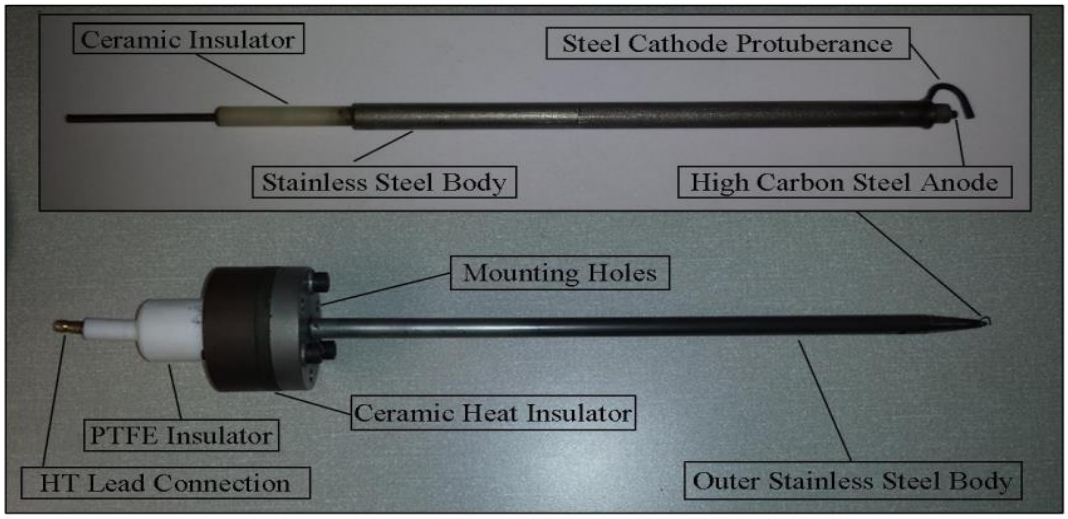

Figure 3.3: Leeds Spark plug [108].

3.2.2.4 High Speed Schlieren Cine Photography

A Schlieren technique is employed to measure the flame speed from which the burning velocities were derived. The density gradient between the burned and unburned mixture results in a degree of light reflection; hence, Schlieren cine photography detects the density difference. This technique is widespread in combustion studies [71, 108]. Figure 3.1 presents the Schlieren setup in the Leeds MK-II combustion vessel. A 20 W tungsten element lamp generates the light, which expands onto a plano-convex lens with a 1000 mm focal length to collimate a 150 mm diameter of the beam through the combustion vessel. The parallel beam then passes through another plano-convex lens, which focuses the beam onto a variable diameter iris of 1-15 mm (pinhole). The camera must capture the image formed at this lens's focal point. The sensitivity of the Schlieren system can be adapted by varying the iris diameter. It is very high at the smallest diameter of 1 mm, providing the optimum Schlieren images. However, the maximum diameter offers low-quality images similar to shadowgraphy images. Adjusting the iris diameter allows the system to achieve the maximum flame surface detail, depending on different mixture conditions. The sensitivity in the current Schlieren system is high as the pinhole diameter is 3-4 mm, and the focal length is 1000 mm.

Although the 2D projection of 3D flame limits the Schlieren images, a clear definition of the flame edge can reduce the overlap effect [108]. The Schlieren images are captured using a high-resolution Phantom ultra-high-speed UHS-12, model v2012, CCD camera. The exposure time is kept to a minimum range of 4 to 10 μs to obtain a clearly defined flame edge. The camera position allows for the maximum field of view, which is limited by the vessel window (150 mm diameter). The camera frame rate varied from 3,000 fps to 30,000 fps, depending on the hydrogen fraction in the mixture.

Low speeds were used for 30% H_2 mixtures, as this flame propagates slower than those with higher H_2 fractions. As the flame speed increased, the frame rate was also increased to obtain an appropriate number of images in each case (around one image per 1-1.5 mm of flame movement). The camera pixel was fixed to 512×512 pixels with a pixel size of 0.265 mm.

The Schlieren calibration was performed at the start of every day to confirm the beam collimation and pixel resolution. Using the high-speed camera, an image was recorded for an imprinted 10 mm^2 grid installed on either vessel's side. One picture is taken of the grid installed between the front lens and the vessel, and the other image is between the vessel and the back lens (Figure 3.1). A MATLAB code is used to confirm the pixel size for both pictures [38, 60, 108]. The variation of ≤ 0.1% between the two images is accepted.

3.2.2.5 Mixture Preparation

The mixture was prepared in the vessel for the targeted equivalence ratio by adding a specified amount of air or fuel at the required partial pressure. The following equations [73] were used to obtain the partial pressure in the mixture preparation:

$$\left(X_{CH_4}\right) CH_4 + \left(X_{H_2} = 1 - X_{CH_4}\right) H_2 + \left(\frac{2}{\phi}\left(1 - X_{H_2}\right) + \frac{X_{H_2}}{2\phi}\right)\left(O_2 + 3.762\, N_2\right) \tag{3.1}$$

$$P_{H_2} = \frac{X_{H_2}}{\left[1 + \left(\left(\frac{2.38}{\phi}\right)\left(4X_{CH_4} + X_{H_2}\right)\right)\right]} * P_u \tag{3.2}$$

$$P_{CH_4} = \frac{X_{CH_4}}{\left[1 + \left(\left(\frac{2.38}{\phi}\right)\left(4X_{CH_4} + X_{H_2}\right)\right)\right]} * P_u \quad (3.3)$$

$$P_{\text{air}} = P_u - P_{CH_4} - P_{H_2} \quad (3.4)$$

P_{H_2}, $P_{CH_4}$and P_{air} are the partial pressures of hydrogen, methane and air, respectively, P_u is the targeted mixture initial pressure (0.1, 0.5 and 1 MPa), X_{H_2} and X_{CH_4} are the mixture volume fractions of hydrogen and methane, respectively, and ϕ is the mixture equivalence ratio.

3.3 Experimental Procedure for Laminar Flame Propagation

The following procedures are applied:

1. The fans are turned on and kept running at 400 rpm.
2. Dry air is added to pressure the vessel to 0.5 MPa, and the pressure is monitored for at least 5 minutes to ensure no leakage. During the leakage test, the temperature must be kept constant to avoid any pressure variations due to temperature change.
3. The vessel must be free from any unwanted gaseous residuals from previous experiments. The vessel is flushed with dry air and evacuated twice to remove the flue gases.
4. The vessel is pressurised by dry air to 0.3 MPa.
5. The heaters are turned on for 2-6 hours to achieve the desired initial temperature.
6. After turning off the heaters, the vessel is evacuated down to 0.002 MPa.

7. The fuel is added depending on the targeted equivalence ratio at the required partial pressure.
8. The dry lab air (O_2:N_2 with a ratio of 21:79 % by mole) is added to the specific initial pressure. The purity of the used fuel (Methane and hydrogen) is 99.995%.
9. The fans are run at a low speed (400 rpm) during the mixture preparation to ensure full mixing and uniform temperature.
10. The fans are switched off for at least 60 s before the ignition to bring the mixture to quiescence.
11. The mixture is ready to be ignited at this stage, and a high-speed Schlieren technique records the flame propagation.
12. After combustion, the flue gases are exhausted to the atmosphere via the exhaust valve to bring the vessel to atmospheric pressure.
13. The dry air is allowed to pass through the vessel and is exhausted into the atmosphere.
14. The fans are reactivated to 400 rpm.
15. If the vessel temperature is low, the heaters are reactivated. However, the dry air is kept running through the vessel to achieve the desired temperature in the case of high vessel temperature.
16. The Schlieren images and combustion pressure are saved.
17. The LabVIEW software is reset.
18. The vacuuming and filling procedure is then repeated for the subsequent explosion.

19. The experiments are repeated three times for each condition, and average values are used in the present work. Reported error bars represent one standard deviation.

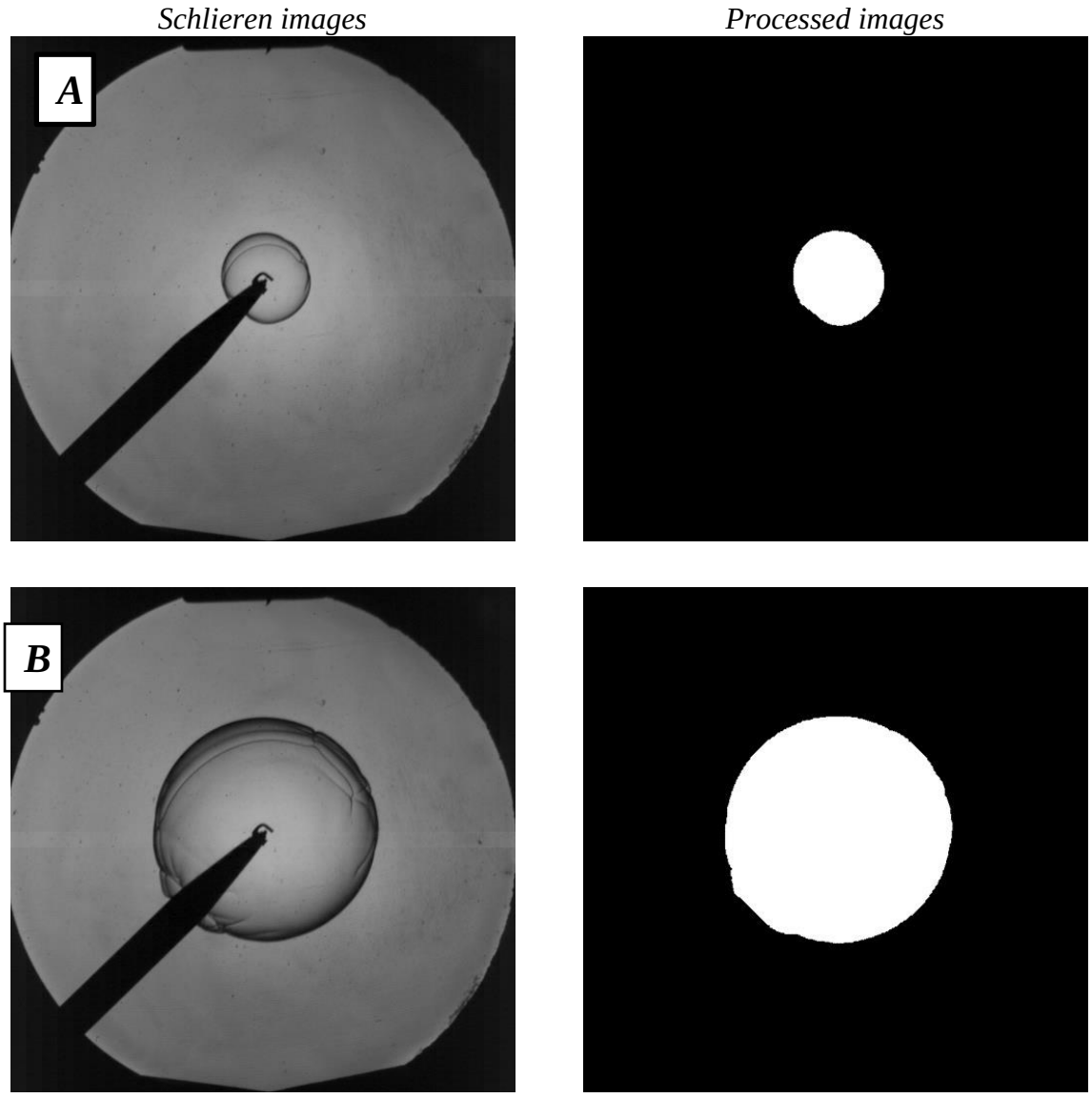

Figure 3.4: Schlieren and processed images for 70% hydrogen, 30% methane laminar flame at 0.1 MPa, 360 K and 0.9 equivalence ratio, A) after 2.5 ms of ignition, and B) after 5 ms of ignition.

Images are processed using a MATLAB code developed in previous studies [64, 108, 156]. Flame edges are specified in the code to identify the burned and unburned regions. This code is used in laminar and turbulent post-processing. The unburnt gas part of the image is subtracted and remains black, and the flame image relating to the burnt gases is white (Figure 2.4). The flame area is then calculated by counting the number of pixels of the white region, and an equivalent flame radius, r_{sch}, is computed from this area by assuming a smooth circular image with the same area. Finally, the time step (dt) is calculated as 1/camera frame rate.

3.3.1 Unstretched Laminar Burning Velocity and Markstein Length

The flame speed, S_n, is calculated from Schlieren images as follows:

$$S_n = \frac{dr_{Sch}}{dt} \tag{3.5}$$

where r_{sch} is the Schlieren flame front radius, dt is the time step, and S_n is the stretched flame speed.

To obtain the unstretched flame speed, S_s, flame speed (S_n) is plotted against stretch rate (α), for example, in Figure 3.5. As discussed in the previous chapter, Equation 2.5 calculates the flame stretch rate. The stretched flame speed is extrapolated to zero stretch rate to obtain the unstretched flame speed (S_s). The data in the S_n-α plot is classified into three categories [71]: (i) the region where ignition energy affected the flame, which is eliminated from the extrapolated data. The spark effect continues up to a 10 mm flame radius at atmospheric pressure [71] and to 5 mm at high-pressure explosions [73]; (ii) the stable region (quasi-steady flame), which is used in the extrapolation to derive the un-stretched flame speed S_s, and (iii) the unstable regime, which starts after the onset of cellularity at a critical flame radius (r_{cl}), where the flame speed increases rapidly because of the high flame surface area [72]. The linear relationship (Equation 2.6) is used to obtain the unstretched flame speed and Markstein length.

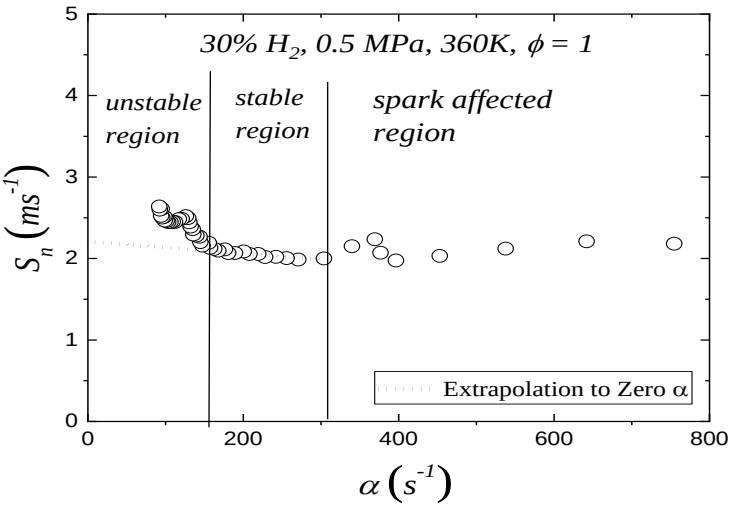

Figure 3.5: Flame speed vs. flame stretch rate for 30% H_2 in CH_4 by volume at 0.5 MPa, 360 K, ϕ=1.

The Markstein length is normalized by flame thickness (δ_l) to obtain the burned gas Markstein number, Ma_b.

$$Ma_b = \frac{L_b}{\delta_l} \tag{3.6}$$

As discussed in Chapter 2, Equation 2.3 has been selected to calculate the flame thickness, δ_l, in the present study. The Markstein number Ma_b is widely used to quantify the effect of the flame stretch rate on the laminar burning velocity [72]. However, there are two contributions to stretch rate: (i) due to flow strain rate and (ii) due to flame curvature stretch [154]. These effects are quantified by strain Markstein number (Ma_{sr}) and curvature Markstein number (Ma_{cr}). Bradley et al. [154] derived Ma_{sr} and Ma_{cr} from an outwardly propagating spherical flame. The linear dependency of S_n on α enables u_l and L_b to be evaluated from Equation 2.6. Then, the values of L_c and L_s are found from ($u_l - u_n = L_s\alpha_s + L_c\alpha_c$), using multiple regression, as described in [154].

Multiple regression is a statistical method used to model the relationship between a dependent variable (u_n: the stretched laminar burning velocity) and two independent variables (L_s and L_c). Values of L_{cr} and L_{sr} are derived from Equation (3.7) as ($L_{sr} = (L_b - L_s)(1/(\rho_u/\rho_b) - 1)$) and $L_{cr} = (L_b - L_c)(1/(\rho_u/\rho_b) - 1)$. Finally, the normalisation of these Markstein lengths by the flame thickness yields the corresponding Markstein numbers.

$$u_l - u_{nr} = L_{sr}\alpha_{sr} + L_{cr}\alpha_{cr} \tag{3.7}$$

where u_n is the stretched laminar burning velocity, u_{nr} is mass burning velocity, α_c and α_s are the curvature and strain stretched rate, respectively, L_c, and L_{cr} are Markstien length associated with curvature stretch and derived from u_n and $u_{nr,}$ respectively, L_s, and L_{sr} are the Markstien length associated with the strain rate and derived from u_n and $u_{nr,}$ respectively [154].

Gu et al. [72] highlighted the importance of Ma_{sr} in practical turbulent applications, as it quantifies the effect of aerodynamic strain on the burning rate in outwardly propagating flames [156]. Ma_{sr} is also useful for analyzing quench effects in turbulent combustion [154]. Moreover, Ma_{sr} is larger than Ma_{cr} ($Ma_{sr} \approx 5Ma_{cr}$) in outwardly propagating flames [60, 72, 154]. However, the method of Bradley et al. [154] is based on the assumption of unity Lewis number, Le. This assumption is not applicable when hydrogen is added to methane/air. Thus, the present study made Ma_{sr} available to interested readers and focused mainly on L_b and Ma_b in the discussion.

From mass conservation across the flame front, considering an idealized one-dimensional planar flame, the unstretched laminar burning velocity, u_l, is calculated from [71]:

$$u_l = \frac{\rho_b}{\rho_u} S_s \tag{3.8}$$

where ρ_u is the unburned gas density at the initial gas temperature (T_u) and ρ_b is the burned gas density at the adiabatic temperature (T_b), assuming that the flame is adiabatic at zero stretch rate [60, 71, 75]. The burned-to-unburned density ratio is called the expansion factor [108]. The chemical equilibrium program, GASEQ [157], was employed to calculate the gas properties at the given temperature and pressure.

As discussed in section 2.1.6, the present study has considered several points to reduce measurement uncertainty. The ignition energy is kept to a minimum (1 mJ) [106], and the ignition-affected data in the early flame propagation is not included in the derivation of the laminar burning velocity [71]. The maximum flame radius used is less than 30% of the inner radius of a large spherical vessel (internal radius =190 mm) to avoid any effect of wall confinement on the measurement of flame speed. Moreover, The extrapolation method and the selected experimental data used are sources of uncertainty in the derived unstretched laminar burning velocities. The uncertainty in the extrapolation approach largely depends on the Lewis number and the normalized stretch rate (Karlovitz stretch number) [76]. The extrapolation approach is based on asymptotic analysis for Lewis numbers close to 1 ($L_b \rightarrow 0$) [76, 154]. The linear extrapolation method (Eq. 2.6) has been adopted in many studies for hydrogen/methane/air mixtures [73, 75, 85, 97]. However, non-linear extrapolation is used for large carbon-content fuels such as n-butane and n-heptane, which have large Lewis numbers (L_e>1) in lean mixtures [110]. Therefore, the present study adopted the linear extrapolation method, with the uncertainty quantified using the correlation of Wu et al. [76]:

$$U_f = Ma_{bLinear} Ka_{mid} = {2L_b}\Big/{R_{f\,mid}} \tag{3.9}$$

where U_f is the uncertainty weight factor, $Ma_{bLinear}$ is the Markstein number from the linear extrapolation, Ka_{mid} is the Karlovitz number in the middle of the extrapolated data (stretch rate normalized by flame thickness), L_b is the Markstein length, and $R_{f\,mid}$ is the flame radius in the middle of the extrapolated data. Wu et al. [76] produced this equation to quantify the uncertainty due to the extrapolation. The uncertainties in the laminar burning velocity depend on the controlling parameters (Ma_{linear} and Ka_{mid}), which can be easily calculated in any experimental study of spherical flame propagation. To minimise the extrapolation error, the measurement should be in -0.05 < MalinearKamid > 0.15; otherwise, the correction must be applied. According to Wu et al. [76], (i) the uncertainty in the extrapolation is negligible (±5%) for -0.05 < U_f < 0.15, (ii) for U_f < -0.05, both linear and nonlinear extrapolation over-predict the unstretched flame speed, (iii) for U_f > 0.15, the linear extrapolation under-predicts the unstretched flame speed.

3.4 Experimental Procedure for Turbulent Flame Propagation

The vessel and mixture preparation are similar to the laminar procedure described in section 3.3. The only difference is that the fans are running during the flame propagation. They are set to the fan speed for the desired u' as in equation 2.14 [137]. As in the laminar investigations, the turbulent experiments are repeated three times at each condition and average values are used in the present data. Reported error bars represent one standard deviation (STDEV.S) of the turbulent burning velocity. Figure 3.6 presents examples of the Schlieren and processed images. Flame edges are specified in the code to identify the burned and unburned regions. The flame area is then calculated by counting the pixels of the white region, and an equivalent flame radius, r_{Sch}, is computed from this area by assuming a smooth circular image with the same area.

3.4.1 Turbulent Burning Velocity

As discussed in Chapter 2, the Schlieren flame radius is used to calculate the turbulent burning velocity (u_t) at the volumetric flame radius. The present study assumed that the thickness of the turbulent flame brush is constant as the flame grows and is not affected by changing the fuel/air mixture, rms velocity, pressure and temperature. Therefore, the factor of 1.11 from Bradley et al. ***[129]*** study is used to determine the turbulent burning velocity (u_t). Following the previous research [127, 129, 135, 158], u_t is determined via the mass conservation equation:

$$u_t = \frac{1}{1.11}\frac{\rho_b}{\rho_u}\frac{dr_{Sch}}{dt} \tag{3.10}$$

where ρ_u is the unburned gas density at initial gas temperature (T_u) and ρ_b is the burned gas density at adiabatic temperature (T_b), assuming that the flame is adiabatic [60, 71, 75]. The chemical equilibrium program, GASEQ [157] is employed to calculate the gas properties at the given temperature, pressure and equivalence ratio.

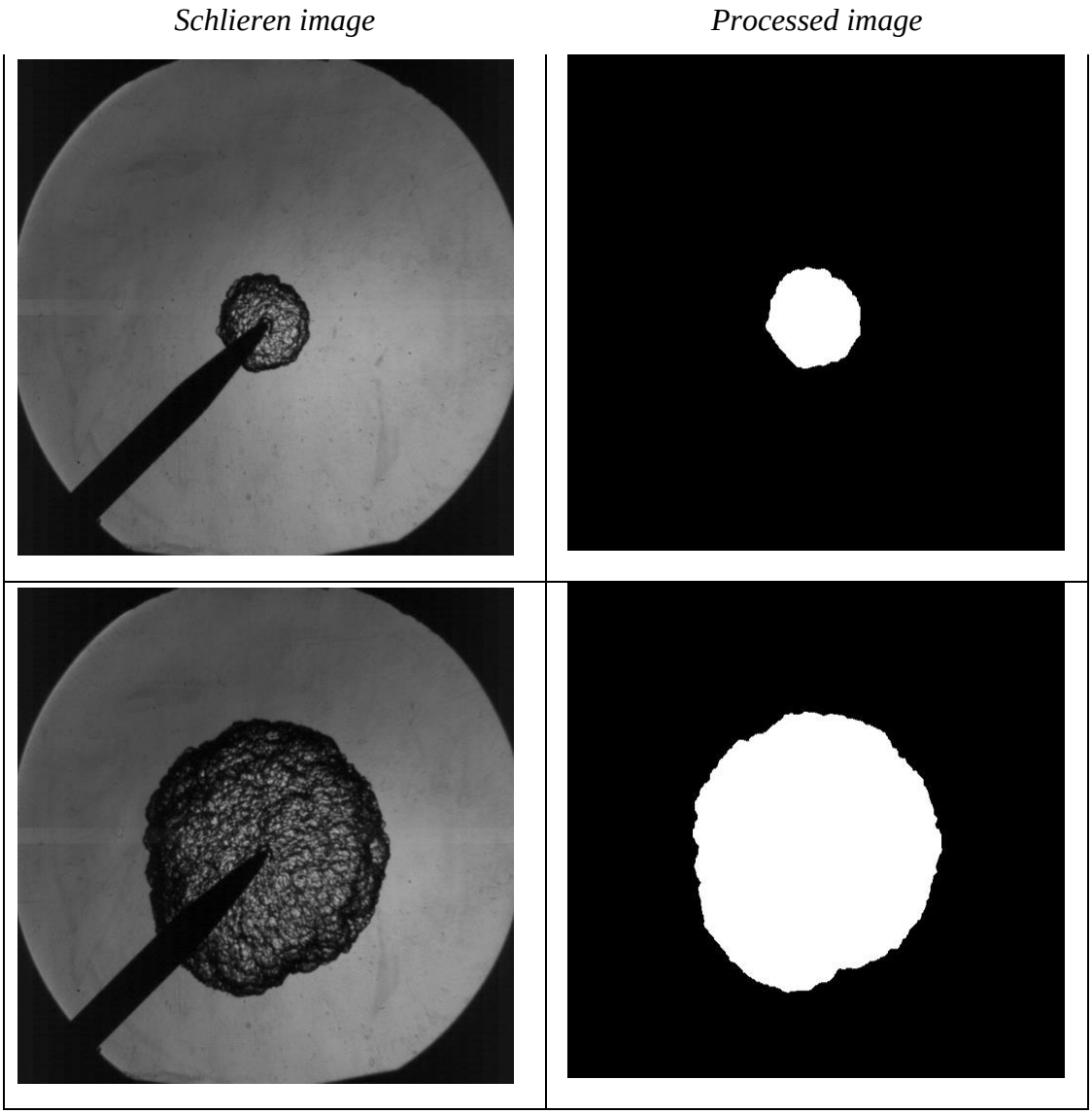

Figure 3.6: Schlieren and processed images for pure hydrogen turbulent flame at 0.5 MPa, 360 K, $u' = 2\ ms^{-1}$ and 0.8 equivalence ratio.

3.4.2 *Experimental Conditions*

Table 3.1 presents the initial conditions of the turbulent experiments performed. The maximum allowable *u'* decreased as pressure increased. This is due to the pressure effect on fan seals, which resists the shaft rotation and reduces fan speed. The minimum allowable temperature increased as the fan speed increased.

For example, in the experiments at an initial temperature of 303 K, the temperature rose to 318 K when the fan speed increased to 8064 rpm to obtain an initial u' of 10 m/s. Moreover, experiments at 1.0 MPa and 303 K were eliminated due to the time required for cooling the bomb and the increase in the initial temperature with high turbulence conditions. The vessel wall temperature increased to high values after several runs. Cooling it down required considerable time (approximately eight hours) due to the vessel wall thickness (100 mm). Thus, these measurements will be considered in future studies.

Table 3-1: The initial experimental conditions.

% H_2 by volume	P_u (MPa)	T_u (K)	u' (m/s)	ϕ
30, 50, 70, 100	0.1	303, 360	2, 6, 10	*for H_2/CH_4 0.8, 0.9, 1, 1.1, 1.2 *for 100% H_2 0.5, 0.8, 1, 1.5, 1.7, 2
30, 50, 70	0.5	303, 360	*for 303 K 2, 6, 7.5 *for 360 K 2, 6, 8.5	0.8, 0.9, 1, 1.1, 1.2
100	0.5	303, 360	*for 303 K 2, 6, 8.5 *for 360 K 2, 6, 9.5	0.5, 0.8, 1, 1.5, 1.7, 2
30, 50, 70, 100	1.0	360	2, 6	*for H_2/CH_4 0.8, 0.9, 1, 1.1, 1.2 *for 100% H_2 0.5, 0.8, 1, 1.5, 1.7, 2

3.5 Numerical Modelling of Turbulent Flame Propagation

As mentioned in Chapter 2, this study uses OpenFoam software (V12) in the CFD simulation. The OpenFOAM solvers use a finite volume approach to solve the partial differential equations. Different turbulence models can be applied to solve the turbulent flame propagation. The turbulent flow governing equations solved in this study are divided into two sets of equations depending on the turbulence model. These models are LES and RANS models. The governing equations that belong to these models are presented below.

3.5.1 The Governing Equations for Large Eddy Simulation (LES)

In LES, a spatial filter decomposes all variables into resolved (filtered) and unresolved (subgrid) components. For example, $\emptyset = \widetilde{\emptyset} + \emptyset'$, where $\widetilde{\emptyset} = \frac{\overline{\rho\emptyset}}{\bar{\rho}}$ is the Favre-filtered variable. According to Sabelnikov and Fureby [159, 160], the mass, momentum, species and energy conservation equations for LES are written as follows:

$$\frac{\partial \bar{\rho}}{\partial t} + \nabla . (\bar{\rho}\tilde{u}) = 0 \tag{3.11}$$

$$\frac{\partial (\bar{\rho}\tilde{u})}{\partial t} + \nabla . (\bar{\rho}\tilde{u} \otimes \tilde{u}) - \nabla . (\overline{\boldsymbol{S}} - \boldsymbol{B}) = - \nabla p \tag{3.12}$$

$$\frac{\partial (\bar{\rho}\tilde{E})}{\partial t} + \nabla . (\bar{\rho}\tilde{u}\tilde{E}) = \nabla . (-\bar{p}\tilde{u} + \tilde{\boldsymbol{S}}\,\tilde{u} + \bar{h} - \boldsymbol{b_E}) \tag{3.13}$$

where: '¯' and '~'symbols represent the filtering and density-weighted filtering; t is time, ρ is mixture density, *u* is velocity, *p* is pressure, $\boldsymbol{S}$ is the resolved stress tensor, representing the momentum transfer due to the molecular diffusivity, $\otimes$ is the tensor product or the outer product, and *T* is the temperature.

The total energy $\tilde{E}$ is calculated as follows:

$$\tilde{E} = \tilde{h} - {}^{\bar{p}}/_{\bar{\rho}} + ({}^{1}/_{2})\tilde{u}^2 + k \tag{3.14}$$

The total enthalpy *h* can be calculated by JANAF format in OpenFOAM,

$$\tilde{h} = R \left(\left(\left((a_5 T + a_4) T + a_3 \right) T + a_2 \right) T + a_1 \right) T + a_0 \tag{3.15}$$

The coefficients $a_0 - a_5$ are obtained from fitting $\tilde{h}$ at different temperatures using the above polynomials. The radiation heat loss is neglected here. The sub-grid stress tensor **B** and the sub-grid flux vector $\mathbf{b_E}$ are calculated as follows:

$$\boldsymbol{B} = \bar{\rho}\left(\widetilde{u \otimes u} - \tilde{u} \otimes \tilde{u}\right) \tag{3.16}$$

$$\boldsymbol{b_E} = \bar{\rho}\left(\widetilde{uE} - \tilde{u}\tilde{E}\right) \tag{3.17}$$

B and $\mathbf{b_E}$ represent the unresolved flow physics that needs to be modelled. The subgrid pressure fluctuation is neglected in the energy equation; see [159, 160]. Therefore, the gas mixture behaves as a linear viscous fluid with Fourier heat conduction and Fickian species diffusion ($\bar{p} \approx \bar{\rho}\, R\, \tilde{T}, \bar{S} \approx 2\mu\widetilde{\boldsymbol{D}}_{\boldsymbol{D}}$, $\bar{h} \approx k\nabla\tilde{T}$, where R is composition gas constant). The viscosity μ is obtained from the Sutherland law:

$$\mu = A_s \frac{\sqrt{T}}{1 + {}^{T_s}/_{T}}, \tag{3.18}$$

where the empirical values: A_s = 1.67212 x 10-6, T_s= 170.672 [48].

The deviatoric part of the rate of strain tensor is modelled as

$$\widetilde{\boldsymbol{D}}_{\boldsymbol{D}} = \frac{1}{2}(\nabla\tilde{u} + \nabla\tilde{u}^T) - \frac{1}{3}(\nabla.\tilde{u})I \tag{3.19}$$

The thermal diffusivity k is calculated as follows:

$$k = {}^{\mu}/_{Pr} \tag{3.20}$$

where Pr is the Prandtl number.

The sub-grid stress tensor and the sub-grid flux are modelled as in [160]:

$$\boldsymbol{B} = \bar{\rho}\left(\widetilde{\tilde{u} \otimes \tilde{u}} - \tilde{\tilde{u}} \otimes \tilde{\tilde{u}}\right) - 2\mu_t \widetilde{\boldsymbol{D}}_{\boldsymbol{D}} \tag{3.21}$$

$$\boldsymbol{b}_{\boldsymbol{E}} = \bar{\rho}\left(\widetilde{\tilde{u}\tilde{E}} - \tilde{\tilde{u}}\tilde{\tilde{E}}\right) - \left({}^{\mu_t}/_{Pr}\right)\nabla\tilde{E} \tag{3.22}$$

where μ_t is the turbulent viscosity, which is related to the turbulent kinetic energy $\tilde{k}$: $\mu_t = C_v \Delta\sqrt{\tilde{k}}$. The turbulent kinetic energy can be calculated as a transport equation as follows:

$$\frac{D}{Dt}\left(\bar{\rho}\tilde{k}\right) - \nabla.\left(\bar{\rho}\, D_k \nabla\tilde{k}\right) = \bar{\rho}\, G - \frac{2}{3}\,\bar{\rho}\,\tilde{k}\,\nabla.\tilde{u} - C_\varepsilon \frac{\bar{\rho}\tilde{k}^{1.5}}{\Delta} + S_k \tag{3.23}$$

where D_k is the turbulent diffusivity coefficient, G is the production of sub-grid-scale kinetic energy due to the mean velocity gradients, $\left(G = B\widetilde{\boldsymbol{D}}_{\boldsymbol{D}}\right)$, S_k is the source term. The model constants C_v and C_ϵ are adjusted based on the local flow characteristics [161].

3.5.2 The Turbulent Governing Equations for RANS model (k-ε)

In the RANS combustion simulation, the time-averaged conservation equations of mass, momentum, species and energy need to be solved [162]:

$$\frac{\partial\rho}{\partial t} + \nabla.(\rho u) = 0 \tag{3.24}$$

$$\frac{\partial(\rho u)}{\partial t} + \nabla.(\rho u u) - \nabla.\bar{\bar{\tau}} = -\nabla p \tag{3.25}$$

$$\frac{\partial \rho Y_i}{\partial t} + \nabla.(\rho Y_i u) + \nabla.J_i = w_i \tag{3.26}$$

$$\frac{\partial(\rho h)}{\partial t} + \nabla.(\rho u h) = -\nabla.q + \frac{\partial p}{\partial t} + u.\nabla p + \bar{\bar{\tau}} : \nabla u \tag{3.27}$$

where:

Y_i is the mass fraction of the *i*-th species, J_i is molecular diffusion flux, w_i is the mass reaction rate of species *i*, and $\bar{\bar{\tau}}$ is the stress tensor:

$$\bar{\bar{\tau}} = -\frac{2}{3}\mu(\nabla . u)\bar{\bar{I}} + \mu[\nabla u + (\nabla u)^T] + \nabla . \underbrace{(-\overline{\rho u' u'})}_{Reynolds\ stress} \tag{3.28}$$

Following the Boussinesq hypothesis, the Reynolds stress tensor is modelled as follows:

$$-\overline{\rho u' u'} = \mu_t(\nabla u + (\nabla u)^T) - \frac{2}{3}\rho k\bar{\bar{I}} - \frac{2}{3}(\nabla . u)\bar{\bar{I}} \tag{3.29}$$

where μ_t is the turbulent eddy viscosity, which is modelled using the k-ϵ model, and $\bar{\bar{I}}$ is identity tensor.

The heat flux vector q is computed as:

$$q = -\lambda \Delta T + \rho \sum_{i=1}^{N} h_i Y_i u_i \tag{3.30}$$

where λ is the mixture thermal conductivity, h_i is the total enthalpy of the species i, and N is the number of species.

The LaunderSharma k-ϵ model is used to simulate the turbulent flow. The turbulent viscosity μ_t is obtained as follows:

$$\mu_t = C_\mu \frac{\rho k^2}{\epsilon} \tag{3.31}$$

where k and ε are the turbulent kinetic energy and turbulent dissipation rate, respectively, they are obtained by solving a transport equation for each component (Equation 3.32 for k and Equation 3.33 for ε). The eddy viscosity (μ_t) is then taken from Equation 3.29 to obtain the Reynolds stress.

$$\frac{\partial(\rho k)}{\partial t} + \nabla . (\rho u k) = \nabla . \left[\left(\mu + \frac{\mu_t}{\sigma_k}\right) \nabla k\right] + P_k + P_b - \rho\epsilon + S_k \quad (3.32)$$

$$\frac{\partial(\rho \epsilon)}{\partial t} + \nabla . (\rho u \epsilon) = \nabla . \left[\left(\mu + \frac{\mu_t}{\sigma_\epsilon}\right) \nabla \epsilon\right] + C_1 \frac{\epsilon}{k}(P_k + C_3 P_b) - C_2 \rho \frac{\epsilon^2}{k} + S_\epsilon \quad (3.33)$$

where:

P_k is production due to mean velocity shear, P_b is production due to buoyancy, S_k is a user-defined source, and the empirical constants in the LaunderSharma k-ϵ model are Cμ =0.09, C_1 = 1.44, C_2 = 1.92, σ_ϵ= 1.3 and σ_k=1.

3.5.3 The Ξ Combustion Model

The Ξ combustion model is implemented in the XiFoam solver, which is used to simulate the turbulent premixed flame [24]. The Weller flame surface wrinkling combustion model (Ξ model) [24] has been chosen to simulate the turbulent flame in the present study, as it balances computational speed and accuracy [48]. The main assumptions in the Ξ model are that the flame is perfectly premixed, the reactions occur in a very thin layer, and the chemistry is very fast (flamelet assumptions). The hydrogen flame follows the flamelet concept, which is applicable when the relevant chemical timescale is short compared to the convection and diffusion timescales (Da > 1) [150].

A single transport equation is solved for the regress variable (b) equation (Equation 3.34 or 3.35) instead of solving for every species. The b provides a mathematical description of flame progression to represent the flame dynamics across a computational domain. It should be noticed that the regress variable (b=1 unburned, b=0 burned) tracks the consumption of the unburned gasses, while the progress variable, c, (c = 1 burned gases, c = 0 fresh gases) tracks the formation of the burned gases.

As the definition of turbulent and laminar burning velocities, which are used to describe the flame dynamic, includes the unburned mass consumption, the b is used in this model. The transport equation for the density-weighted mean reaction regress variable 'b' is solved to simulate the flame propagation [24]. The regress variable is defined as a function of fuel mass fraction ($\tilde{Y}^F$) [45]: $\tilde{b} = \left(\tilde{Y}^F - \tilde{Y}_u^F\right) \Big/ \left(\tilde{Y}_b^F - \tilde{Y}_u^F\right)$, or ($\tilde{b} = 1 - \frac{\tilde{T} - T_u}{T_b - T_u}$), where the subscripts 'u' and 'b' represent the unburned and burned gas, respectively. According to Weller et al. [25], the filtered transport equation (LES equation) for the density-weighted mean reaction regress variable 'b' can be written as:

$$\frac{\partial}{\partial t}\left(\bar{\rho}\tilde{b}\right) + \nabla\left(\bar{\rho}\tilde{u}\tilde{b}\right) - \nabla.\left(\bar{\rho}\frac{\mu_t}{Sc_t}\nabla\tilde{b}\right) = -\bar{\rho}S_u\Xi\left|\nabla\tilde{b}\right| \tag{3.34}$$

In RANS simulation, the transport equation for the density-weighted mean reaction regress variable 'b' can be written as [49]:

$$\frac{\partial}{\partial t}(\rho b) + \nabla(\rho u b) - \nabla.\left(\frac{\mu_t}{Sc_t}\nabla b\right) = -\rho_u S_u \Xi\left|\nabla b\right| \tag{3.35}$$

where the Schmidt number is calculated as: $Sc_t = \frac{\mu}{\rho D}$, D is molecular diffusion rate, S_u is the modelled laminar burning velocity, and Ξ is the wrinkling factor. The wrinkling factor is modelled using an algebraic equation [49] as follows:

$$\Xi = \frac{u_t}{S_u} \tag{3.36}$$

The modelled laminar burning velocity S_u used in Equations 3.34-3.36 has been modelled in two methods:

1. S_u is assumed to be constant and equal to the laminar burning velocity u_l [24]. Using the initial *P, T* and equivalence ratio (φ), u_l can obtained from the experiments [12]. It can also be calculated using the available kinetics code [23].

2. S_u can be calculated using the transport equation suggested by Weller et al. [25]. The stretching effect of turbulence is considered in this method.

$$\frac{\partial S_u}{\partial t} + \tilde{u}_s.\nabla S_u = -\sigma_s S_u + \sigma_s S_u^{\infty} \frac{(u_l - S_u)}{(S_u - S_u^{\infty})} \tag{3.37}$$

where u_s is the surface-filtered velocity of the flame, σ_s is the surface-filtered resolved strain rate, S_u^{∞} is the laminar burning velocity balanced with the local resolved strain rate [45]. S_u^{∞}, u_s and, σ_s are calculated using algebraic equations as in [25]. The unstretched laminar burning velocity (u_l) is modelled as function of *P, T* and φ [163]:

$$\begin{aligned} u_l &= [1.683 - 1.1001\varphi + 2.4664\varphi^2 - 1.4492\varphi^3 + 2.676\varphi^4] \\ &\times \left(\frac{P}{10}\right)^{(-0.71+0.8\varphi-0.25\varphi^2)} \left(\frac{T}{500}\right)^{(5.61-7.75\varphi+5.54\varphi^2-1.61\varphi^3+0.151\varphi^4)} \end{aligned} \tag{3.38}$$

This correlation has been validated for hydrogen/air flame with an initial temperature from 270-620 K, equivalence ratio of 0.5-5 and initial pressure of 1-30 atm [163].

The turbulent burning velocity (u_t) in equation 3.36 is modelled using two empirical correlations extracted from the current experiments.

1- **U-K correlation:**

$$u_t/u_k' = \alpha\, {K_{a1}}^{\beta} \tag{3.39}$$

where α and β are correlation constants, which are functions of Ma_b, u_t is the turbulent burning velocity, K_{a1} is Karlovitz stretch factor, the effective rms velocity u'_k is calculated from the current experimental measurements using the equation presented in section 2.2.1 and implemented in the model as a function of the distance from the ignition to the cell centre.

$$u'_k = (-0.000132u' - 0.000124)\, r^2 + (0.01499\, u' + 0.0008682)\, r + (0.371174\, u' - 0.111635) \quad (3.40)$$

Where: r is the distance from the ignition to the cell centre, and u' is the rms velocity calculated from the fan speed (equation 2.14). This equation is valid for 2 m/s ≤ u' ≥ 10 m/s.

2- **Empirical correlation based on general scaling parameters:**

$$\frac{u_t}{u_l}_{/K_{a1}} = 0.7 \left(\frac{D_a}{Le}\right)^{0.86} \quad (3.41)$$

It is worth noticing that u_t is normalized by u_l in equation 3.43, which is produced by the KAUST combustion group [123]. However, the Leeds combustion group [127, 135] normalized u_t by u'_k in Equation 3.39. These two correlations have never been used in a numerical model. The present study is the first to test these correlations for predictions of turbulent burning velocity (Eqs. 3.39 and 3.41). In addition, the present work has tested two methods for predicting laminar burning velocity (S_u=u_l and the transport equation 3.39).

3.5.4 Case Setting and Boundary Conditions

An eighth (1/8) of the experimental spherical combustion vessel (Leeds MK2 vessel [12, 71]) is simulated, assuming that the flame propagation is symmetrical in the chamber to reduce computational costs (Figure 3.7). The full vessel contains 30 L of hydrogen/air with an equivalence ratio (φ=1 and 0.5). Symmetric boundary conditions are applied on three sides of the geometry,

and the no-slip boundary condition is applied on the vessel wall. The gradient of any variable is zero on the symmetry plane. The initial mixture temperature is 360 K, the same as the wall's. The mixture is ignited with initial pressure (0.1 MPa, 0.5 MPa, 1.0 MPa) and initial rms velocity (u'= 2 ms^{-1} and 6 ms^{-1}). Based on the assumption that the turbulent flow is isotropic in the vessel, the initial turbulent kinetic energy is obtained from u' [45] as: $k = \frac{3}{2} u'^2$ [45, 164].

Table 3-2: The initial and boundary conditions in the numerical simulation

Variable	Description	Boundary	
		Wall	InternalField
alphat	Turbulent thermal difusifity (kg/m/s)	ZeroGradient	Uniform 0
b	Regress variable (dimentionless)	ZeroGradient	Uniform 1
k	The turbulent kinetic energy (m^2s^{-2})	ZeroGradient	Uniform $\frac{3}{2} u'^2$
epsilon	The turbulent dissipation rate (m^2s^{-2})	ZeroGradient	Uniform 375
Su	Laminar flame speed (ms^{-1})	ZeroGradient	Uniform 0.43
T	Temperature (K)	ZeroGradient	Uniform 360
P	Pressure (Pa)	ZeroGradient	Uniform (pressure value)
U	Velocity Field (ms^{-1})	fixedValue (0 0 0)	Uniform (0 0 0)
Ξ	The flame wrinkling factor (dimensionless)	ZeroGradient	Uniform 1

The ignition is modelled as a small hot spot (radius= 2 mm) in the chamber's centre with the value of 'b' set as 0.4 to initiate the flame (b value must be between 1 and 0 to ignite the mixture) [25, 45, 49]. The domain is set up as a hydrogen/air mixture with a specific equivalence ratio. The initial and boundary conditions are presented in Table 3.2.

In OpenFoam, the discretizations of all conservation equations are based on the finite volume method. The time and convection terms are solved with the Gauss limited Linear scheme and second-order accuracy. The preconditioned Conjugate Gradient (PCG) algorithm is adopted to decouple the pressure and velocity in solving the algebraic equations obtained after discretization. The tolerances are $1x10^{-6}$ for pressure and density residuals and $1x10^{-5}$ for other variables.

In the k-ε simulation, three mesh sizes are tested to validate the mesh dependency, with 600,000, 1,000,000 and 1,400,000 elements. It is recognized that carrying out mesh dependency test in LES is complicated by the use of filters. In LES simulation, the filter is applied based on the mesh size. The finer mesh resolves smaller turbulent eddies. Therefore, the comparison between cases of different mesh sizes is impossible. Instead, the mesh quality can be checked based on the flow length scales, namely the Taylor length scale (λ)[165]. From the experimental analysis (as will be presented in Chapter 5), λ length scale is ~1.5 mm for 0.1 MPa and ~0.62 mm for 1.0 MPa with *u'=6 m/s.* Therefore, the mesh with a 0.62 mm element length can resolve the most energetic turbulent scales. The maximum available computing and time resources are used to develop the structured mesh with 10,509,720 grid points. This means that the element length is ≤ 0.62 mm, which can meet the current criteria. The time step is dynamically adjusted based on the maximum Courant number ($\frac{u\Delta t}{\Delta X}$), where *u* is flow velocity, *Δt* is time step, and *Δx* is grid size. The maximum courant number of 0.1 with a minimum time step of $1x10^{-6}$ is used in this simulation. In the LES simulation, 40 cores with memory of 1 GB per core were used in parallel. The LES simulation took around 40 hours. However, 24 cores with 1 GB were used for k-ε simulation. The k-ε simulation took around 8 hours. This work was undertaken on ARC4, part of the High Performance Computing facilities at the University of Leeds, UK.

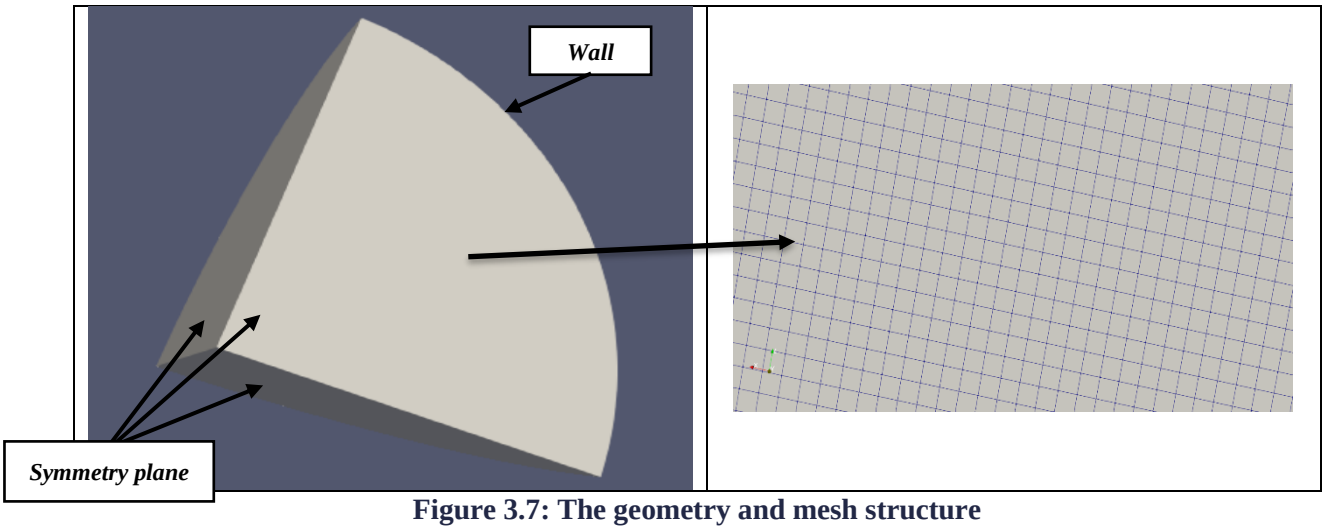

Figure 3.7: The geometry and mesh structure

Chapter 4: Laminar Burning Velocities and Markstein Numbers

4.1 Introduction

Spherically expanding explosions have been employed to measure the laminar flame speeds for H_2/CH_4/air mixtures over a wide range of H_2 fractions (30%, 50%, 70 and 100% hydrogen by volume) at initial temperatures of 303 K and 360 K and pressures of 0.1, 0.5 and 1.0 MPa. The equivalence ratio (ϕ) varied from 0.5 to 2.5 for hydrogen/air and from 0.8 to 1.2 for methane/hydrogen/air mixtures. The corresponding laminar burning velocities, u_l, at zero stretch rate, are derived and presented in this chapter. The u_l in this study is derived at constant pressure. Figure 4.1 presents the flame pressure as a function of time correlated with the flame visualisations (flame radius) for different mixtures, pressure, temperature and equivalence ratio. There is no pressure increase while the flame reaches the rig edge.

To illustrate the effects of flame stretch upon burning velocities, the Markstein length, L_b, Markstein number, Ma_b, and strain rate Markstein number, Ma_{sr}, have also been derived from flame speed measurements. Uncertainties in the derived quantities are also discussed. This chapter is organized as follows. Section 4.2 presents the flame instabilities, and Section 4.3 discusses the flame speed and flame stretch rate. The unstretched laminar burning velocity is shown in Section 4.4. Section 4.5 presents Marksein's length and number. Section 4.6 presents the comparison of the experimentally derived laminar burning velocities against numerical predictions from three recently developed kinetic mechanisms for methane/hydrogen oxidation (the San Diego [116, 119], the Konnov [26] and the Aramco 2 [115] reduced mechanisms). Finally, chapter conclusions are drawn in Section 4.7.

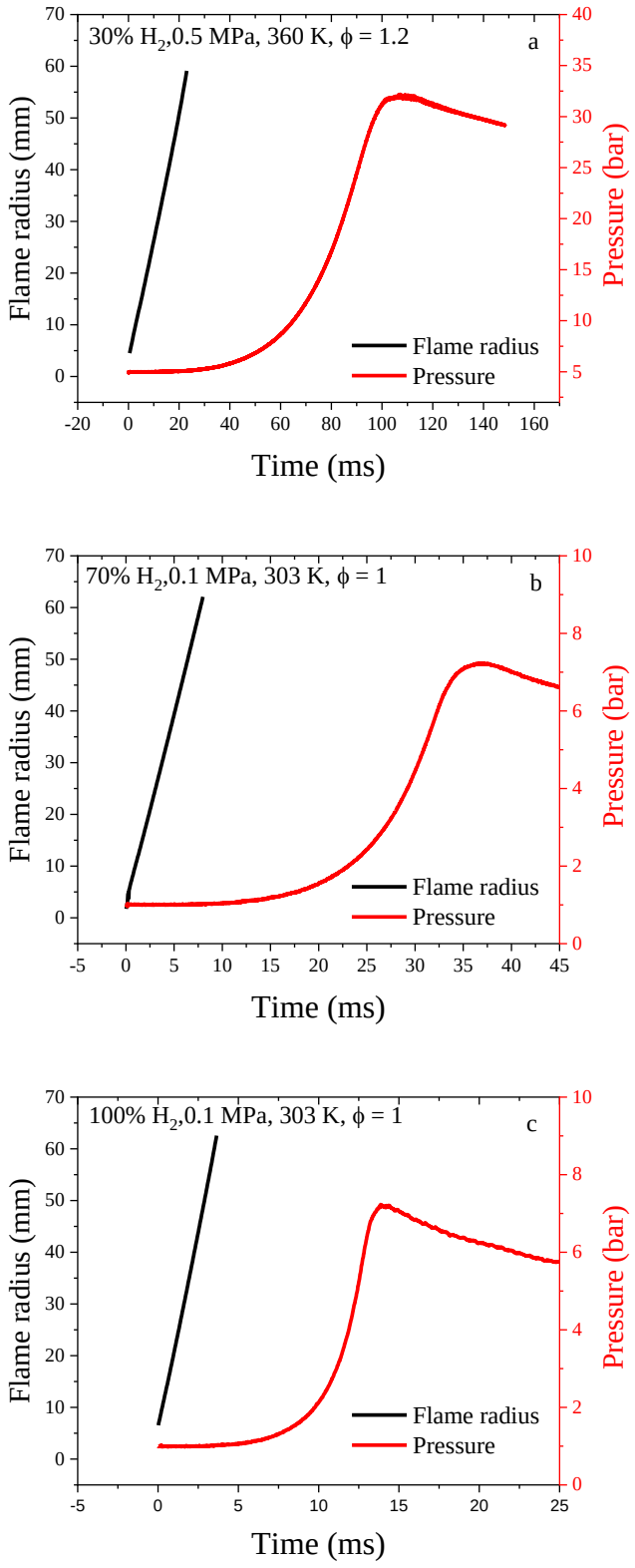

Figure 4.1: The flame visualisation and pressure as a function of time, a) 30 % H_2, 0.5 MPa, 360 K, b) 70% H_2, 0.1 MPa, 303 K and c) 100% H_2, 0.1 MPa, 303 K.

4.2 Flame Instabilities Observation

Figures 4.2 and 4.3 show examples of flame front images at different flame radii, *r*, for various hydrogen volume fractions, temperatures, and pressures. The Schlieren images of the flame front are used to identify the transition from the stable to the unstable region. The flame front is stable for 30% and 50% H_2 at 0.1 MPa, with only a few cracks caused as the flame passes through the spark electrode [72]. This was the case in most low-pressure explosions except for the lean mixture with 70% H_2 and lean and stoichiometric mixtures with 100% H_2, in which the TD and DL instabilities were developed. The flame instabilities also exist in the high initial pressure cases with all hydrogen fractions. The flame propagates smoothly in the early stages, as the stretch rate is sufficient to maintain a smooth flame surface. Following this, and with a reduction in the stretch rate, cellular instability develops at the critical flame radius (r_{cl}), increasing the flame speed [88, 166]. Cracks resulting from ignition effects [98] were shown in the stable flame front. The flame speed is plotted as a function of the flame radius or flame stretch rate to discriminate between cracked and cellular flames. The transition point (i.e. the onset of instability) started when the flame speed increased significantly (this will be presented in the next section).

Interactions between the Darrieus–Landau (DL) and Thermal Diffusion (TD) instabilities are the main cause of cells forming in the spherical flame propagations [96, 98]. In the laminar premixed explosion, the competition between heat conduction from the flame and reactant diffusion towards the flame results in TD instability. The mixture's Lewis number (*Le*) is the ratio of thermal diffusivity to mass diffusivity. The TD instability is enhanced with mixtures of *Le* below the critical value (≈ 0.8) [38, 93]. For 0.1 MPa, cellular instability was not present at 30% and 50% H_2 as the Lewis number of these mixtures is within the stable regime ($0.8 < L_e < 1.4$) [94].

As the hydrogen fraction increased to 70%, flame front cellularity was shown at ϕ=0.8 (*Le*<0.8) and ϕ=0.8 and 1 for 100% H_2. The hydrogen, which has strong mass diffusion, decreases *Le* and enhances the TD instability [99]. In contrast, flame instability has not been observed for rich mixtures with high H_2 concentrations within the field of view under initial pressure 0.1 MPa, as *Le* > 1.

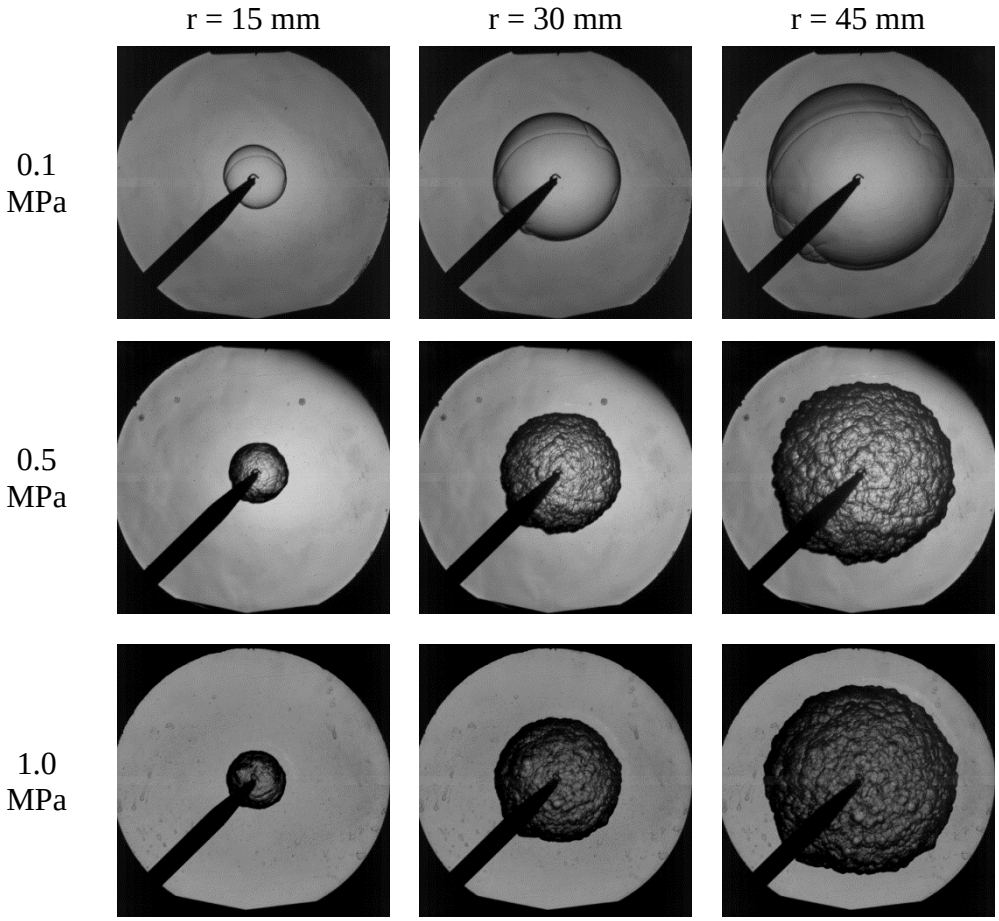

Figure 4.2: Flame images for 50% H_2, ϕ =0.9 at 360 K with different initial pressures.

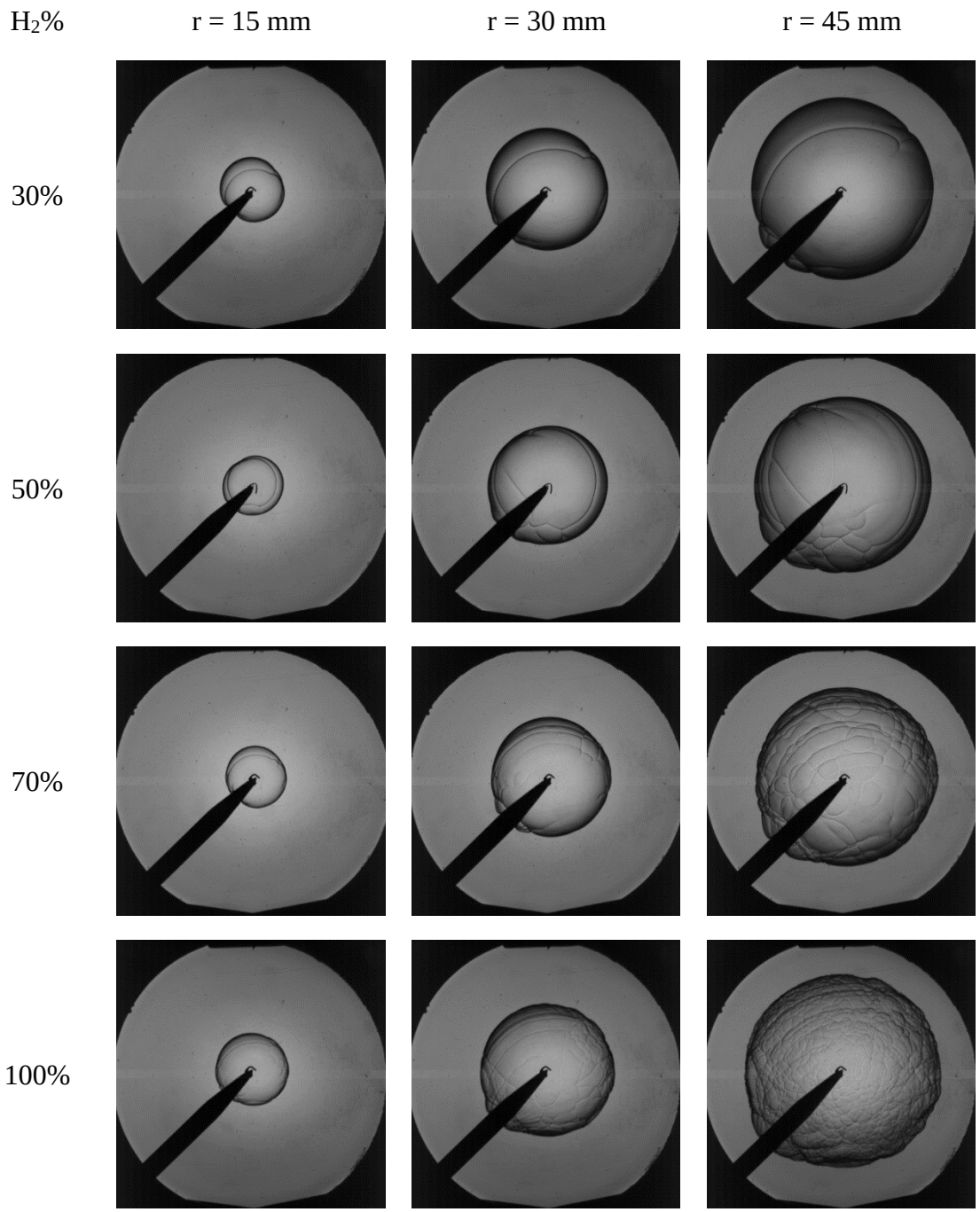

Figure 4.3: Flame images for an initial pressure of 0.1 MPa, ϕ =0.8 at 303 K with different H_2 volume fractions.

For high-pressure explosions (0.5 and 1 MPa), cellularity has been observed in all mixtures due to DL and TD instabilities. Increased pressure promotes DL instability, which is generated by the interaction of the flame with hydrodynamic disturbances. The DL instability develops as the flame thickness decreases and/or the density ratio (ρ_u/ρ_b) increases [60, 73, 93]. As the initial pressure increases at a specific initial temperature, the change in density ratio is small, while the decrease in the flame thickness is noticeable, resulting in hydrodynamic instability. As the initial temperature decreases at a specific pressure, the density ratio increases while the change in flame thickness is small, advancing the onset of instability ($r_{cl} \propto T_u$). Thus, the DL instability is dominant in high-pressure and low-temperature explosions due to the increased density ratio and decreased flame thickness.

The onset of cellularity, which is the transition point between the stable and unstable regimes, depends on thermal-diffusive and hydrodynamic effects. Increasing hydrogen fraction and pressure leads to the earlier onset of instability and a smaller critical flame radius. As the hydrogen fraction increases, Lewis number and flame thickness decrease, leading to the TD and DL instabilities. This trend is presented in Figure 4.4, which shows the critical flame radius for a stoichiometric mixture at 360 K. The critical flame radii for all cases are presented in Tables 4.1-4. As the hydrogen fraction increases, the onset of instability appears earlier over the flame surface (reduced critical flame radius). For 0.5 MPa, 360 K and ϕ = 1, r_{cl} is 26 mm for 30% H_2, 13.2 mm for 50% H_2, 10.5 mm for 70% H_2 and 10 mm for pure H_2 fuel. r_{cl} also decreased with increasing pressure for all mixtures. r_{cl} for 30% H_2 decreased from 26 mm at 0.5 MPa to 13 mm when the pressure increased to 1.0 MPa. So, in summary, adding hydrogen, increasing pressure and reducing the temperature all promote the onset of cellularity.

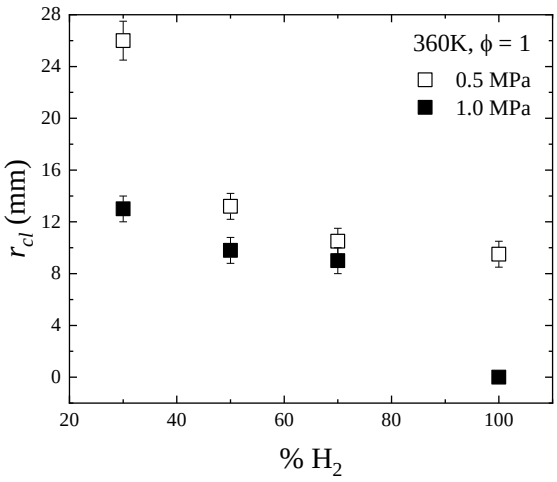

Figure 4.4: Critical flame radius (mm) vs. volumetric hydrogen fractions at 360 K and ϕ= 1.

4.3 Flame Speeds and Stretch Rate

As the hydrogen fraction increases, the flame speed increases for all mixtures. As observed previously [17, 82, 83], hydrogen increases the flame temperature and supplies more free active radicals to the reaction. In all mixtures considered here, the flame speed was high in the early stages of the flame propagation due to the influence of the ignition energy [72, 73]. The flame speed then decreases as the influence of the spark reduces [167] and before combustion is fully established. A fully developed laminar flame (stable region) is obtained until the onset of instability when the flame accelerates. The effects of spark and instabilities were presented in Chapter 3 (Figure 3.5).

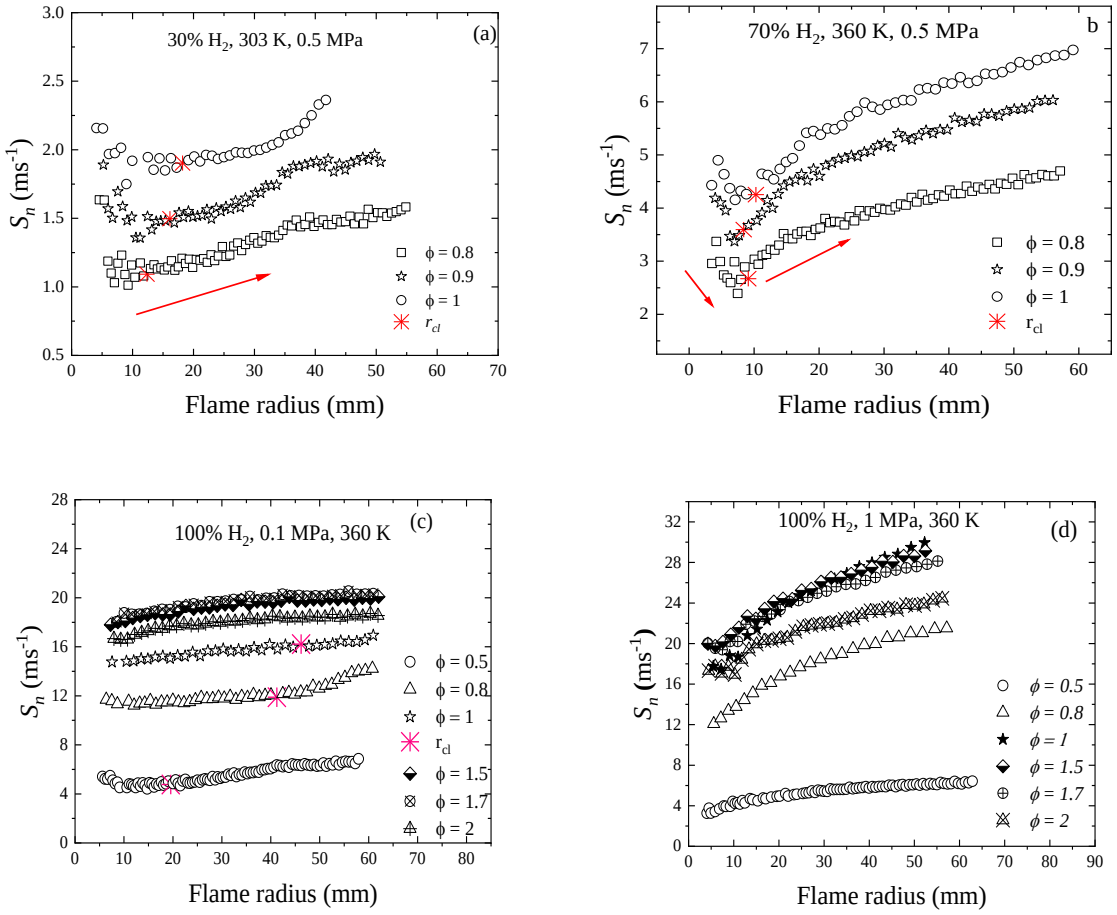

Figure 4.5: Flame speed (ms^{-1}) vs flame radius (mm) with different equivalence ratios. a) 30% H_2, 0.5 MPa, b) 70% H_2, 0.5 MPa, c) 100% H_2, 0.1 MPa, and d) 100% H_2, 1 MPa.

In the high-pressure explosion with 30% H_2, the flame speed in the stable region increased as the flame radius increased (the red arrow in Figure 4.5a). However, for 70% H_2, the flame speed decreases up to the critical flame radius (the red arrows in Figure 4.5b). Then, it increases rapidly due to the increased flame surface area [166]. Neither trend was observed for pure hydrogen at 1.0 MPa (Figure 4.5d). In this case, the flame speed increased with the flame radius from the early stages of flame propagation due to the early development of the flame instability. Laminar burning velocity measurements, in this case, are not possible due to the absence of a stable region with laminar flame propagation.

The slope of the flame speed, which is a function of flame radius for 1.0 MPa, is higher than the cellularity-free flame propagation slope at 0.1 MPa (Figure 4.5c). The flame speed increases rapidly in the high cellular flame, as in the cases of 70% and 100% H_2 at high initial pressure (Figure 4.5 b and d). The flame instabilities accelerate the flame propagation. Moreover, the mixture stoichiometry has a noticeable influence on the flame speed, as seen in the high speed in the cases of ϕ = 1, 1.5 and 1.7. This trend will be discussed in the following sections.

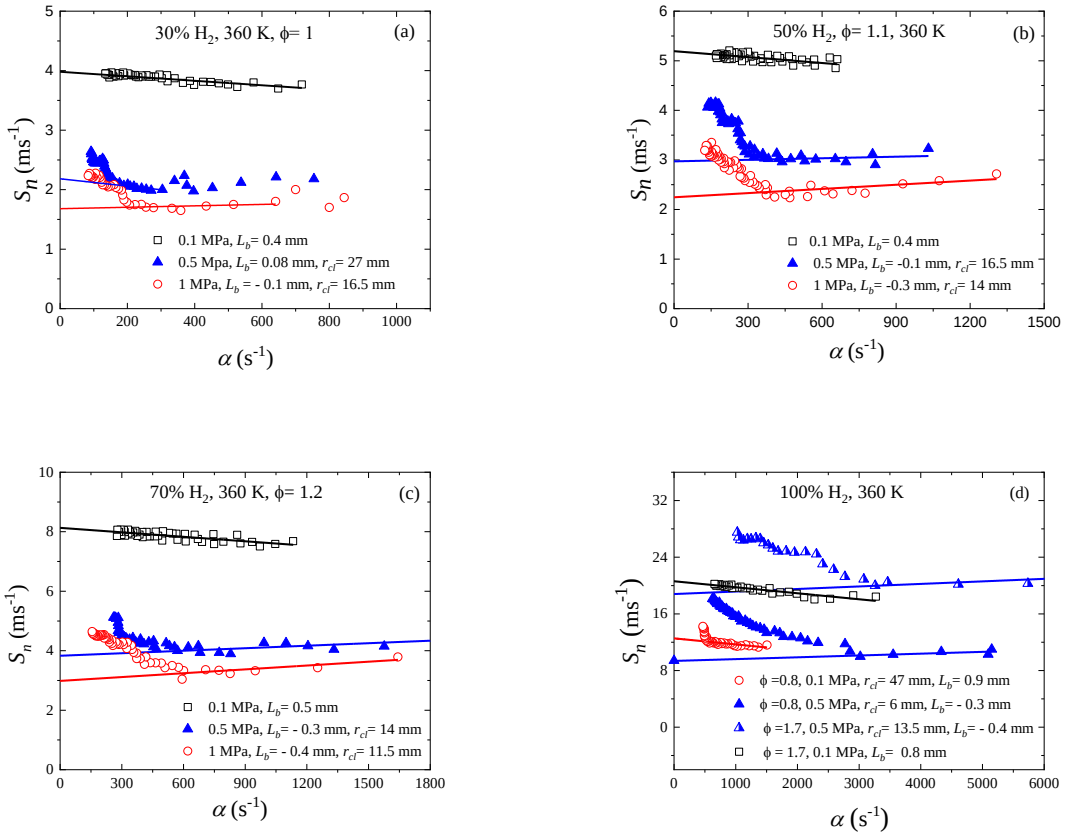

Figure 4.6: Flame speed (ms^{-1}) vs. stretch rate (s^{-1}) at 360 K for 30, 50, 70, and 100% volumetric fraction of hydrogen for different initial pressures and equivalence ratios.

Figures 4.6 and 4.7 show the variation of flame speed with stretch rate at different temperatures, pressures, H_2 fractions and equivalence ratios. The extrapolated data, Markstein length L_b and critical flame radius r_{cl} are also shown.

For low-pressure explosions (0.1 MPa), the flame propagated smoothly without flame cellularity within the field of view, and the value of S_n decreased with increasing stretch rate, indicating positive Markstein lengths in the rich explosions of 30%, 50% and 70% H_2 mixtures (Figures 4.6 and 4.7a-c). As the initial pressure increased, the gradient of the S_n-α curve decreased. For the stoichiometric mixture of 30% H_2, L_b decreased from 0.4 mm at 0.1 MPa to 0.08 mm at 0.5 MPa and -0.1 mm at 1.0 MPa. In the negative L_b cases, S_n increases as the stretch rate increases, lowering the unstretched flame speed (S_s) and laminar burning velocity (u_l). This is the opposite of what happens for the positive L_b cases.

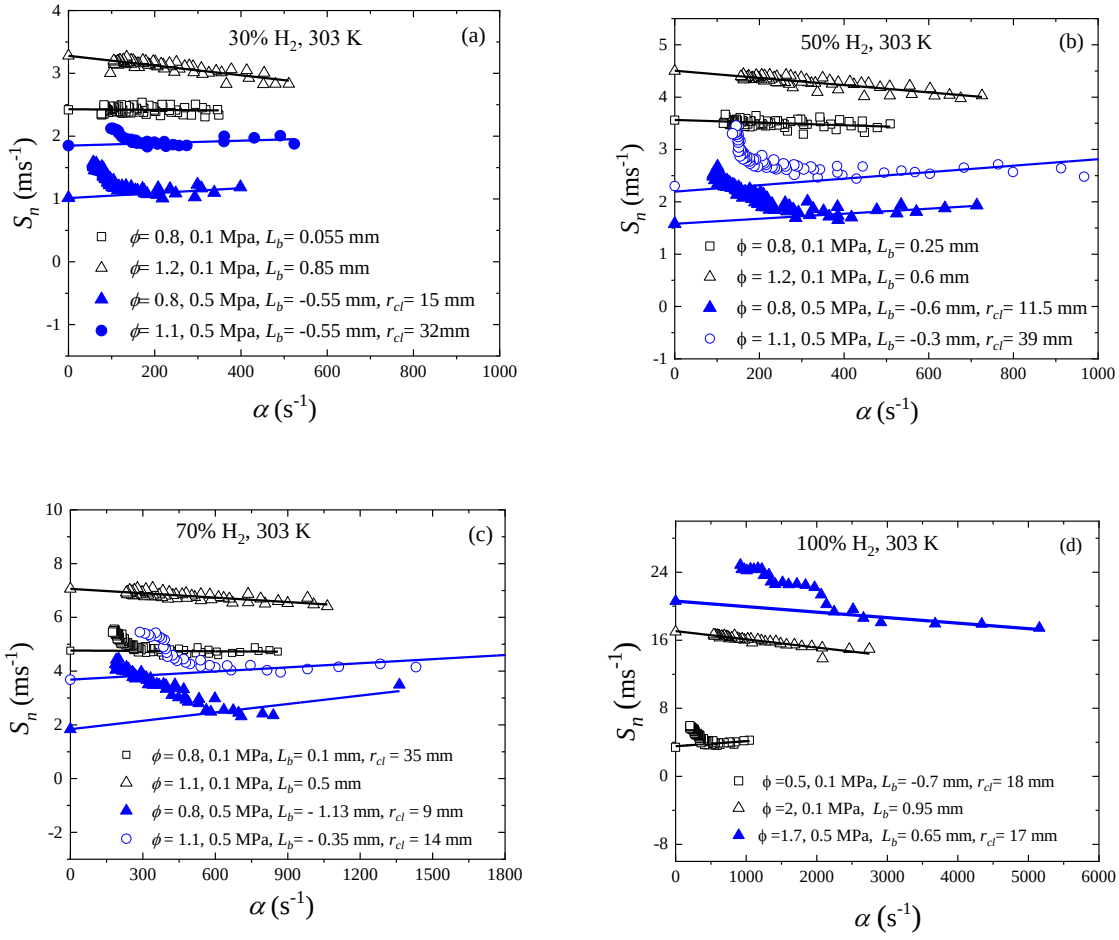

Figure 4.7: Flame speed (ms^{-1}) vs. stretch rate (s^{-1}) at 303 K for 30, 50, 70, and 100% volumetric fraction of hydrogen for different initial pressures and equivalence ratios.

There are different sources of uncertainty in the derivation of laminar burning velocities from the measurements. Firstly, the uncertainty due to the linear extrapolation is tested using Eq. 3.9. In all cases, the uncertainty indicator (U_f) values vary between -0.05 and 0.15, indicating that linear extrapolation is valid and leads to uncertainties in the data presented here $< \pm 5\%$ [76]. Thus, linear extrapolation (Eq. 2.6) is used to obtain the unstretched flame speed and Markstein length L_b. The second and most important source of uncertainty is the choice of the stable region (i.e. the thresholds which define the end of the spark effect and the onset of instability). The stable region is compacted at high pressures and hydrogen fractions (Figures. 4.6 and 4.7 c & d). The present study used minimum spark energy in all explosions (1 mJ) [106], as adding hydrogen reduces the required ignition energy. The end of the spark energy effect was taken to be at a flame radius = 10 mm for 0.1 MPa [71] and 5 mm for higher-pressure explosions [73]. Determining the onset of instability precisely is not straightforward. An example of the flame around the onset of instability is presented in Figure 4.8 for 50% H_2 with 0.5 MPa, 360K and $\phi = 1$. The onset of instability could be associated with any of the six consecutive images. This uncertainty has been accounted for in the present study.

The sensitivity of u_l to the selected point of instability is demonstrated in Figure 4.9. Here, the number of points used for the extrapolation varies to account for uncertainties in defining the boundary of the onset of instability, as illustrated in Figure 4.8. The uncertainty increased with the initial pressure and hydrogen fraction. The uncertainty in the laminar burning velocity increased from ±1.5% of u_l for 30% H_2 to ±3.5% for 70% H_2 and ±12% for pure H_2 at 0.5 MPa (Figures 4.9a-c). As the initial pressure increased from 0.5 MPa to 1 MPa, the uncertainty increased from ±3.5% of u_l to ±7.5% with 70% H_2.

The uncertainty increased at high pressures and hydrogen concentrations due to the smaller number of points used in the extrapolation. For example, there was a shortage of data points for the cases with 100% H_2, ϕ= 0.8, 0.5 MPa and 360 K, as the spark effect vanished at a flame radius, r =5 mm, and the onset of instability was determined to be between r = 6 and 7.5 mm. These uncertainties are included in the error bars of further results presented in this work. To illustrate the uncertainty calculation, let's take three repeated experiments for stoichiometric flames of 50% H_2,360 K and 0.5 MPa. The u_l are 0.433, 0.455 and 0.435 ms^{-1}, and the STDEV.S is 0.012 ms^{-1}. The uncertainty due to the onset of instability is 0.024 ms^{-1}. Thus, the u_l reported for this case is 0.44 $\pm$0.036 ms^{-1}.

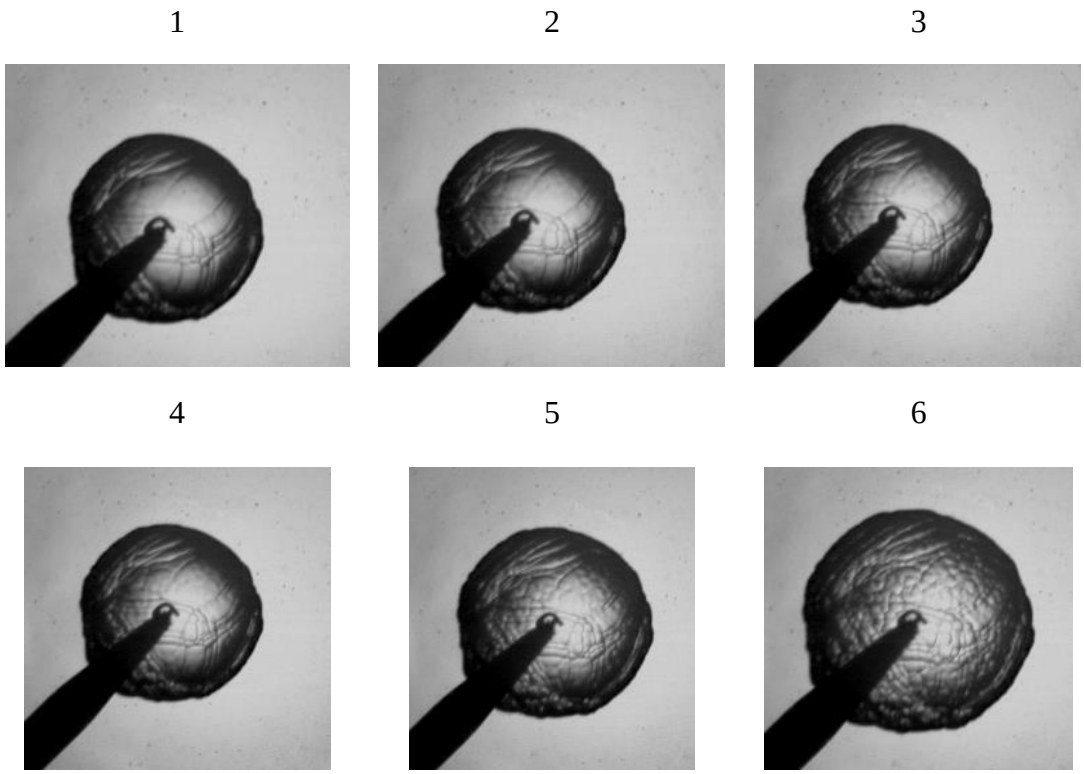

Figure 4.8: Possible instability onsets for the case with 50% H_2, 0.5 MPa, 360K and ϕ=1, image with label 1 at 3.75 ms after ignition, the time step is 0.25 ms.

4.4 Unstretched Laminar Burning Velocities

The effects of stretch are eliminated by extrapolating the stretched flame speed at zero stretch rate. The unstretched flame speed (S_s) is multiplied by the density ratio (Eq. 3.8) to obtain the unstretched laminar burning velocity (u_l). Figures 4.10-11 show the variation of un-stretched laminar burning velocity with equivalence ratio for different H_2 fractions, pressures and temperatures. As the hydrogen fraction increases, the laminar burning velocity increases. The maximum laminar burning velocity occurs on the rich side of stoichiometric conditions. For example, 30% and 50% H_2 occurs at $\phi = 1.1$. However, it shifts to $\phi = 1.2$ for 70% H_2 and to $\phi = 1.7$ for a pure H_2 explosion. This trend quantifies the effect of hydrogen volume fraction on laminar burning velocity. Hu et al. [75] have highlighted three regimes in H_2/CH_4 mixture flame propagation: (a) methane-dominated propagation for $H_2 < 60\%$, (b) a transition regime for $60\% < H_2 < 80\%$ and (c) methane-inhibited hydrogen propagation where $H_2 > 80\ \%$. Therefore, the hydrogen fraction has the dominant effect on u_l.

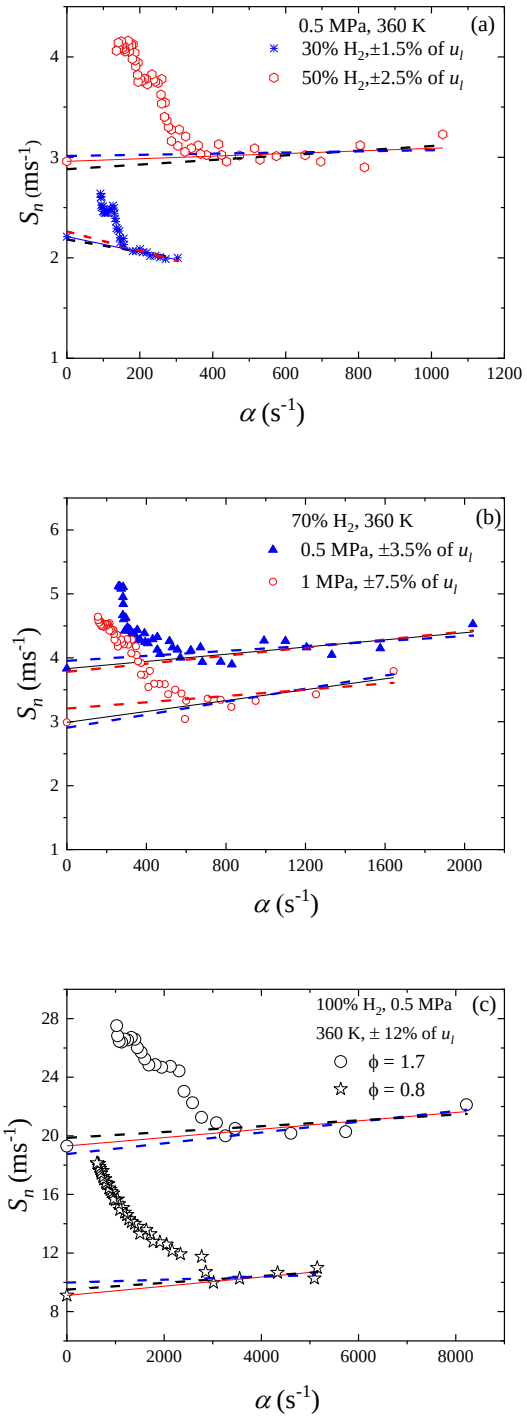

Figure 4.9: The measurement uncertainty in the laminar burning velocity due to the choice of the onset of instability condition.

In all experimental conditions for the methane-H_2 mixtures, the burning velocity decreased as the pressure increased for all equivalence ratios. This behaviour was the same for pure H_2 at 360 K. However, at the lower temperature (303 K), the burning velocities overlap within the uncertainty ranges at ϕ = 1.5 and 1.7 as the initial pressure increased from 0.1 to 0.5 MPa (Figure 4.11a). The laminar burning velocities at an initial temperature of 360 K slightly increased with increasing temperature, and they still overlapped within the uncertainty range (Figure 4.11b). Two essential reactions have a substantial effect on the laminar burning velocity [168]:

$H + O_2 = OH + O$ ----- (R1)

$H + O_2 + M = HO_2 + M$ ----- (R2)

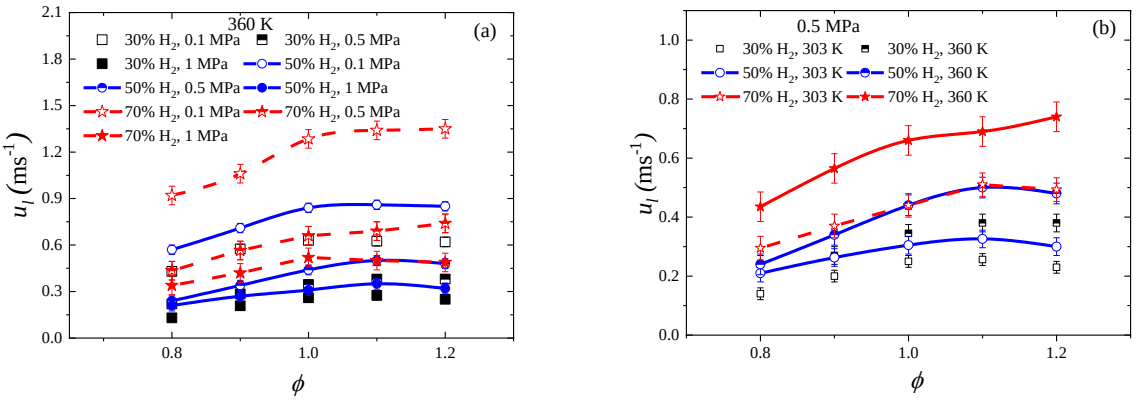

Figure 4.10: Unstretched laminar burning velocity vs. equivalence ratio for 30, 50 and 70% hydrogen fractions at different initial pressures and temperatures (a) at 360 K and different initial pressure, (b) at 0.5 MPa and different initial temperatures.

The chain branching reaction (R1) is endothermic and very sensitive to temperature changes. On the other hand, the radical termination exothermic reaction (R2) is strongly affected by pressure. HO_2 is produced in R2 at high pressures and is relatively inactive at low to intermediate temperatures, resulting in lower flame speeds at high pressures under these conditions [168]. This pressure effect on the laminar burning velocity will be discussed further in section 4.6.

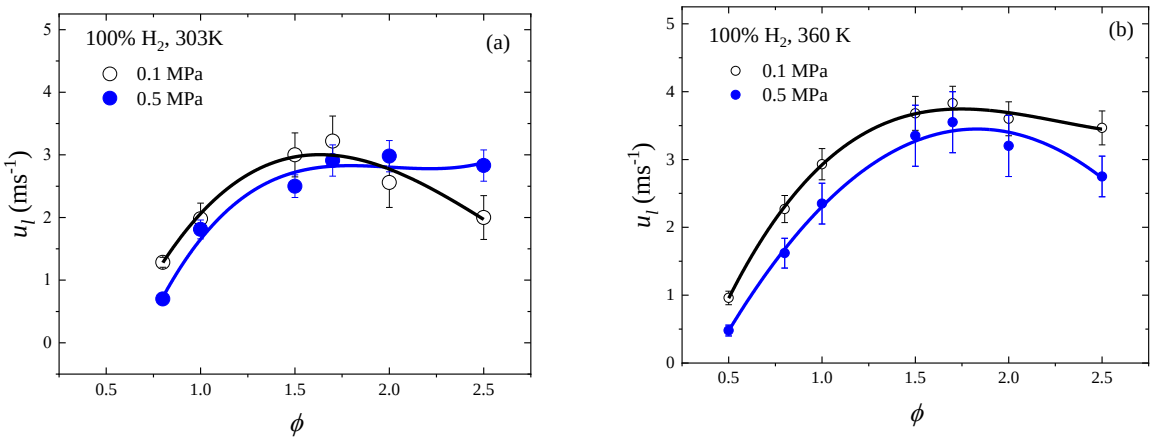

Figure 4.11: Unstretched laminar burning velocity with equivalence ratio for 100% hydrogen at different initial pressures and temperatures, (a) 303 K and (b) 360 K.

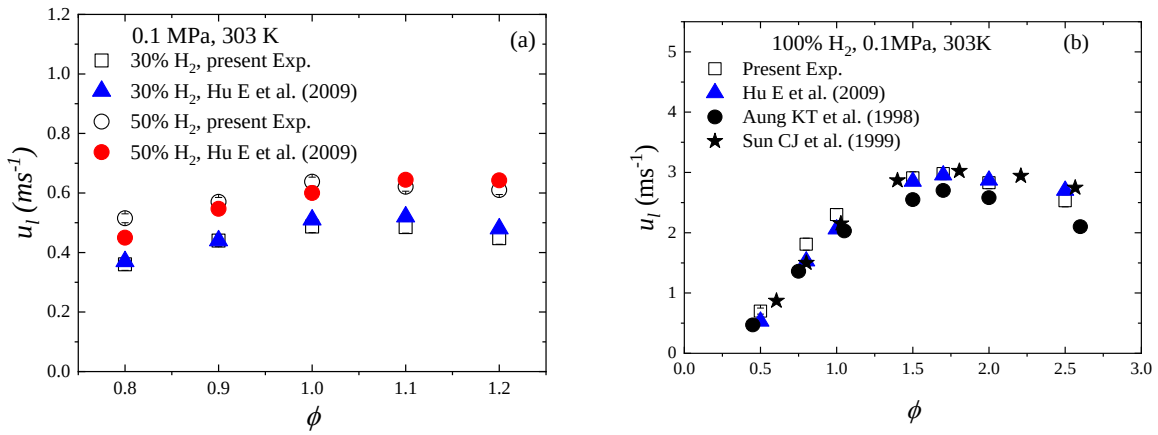

Figure 4.12: Unstretched laminar burning velocity with equivalence ratio for present and previous studies at 0.1 MPa and 303K, (a) H_2/CH_4 and (b) pure H_2.

Figure 4.12 compares the current results of the unstretched laminar burning velocity with those from the literature at 0.1 MPa [75, 80, 169, 170]. There is a good agreement between the present and previous results, with a maximum scatter of ±13% in the burning velocities for lean hydrogen explosions. The issue of experimental scatter is well-reported in the literature [110, 171, 172]. The primary sources of scatter in the lean hydrogen measurement are the extrapolation method (linear or nonlinear) and the limited number of points used in the extrapolation [172].

Such comparisons were not possible under high pressure, where the current work presents novel data unavailable in the literature. However, the excellent agreement found for overlapping conditions indicates the robustness of the current study.

4.5 Markstein number and Markstein length

The Markstein number is used to quantify the effect of flame stretch rate on the flame speed and, hence, the unstretched laminar burning velocity [66, 72]. The impact of stretch rate on flame speed depends on the Zel′dovich number, *Ze*, and the *Le [17]*. *Ze* represents the sensitivity of chemical reaction rate to temperature changes, and it is defined as $Z_e = \frac{E_a}{RT_b^2}(T_b - T_u)$, where E_a is the activation energy, R is the universal gas constant, and T_b and T_u are the adiabatic and unburned mixture temperature, respectively. The Markstein length (L_b) is a function of the physical and chemical properties of the mixture (*Le* and *Ze*). As the hydrogen fraction increases, non-dimensional activation energy (Zel′dovich number, *Ze*) decreases due to the increased adiabatic flame temperature, and *Le* decreases due to the hydrogen diffusivity [17]. Moreover, previous research on premixed pure H_2 and pure CH_4 [67, 72] determined L_b in terms of the Lewis number (L_b= - 0.059 mm with *Le* = 0.3 for pure H_2, and L_b= 0.74 mm with *Le*= 0.9 for pure CH_4).

Figures 4.13&4.14 show the effects of hydrogen, pressure and temperature on L_b for different mixtures. For lean and stoichiometric mixtures at 0.1 MPa, L_b increases with H_2 fraction (Figure 4.13a&b). However, L_b decreases with H_2 fraction for lean and stoichiometric mixtures at higher initial pressures. As the pressure rises, L_b decreases except for rich mixtures with 50 and 70% H_2 fraction (Figure 4.13c), where L_b increases slightly when the pressure increases from 0.5 to 1.0 MPa. As the temperature is increased from 303 to 360 K at 0.5 MPa, L_b increases significantly in the lean and stoichiometric mixtures (Figures 4.13 a&b) but decreases slightly in the rich mixtures (Figure 4.13c).

The data for pure hydrogen at 1 MPa is not presented here due to the early onset of flame cellularity. Compared with previous results [72] for pure CH_4 explosions at 0.1, 0.5, and 1.0 MPa, the present L_b is lower than the pure CH_4 results. This is expected as L_b for H_2 is lower than that of CH_4, which means adding hydrogen to methane lowers L_b.

Markstein length is normalized by the flame thickness to obtain the Markstein number (Ma_b). A negative Ma_b indicates that the flame is highly sensitive to stretch, while a positive Ma_b means that the flame is less sensitive to the stretch [39]. This will be discussed further in the turbulent flame propagation (next chapter). The strain rate Markstein number (Ma_{sr}) was calculated using the method described in section 3.3.1. However, this method was based on the assumption that Le =1 [154]. Therefore, the discussion here is focused on the Ma_b. Figures 4.15&16 show how Ma_b and Ma_{sr} vary with H_2 fraction for a range of equivalence ratios, pressures and temperatures. Ma_b decreases with pressure and hydrogen fraction in the lean and rich mixtures (Figure 4.15a), except for the case with ϕ = 0.8 at 0.1 MPa, where the Ma_b increases with increased H_2 fraction. In the lean mixture, Ma_{sr} increases as pressure increases. However, as the H_2 fraction increases, Ma_{sr} varies non-monotonically for lean and rich cases (Figure 4.15b).

Figure 4.16 presents Ma_b and Ma_{sr} for pure H_2 at 0.1 and 0.5 MPa as a function of equivalence ratio. It can be seen that Ma_b decreases with pressure. For 0.1 MPa, Ma_b increases as the mixture changes from lean to rich and eventually decreases for $\phi \geq 2$. The maximum Ma_b was at ϕ = 1.7, corresponding to the minimum flame thickness and maximum u_l. However, at 0.5 MPa, Ma_b decreases as the mixture changes from lean to rich, achieving its minimum value at ϕ= 1.7, increasing afterwards. Ma_{sr} increases with pressure for $\phi \leq 1.5$, while it decreases with pressure for $\phi > 1.5$ (Figure 4.16b).

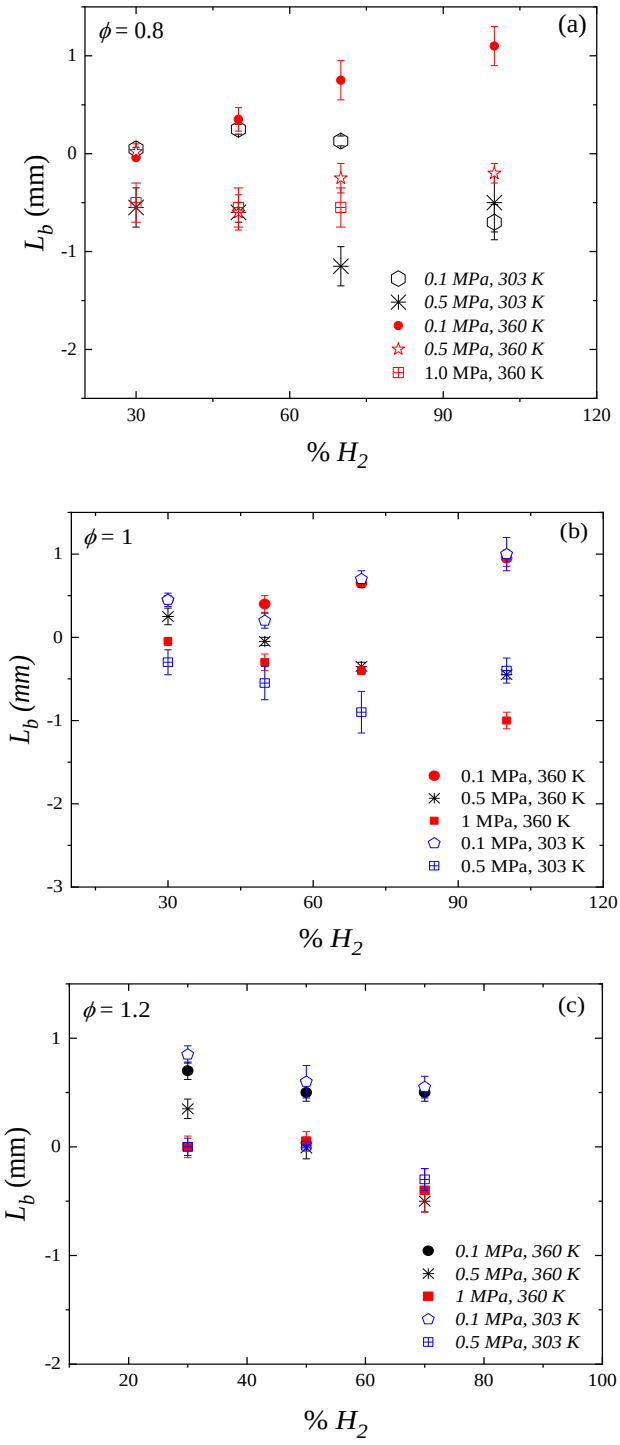

Figure 4.13: Markstein length vs. hydrogen fraction for lean, stoichiometric and rich mixtures at different initial pressures and temperatures, (a) ϕ= 0.8, (b) ϕ= 1 and (c) ϕ= 1.2.

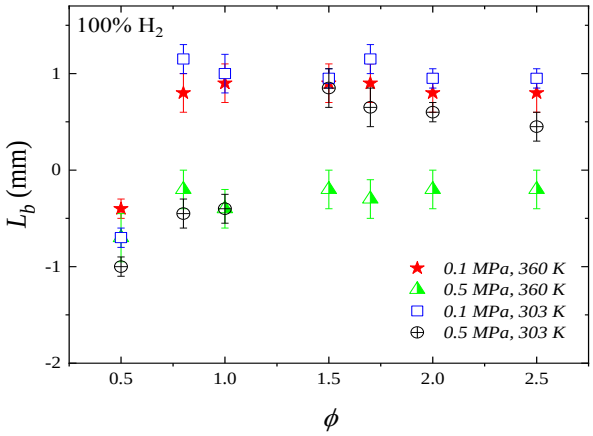

Figure 4.14: The impact of pressure and temperature on the Markstein length at different equivalence ratios for pure hydrogen.

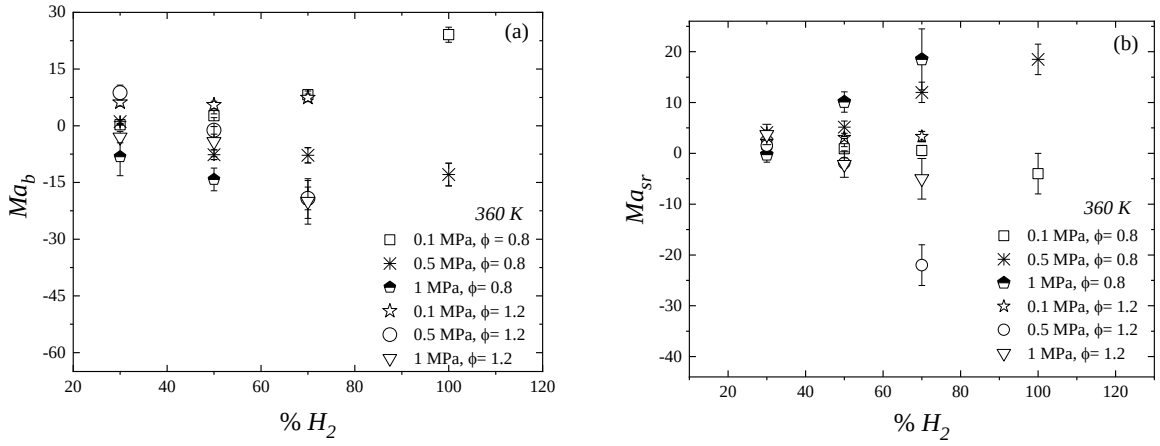

Figure 4.15: Markstein number vs. hydrogen fraction at ϕ = 0.8 and 1.2 and different initial pressures, (a) Ma_b and (b) Ma_{sr}.

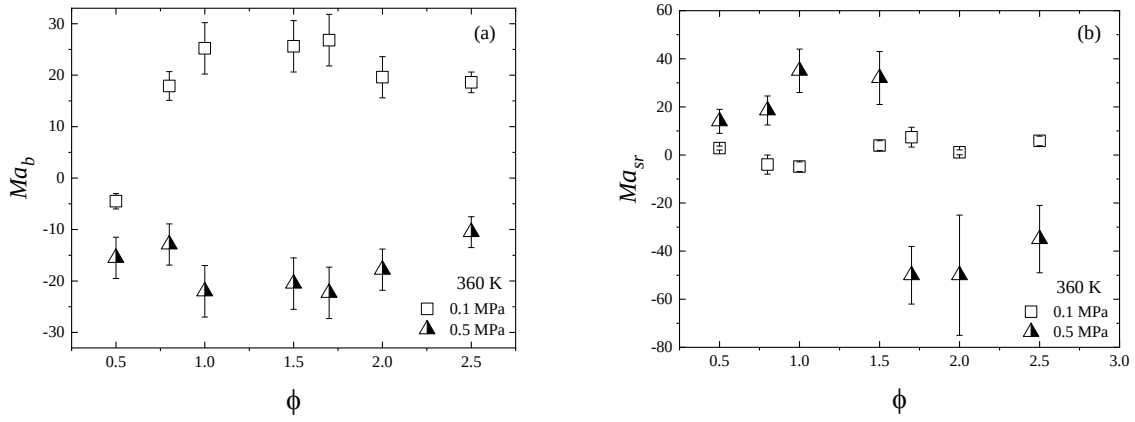

Figure 4.16: Total Markstein number and strain rate Markstein number vs. equivalence ratio for pure hydrogen at different initial pressures, (a) Ma_b and (b) Ma_{sr}.

As explained in the discussion in Figure 4.9, the uncertainty in the derived values of L_b, Ma_b and Ma_{sr} is significant in the high-pressure cases with high H_2 volume fractions, and this was also reported in [97]. For example, Ma_{sr} and Ma_b for the cases with ϕ = 0.8, 70% H_2 at 1 MPa and ϕ = 2, 100% H_2 at 0.5 MPa have a large error bar which varies from 30 to 60% of the original value (Figures 4.15&16). On the other hand, the error bar is small in the cases with 30 and 50% H_2 at 0.1 MPa (≤ 20% of the original value). The considerable uncertainty is due to the compact range of extrapolated points (stable regime), as discussed with respect to Figure 4.9. At 1 MPa with ϕ = 0.8 and 70% H_2, the stable regime was between flame radius, r = 5 mm to r = 7.5±1 mm, while it was in the range of 10-65 mm at 0.1 MPa with ϕ= 1 and 30% H_2. The uncertainty in the high-pressure and high H_2 cases is affected from both sides (spark effects and the onset of instability) due to the minimal number of points used in the extrapolation.

All the experimental data for laminar flame propagation reported in this study are presented in Tables 4.1 to 4.4. Figures 4.3 to 4.15 have already shown trends in the laminar burning velocity, critical flame radius, and Markstein length/number for some of the mixtures studied. However, some of the results are not presented in the above figures; hence, more details are shown in the tables. The laminar burning velocity data can be used to validate available kinetics and to create a flamelet library for numerical simulations. Markstein number is useful for indicating the flame sensitivity to the stretch rate. The flame thickness with laminar burning velocity can be used with the turbulent scales to identify the combustion regime in the turbulent regime diagram, which will be presented in the next chapter.

Table 4-1: Laminar burning velocity, Markstein length, critical flame radius, flame thickness, burned gas and strain Markstein number for 30% hydrogen fraction

Experimental Conditions	ϕ	u_l (m/s)	L_b (mm)	r_{cl} (mm)	δ_l (mm)	Ma_b	Ma_{sr}
0.1±0.0025 MPa, 303±2 K	0.8	0.36 ±0.012	0.055 ±0.006		0.156	0.35 ±0.06	1.55±0.18
	0.9	0.44±0.024	0.25 ±0.006		0.135	1.8 ±0.6	1.63±0.12
	1.0	0.487±0.024	0.45 ±0.006		0.118	3.8 ±0.7	1.85±0.18
	1.1	0.485±0.024	0.6 ±0.006		0.119	5 ±0.06	2.1±0.18
	1.2	0.448±0.024	0.85 ±0.006		0.130	6.5 ±0.5	2.37±0.12
0.1±0.0025 MPa, 360±2 K	0.8	0.43±0.024	0.04±0.012		0.156	0.25±0.06	1.75±0.12
	0.9	0.575±0.024	0.4±0.012		0.118	3.4±0.8	2.37±0.12
	1.0	0.63±0.024	0.45±0.012		0.108	4.1±0.6	2.42±0.12
	1.1	0.625±0.024	0.5±0.012		0.110	4.5±1.2	2.5±0.24
	1.2	0.62±0.024	0.7±0.012		0.111	6.2±0.12	2.38±0.12
0.5±0.0025 MPa, 303±2 K	0.8	0.14±0.024	-0.55±0.24	15.5±1.2	0.0889	-6.1±1.8	1.5±1.8
	0.9	0.2±0.024	-0.35±0.12	17.5±1.2	0.0605	-5.8±1	1.8±0.6
	1.0	0.25±0.024	-0.3±0.06	18.5±1.2	0.0498	-6±0.6	1.1±1.8
	1.1	0.256±0.024	-0.2±0.06	26±1.2	0.0493	-4±0.6	0.9±0.36
	1.2	0.23±0.024	-0.55±0.08	33±1.2	0.055	-3.9±0.6	0.8±0.18
0.5±0.0025 MPa, 360±2 K	0.8	0.24±0.024	0.07±0.024	24±1.2	0.0616	1.1±1	4.1±0.6
	0.9	0.27±0.024	0.02±0.024	26±1.2	0.0548	0.36±0.24	-4±1.2
	1.0	0.34±0.024	0.2±0.18	26±1.2	0.0429	6.3±3.6	1.3±2
	1.1	0.38±0.024	0.25±0.12	29.5±1.2	0.0395	6.25±2.4	-2±2
	1.2	0.38±0.024	0.35±0.12	37.7±1.2	0.0395	8.75±3	1.5±1.8
1.0±0.0025 MPa, 360±2 K	0.8	0.13±0.018	-0.5±0.24	11±1.2	0.0594	-8.2±4.8	-0.25±1.2
	0.9	0.2±0.018	-0.1±0.06	13±1.2	0.0373	-2.6±0.6	-1.1±0.63
	1.0	0.26±0.018	-0.05±0.06	15.5±1.2	0.03	-2.5±1	-3.8±2
	1.1	0.27±0.018	-0.1±0.11	16.5±1.2	0.0287	-5±2.4	6.25±3.6
	1.2	0.25±0.018	0.01±0.09	25±1.2	0.0316	-3±2.4	3.7±1.7

Table 4-2: Laminar burning velocity, Markstein length, critical flame radius, flame thickness, burned gas and strain Markstein number for 50% hydrogen fraction

Experimental Conditions	ϕ	u_l (m/s)	L_b (mm)	r_{cl} (mm)	δ_l (mm)	Ma_b	Ma_{sr}
0.1±0.0025 MPa, 303±2 K	0.8	0.51±0.036	0.25±0.06		0.12	2±0.6	1.45±0.6
	0.9	0.57±0.036	0.4±0.02		0.109	3.6±0.12	1.44±0.12
	1.0	0.63±0.036	0.2±0.02		0.1	2±0.24	1.85±0.24
	1.1	0.62±0.036	0.4±0.12		0.103	3.8±1.2	1.9±0.36
	1.2	0.61±0.036	0.6±0.12		0.106	5.6±1.2	2.15±0.18
0.1±0.0025 MPa, 360±2 K	0.8	0.57±0.036	0.35±0.06		0.13	2.65±0.6	0.9±0.36
	0.9	0.71±0.036	0.2±0.04		0.105	1.89±0.6	1.4±0.6
	1.0	0.84±0.048	0.4±0.12		0.09	5.4±1.5	2.7±0.7
	1.1	0.86±0.036	0.5±0.12		0.089	5.5±1.5	2.95±0.48
	1.2	0.85±0.036	0.5±0.04		0.091	5.48±0.12	3.1±0.6
0.5±0.0025 MPa, 303±2 K	0.8	0.21±0.036	-0.6±0.24	11.5±1.2	0.075	-7.79±2.4	3.05±0.8
	0.9	0.26±0.036	-0.7±0.24	12.2±1.2	0.05	-13.8±2.4	5.1±1.2
	1.0	0.30±0.036	-0.55±0.24	13.4±1.2	0.045	-12.1±2.4	1.35±0.8
	1.1	0.32±0.036	-0.3±0.18	17.3±1.2	0.043	-6.9±2.4	2.1±0.9
	1.2	0.3±0.036	0.03±0.024	39±1.2	0.047	0.62±2.4	3.15±0.6
0.5±0.0025 MPa, 360±2 K	0.8	0.24±0.036	-0.6±0.12	12±1.2	0.078	-7.65±1.2	5.15±1.2
	0.9	0.34±0.036	-0.15±0.09	13.2±1.2	0.047	-3.1±1.8	13.73±3.6
	1.0	0.44±0.036	-0.09±0.06	15±1.2	0.037	-2.4±1.2	8.73±3
	1.1	0.5±0.036	-0.06±0.06	18±1.2	0.033	-1.9±1.8	-0.8±0.8
	1.2	0.48±0.036	-0.075±0.04	25±1.2	0.035	-1.2±1.2	-1.9±0.7
1.0±0.0025 MPa, 360±2 K	0.8	0.22±0.036	-0.55±0.12	8±1.2	0.038	-14.2±2.4	10.1±2.4
	0.9	0.27±0.036	-0.45±0.24	9.8±1.2	0.031	-13.4±4.8	11±4.8
	1.0	0.31±0.036	-0.3±0.18	11.2±1.2	0.027	-10.2±4.8	12±8
	1.1	0.35±0.036	-0.25±0.1.2	13.3±1.2	0.025	-10.1±3.6	1±3.6
	1.2	0.32±0.036	-0.1±0.08	21.5±1.2	0.027	-4.2±4.8	-2.2±1.8

Table 4-3: Laminar burning velocity, Markstein length, critical flame radius flame, thickness, burned gas and strain Markstein number for 70% hydrogen fraction

Experimental Conditions	ϕ	u_l (m/s)	L_b (mm)	r_{cl} (mm)	δ_l (mm)	Ma_b	Ma_{sr}
0.1±0.0025 MPa, 303±2 K	0.8	0.71±0.06	0.1±0.06	35±1.2	0.097	1.25±1.2	1.2±0.36
	0.9	0.84±0.06	0.35±0.06	40±1.2	0.085	4.1±1	1.7±0.3
	1.0	0.95±0.048	0.7±0.0	-	0.076	9.1±0.00	1.55±0.6
	1.1	0.99±0.042	0.5±0.0	-	0.075	6.62±0.06	2.1±0.6
	1.2	0.99±0.048	0.55±0.06	-	0.077	6.1±0.48	1.7±0.42
0.1±0.0025 MPa, 360±2 K	0.8	0.92±0.06	0.75±0.08	46±1.2	0.091	8.2±1.2	0.55±0.6
	0.9	1.06±0.06	0.65±0.1	53±1.2	0.08	8±1.2	1.34±1.8
	1.0	1.28±0.07	0.65±0.12		0.067	9.65±1.8	1.2±0.6
	1.1	1.34±0.052	0.6±0.06		0.067	9±1.2	2.2±1
	1.2	1.35±0.048	0.5±0.12		0.067	7.4±0.6	3.3±1
0.5±0.0025 MPa, 303±2 K	0.8	0.29±0.048	-1.15±0.3	8.2±0.6	0.052	-22±4.8	1.05±0.6
	0.9	0.37±0.048	-0.8±0.18	10±0.6	0.042	-19.2±2.4	1.75±1.2
	1.0	0.44±0.048	-0.9±0.36	11.7±0.6	0.035	-24.5±8	3±6
	1.1	0.51±0.048	-0.35±0.3	13.8±0.6	0.031	-12±4.8	-1.2±1.8
	1.2	0.49±0.048	-0.3±0.3	14.5±0.6	0.033	-9±4.8	-0.2±0.36
0.5±0.0025 MPa, 360±2 K	0.8	0.43±0.06	-0.25±0.24	9.1±0.6	0.042	-5.8±4.8	12±2.4
	0.9	0.56±0.06	-0.25±0.12	10.5±0.6	0.032	-7.6±3.6	31±11
	1.0	0.66±0.06	-0.35±0.18	11±0.6	0.028	-12.3±4.8	35±11
	1.1	0.69±0.055	-0.55±0.24	12.4±0.6	0.027	-20±3.6	-7±8.5
	1.2	0.74±0.055	-0.5±0.12	13±0.6	0.026	-19.2±3.6	-22±4.8
1.0±0.0025 MPa, 360±2 K	0.8	0.34±0.048	-0.55±0.18	7.5±0.6	0.028	-19.5±3	18.5±5
	0.9	0.42±0.048	-0.75±0.24	9±0.6	0.023	-33±4.8	30±6
	1.0	0.52±0.048	-0.4±0.12	9.5±0.6	0.019	-21±4.8	30±8
	1.1	0.5±0.058	-0.6±0.12	10.6±0.6	0.02	-28±4.8	28±7
	1.2	0.49±0.06	-0.4±0.12	11.9±0.6	0.025	-20±4.8	-3±6

Table 4-4: Laminar burning velocity, Markstein length, critical flame radius, flame thickness, burned gas and strain Markstein number for pure hydrogen explosions

Experimental Conditions	ϕ	u_l (m/s)	L_b (mm)	r_{cl} (mm)	δ_l (mm)	Ma_b	Ma_{sr}
0.1±0.0025 MPa, 303±2 K	0.5	0.7±0.06	-0.7±0.24	18±1.2	0.103	-6.7±0.6	12.3±2.4
	0.8	1.79±0.12	1.15±0.3	36±1.2	0.047	24.1±2.5	-1.1±1.2
	1.0	2.3±0.12	1.0±0.3	45.5±1.2	0.04	25±4.8	0.44±0.48
	1.5	2.91±0.06	0.95±0.18	-	0.037	25.2±3.6	6.2±1.2
	1.7	2.98±0.06	1.15±0.18	-	0.038	30±2.4	9.85±2.4
	2	2.83±0.07	0.95±0.18	-	0.043	22±3.6	4.6±1.2
	2.5	2.53±0.06	0.95±0.18	-	0.052	18±1.2	3.8±1.2
0.1±0.0025 MPa, 360±2 K	0.5	0.98±0.07	-0.3±0.18	19.4±1.2	0.087	-4.5±2.4	2.85±1.2
	0.8	2.27±0.08	0.8±0.18	41.8±1.2	0.044	17.9±3.6	-4±4.8
	1.0	2.93±0.12	0.95±0.3	57±1.2	0.037	25.2±6	-4.87±1.8
	1.5	3.68±0.08	0.9±0.06	-	0.035	25.6±1.2	3.9±2.4
	1.7	3.83±0.06	0.95±0.12	-	0.035	26.8±2.4	7.4±4.9
	2	3.55±0.06	0.8±0.12	-	0.04	19.6±1.2	1.1±1.2
	2.5	3.46±0.06	0.85±0.18	-	0.045	18.6±2.4	5.85±1.2
0.5±0.0025 MPa, 303±2 K	0.5	0.24±0.12	-1±0.6	6.2±0.6	0.0166	-2.7±1.2	2.7±1.2
	0.8	1.28±0.15	-0.45±0.6	7±0.6	0.100	-3.95±2.4	2.1±1.2
	1.0	1.98±0.24	-0.4±0.6	11±0.6	0.169	-5±2.4	3.5±3
	1.5	3±0.36	0.85±0.18	16±0.6	0.307	13.4±3.6	3.65±2.4
	1.7	3.22±0.36	0.65±0.6	17.5±0.6	0.349	11.5±4.8	-1±3.6
	2	2.56±0.36	0.6±0.36	21.4±0.6	0.286	7.2±2.4	0.17±0.18
	2.5	2±0.3	0.45±0.48	30±0.6	0.244	3.8±3.6	0.6±2.4
0.5±0.0025 MPa, 360±2 K	0.5	0.48±0.36	-0.7±0.48	6.3±0.6	0.045	-15.5±2.4	14±4.8
	0.8	1.62±0.2	-0.2±0.24	6.6±0.6	0.015	-12.9±2.4	18.5±4.8
	1.0	2.35±0.3	-0.45±0.36	10±1.8	0.011	-22.7±4.8	35±12
	1.5	3.35±0.4	-0.2±0.18	13±1.8	0.0097	-20.5±4	32±14
	1.7	3.55±0.42	-0.3±0.24	14±0.6	0.0096	-25.3±6	-50±29
	2	3.2±0.36	-0.2±0.18	14.5±0.6	0.0111	-17.8±3.6	-50±29
	2.5	2.75±0.36	-0.15±0.12	17.5±0.6	0.014	-10.5±4.8	-35±19

4.6 Comparisons between the experimental laminar burning velocities and kinetic mechanisms for methane/hydrogen/air mixtures

An important reason for measuring the unstretched laminar burning velocity is to provide reliable data for validating kinetics models used in the optimal combustor design in practical applications. However, there is uncertainty in both the experimental measurements (as discussed above) and numerical predictions [26]. For the comparisons reported here, the premixed laminar burning velocity was calculated using the one-dimensional steady freely propagating planar flame code, Chemkin-Pro 2021. As explained in Chapter 3, the 1D planar flame is modelled in this code by solving the governing continuity, energy and species conservation equations using detailed chemical kinetics. Thermal diffusion (the Soret effect) and a multi-component diffusion model were used to evaluate the transport properties [117].

Three H_2/CH_4 mechanisms were compared with the experimentally derived laminar burning velocities. These are (i) the latest version of the San Diego mechanism, which has 58 species and 270 elementary reactions [116, 119]; (ii) the Konnov reduced mechanism with 27 species and 177 elementary reactions [26, 115]; and (iii) the Aramco 2 reduced mechanism with 25 species and 105 elementary reactions [115]. These mechanisms were selected as they were previously validated using low-pressure experimental data [26, 115, 116]. They cover a range of mechanism sizes with respect to the number of species, with the lowest having 25 species and the highest 58.

A comparison of predicted and experimentally derived laminar burning velocities for pure H_2-air and H_2-CH_4-air mixtures at 0.1, 0.5 and 1 MPa is presented in Figures 4.17-20. The numerical predictions for low-pressure explosions agree well with the experimentally derived laminar burning velocities. However, there is worse agreement for rich mixture explosions, particularly as the pressure increases (Figures 4.18&20), although the numerical predictions remain within the uncertainty of the experimental measurements. For pure hydrogen at $\phi = 2.5$,

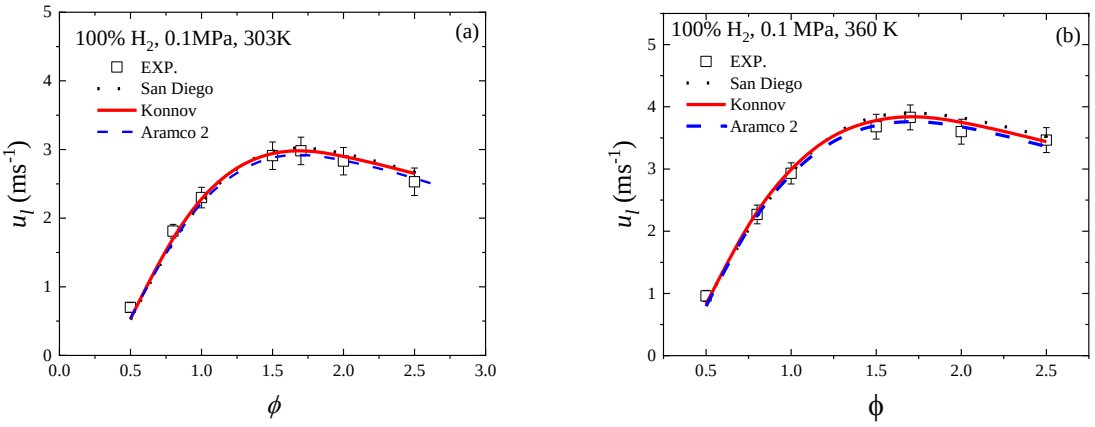

Figure 4.17: Comparison between the experimentally derived laminar burning velocities for pure hydrogen with numerical predictions using different mechanisms at 0.1 MPa, (a) 303 K and (b) 360K.

all the mechanisms produced higher laminar burning velocities than the experiments. The Aramco 2.0 and Konnov mechanisms give similar predictions across all conditions (Figures 4.17&18). The San Diego mechanism predicts higher H_2/CH_4 burning velocities compared to the other two schemes (Figure 4.19). At higher pressures, there is a more significant deviation between the predicted burning velocities from the three schemes, and for these conditions, the Aramco scheme gives the highest predictions (Figure 4.20a). The C1-C2 chemistry is now playing a role, and the Aramco and Konnov schemes use the PLOG formulation for some pressure-dependent reactions within the C1-C2 scheme, whereas the San Diego mechanism uses Troe fall-off. The schemes have clear differences in the parameterization of key pressure-dependent reactions.

Another difference between the predicted and experimental laminar burning velocities is observed for pure hydrogen at high pressure and low temperature. As shown in Figure 4.11, the laminar burning velocities at equivalence ratios of 1.5 and 1.7 for 303 K did not decrease as the pressure increased from 0.1 to 0.5 MPa. This trend is reasonably well matched by predictions based on the Aramco 2.0 and Konnov kinetics, which show convergence of the predicted u_l at ϕ = 1.5 (Figure 4.21). However, the predicted u_l using the San Diego mechanism decreases as the pressure

increases overall values of ϕ. To clarify the prediction of u_l with the rise in pressure, the species concentrations and net rate of reaction are presented. Previous reaction analysis on methane/hydrogen/air mixtures [75, 116] showed that as the initial pressure increased, the mole fraction of the three active radicals (H, O, OH) declined significantly, lowering the laminar burning velocity. The Konnov and San Diego mechanisms present the mole fraction of these active species for a small interval of 0.1-0.2 mm in which the main chemical reactions occur (Figure 4.22).

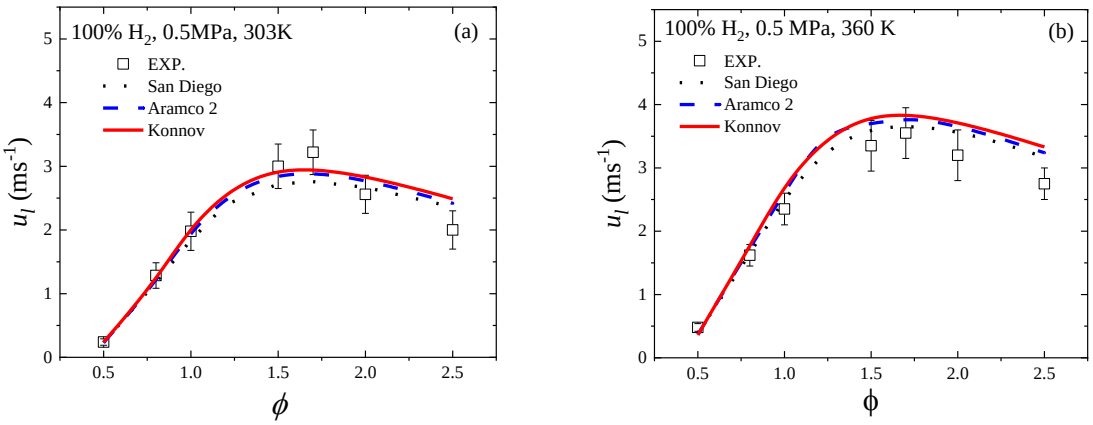

Figure 4.18: Comparison between the experimentally derived laminar burning velocities for pure hydrogen with numerical predictions using different mechanisms at 0.5 MPa, (a) 303 K and (b) 360K.

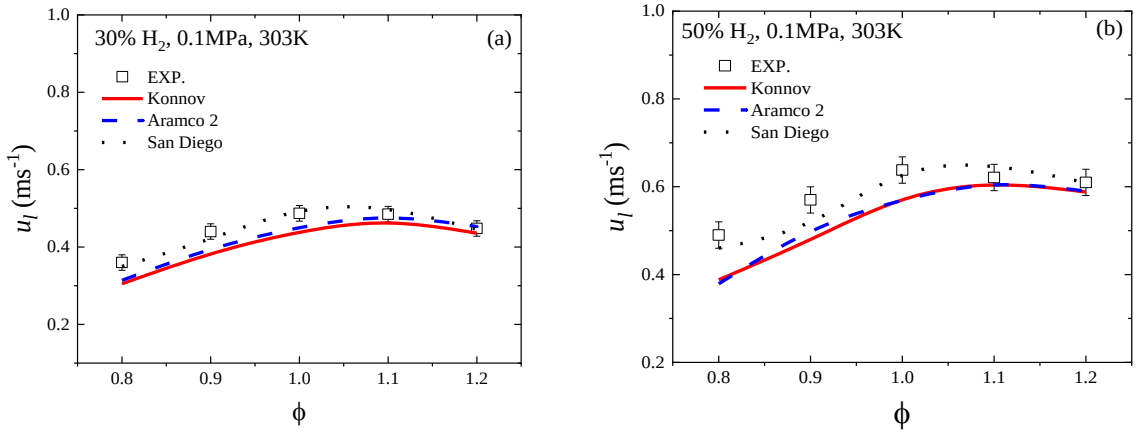

Figure 4.19: Comparison between experimentally derived laminar burning velocities for methane/hydrogen mixtures with different mechanisms at 0.1 MPa and 303 K, (a) 30% H_2 and (b) 50% H_2.

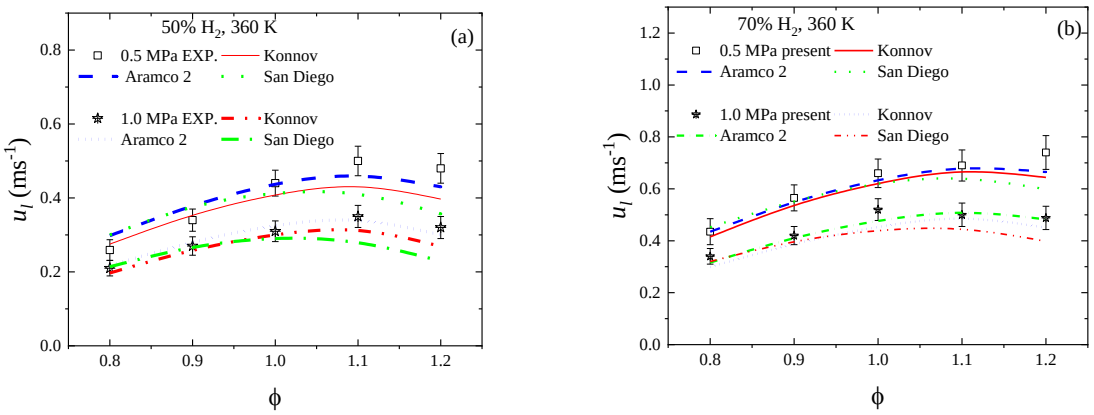

Figure 4.20: Comparison between experimentally derived laminar burning velocities for methane/hydrogen mixtures with different mechanisms at 0.5, 1.0 MPa and 360 K, (a) 50% H_2 and (b) 70% H_2.

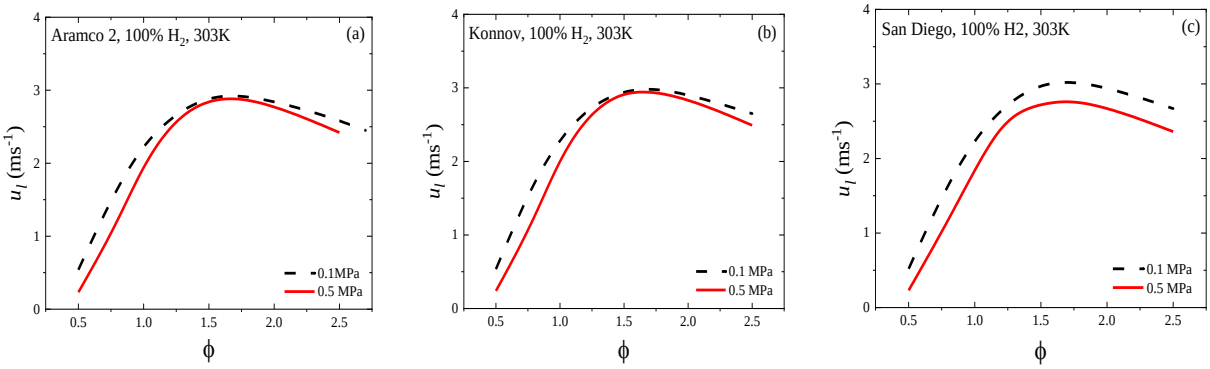

Figure 4.21: Numerical predictions of laminar burning velocities vs. equivalence ratio for pure hydrogen at two different pressures and 303 K.

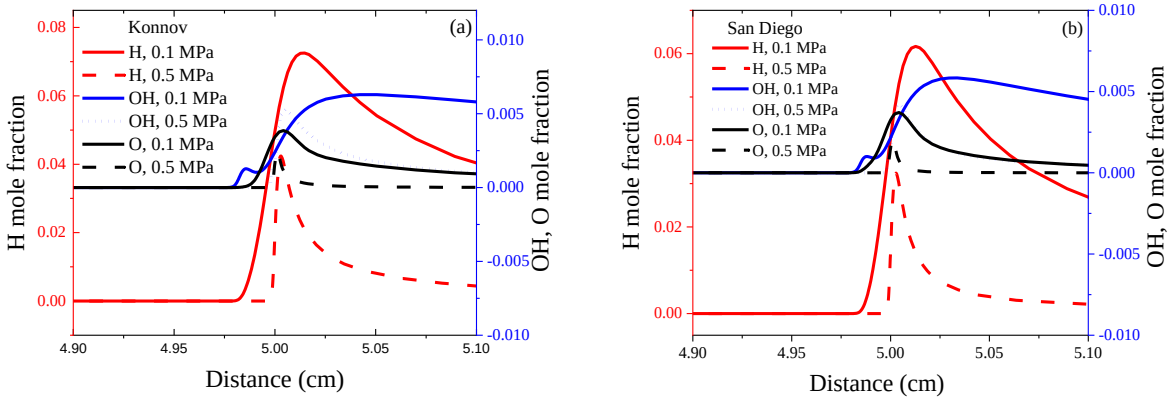

Figure 4.22: Active radical concentrations for pure H_2 at 303K and ϕ = 1.7, from (a) Konnov and (b) San Diego mechanism.

The Konnov mechanism showed that as the pressure increases from 0.1 to 0.5 MPa, the peak mole fractions of H, O and OH reduce by 42%, 50% and 8%, respectively. However, the reductions in these species mole fractions become 48%, 57% and 26% when using the San Diego scheme. It is clear that as the pressure increases, the reduction in active radical concentrations is more significant for the San Diego mechanism than for the Konnov scheme, which could explain the differences between the laminar burning velocities predicted from the two schemes.

To further investigate the reasons for these differences, the net rates of selected pressure-dependent reactions are presented in Figure 4.23. The difference between the two schemes for the main chain branching reaction rate $H+O_2=OH+O$ is tiny at both pressures and thus is not shown. The description of the competing termination reaction $H+O_2 (+M) = HO_2 (+M)$ varies between the schemes. Each scheme uses a Troe fall-off formulation, but the parameterization of the low-pressure limit Arrhenius expressions and collider efficiencies for species such as H_2O and H_2 differ. However, this leads to only minor differences in the peak rate of reactions. $H+O_2 (+M) = HO_2 (+M)$, $OH+OH (+M) =H_2O_2 (+M)$ between the two schemes for the H_2 air flame at 303K and $\phi = 1.7$ (Figure 4.23a).

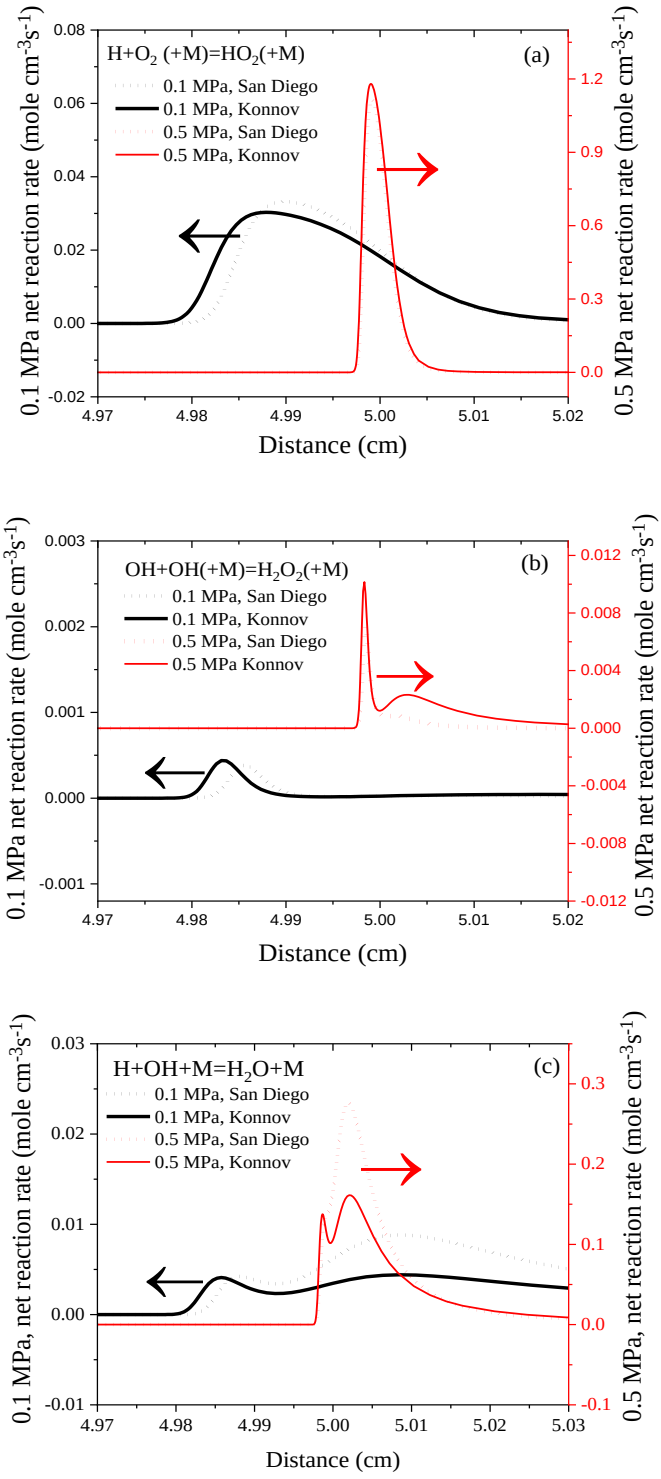

Figure 4.23: Net rate of key pressure-dependent reactions for a pure H_2/air flame at 303 K and ϕ = 1.7, from simulations using the San Diego and Konnov reaction mechanisms (a) $H+O_2$ (+M) = HO_2 (+M), (b) $OH+OH(+M)=H_2O_2(+M)$ and (c) $H+OH+M=H_2O+M$

There are also slight differences in the net rate of reaction OH+OH (+M) =H_2O_2 (+M) between the two schemes, as presented in Figure 4.23b. The reaction is described in H_2O_2 (+M)=OH+OH (+M), using the same low and high-pressure limits and collider efficiencies in the Aramco and Konnov schemes. However, a slight difference exists in the Troe parameters. The San Diego mechanism expresses this reaction in its reverse form, OH+OH (+M) =H_2O_2 (+M), but again, this does not lead to significant discrepancies in the net reaction rate. However, there are pretty large discrepancies in the net rate of the radical recombination reaction H+OH+M=H_2O+M between the Konnov and San Diego schemes (Figure 4.23c), which will impact the concentration of the active radial pool. These are particularly pronounced for the high-pressure conditions and could explain the lower radical concentrations predicted using the San Diego scheme at higher pressures, leading to lower predicted burning velocity.

4.7 Conclusions

Flame speeds, unstretched laminar burning velocities and Markstein numbers for H_2 and H_2/CH_4/air mixtures were derived from experimental measurements at elevated pressure using a spherically expanding explosion technique. The following conclusions can be drawn:

1- Laminar burning velocities increase with both the H_2 fraction in the mixture and with temperature. As the pressure increased, the laminar burning velocity decreased except for pure hydrogen/air mixtures and low-temperature explosions at ϕ = 1.5 and 1.7, where the burning velocity is unaffected by pressure. The latter is due to the low H and OH mole fraction reduction in such cases.

2- For high-pressure explosions (0.5 and 1 MPa), cellularity has been observed in all mixtures due to the DL and TD instabilities. Cellularity is observed more quickly for larger hydrogen volume fractions, pressures, and lower temperatures.

3- Ma_{sr} varies non-monotonically with the pressure and hydrogen fractions due to the competing effects of the Zel′dovich, Ze, and Lewis numbers, *Le*.

4- For pure H_2 explosions, Ma_{sr} increases with pressure for $\phi \leq 1.5$ and decreases with pressure for $\phi > 1.5$ due to the increased value of *Le* in the rich H_2/air mixture.

5- Uncertainties in the values of u_l, L_b, Ma_b, and Ma_{sr} are caused by an increase in extrapolation uncertainty with increasing pressure and H_2 volumetric fraction due to the lower number of experimental points available for use within the extrapolation.

6- The experimentally derived laminar burning velocities agree with predictions based on recently developed H_2/CH_4 mechanisms within the San Diego, Konnov and Aramco2.0 models. Although the agreement between numerical and experiment becomes poorer for rich-pure hydrogen explosions, predictions remain within the limits of uncertainty in the experimental results.

The Ma_b and u_l from this chapter will be used in chapter 4 to analyze the turbulent flame propagation. They will be used in the numerical model to calculate the wrinkling factor in Chapter 6.

Chapter 5: Turbulent Burning Velocities

5.1 Introduction

This work employed a Schlieren technique to measure flame speeds for H_2/CH_4/air mixtures in a spherical stainless steel combustion vessel (Leeds MK II), from which turbulent burning velocities were derived. The hydrogen volume fractions were 30, 50, 70 and 100%. The initial pressures were 0.1, 0.5 and 1.0 MPa, and the initial temperatures were 303 and 360 K. The equivalence ratio (ϕ) was varied between 0.5 to 2 for pure hydrogen and from 0.8 to 1.2 for methane/hydrogen mixtures. The root mean square (rms) turbulent velocity (u') was varied from 2.0 to 10.0 ms^{-1}. The objectives of this study are: (a) to present an extensive experimental database of turbulent burning velocities for these mixtures over a wide range of conditions; (b) to establish a new correlation for u_t for a flame with Lewis numbers, *Le*, not equal to unity, and (c) to quantify the dependence of turbulent burning velocity on pressure, temperature, stretch rate, laminar flame instability and rms velocity. This chapter is organised as follows: Section 5.2 presents the current experimental conditions on the turbulent regime diagram, while Section 5.3 presents flame images to visualise the flame wrinkling, Section 5.4 presents the turbulent burning velocity as a function of flame radius and equivalence ratio, Section 5.5 discusses the effect of flame stretch rate and instabilities on the turbulent burning velocity, Section 5.6 presents empirical correlations of turbulent burning velocity, and finally the conclusion of this chapter is given in Section 5.7.

5.2 Turbulence regimes

Various regimes have been used to describe how turbulent premixed flames depend on the most influential parameters [41-43]. These encompass chemical scales (such as u_l and δ_l) and turbulent scales (including L, λ, η, and u'). The integral scales primarily govern flame convection and can only induce significant wrinkling in large flame kernels [125, 126].

In contrast, the Kolmogorov scales may lack the requisite energy for effective flame wrinkling [43]. Therefore, the Taylor scales are central to flame wrinkling due to their responsibility for shear forces.

The Taylor- and Kolmogorov- length scales, λ and η, are obtained using Equations 2.15 and 2.16, respectively [126]. Tables 5.1 and 5.2 provide data for λ and η length scales concerning 50% H_2 at ϕ=1 and 100% H_2 at ϕ=1.5, respectively. The data presented in these tables encompasses CH_4/H_2/air and H_2/air mixtures. The equivalence ratio has a minor impact on the turbulent length scale, primarily because air is the dominant medium. For CH_4/H_2/air mixtures, slight variations in λ and η (within $\leq \pm 5$ per cent) arise due to hydrogen volume fraction and equivalence ratio. In the case of H_2/air mixtures, changes in equivalence ratio result in variations of $\leq \pm 11\%$ in λ and η. The current study excluded the length scales at 303 K and 1 MPa as they were not studied (discussed in Chapter 3). Notably, initial pressure and temperature exert noticeable effects on the Taylor scale (λ), with λ decreasing as the pressure increases and increasing as the temperature rises. This is due to the unburned kinematic viscosity (υ) change, which affects the Reynolds number. Additionally, as the Reynolds number increases, Taylor scales (λ) decrease with higher fan speeds (u'). Hence, pressure, temperature, and u' emerge as the most influential parameters determining the Taylor scale and, consequently, flame wrinkling.

Table 5-1: Taylor (λ) and Kolmogorov (η) length scales for 50% H_2 with ϕ=1 at various experimental pressures, temperatures and rms turbulent velocities.

		0.1 MPa			0.5 MPa			1 MPa	
303 K	u' ms^{-1}	2	6	10	2	6	7.5		
	η mm	0.061	0.026	0.018	0.018	0.008	0.0068		
	λ mm	1.66	0.96	0.74	0.74	0.43	0.38		
360 K	u' ms^{-1}	2	6	10	2	6	8.5	2	6
	η mm	0.077	0.033	0.028	0.023	0.01	0.0077	0.013	0.006
	λ mm	1.94	1.12	0.89	0.86	0.5	0.4	0.61	0.34

Table 5-2: Taylor (λ) and Kolmogorov (η) length scales for 100% H_2 with ϕ=1.5 at various experimental pressures, temperatures and rms turbulent velocities.

		0.1 MPa			0.5 MPa			1 MPa	
303 K	u' ms^{-1}	2	6	10	2	6	8		
	η mm	0.078	0.034	0.023	0.023	0.01	0.0083		
	λ mm	1.98	1.14	0.88	0.88	0.51	0.443		
360 K	u' ms^{-1}	2	6	10	2	6	9.5	2	6
	η mm	0.099	0.043	0.029	0.029	0.013	0.0092	0.017	0.0077
	λ mm	2.3	1.3	1	1	0.59	0.47	0.72	0.42

Figures 5.1a-b depict the experimental conditions and turbulence parameters outlined within Modified Peters-Borghi's diagram [41-43]. The Y-axis represents the wrinkling factor (u'/u_l), while the X-axis denotes the size of the wrinkling (L/δ_l). The lines (in different colours and styles) in this diagram represent constant values for the Reynolds number (*Re),* Karlovitz number *(K_a),* Damköhler number *(Da)* and the effective turbulent length scale (l_s*),* respectively. According to the Klimov-Williams criteria (discussed in Chapter 1), nearly all flames with 30% H_2, and some with 50% and 70% H_2 (those at high initial pressure), fall within the reaction sheet (thickened flamelets) regime ($K_a > 1$), primarily due to their low laminar burning velocity and, consequently, an extended chemical time scale. However, these flames may not experience disturbances at the Kolmogorov scale (η), as these lack the requisite momentum for effective mass and heat transfer in and out of the preheat zone [44]. This assessment is consistent with the criteria established by Poinsot et al. [42] and Pope [43], as indicated by the line $\delta_l = l_s = 13\eta$. Consequently, all experiments fall below this line (red dash-dotted line), signifying the existence of flamelets for all experimental conditions. The flamelet assumption is valid in wrinkled and corrugated flamelet regimes, where chemical reactions occur significantly faster than turbulent mixing [173]. Some experiments with 100% H_2 fall within the wrinkled flamelet regime, primarily due to the high laminar burning velocity. Pure hydrogen exhibits a short chemical time scale and a thin flame structure. Consequently, K_a decreases as u'/u_l decreases and L/δ_l increases.

This suggests that the flame surface for pure hydrogen exhibits laminar-like propagation (spherical flame) with large-scale wrinkles, as will be discussed in the following sections.

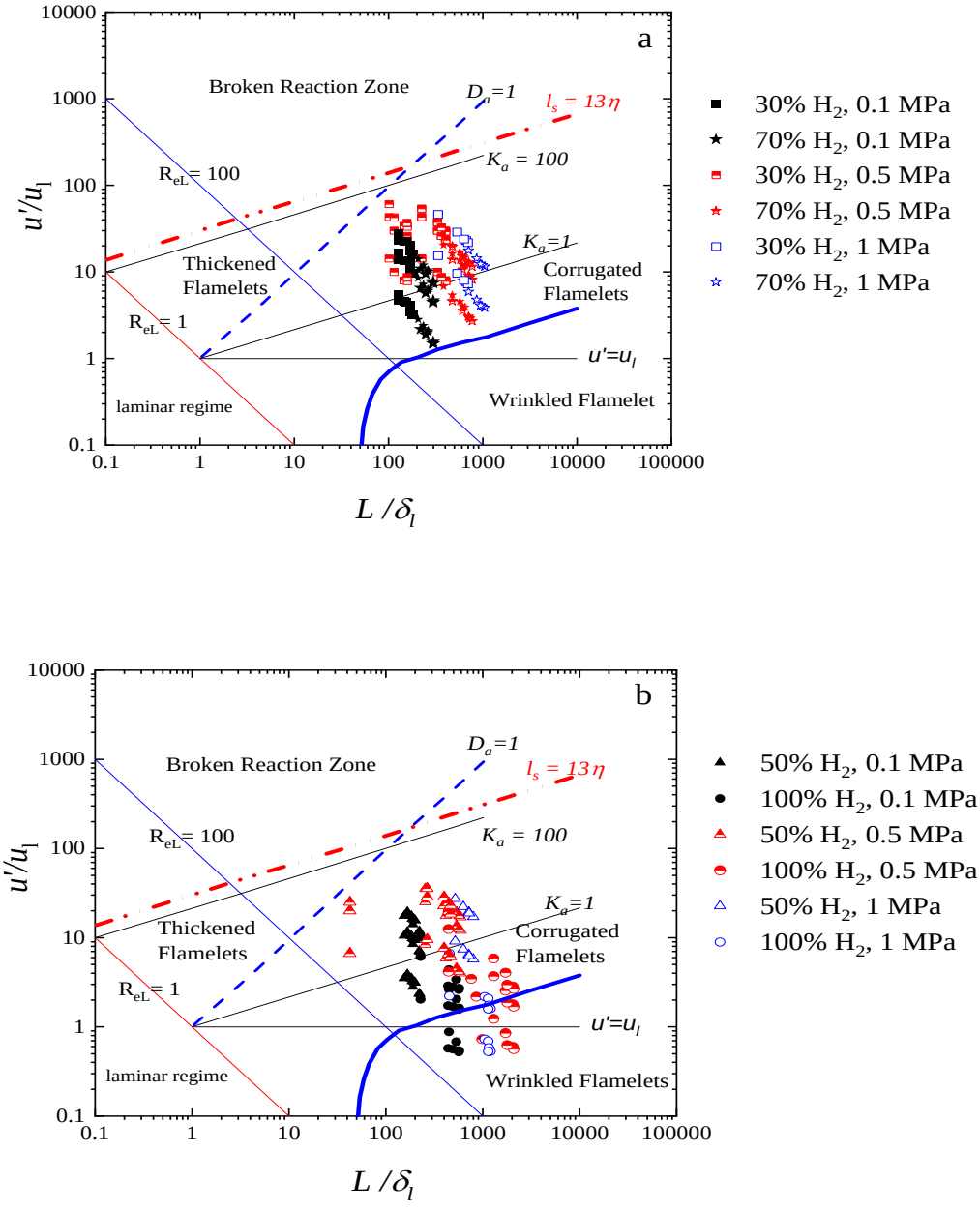

Figure 5.1: Modified Peters-Borghi's diagram [42-44], with the present experimental conditions, with laminar burning velocity and flame thickness taken from [12]. The legends for the present experimental conditions and turbulence parameters represent (a) 30, 70% H_2 and (b) 50, 100% H_2. ϕ ϵ[0.8 1.2] for mixtures with 30% ,50% and 70% H2; [0.5 2] for pure H2.

5.3 Turbulent flame radius and flame images

Figure 5.2 illustrates the time history of the flame radius (r_v) for methane-hydrogen mixtures with various *u'* at 0.5 MPa, 360K and ϕ = 1. The r_v-time curves exhibit an upward concave shape in all these experiments, signifying flame acceleration over time. Flame propagation speed increases with greater hydrogen volume fractions and fan speeds, *u'*. For instance, at u' = 2 ms^{-1}, the flame reaches the optical field of view's limits (r_v = 55 mm) after 5 ms for 30% H_2, whereas it takes approximately 3.5 ms for 100% H_2. Notably, the maximum flame radius varies with the fan speed. The maximum flame radius is achieved at the lowest fan speed, measuring around 55 mm for u' = 2.0 ms^{-1}, while it falls within the range of 37 mm (50% H_2) to 47 mm (100% H_2) at higher fan speeds. At high fan speeds, large turbulent eddies cause erratic displacement of the small flame kernel during the early stages of flame propagation, as depicted in Figures 5.3a-b. Consequently, the flame reaches the optical field of view's limits before further development can occur. At high fan speeds, the flame drift is more prominent at lower H_2 volume fractions than at higher H_2 volume fractions. A comparison between Figures 5.3b&c shows that the flame drifts to the left for 50% H_2, while it remains centred for 100% H_2 with a high fan speed (u' = 9.5 ms^{-1}). The increase in H_2 fraction leads to reduced chemical time scales, causing the flame to develop before large turbulent eddies have a significant impact. Referring back to the regime diagram (Figure 5.1b), the pure hydrogen flame is situated within the wrinkled flamelets regime, indicating that hydrogen flame propagation exhibits a spherical flame with a wrinkled surface (Figure 5.3c).

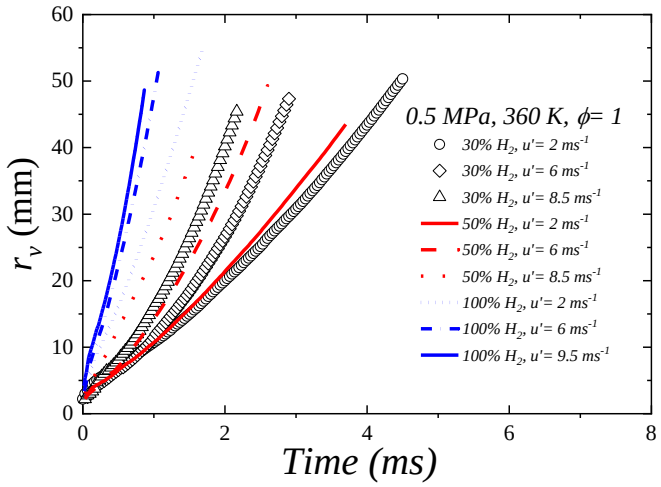

Figure 5.2: The equivalent flame radius vs. time for stoichiometric mixtures at 0.5 MPa and 360 K.

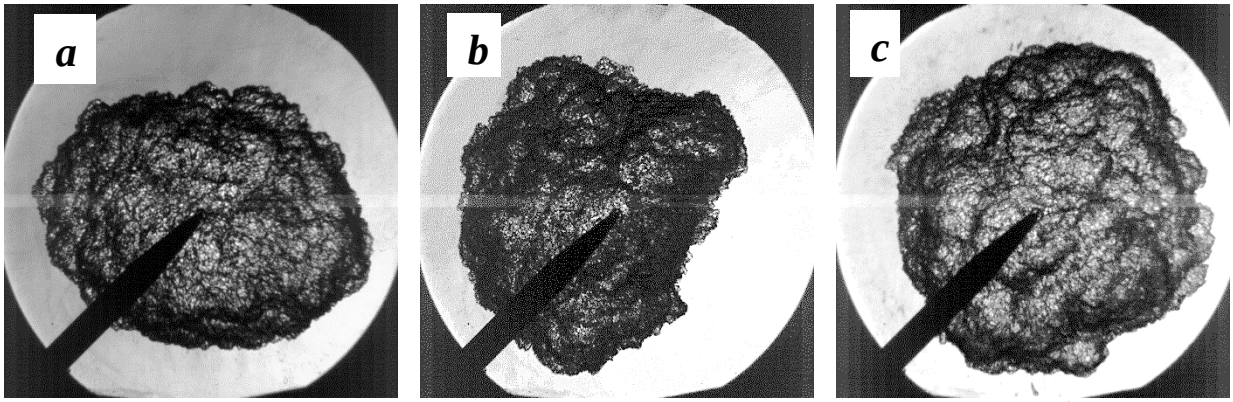

Figure 5.3: Flame images, *Pu* = 0.5 MPa, *Tu*= 360 K and ϕ =0.8, (a) 50% H_2, *u'*= 2 ms^{-1}, (b) 50% H_2, *u'*= 8.5 ms^{-1} and (c) 100% H_2, *u'*= 9.5 ms^{-1}

For a fixed fuel/air mixture, initial temperature, and *u'*, an increase in pressure has three primary effects: (i) Taylor length scales decrease, (ii) Markstein length decreases, indicating a positive stretch rate effect on the flame speed, (iii) the mixture reactivity decreases, as indicated by a lower laminar burning velocity u_l, allowing for more time for the flame to be wrinkled by the turbulent scales and (iv) the Darrieus–Landau (DL) instability is enhanced due to the smaller flame thickness. Therefore, a reduction in Taylor scales imposes a positive stretch on the flame. While the stretch effect can be quantified using the Markstein number (Ma_b) [12, 44, 127], flame wrinkling results from the combined influences of stretch, chemical, turbulent scales and instability effects in this scenario.

Consequently, the finest flame wrinkling scales are observed at the highest pressure. Low Ma_b values, extensive chemical time scales, reduced Taylor eddies, and flame thicknesses collectively contribute to finer flame wrinkling. This effect is also noticeable at fixed u'_k, P_u, T_u, and ϕ (Figures 5.4a-d). As the hydrogen volume fraction increases, Ma_b and u_l increase, leading to larger flame wrinkling scales. A clear distinction can be observed when comparing the images for 30% H_2 (with more condensed scales) and 100% H_2 (with less condensed scales). In the case of 30% H_2, turbulent eddies have more time to create surface wrinkles, thanks to the longer chemical lifetime of the flame [126]. The flame with 30% H_2 falls into the thickened flamelet regime with fine surface scales, while the flame with 100% H_2 sits in the wrinkled flamelet regime (Figures 5.1a & b). Moreover, an increase in u' reduces λ, resulting in smaller flame wrinkling scales. Flame wrinkling is also observed at different times after ignition in the same experiment. The flame at r_v = 12 mm exhibits larger wrinkling scales than at r_v = 40 mm. The proportion of affected eddies, which can wrinkle the flame, increases as the flame kernel expands [125]. This phenomenon has been quantified in terms of an increasing effective rms velocity, u'_k, as the flame radius increases.

It is very challenging to qualitatively assess the effect of stretch on flame wrinkling, as this interacts with the impact of the TD and DL instabilities. The flame images for 100% H_2 at T_u = 360 K, r_v = 40 mm, and u' = 2 ms^{-1} are presented in Figures 5.5a-d. Both chemical and turbulent scales are held constant to investigate the stretch effect on the turbulent flame. In Figures 5.5a-b, there is an 8% difference in the laminar burning velocity for these cases, while in Figures 5.5c-d, the difference is 6%. The sole parameter that changes is Ma_b, which is 25.6 for ϕ = 1.5, 19.6 for ϕ = 2 at 0.1 MPa, and -22.7 for ϕ = 1, -10.5 for ϕ = 2.5 at 0.5 MPa. However, flame thickness decreases with pressure, which enhances the DL instability.

Flames with lower Ma_b values allow for more wrinkling, but these differences can be challenging to identify. This difficulty arises from the need to achieve a significant change in Ma_b and a transition from positive to negative Ma_b while keeping the laminar burning velocity and flame thickness constant. Such a transition is not feasible under the current conditions.

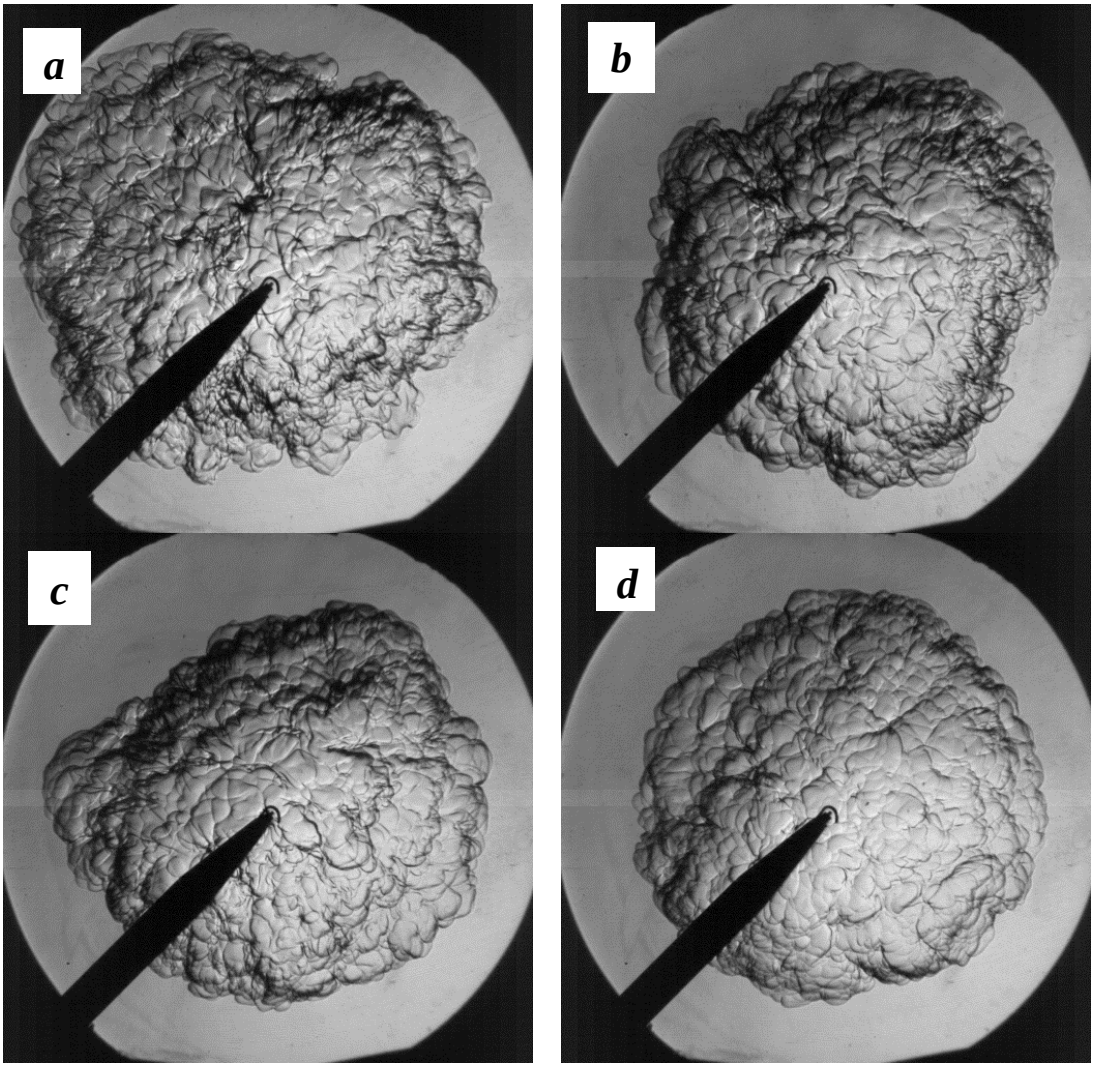

Figure 5.4: Flame images at r_v= 45 mm, 0.1 MPa, 360 K, u'= 2 ms^{-1} and ϕ= 1, (a) 30% H_2, Ma_b= 4.1, (b) 50% H_2, Ma_b= 5.4, (c) 70% H_2, Ma_b= 9.65 and (d) 100% H_2, Ma_b= 25.2.

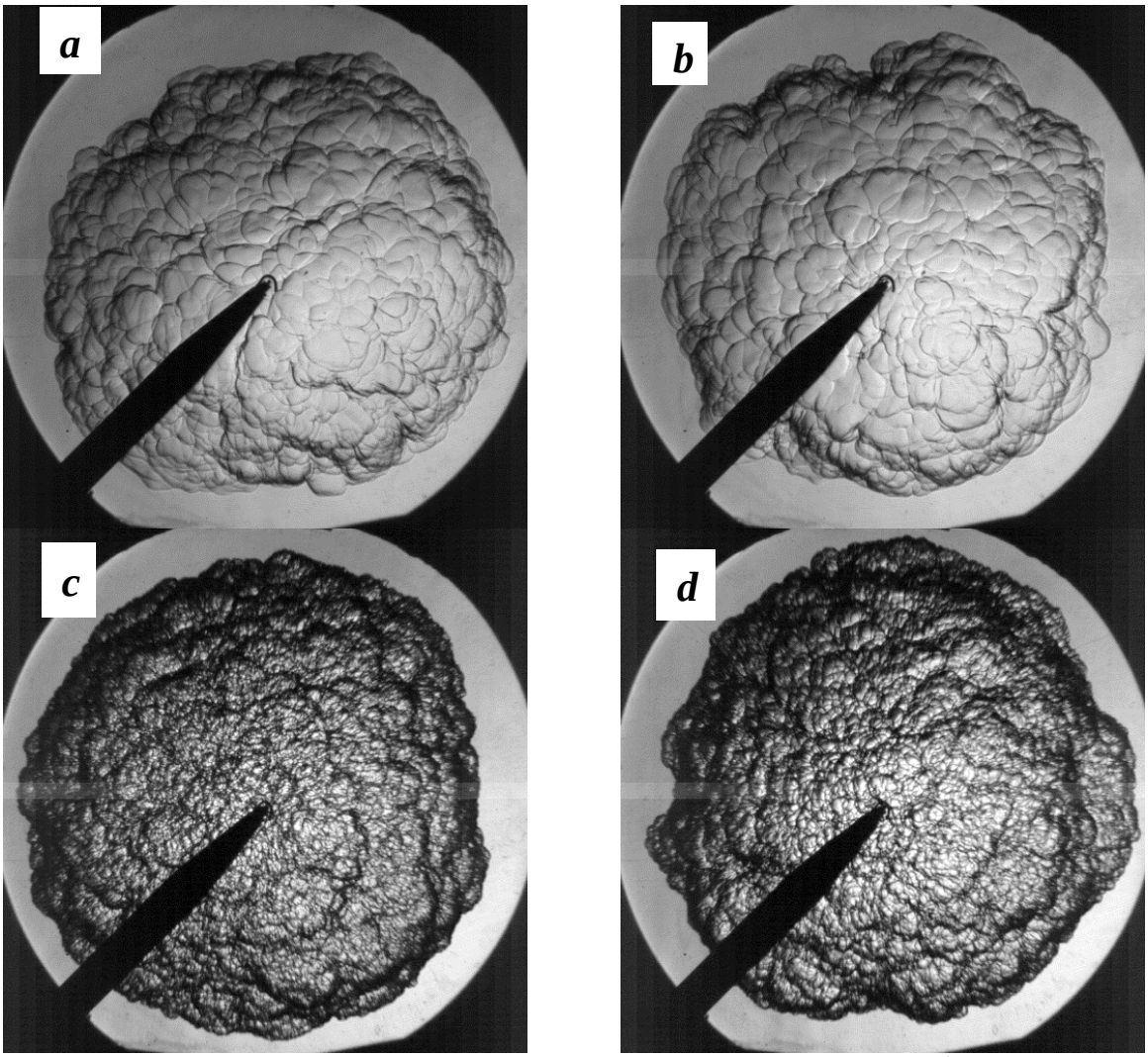

Figure 5.5: Flame images for 100% H_2 at T_u= 360K, r_v= 40 mm, and u'= 2 ms^{-1} (a) P_u= 0.1 MPa, Ma_b= 25.6, ϕ= 1.5, u_l= 3.68 ms^{-1}, (b) P_u= 0.1 MPa, Ma_b= 19.6, ϕ= 2 u_l= 3.55 ms^{-1}, (c) P_u= 0.5 MPa, Ma_b= -22.7, ϕ= 1, u_l= 2.35 ms^{-1}, (d) P_u= 0.5 MPa, Ma_b= -10.5, ϕ= 2.5, u_l= 2.75 ms^{-1}.

5.4 Turbulent Burning Velocity u_t

Figures 5.6 and 5.7 depict u_t as a function of the flame radius, r_v, for various CH_4/H_2/air mixtures, pressures, and u' values. Initially, the turbulent burning velocity is relatively slow at the onset of the explosion, gradually increasing as the flame develops. This behaviour has been previously explained [125]: when the flame initiates from the central ignition source, the flame surface can only be wrinkled by eddies with length scales smaller than the size of the flame kernel. This implies that the effective rms turbulent velocity (u'_k) is smaller in the centre and increases toward the vessel wall until it reaches the value of u'.

In other words, the proportion of turbulent eddies affecting the flame grows as the flame kernel expands [125, 127, 135]. Consequently, spherical turbulent flame experiments provide data for turbulent burning velocities over a range of turbulent scales [145]. Figure 5.8 illustrates the relationship between u_t and u'_k, showing that u_t increases linearly with u'_k. In each explosion, the maximum u_t is observed at the maximum u'_k, as u'_k approaches u'. This pattern is consistently observed across all conditions. Moreover, $u_t > u'_k + u_l$ for the mixture with 100% hydrogen, while $u_t < u'_k + u_l$ for 30% hydrogen. This trend can be seen at $u' = 2$ ms^{-1} in figure 5.8a and d. The increased u_t is due to the diffusional-thermal instabilities of hydrogen [123].

It is widely recognised that elevated pressures can reduce the burning rate in laminar explosions due to the promotion of chain-terminating reactions [12, 168]. However, for mild turbulent conditions, such as $u' = 2$ ms^{-1} in Figure 5.6, u_t of the CH_4/H_2 mixture remains relatively constant as the initial pressure is increased from low (0.1 MPa) to high (1 MPa). This trend was observed previously for iso-octane/air flame [126]; the turbulent burning velocity was not affected by pressure increase with low rms velocity (1 ms^{-1}). In the case of 30% H_2 with $\phi = 0.9$, at $u' \geq 6$ ms^{-1}, u_t increases by approximately 15% as the pressure increases from 0.1 to 0.5 MPa and by approximately 10% as the pressure increases from 0.5 to 1 MPa. Similarly, for 70% H_2 at high $u' = 6$ ms^{-1} and $\phi = 1.2$, u_t remains relatively unchanged as the pressure is increased from 0.5 to 1 MPa.

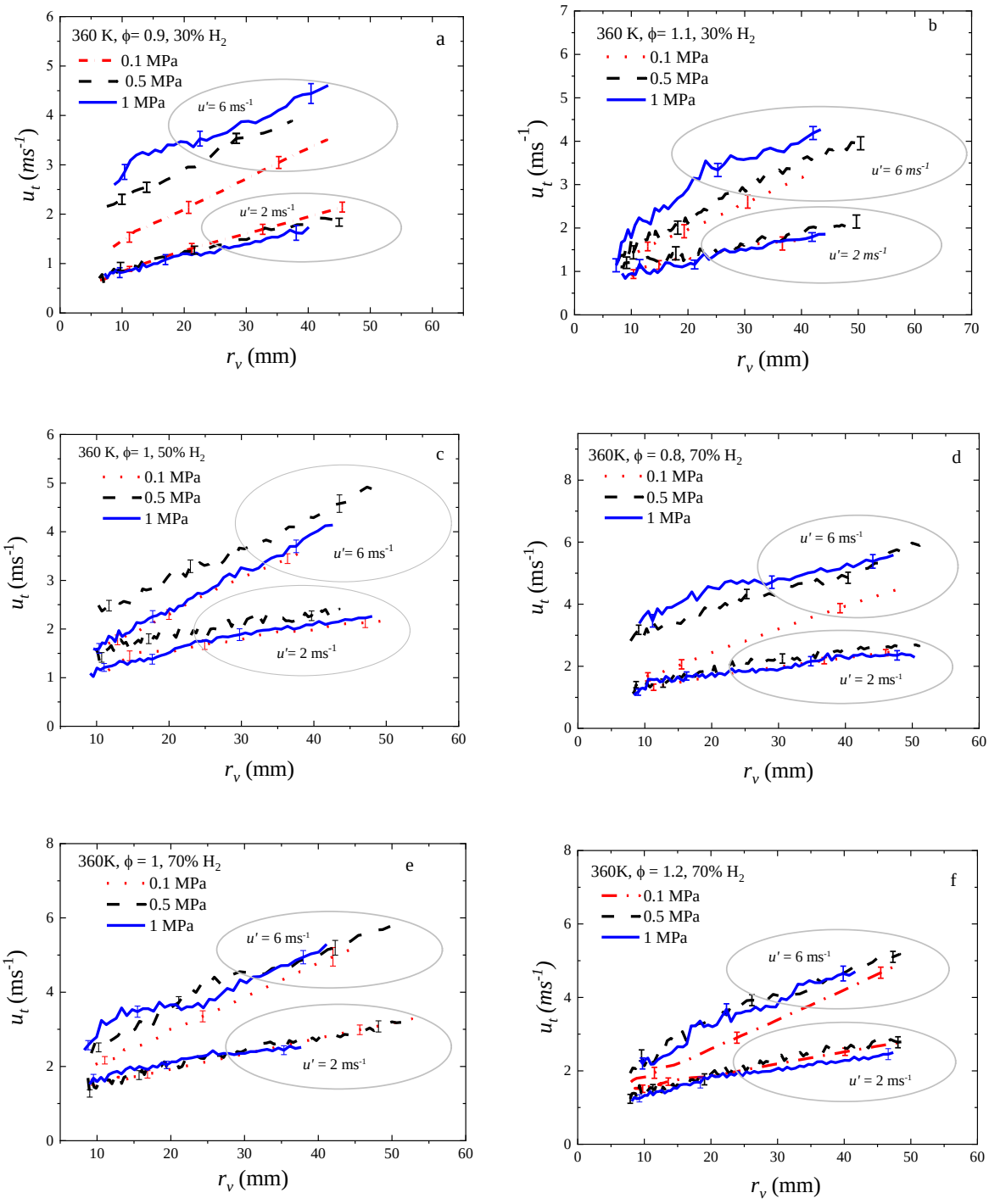

Figure 5.6: The variation of turbulent burning velocity with the flame radius for CH_4/H_2/air mixtures at different pressures and initial rms velocities, (a) 30% H_2, ϕ=0.9, (b) 30% H_2, ϕ= 1.1, (c) 50% H_2, ϕ= 1, (d) 70% H_2, ϕ= 0.8, (e) 70% H_2, ϕ= 1, and (e) 70% H_2, ϕ= 1.2.

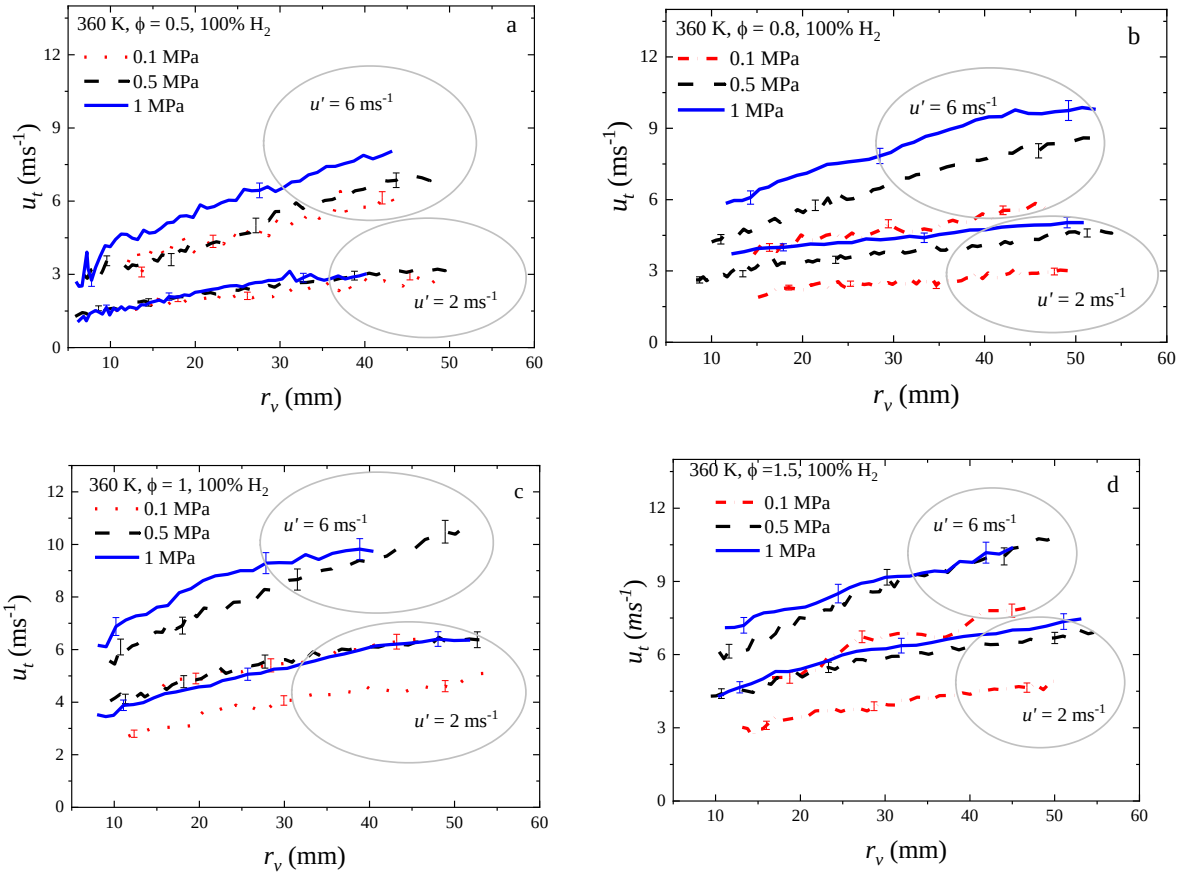

Figure 5.7: The variation of turbulent burning velocity with the flame radius for H_2/air mixtures at different pressures and initial rms velocities, (a) ϕ=0.5, (b) ϕ= 0.8, (c) ϕ= 1, and (d) ϕ= 1.5.

As mentioned earlier, the increase in pressure results in (i) positive flame stretch (indicated by negative Ma_b), (ii) a reduction in Taylor length scales, (iii) a decrease in the flame reactivity, i.e., the laminar burning velocity (u_l) and (iv) enhancement in the flame instabilities [123]. These effects collectively lead to a finer, more wrinkled flame structure, increasing the turbulent burning velocity [126]. When comparing Figure 5.7a and b with d at u' = 6 ms^{-1}, it is apparent that u_t rises as the pressure increases from 0.5 to 1 MPa for lean mixtures, while there is no significant change for rich mixtures. This can be attributed to the DT instability as Lewis number, Le, < 1 with lean mixtures and $Le \geq 1$ for rich mixtures [94]. The increase in pressure results in a finer flame structure but with lower flame reactivity (u_l). Additionally, the interaction between the turbulent flow and flame is contingent upon the flame's dependence on the stretch rate.

This can be inferred from the fact that Ma_b for lean hydrogen is lower than that for rich hydrogen, as shown in the previous chapter. Changing the pressure leads to alterations in chemical and turbulent time scales along with the Markstein number and flame instabilities.

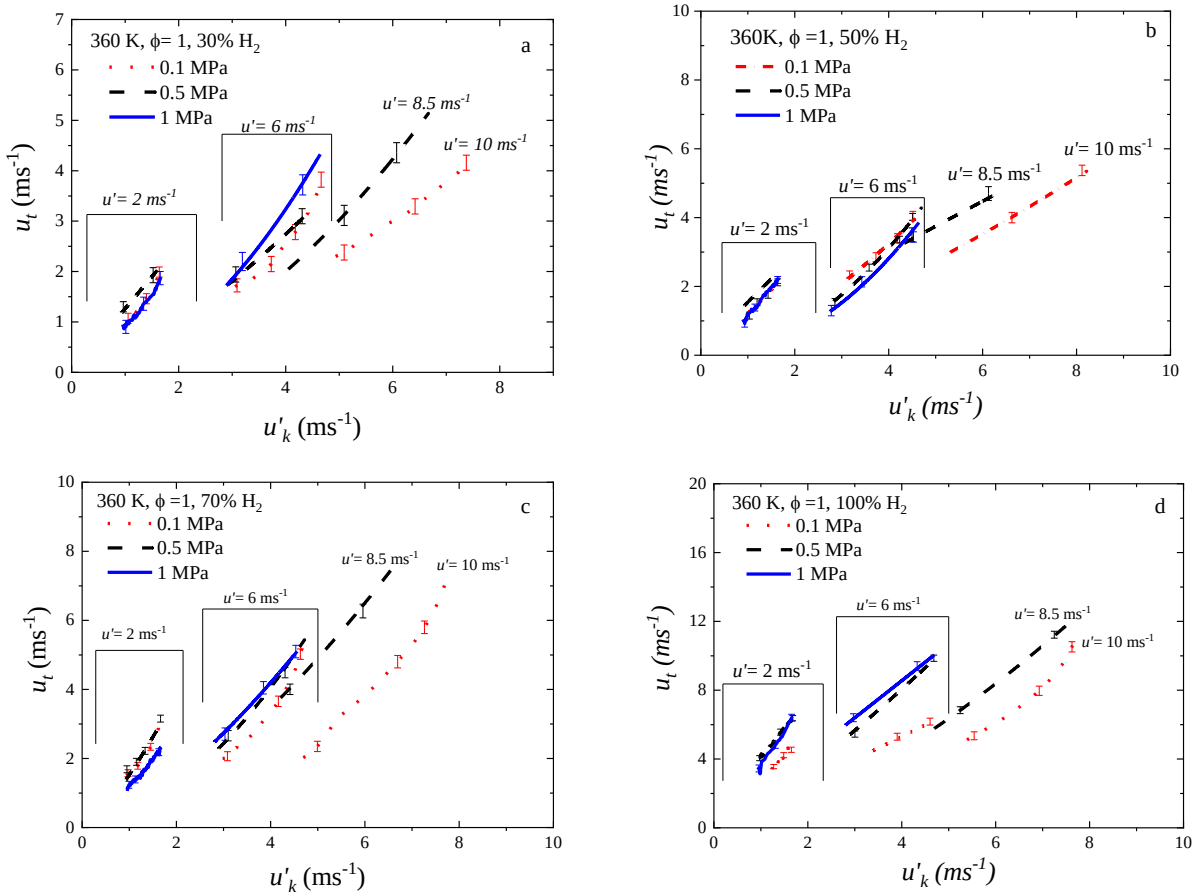

Figure 5.8: Variation of turbulent burning velocity u_t with the effective rms velocity u'_k for different mixtures, pressures and initial rms velocities u' with ϕ = 1 and T=360, (a) 30% H_2, (b) 50% H_2, (c) 70% H_2 and (d) 100% H_2.

The effect of flame stretch and the DL and TD flame instabilities can be quantified while keeping the chemical and turbulent scales constant, as illustrated in Figure 5.9. Ma_b decreases from -10.5 to -22.7, and *Le* increases from ~1.1 to ~ 1.8 as ϕ increases from 1 to 2.5 while u' is constant. For ϕ= 2.5, u_l is 14% higher than u_l at ϕ= 1, as presented in chapter 4. However, u_t for ϕ= 2.5 is approximately 20% lower than u_t at ϕ= 1. This is due to the stretch (Ma_b) and laminar flame instabilities (*Le*) effect. This trend has also been observed in previous studies, where fuels with negative Ma_b burn faster in turbulent spherical flames than those with positive Ma_b [127, 174, 175]. Moreover, the mixture with high laminar flame cellularity (lower *Le*) has more turbulent flame wrinkling than the mixture with low laminar flame cellularity (higher *Le*) [123].

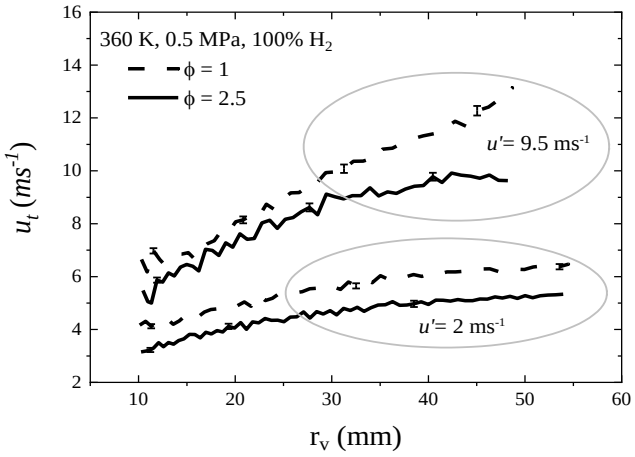

Figure 5.9: Variation of turbulent burning velocity with the flame radius for H_2/air mixtures at 360 K, 0.5 MPa and initial rms velocities. For ϕ= 1, Ma_b= -22.7 and u_l= 2.35 ms^{-1}. For ϕ= 2.5, Ma_b= -10.5, u_l= 2.75 ms^{-1}.

The turbulent burning velocities at a volumetric flame radius of 30 mm are depicted as functions of equivalence ratio in Figures 5.10 and 5.11, including all experimental conditions. The corresponding effective rms velocity, u'_k at 30 mm, is given in Table 5.3. In these Figures, it is evident that u_t increases with the hydrogen fraction, u'_k, and initial temperature. Moreover, higher u' values reduce λ, resulting in more flame wrinkling. Pressure has an interesting effect: u_t remains relatively constant at low fan speeds (u' = 2 ms^{-1}) but increases with pressure at $u' \geq 6$ ms^{-1}, as discussed earlier. As the equivalence ratio changes, u_t varies and peaks at lean conditions for H_2/CH_4 and rich conditions for pure H_2 flames. This variation can be attributed to modifications in flame reactivity, flame thickness, and flame stretch rate (u_l and Ma_b) [44, 66].

The maximum u_t for H_2/CH_4 mixtures occurs on the lean side (ϕ= 0.9 – 1.0). Notably, Ma_b and Le are lower on the lean side than the rich side despite higher u_l as discussed in Figure 5.9. Conversely, for most pure H_2 flames, the maximum u_t appears on the rich side (ϕ= 1.7). This is observed even though Ma_b and Le are lower on the lean side. It is important to note that u_l at ϕ= 1.7 is 8-10 times higher than at ϕ= 0.5. For H_2/CH_4/air mixtures, the stretch and laminar flame instability effects dominate the flame reactivity since the change in u_l is relatively small (≤ 20%) when ϕ varies from 0.8 to 1.2. In contrast, in pure H_2 flames, flame reactivity takes precedence over the stretch and cellularity effects.

Table 5-3: The effective rms fluctuation velocity $u'k$ at r_v= 30 mm for all experimental u'.

u' ms^{-1}	2	6	7.5	8.5	9.5	10
u'_k ms^{-1}	1.409	4.23	5.29	6.0	6.7	7.05

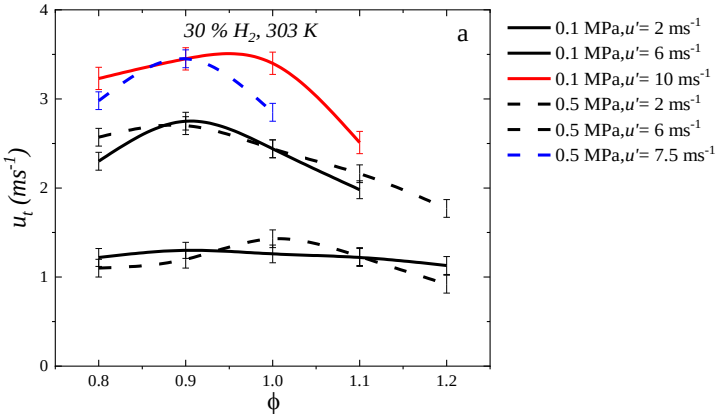
30 % H2, 303 K
a
0.1 MPa,u'= 2 ms-1
0.1 MPa,u'= 6 ms-1
0.1 MPa,u'= 10 ms-1
0.5 MPa,u'= 2 ms-1
0.5 MPa,u'= 6 ms-1
0.5 MPa,u'= 7.5 ms-1
ut (ms-1)
ϕ

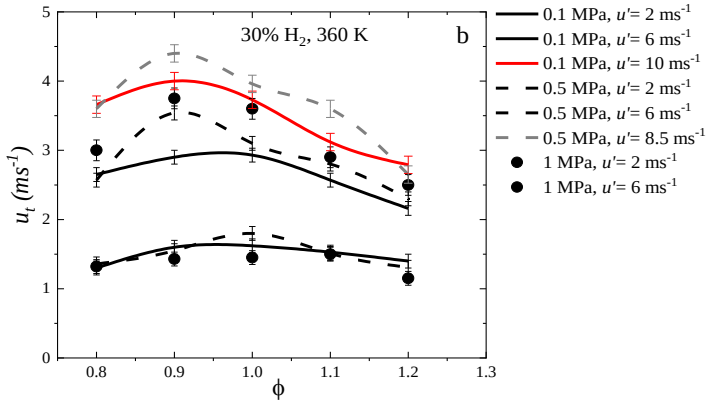
30% H2, 360 K
b
0.1 MPa, u'= 2 ms-1
0.1 MPa, u'= 6 ms-1
0.1 MPa, u'= 10 ms-1
0.5 MPa, u'= 2 ms-1
0.5 MPa, u'= 6 ms-1
0.5 MPa, u'= 8.5 ms-1
1 MPa, u'= 2 ms-1
1 MPa, u'= 6 ms-1
ut (ms-1)
ϕ

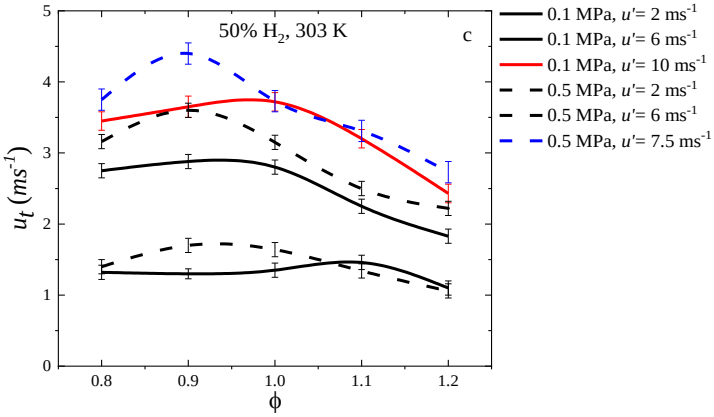
50% H2, 303 K
c
0.1 MPa, u'= 2 ms-1
0.1 MPa, u'= 6 ms-1
0.1 MPa, u'= 10 ms-1
0.5 MPa, u'= 2 ms-1
0.5 MPa, u'= 6 ms-1
0.5 MPa, u'= 7.5 ms-1
ut (ms-1)
ϕ

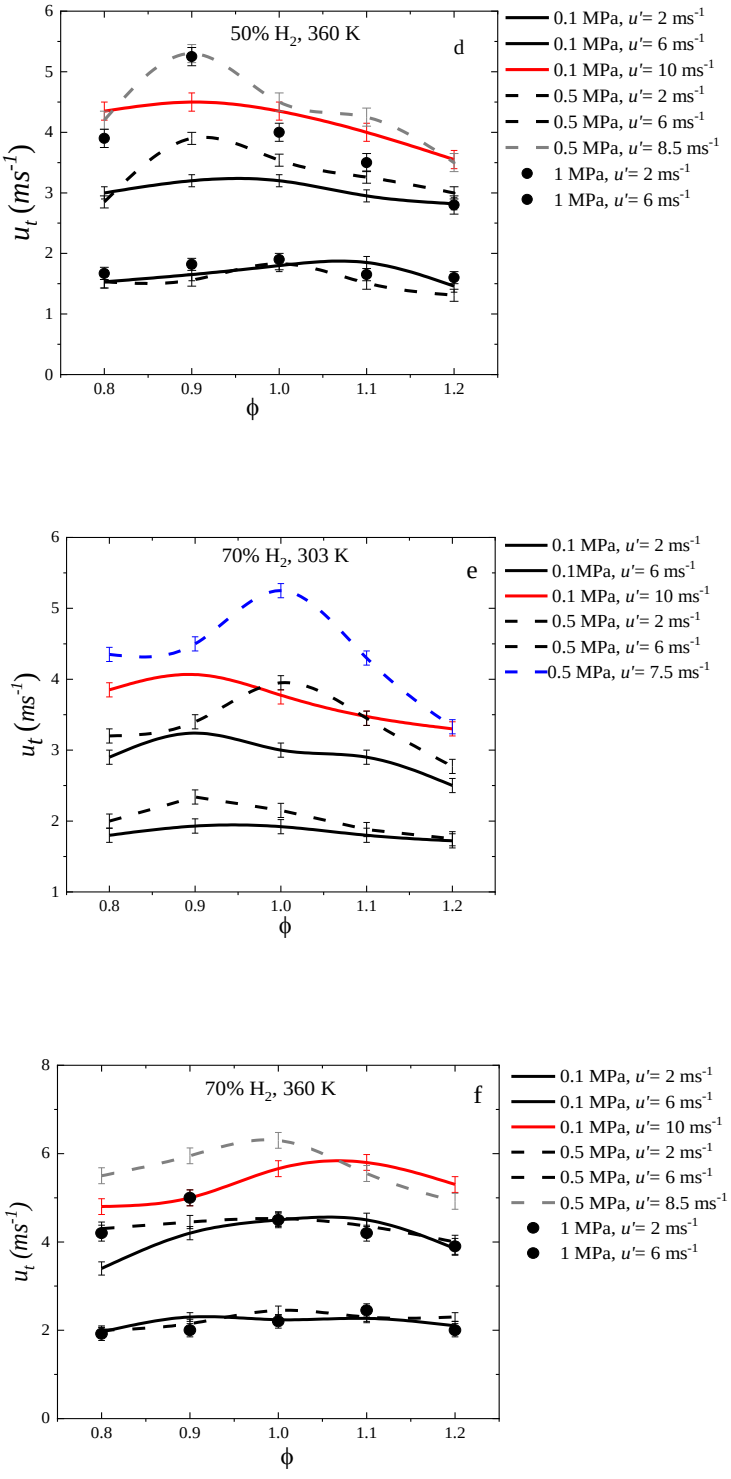

Figure 5.10: Variation of turbulent burning velocity at r_v= 30 mm with equivalence ratio for different fuel mixtures, pressures, temperatures and initial rms velocities

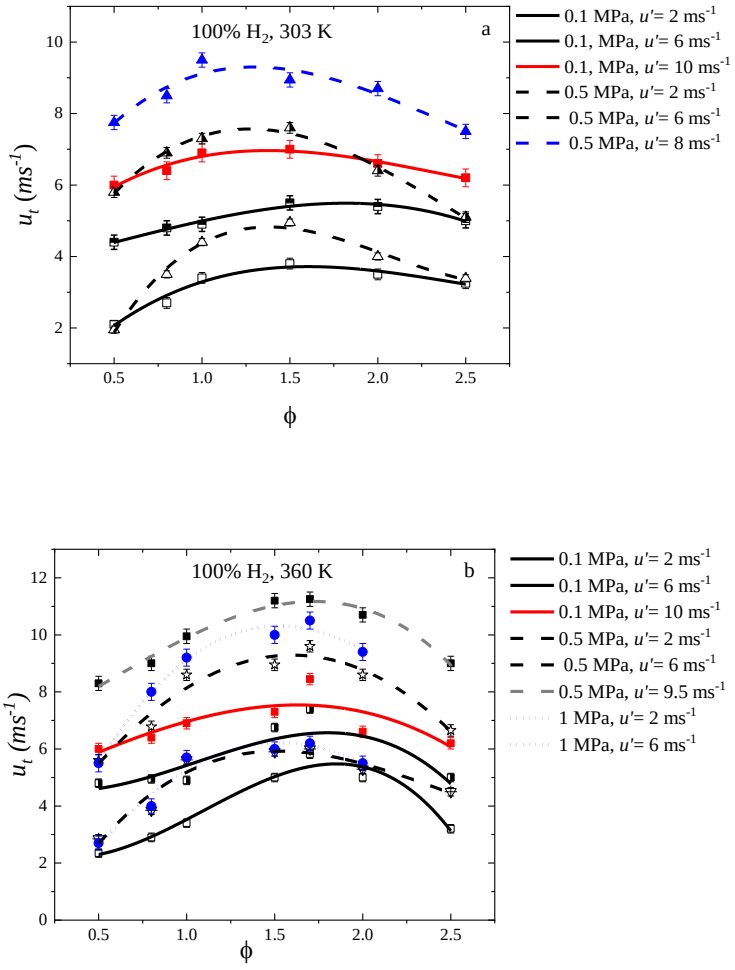

Figure 5.11: Variation of turbulent burning velocity at r_v= 30 mm with equivalence ratio for hydrogen flame at different pressures, temperatures and initial rms velocities.

Some studies [176-179] reported that u_t increases linearly with u', up to a point where it reaches a steady state, and further increases in u' do not lead to changes in u_t. This phenomenon, often referred to as the 'bending' of the turbulent burning velocity, is explained in detail in a DNS study [179]. In the explosions conducted in this study, it is evident that u_t increases with u', regardless of the initial pressure, temperature, and H_2 volume fractions. To explore the presence or absence of the turbulent bending phenomenon, u_t is plotted as a function of u' for stoichiometric mixtures with different H_2 volume fractions and pressures in Figure 5.12. In these specific explosions, bending behaviour is not observed, and u_t continues to increase with u'. However, the rate of increase in u_t varies for the cases of 30%, 50%, and 70% H_2 at 0.1 MPa when u' is increased from 6 to 10 ms^{-1}. This variation may be attributed to flame-to-flame interactions or 'bending.' Pure hydrogen explosions exhibit no bending, as K_a values are lower than in CH_4/H_2 flames. Flame-to-flame interaction plays a more prominent role in premixed explosions with high K_a values, mainly due to an increased u'/u_l ratio, which alters the flame surface area [179, 180]. However, bending was not observed in any of the high-pressure explosions, as the flame thickness decreases at higher pressures, reducing K_a values.

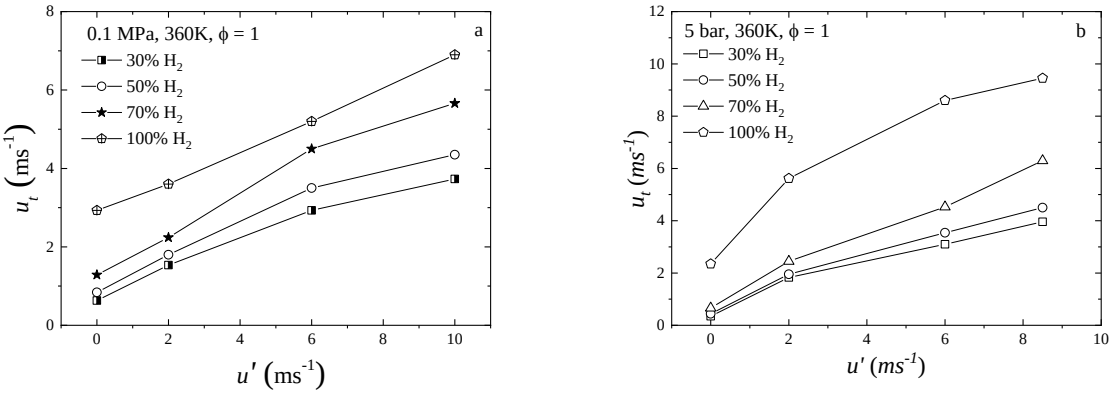

Figure 5.12: Variation of turbulent burning velocity u_t with u' for stoichiometric mixture with different H_2 volume fractions and pressures.

5.5 Effect of Flame Stretch Rate and Flame Instabilities on Turbulent Burning Velocity

In the flamelet regime, flame stretch rates can significantly influence the localised flame propagation speed, potentially leading to flame extinction. This underscores the importance of quantifying the effect of stretch on turbulent premixed flames. The laminar flamelet model for interpreting turbulent premixed flames suggests that the influence of stretch rates depends on the Lewis number, *Le*. The Markstein number, Ma_b, is a parameter that can be experimentally measured and represents the effect of the Lewis number [127]. The literature has reported that mixtures with $Le < 1$, signifying the presence of DT instability, burn faster than those with $Le > 1$ [123, 181]. A similar observation in the literature was found that u_t is slower for mixtures with $Le > 1.0$ and positive Ma_b values [126].

To quantify the effect of stretch on u_t, it is normalised by u_l to mitigate the influence of chemical scales and is plotted as a function of Ma_b in Figure 5.13. In this context, chemical and turbulent length scales must be held constant to investigate the impact of flame stretch and instabilities. At fixed u' and pressure, the normalised u_t increases in the negative range of Ma_b (low *Le*) but decreases as Ma_b becomes more negative. For instance, in the case of 50% H_2, the peak value of the normalised u_t occurs in the range of $-10 < Ma_b < -5$, while for 100% H_2, it peaks in the range of $-16 < Ma_b < -14$ and the curves are flattened in the most negative regime. This observation is attributed to the fact that laminar burning velocity significantly influences the turbulent burning velocity in this region. In the case of pure H_2, the most negative Ma_b is associated with the lean side, where u_l at $\phi = 1.7$ is 8-10 times that at $\phi = 0.5$. This demonstrates that the effect of chemical time scales dominates the effects of stretch and flame instability in pure H_2 flames.

The flames here are in the wrinkled flamelet regime (Figure 5.1), where the effect of turbulent eddies is not significant enough to compete with the advancement of the flame front due to the high laminar burning velocity. Hence, in this region, laminar flame propagation dominates over the corrugation of the flame front by turbulence. It can also be stated that the claim that positive stretch (negative Ma_b) increases the turbulent burning velocity is not universally valid.

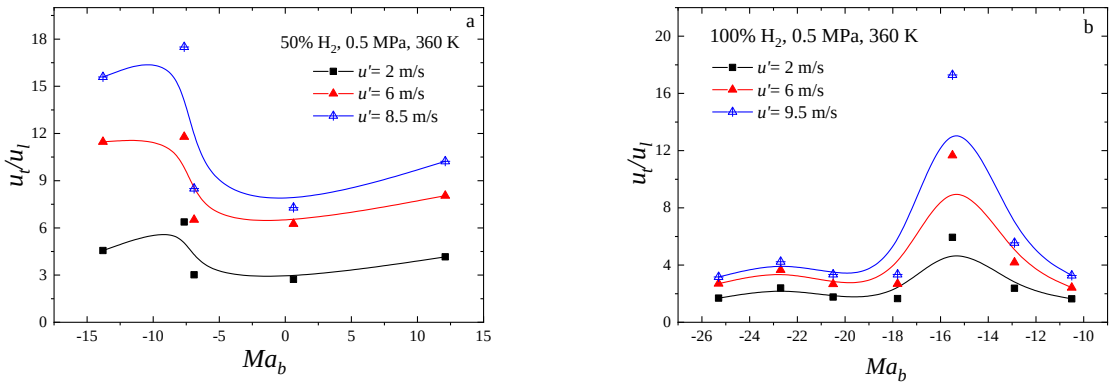

Figure 5.13: Variation of normalised turbulent burning velocity with Markstein number Ma_b at 0.5 MPa and 360K (a) 50% H_2, ϕ = 0.8-1.2 and (b) 100% H_2, ϕ = 0.5-2.

The influence of stretch can also be examined using the classical *U-K* diagram [66], to which the present data has been added, as shown in Figure 5.14. In this diagram, the y-axis represents *U*, which is u_t/u'_k, while the x-axis represents the Karlovitz stretch factor (K_{a1}), and the numbers adjacent to the black solid lines represent values of Ma_{sr} from [66]. This diagram, initially developed in [127, 135], illustrates the effect of stretch on turbulent burning velocity and its potential to lead to flame extinction. The regime under Ma_{sr}=5 is recognised as the flame extinction regime [66]. Notably, none of the present experiments fall within this regime, owing to the increased flame resistance to strain-induced extinction due to the addition of hydrogen [15, 16]. Nevertheless, experiments involving 50% or less hydrogen volume fractions at 303 K are closer to the flame extinction regime than those with 70% or higher.

Flame extinction was observed in the case with 30% H_2, 303 K, $\phi \geq 1.1$, and $u' \geq 6$ ms^{-1}. This could be due to the low flame reactivity (low u_l) and the elevated heat loss linked to the lower fresh gas temperature. It is worth noting that flame extinction was not observed under the same conditions with an initial temperature of 360 K. Additionally, more than half of the present measurements are in the region with $K_{a1} \leq 0.1$, and most of the data for pure H_2 falls within the region of $K_{a1} \leq 0.01$. As discussed previously, the increased H_2 fraction leads to higher u_l and reduced flame thickness, resulting in low K_{a1} values. In reference to the regime diagram, explosions with 100% H_2 are in the flamelet regime, as $K_{a1} << 1$. The flames in the low K_{a1} region exhibit high U values. According to Bradley et al. [127], the stretch and flame instability effects are attributed to high normalised turbulent velocity in the low K_{a1} region. However, it is essential to consider the chemical time scale (u_l) when analysing the stretch effect, as discussed in relation to Figure 5.13. Therefore, this study suggests that the high turbulent velocity values in hydrogen flames primarily result from the high flame reactivity.

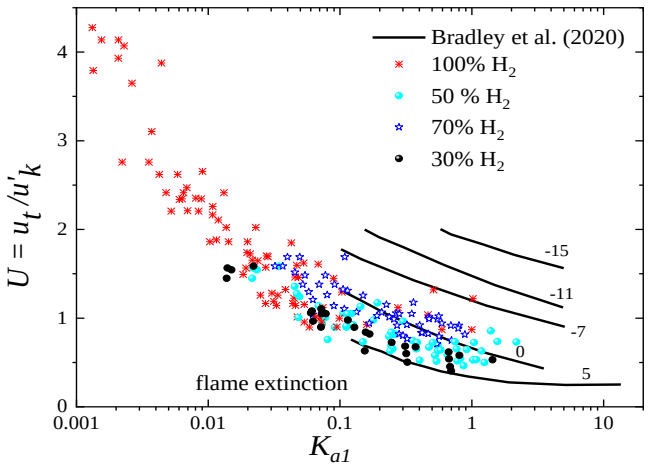

Figure 5.14: The present experimental measurements in the *U-K* diagram.

5.6 Turbulent burning velocity correlation

The turbulent burning velocity is a crucial physical parameter in turbulent combustion, often serving as an input parameter for combustion modelling [23-25, 49]. Different scaling parameters have been used to correlate u_t/u' and u_t/u_l by considering the effect of flame stretch, Lewis number, turbulent length scales and pressure [123]. The primary factors governing the turbulent burning velocity are the turbulent transport of heat and mass within mixtures, the chemical time scales (u_l and δ_l), flame stretch rate and the total surface area of wrinkled flamelets associated with turbulent flow intensity and pressure. Based on the literature review, the best performance is obtained from two correlations: (i) *U-K*$_{a1}$ correlation [66, 127, 135] and (ii) The general scaling law $^{u_t}/_{u_l} = f\left(\left(^{u'}/_{u_l}\right)^{\alpha}, \left(^{L}/_{\delta_l}\right)^{\beta}, Le^{\gamma}\right)$ [123]. The present study focussed on these correlations, which are presented in the current section. The *U-K* correlation [66, 127, 135] allows the turbulent burning velocity to be correlated under the current fuel and operational conditions.

$$U = {}^{u_t}/_{u_k'} = \alpha {K_{a1}}^{\beta} \tag{5.1}$$

The Karlovitz stretch factor (K_{a1}) is given in chapter 3. The constants (α and β) in Equation 5.1 are functions of Markstein number (Ma_b), which account for the effects of *Le*, curvature stretch, and strain rates [174]. This is the main difference between the present and previous correlations [66, 127, 135]. Ma_{sr} is based on previous studies [68, 182, 183] that emphasised the sensitivity of turbulent burning velocity to strain rate, making curvature stretch less significant, enabling it to be neglected. However, recent DNS research on lean premixed hydrogen flames [53] has indicated that the effect of curvature stretch on turbulent burning velocity is more substantial than previously thought.

Moreover, the method used to evaluate Ma_{sr} was built on the assumption that $Le=1$ is unsuitable for the current fuel/air-premixed flames [154]. Therefore, the present study correlated α and β as a function of Ma_b to include the curvature and strain effects [72, 154]. Moreover, Ma_b is a strong function of Le [44, 135], which has been shown to have an appreciable effect on turbulent burning velocity, as discussed earlier and presented in the literature [123, 138].

$U = {u_t}/{u_k'}$ is plotted as a function of K_{a1} in Figures 5.15a-c for different values of the fuel mixture and Ma_b. The current fuel mixtures are classified based on K_{a1} and Ma_b to improve the accuracy of the u_t correlation. Since pure hydrogen flames have low K_{a1} values ranging from 0-0.1, the hydrogen correlation is separated from the CH_4/H_2 one. Figure 5.15a shows the pure hydrogen plot with negative and positive Ma_b. The U value for pure hydrogen increases as K_{a1} decreases. In very small K_{a1} ranging between 0 and 0.01, the U value sharply increases. Two correlations for hydrogen flames are presented in Equation 5.2 for negative or positive Ma_b values. For H_2/CH_4 mixture with higher K_{a1}, two correlations are presented in Equation 5.3 for negative and positive Ma_b. The correlation coefficient R^2 values for the above expressions ranged between 0.7 and 0.8. The U-K correlation can be recast to ${u_t}/{u'} = f\left(\left({u'}/{u_l}\right)^A, \left({\lambda}/{\delta_l}\right)^B\right)$ to match the Damköhler hypothesis. Note that the effect of Le is included in the constants A and B as they are functions of Ma_b.

It is important to note the following points about the above correlations: (a) it has a low sensitivity to $Ma_{b,}$ and as a result, the effect of the large error bar in Ma_b on the correlation performance is minimised (b) it is valid for the u_t measured on the reference radii r_v around which the volume of the unburned gases equals to the volume of the burned gases (changing this reference would require the correlation to be modified), (c) the fluctuation turbulent velocity used here is the effective turbulent velocity u'_k which is usually lower than the rms velocity u' depending on the flame radius, (d) the Prandtl number has been included in this correlation as has been given in chapter 3 (with the present of hydrogen Prandtl number ≠1), and (e) the correlation covered the regime with a wide range of Karlovitz stretch factor (0.001-1.2). The regime with a very low Karlovitz number (≤0.1) was considered to be unstable in previous studies [66, 127, 135].

For 100% H_2

$$\alpha, \beta = \begin{cases} \alpha = 0.00175(300 - Ma_b) \pm 0.1, \beta = -0.013(0.1Ma_b + 22) \pm 0.04, for\ positive\ Ma_b, 0.01 > K_a \leq 0.1 \\ \alpha = 0.00168(300 - Ma_b) \pm 0.1, \beta = -0.015(0.1Ma_b + 22) \pm 0.04, for\ negative\ Ma_{b,} K_a \leq 0.01 \end{cases} \quad (5.2)$$

For CH_4/H_2

$$\alpha, \beta = \begin{cases} \alpha = 0.0016(348 - Ma_b) \pm 0.05, \quad \beta = -0.009(Ma_b + 24) \pm 0.05, for\ positive\ Ma_b, \\ \alpha = 0.0212(348 - Ma_b) \pm 0.03, \quad \beta = -0.01(0.1Ma_b + 22) \pm 0.025, for\ negative\ Ma_b \end{cases} \quad (5.3)$$

The general scaling parameters from the literature, based on the Damköhler hypothesis, are used to evaluate the current measurements (Figure 5.16). The present data seems to be bound around the correlation of [123] $\left\{ {u_t}/{u_l}_{K_{a1}} = 0.47 \left({D_a}/{Le} \right)^{0.86} \right\}$ with R^2~0.7. The relatively low R^2 value maybe due to the present data being spread over a wide range of turbulent regimes (Figure 5.1). Therefore, the current data fits better (with R^2=0.85) with the line $\left\{ {u_t}/{u_l}_{K_{a1}} = 0.7 \left({D_a}/{Le} \right)^{0.86} \right\}$. This suggests slight differences between the power exponents of the present data and the literature. This difference was also evident in previous studies [123, 184] which can be due to the differences in either u_t, u_l, δ_l and/or K_{a1}. In addition, the present correlation confirms the previous finding [123] that the performance of general turbulent correlations of the form $\left\{ {u_t}/{u_l} = (A)^a (B)^b \right\}$ must include any pair of independent parameters A and B taken from (u'/u_l, L/δ_l, D_a, K_{a1}, R_{eL}), because they are coordinate axes or boundary curves in a combustion regime diagram [185]. Both correlations in Figures 5.15 and 5.16 include at least a pair of these independent parameters. Although both correlations provide good performance in u_t prediction, the scaling parameters in Figure 5.16 are preferred, due to the large uncertainty in the Ma_b values.

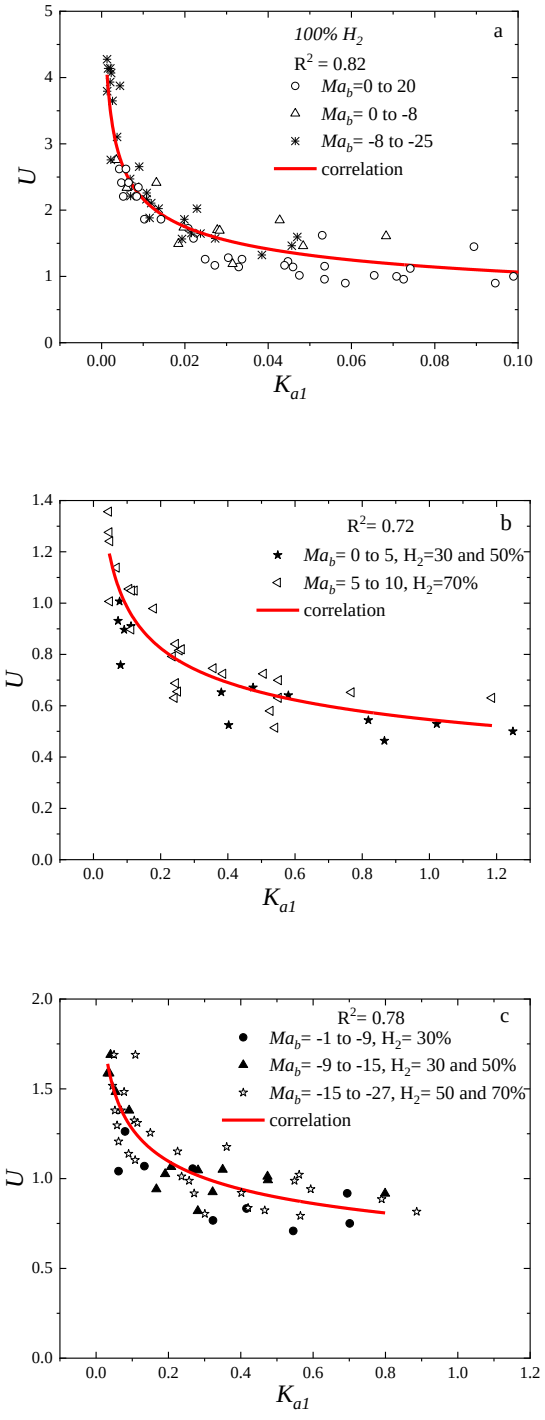

Figure 5.15: Correlation of u_t/u'_k with *Ka1* for different fuel mixtures and Ma_b, (a) pure H_2, Ma_b from -25 to 20, (b) H_2/CH_4, positive Ma_b and (c) H_2/CH_4, negative Ma_b

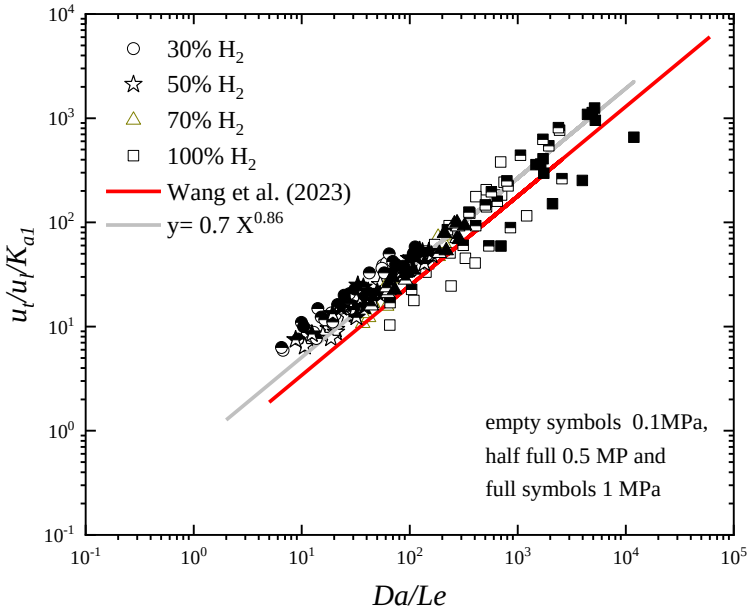

Figure 5.16: Normalised turbulent flame speed $u_t/u_l/K_{a1}$ as a function of *Da /Le* for present data and literature correlation [123]

5.7 Chapter Conclusions

This study determined turbulent burning velocities for hydrogen/air and methane/hydrogen/air mixtures through spherical flame propagation experiments utilising the Schlieren technique. A broad spectrum of hydrogen volume fractions, equivalence ratios, initial pressures, and rms velocities were explored, particularly under elevated conditions. Several key conclusions can be drawn from this investigation:

- Most of the flames with 30% H_2, and some with 50% and 70% H_2 (those at high initial pressure), fall within the reaction sheet (thickened flamelets) regime ($Ka > 1$), primarily due to their low laminar burning velocity and, consequently, an extended chemical time scale. However, the flame with 100% H_2 falls within the wrinkled and corrugated flamelet regime, primarily due to the high laminar burning velocity. This suggests that the flame surface for pure hydrogen exhibits laminar-like propagation (spherical flame) with large-scale wrinkles.

- Turbulent burning velocity increases with higher hydrogen volume fractions, elevated fan speeds (u'), and increased temperature. At $u' = 2$ ms^{-1}, variations in initial pressure do not significantly affect u_t; however, for $u' \geq 6$ ms^{-1}, an increase in pressure leads to higher u_t.

- Pure hydrogen flames exhibit short chemical time scales, enabling flame development before the substantial impact of large turbulent eddies. This results in spherical flame propagation with a wrinkled surface.

- The most refined flame wrinkling scales are observed at higher pressures due to reduced turbulent Taylor scales and extended chemical time scales. An increase in u' reduces the Taylor length scales, leading to finer flame wrinkling scales.

- Flame wrinkling scales are more condensed for 30% H_2 flames than 100% H_2 flames. This is attributed to turbulent eddies having more time to wrinkle the surface in cases with a longer chemical lifetime, as with 30% H_2.

- The normalised turbulent burning velocity peaks within a range of Ma_b values and then flattens to low values as Ma_b becomes more negative, indicating the dominance of laminar burning velocity over turbulence effects (chemical time scales) on u_t for these regions.
- This influence is also evident in the *U-K* diagram. Therefore, chemical reactivity precedes the effects of stretch and flame instability. It should be noted that the assertion that positive stretch (negative Ma_b) consistently increases turbulent burning velocity is not universally valid.
- The turbulent burning velocity correlations will be used to calculate the wrinkling factor in the numerical simulation (next chapter). In addition, the experimental flame propagation rate with time will be used to validate the numerical model.

Chapter 6: Simulation of turbulent hydrogen/air flame propagation

6.1 Introduction

CFD tools can provide information about spherical flames that is difficult to obtain experimentally [45]. Premixed turbulent combustion modelling is more complicated than non-premixed modelling due to the more significant interaction between turbulence and chemistry. As discussed in Chapter 5, the hydrogen flame follows the flamelet concept, which is applicable when the relevant chemical timescale is short compared to the convection and diffusion timescales (Damköhler number > 1). Thus, the Weller flame surface wrinkling combustion (Ξ) model [24] has been chosen to simulate the combustion in a spherical flame propagation. The main assumptions in the Ξ model are that the flame is perfectly premixed, the reactions occur in a very thin layer, and the chemistry is very fast - the flamelet assumptions. This chapter is organized as follows: Section 6.2 presents the results of the original XiFoam solver, Section 6.3 gives a mesh dependency analysis for the model, Section 6.4 presents the model validation, Section 6.5 discusses the velocity and temperature field, Section 6.6 presents the flame surface wrinkling, Section 6.7 present the practical application of the current model (flame zone simulation in gas turbine combustor) and the conclusions are given in Section 6.8.

6.2 The original Ξ combustion model

The XiFoam solver uses two methods to calculate the wrinkling factor (Ξ) in the source term of the transport equation for the density-weighted mean reaction regress variable (equations 3.34 and 3.35). These methods are based on the Gulder correlation [45] and transport Ξ equation [25]. These methods are tested in the present study. Figure 6.1 compares the flame radius rate of evolution for the experimental results and LES simulations using the original XiFoam method of calculating Ξ. The flame radius in the numerical simulation is calculated from the flame images, which are recorded every 0.5 ms time step.

The images were imported into paint software to calculate the flame radius. The initial conditions are 360 K, 0.5 MPa, ϕ = 1, and u'= 6 ms^{-1}. Although the present experiments include a wide range of conditions, the pressure, ϕ and u' are in the centre of the studied conditions. The flame propagation in the numerical simulation is slower than in the experiment. The error in the algebraic method prediction is 46%, and 40% in the transport method. The turbulent correlation is suitable for mixtures with an un-unity Lewis number. Therefore, the present study calculates the wrinkling factor using different empirical correlations for the turbulent burning velocity. As given in Chapter 3, the experimental correlation for the turbulent burning velocity (equations 3.39 and 3.41) is used to calculate Ξ and solve the transport equation for the density-weighted mean reaction regress variable (equations 3.34 and 3.35).

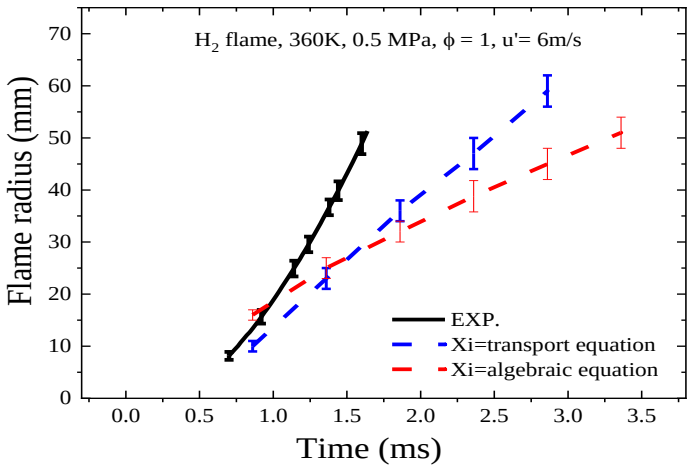

Figure 6.1: Evolution of the flame radius with time from the experiment and the original Xifoam simulation methods.

6.3 Mesh Dependency in the k-ε Turbulence Model

The mesh dependency for the *k-ε* turbulence model is tested with three mesh sizes (case A=0.6, case B=1 and case C=1.4 million elements). The mesh was hexahedral with volume of 6 mm^3, 3.6 mm^3 and 2.57 mm^3, respectively. Figure 6.2 presents the flame radius as a function of time for stoichiometric hydrogen/air at 360 K and 0.5 MPa. The agreement with the experimental result is good for all cases, which will be discussed in more detail below. The result showed that there is not a significant difference in the flame radius prediction between these cases.

Therefore, Case A, with 0.6 million elements, was chosen for the *k-ε* turbulence model to investigate the turbulent flame propagation.

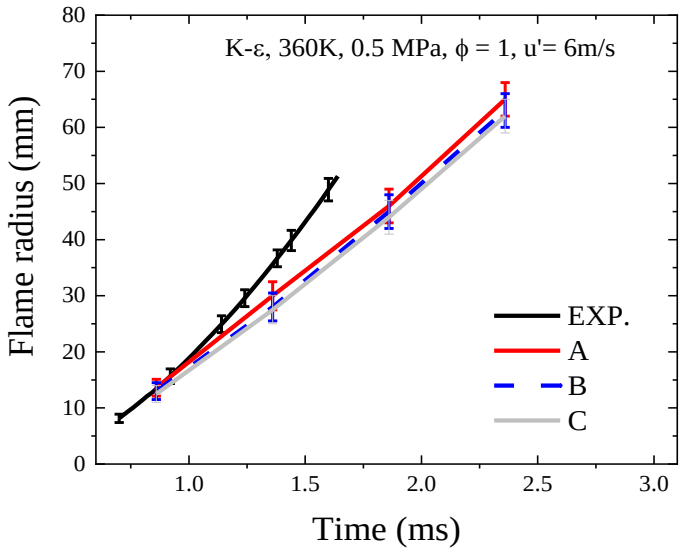

Figure 6.2: Flame radius with time for stoichiometric hydrogen/air at 360K and 0.5 MPa with three mesh sizes.

6.4 Model Validation

A range of different parameters have been tested to validate the numerical model. These are presented in this section as follows: (1) the laminar burning velocity, (2) combustion and turbulent model validation, and (3) the turbulent burning velocity correlation.

6.4.1 Laminar Burning Velocity Validation

The Ξ model does not solve for the combustion chemistry. Instead, the laminar burning velocity (S_u) is implemented in the source term of the transport equation for the density-weighted mean reaction regress variable (equations 3.34-36). As discussed in Chapter 3, S_u can be modelled using the transport equation suggested by Weller et al. [25]. The u_l in the transport equation is calculated by the empirical correlation presented in equation 3.38 [163]. The current experimental laminar burning velocity (u_l) is used to validate this correlation (Figure 6.3). The u_l from equation 3.38 provides good agreement with the experiment and can be used to solve the transport equation for S_u. It can be noticed that the uncertainty in this correlation is around 20 %. This has also been reported in [12, 163].

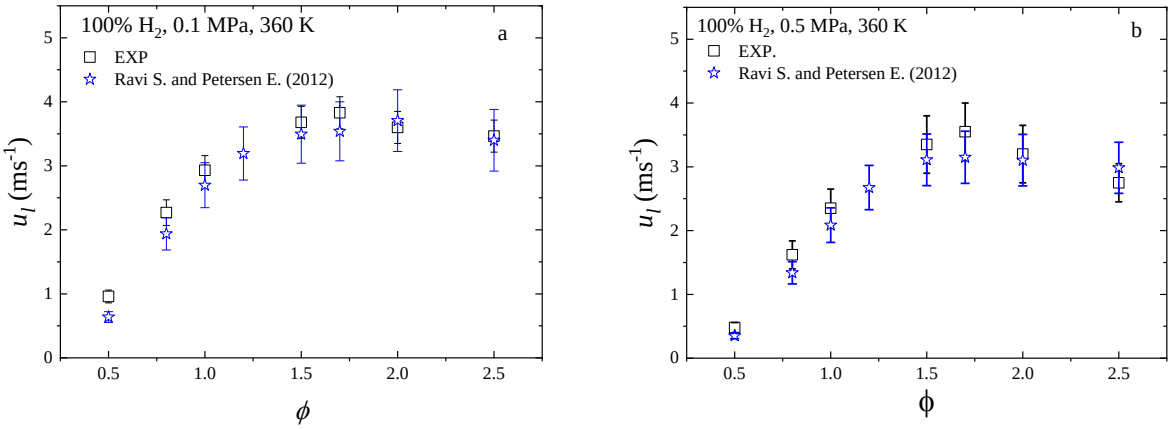

Figure 6.3: The comparison between u_l from the present experiment and correlation in [163], (a) 0.1 MPa and (b) 0.5 MPa.

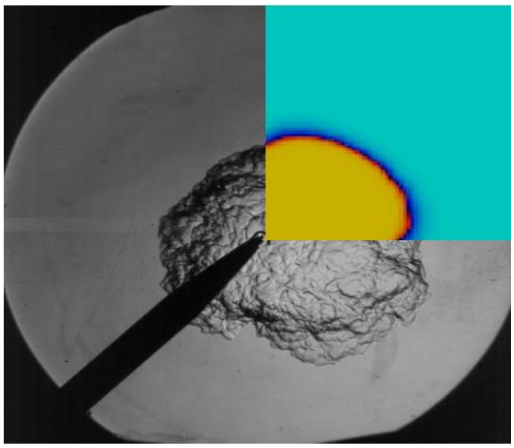

Figure 6.4: Experimental and numerical hydrogen flame (LES simulation), 1 ms after ignition, at 0.1 MPa, 360 K and *u'*= 6 m/s.

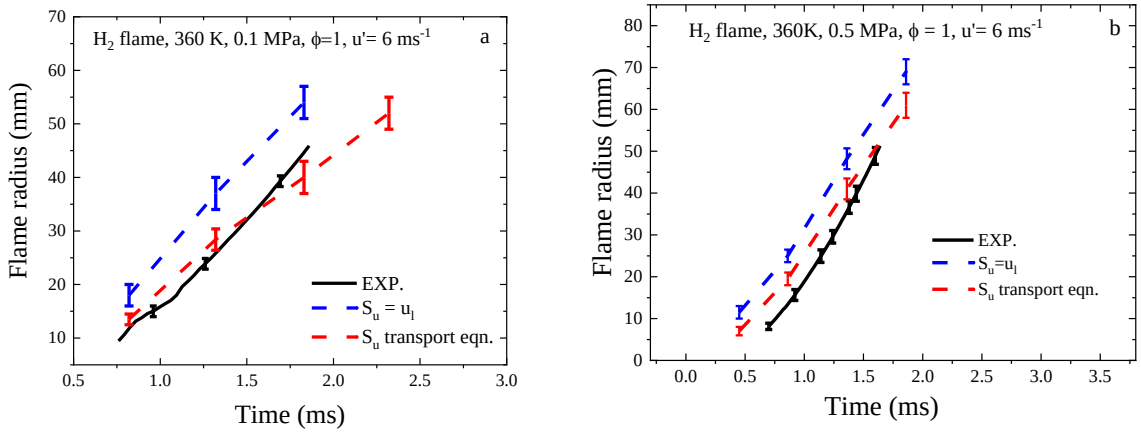

Figure 6.5: Flame radius vs time for experimental and LES simulation with two combustion models (S_u constant and transport equation) for stoichiometric hydrogen flame at 360 K, and *u'*= 6 ms^{-1}, (a) 0.1 MPa and (b) 0.5 MPa.

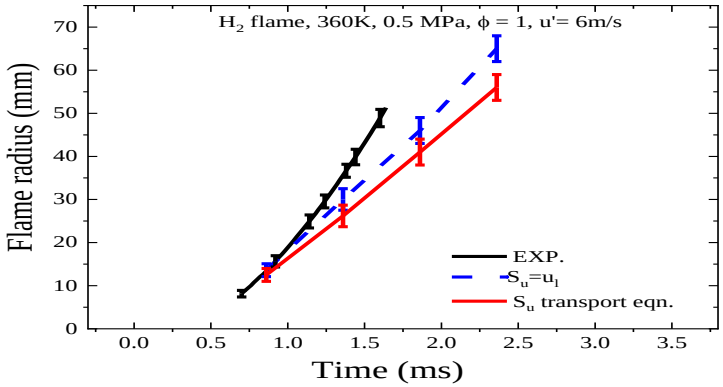

Figure 6.6: Flame radius vs time for experimental and k-ε simulation with two combustion models (S_u constant and transport equation) for stoichiometric hydrogen flame at 360 K, 0.5 MPa, and *u'*= 6 ms^{-1}.

6.4.2 Combustion and Turbulence Model Validation

As outlined in Chapter 3 for the combustion model, S_u can be modelled in two ways: first, as a constant, which equals the experimental laminar burning velocity (u_l), and second, by using the transport equation 3.37. The dynamic-k-equation LES and k-ε models simulate the turbulent spherical flame propagation. Figure 6.4 presents the experimental and numerical hydrogen flame with LES simulation after 1 ms of ignition at 0.1 MPa, 360. Figures 6.5 and 6.6 present the flame radius as a function of time from the experiments and simulations with two combustion models (S_u constant and transport equation) for a stoichiometric hydrogen flame at 360 K with different pressures and rms velocities. In the LES simulation, the maximum predicted error in the flame radius is around 13% for the S_u = transport equation and 22% for $S_u = u_l$. However, the maximum predicted error in the flame radius is around 25% for the S_u = transport equation and 16% for $S_u = u_l$ in the k-ε simulation. The method using constant laminar burning velocity agrees better with the experiments than that S_u derived from the transport equation in the k-ε simulation because this model solves the time-averaged Navier-Stokes equations and accounts for the flow main effects. Thus, this study recommends the combustion model with the transport equation for the LES method and a constant u_l for the k-ε method.

Figure 6.7 compares the flame isotherm-surface at 2000 K of the k-ε (0.6 million elements) and LES simulations (10,509,720 elements) for a stoichiometric hydrogen flame at 360 K, 0.5 MPa, and $u' = 6$ ms^{-1}. The LES simulation can predict the turbulent flame wrinkling, while the k-ε simulation cannot predict it. The flame surface from the k-ε simulation is smooth without flame wrinkling, as the RANS simulation solves the time-averaged Navier-Stokes equations and accounts for the turbulent flow's time-averaged effects.

The *k-ε* simulations do not resolve the turbulent eddies but are represented by a statistical model. As a result, the *k-ε* model is less accurate when dealing with turbulent wrinkling. In contrast, LES resolves the large eddies (the energy-containing structures) directly by solving for the large turbulent scales, while the smaller eddies (which have less impact on the flow dynamics) are modelled using a sub-grid-scale model. By resolving the larger turbulent structures, LES provides a more accurate representation of the flow field, especially in regions where turbulence and combustion interactions are significant (i.e. near the flame front).

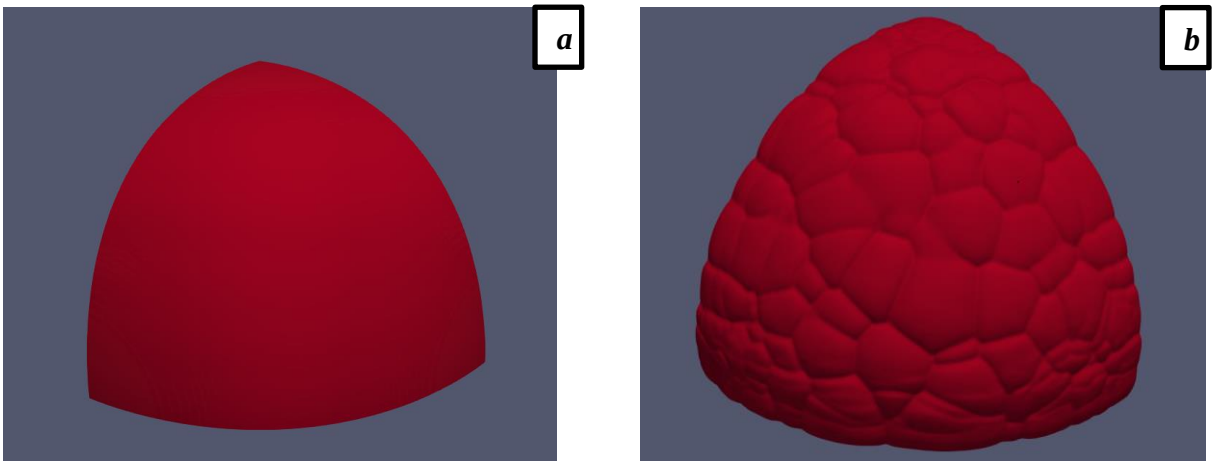

Figure 6.7: Flame isotherm-surface at 2000 K after 2.5 ms of ignition for stoichiometric hydrogen flame at 360 K, 0.5 MPa, and *u'*= 6 ms^{-1}, (a) k-ε and (b) LES simulation.

6.4.3 Turbulent burning velocity correlations

Two turbulent burning velocity correlations have been presented in Chapters 3 and 5, the *U-K* (equation 3.39) and the D_a/Le correlation (equation 3.41). The u_t is a function of $u'k$ in equation 3.39. The u'_k is calculated from equation 3.40 to include the effect of running fans during the flame propagation. The u'_k equation is a function of fan speed and flame radius. Therefore, the rms velocity in numerical simulation is changed as the flame radius increases to consider the running fans' effect during the turbulent flame propagation. However, the $u'k$ is not included in equation 3.41, which accounts for a constant rms velocity, the global u'.

The LES model is used to simulate the spherical flame propagation at initial pressure 0.5 MPa, temperature 360 K, u'= 6 ms^{-1}, and ϕ = 1. The transport equation is used to calculate the laminar burning velocity. The results showed that the *U-K* correlation agrees better with the experimental flame propagation than the *Da/Le* correlation (Figure 6.8). The maximum difference between the predicted flame radius and the experiments is 11% for the *U-K* correlation and 24% for the *Da/Le* correlation. As discussed in Chapter 5, the *U-K* correlation accounts for the flame wrinkling effect as a function of the flame kernel (*u'k*). The rms velocity in the *Da/Le* correlation is taken as 6 ms^{-1}, while it was taken as a function of flame radius in the *U-K* correlation (lower than 6 ms^{-1}). The high value of rms velocity in the *Da/Le* correlation increases the turbulent burning velocity. Therefore, the *U-K* correlation has been chosen for further investigation.

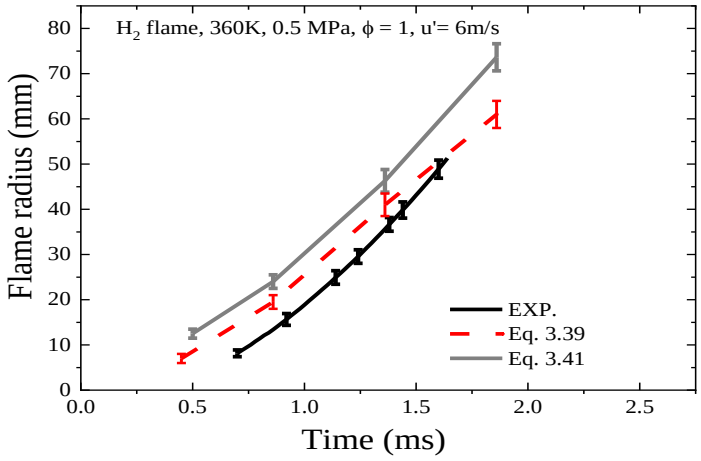

Figure 6.8: The flame radius vs time for experimental and LES simulation with two Ξ calculations (equations 3.39 and 3.41) for stoichiometric hydrogen flame at 360 K, 0.5 MPa, and *u'*= 6 ms^{-1}.

The LES turbulence model, with the *U-K* correlation and S_u transport equation, has been used to simulate the propagation of the hydrogen flame (Figure 6.9). It has been noticed that the slope of the experimental flame radius is concave upwards as time progresses while it declines in the numerical simulation. Experimentally (as discussed in Chapter 5), the acceleration in the flame propagation results from two factors: (i) as the flame kernel increases, the proportion of the effective turbulent eddies increases [125, 127, 158], and (ii) as the flame radius reaches 60 mm, the vessel pressure increases, reducing the Taylor scales and enhancing flame wrinkling. The Ξ is modelled using an algebraic equation based on the experimental correlation equation 3.39. The first effect is accounted for in the model Ξ, which is in the u'_k value (equation 3.40). However, the second effect is not included in the current modelling. Equations 3.39 and 3.41 are derived using the Schlieren technique, in which the flame propagation is recorded within limited optical access (≤60 mm flame radius). The images are recorded during the period of constant pressure [126]. This means that equations 3.39-41 are valid only for flame radius ≤60 mm in the flame propagation at constant pressure. Therefore, the present study recommends the *U-K* correlation for hydrogen/air flame propagation at constant pressure conditions, such as in a gas turbine.

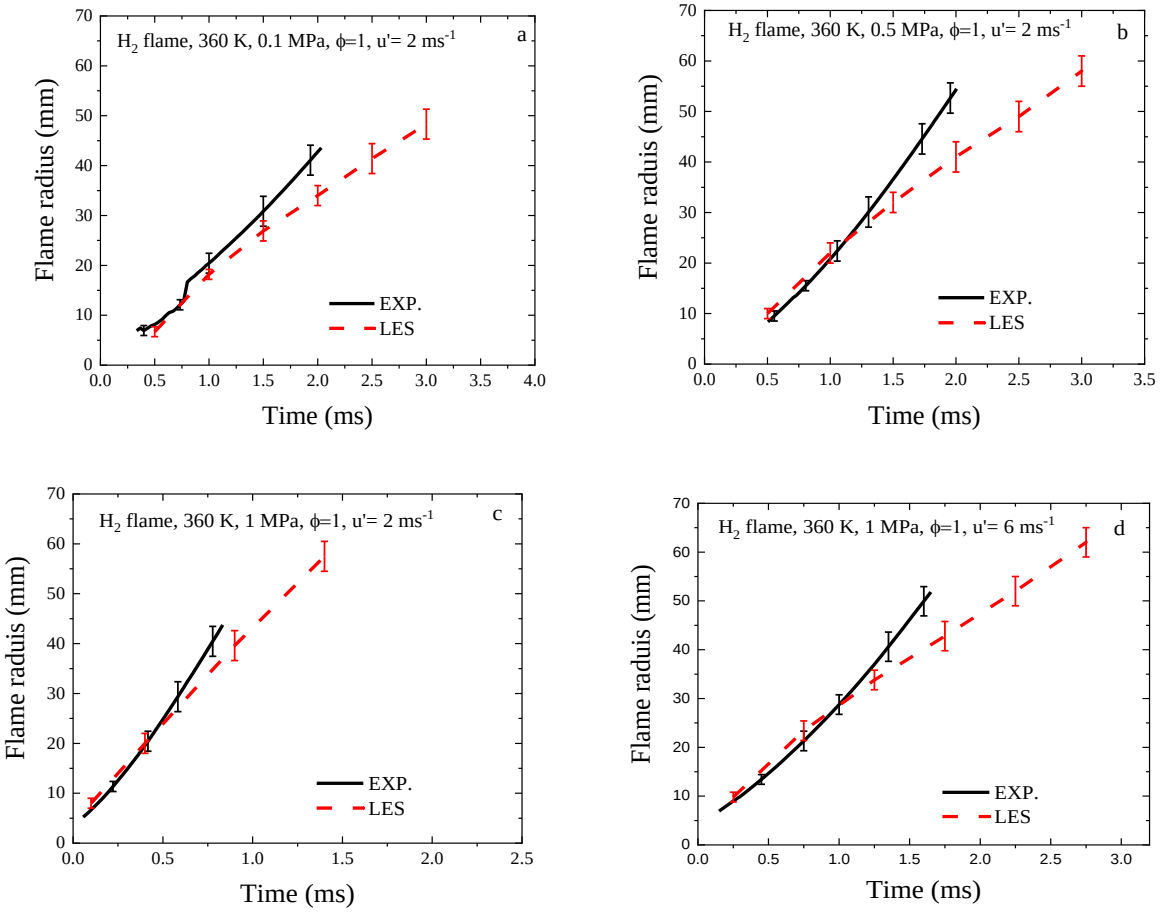

Figure 6.9: Flame radius vs. time for experimental and LES simulation for stoichiometric hydrogen flame at 360 K, (a) 0.1 MPa *u'*= 2 ms^{-1}, (b) 0.5 MPa *u'*= 2 ms^{-1} (c) 1 MPa *u'*= 2 ms^{-1}and (c) 1 MPa *u'*= 6 ms^{-1}

6.5 Velocity and Temperature Field

A stoichiometric hydrogen flame is used to analyse the velocity and temperature field. Figures 6.10 and 6.11 present the temperature contours and flow velocity vectors after 3 ms of ignition for different pressures and rms velocities. The burned mixture moves toward the centre, while the flow ahead of the flame is accelerated radially outward due to the burned gas expansion. A strong outwards velocity pulse ahead of the flame is generated due to the combined influences of a high hydrogen burning rate and high volumetric expansion [65]. As the pressure and rms velocity increase, the velocity ahead of the flame increases. This results from the high burning rate (u_t) at high pressure and rms velocity.

The PIV measurements have reported the interaction between the turbulent flow and the flame propagation in the spherical vessel [65].

As discussed in Chapter 2, the CFD simulation can provide information about the turbulent flow that is difficult to obtain experimentally. Figures 6.12-6.14 present the velocity magnitude for the radial line at times 1.5 and 2.5 ms with different pressure and rms velocities. The right Y-axes represent the regress variable to identify the flame position (b = 0 burned gases, b=1 unburned gases). The maximum velocity magnitude is within the flame when the mixture starts burning (b =0.8-0.95). The peak value of the velocity is associated with the peak value of the pressure wave, as shown in Figures 6.15-6.17. The pressure is not uniform in Figures 6.15-6.17 due to the expansion of the burned gases, which pushes the unburned gases outward and results in dynamic variation in the pressure field. In addition, a localized pressure variation can result from the local variation in the flame surface area introduced by the wrinkling combustion factor. As reported in the literature, the pressure gradient within the flame creates a velocity wave associated with it [45].

Moreover, the maximum velocity increases as *u'* increases (*U_magnitude* =15 m/s at *u'*= 2 m/s and *U_magnitude* = 28 m/s at *u'*= 6 m/s (Figures 6.12 and 6.13). This is due to the increased turbulent kinetic energy. The peak value of pressure increases for turbulent kinetic energy [45]. Another reason for the peak velocity difference is that as rms velocity increases, u_t rises, resulting in an increased velocity pulse (the higher burning rate results in higher volume expansion). In addition, the velocity at 1.5 ms is higher than at 2.5 ms for the same case, as can be seen in 6 ms^{-1}, 0.5 and 1 MPa. This is due to the wall confinement, which reduces the maximum velocity as the flame approaches the wall.

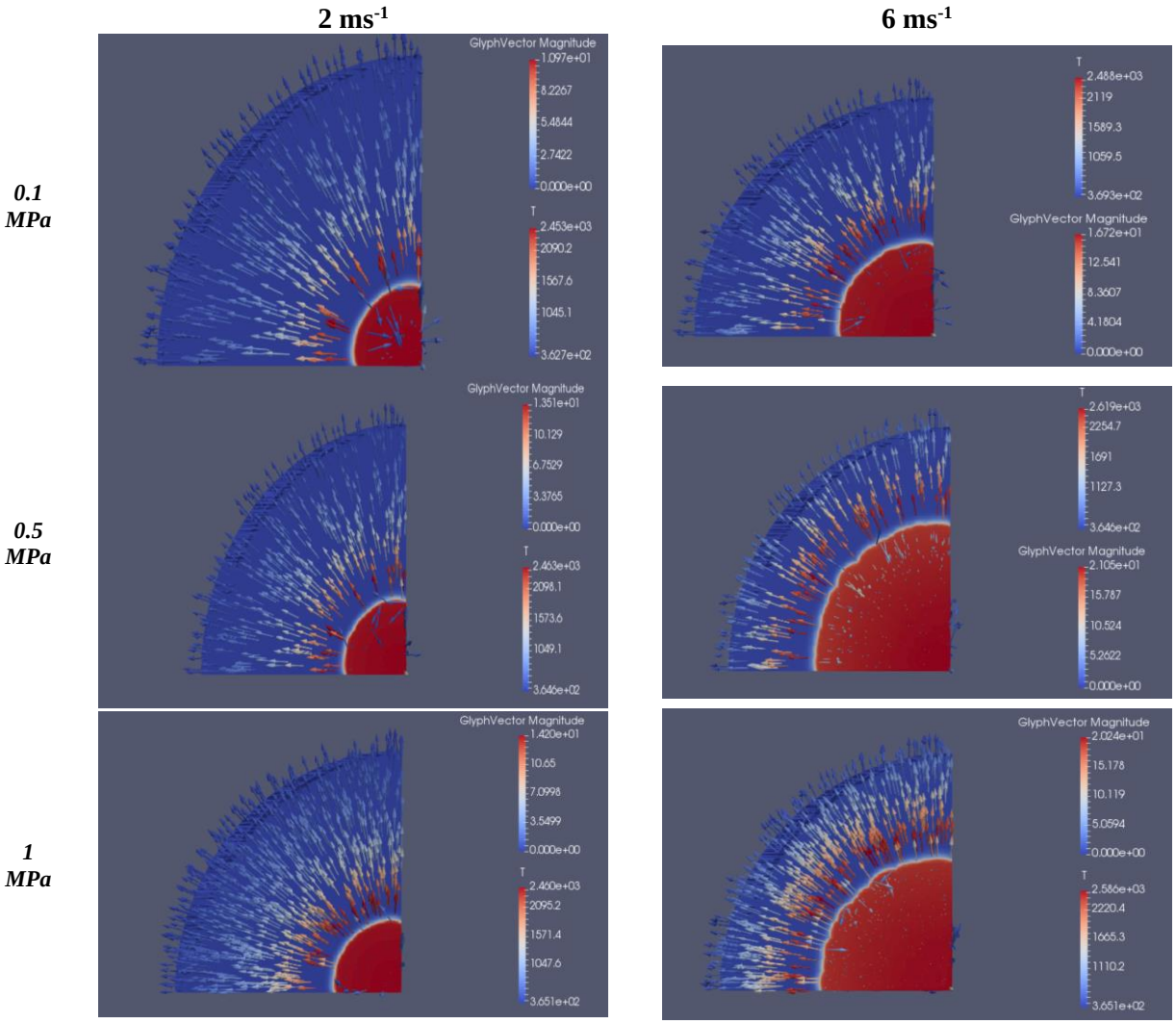

Figure 6.10: Temperature (K) contour and flow velocity vector ms^{-1} after 3 ms of ignition for different pressures and rms velocities.

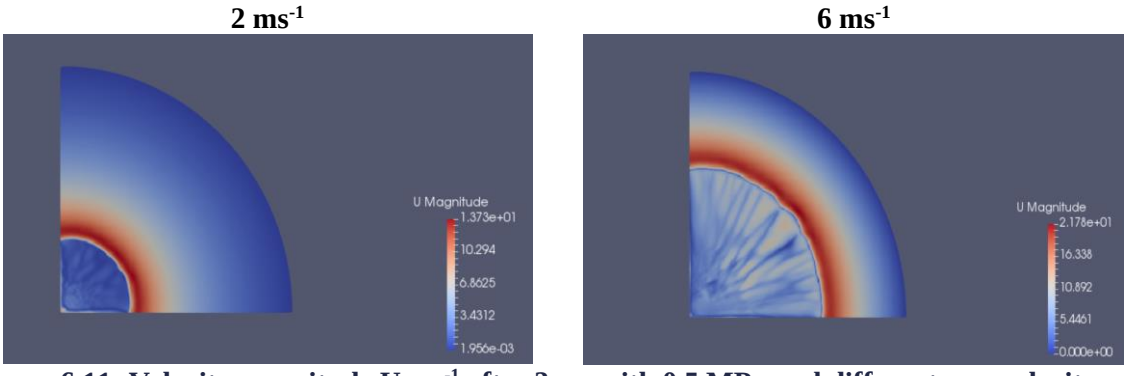

Figure 6.11: Velocity magnitude U ms^{-1} after 3 ms with 0.5 MPa and different rms velocity.

Figure 6.18 presents the temperature distribution for a hydrogen flame at two time steps: the initial pressure is 0.5 MPa, the temperature is 360 K, and the rms velocity is 6 ms^{-1}. The temperature distribution during the swift flame propagation (hydrogen/air) is challenging to measure. However, the present numerical model can predict the temperature during the hydrogen flame propagation. Temperature prediction is crucial in practical applications such as gas turbines. As reported in Chapter 1, the hydrogen in a gas turbine increases the flame temperature, resulting in elevated equipment temperature and potentially NOx emissions [13]. Thus, gas turbine manufacturers have applied different methods to achieve moderate flame temperature, such as adding more air than stoichiometric and fuel dilution [13]. Moreover, when the hydrogen is replaced by natural gas in a gas turbine, the enthalpy drops and the products' heat transfer coefficient changes, affecting the turbine blades cooling system. Therefore, gas turbine designers can use the current model (k-ε or LES with U-K correlation) to predict the combustion chamber's temperature distribution.

1.5 ms

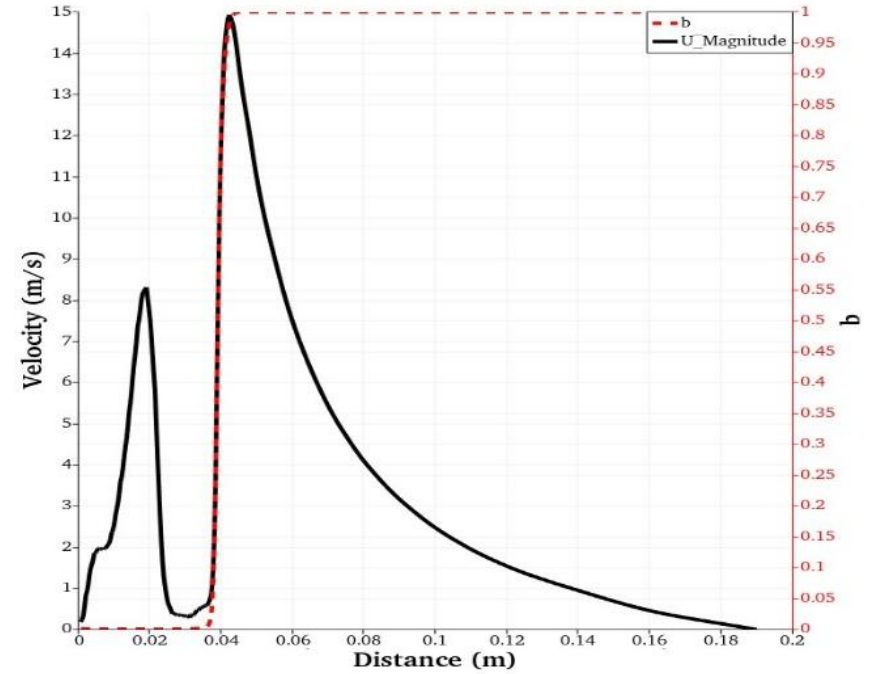

2.5 ms

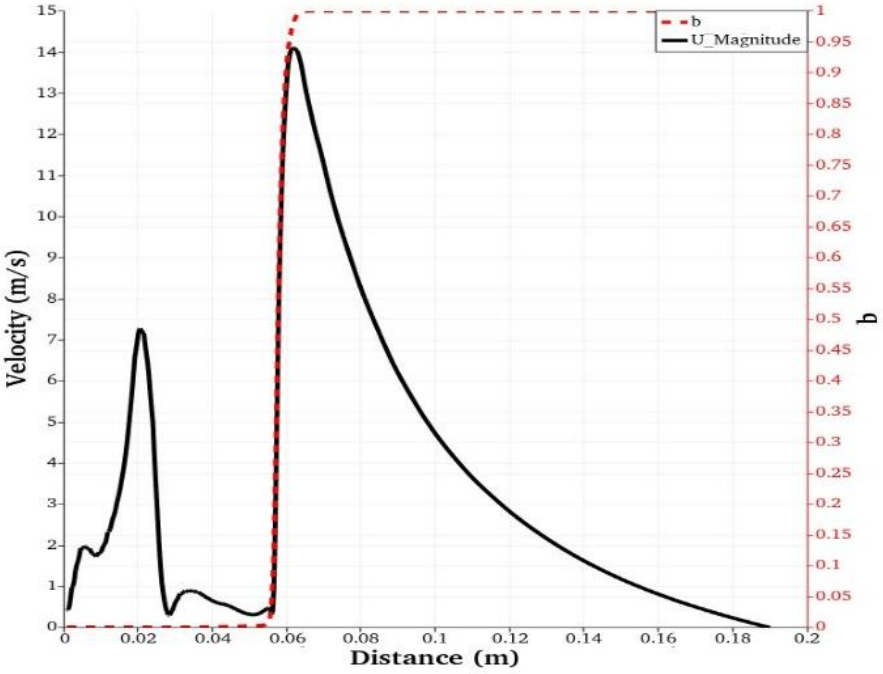

Figure 6.12: Velocity magnitude (left axes) for a radial line at steps 1.5 and 2.5 ms with 0.1 MPa and *u'* = 2 ms^{-1}; the right axes represent the regress variable (b = 0 burned gases, b=1 unburned gases).

1.5 ms

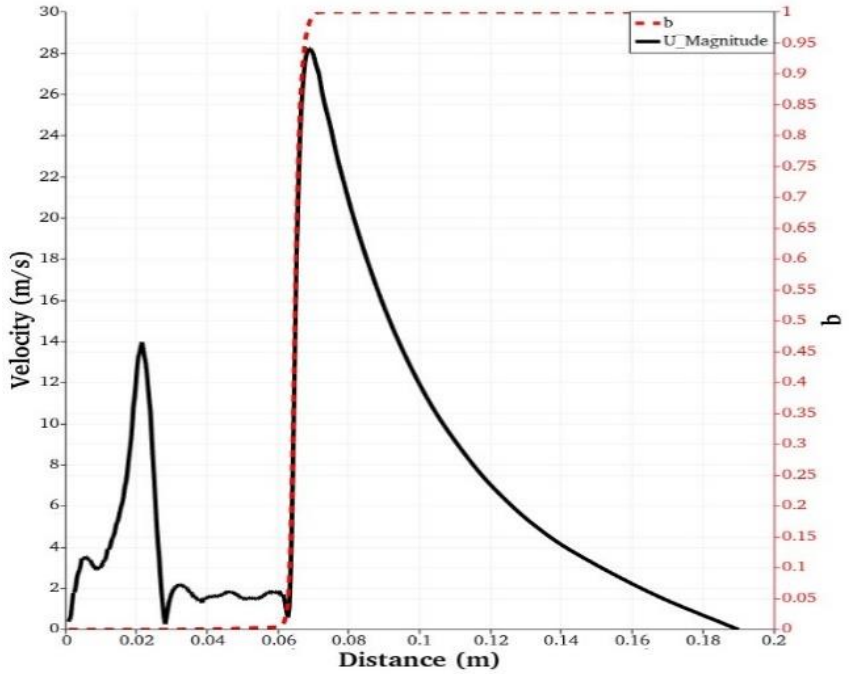

2.5 ms

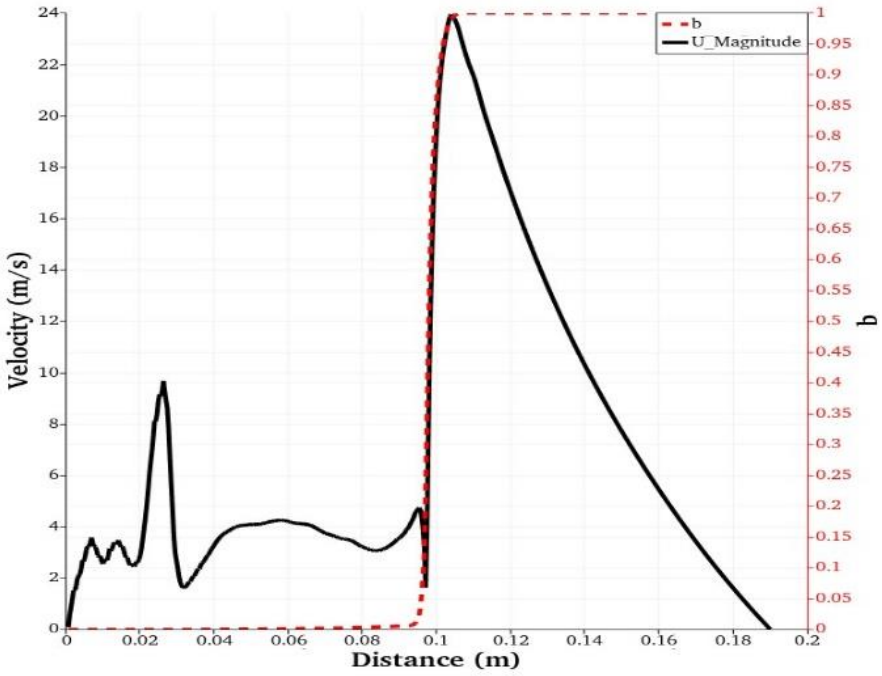

Figure 6.13: Velocity magnitude (left axes) for a radial line at steps 1.5 and 2.5 ms with 1 MPa and *u'* = 6 ms^{-1}; the right axes represent the regress variable (b = 0 burned gases, b=1 unburned gases).

1.5 ms

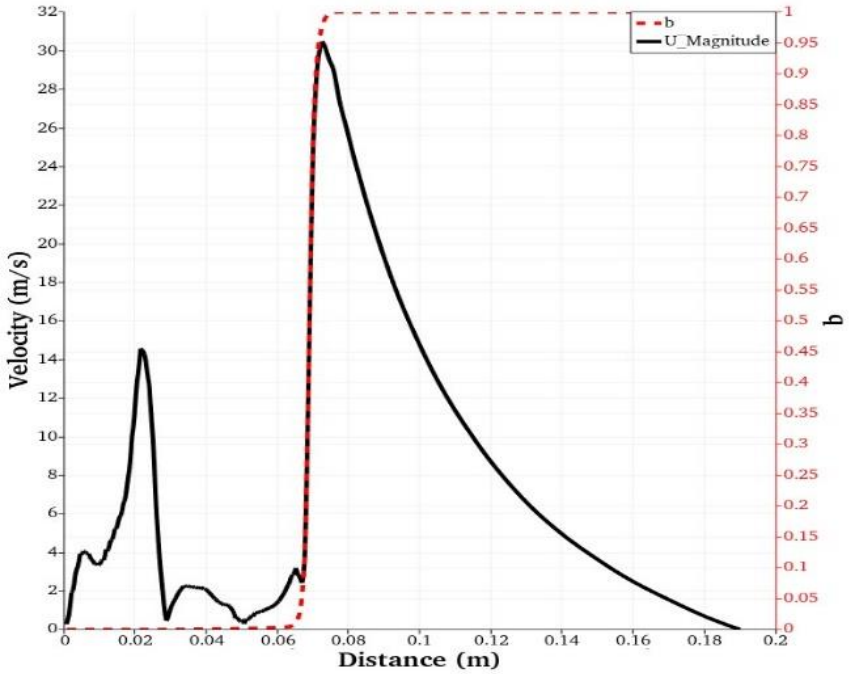

2.5 ms

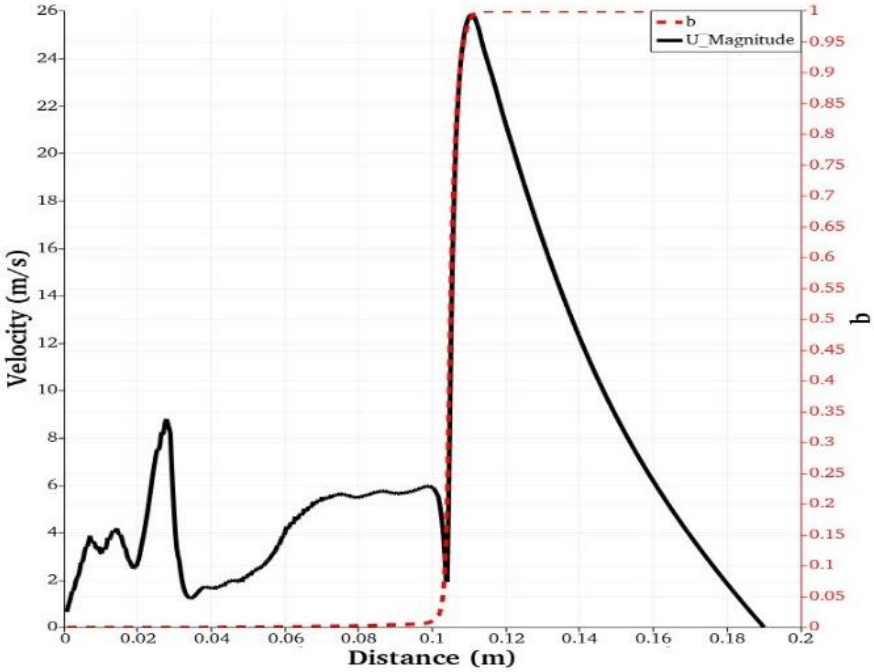

Figure 6.14: Velocity magnitude (left axes) for a radial line at steps 1.5 and 2.5 ms with 0.5 MPa and *u'* = 6ms^{-1}; the right axes represent the regress variable (b = 0 burned gases, b=1 unburned gases).

1.5 ms

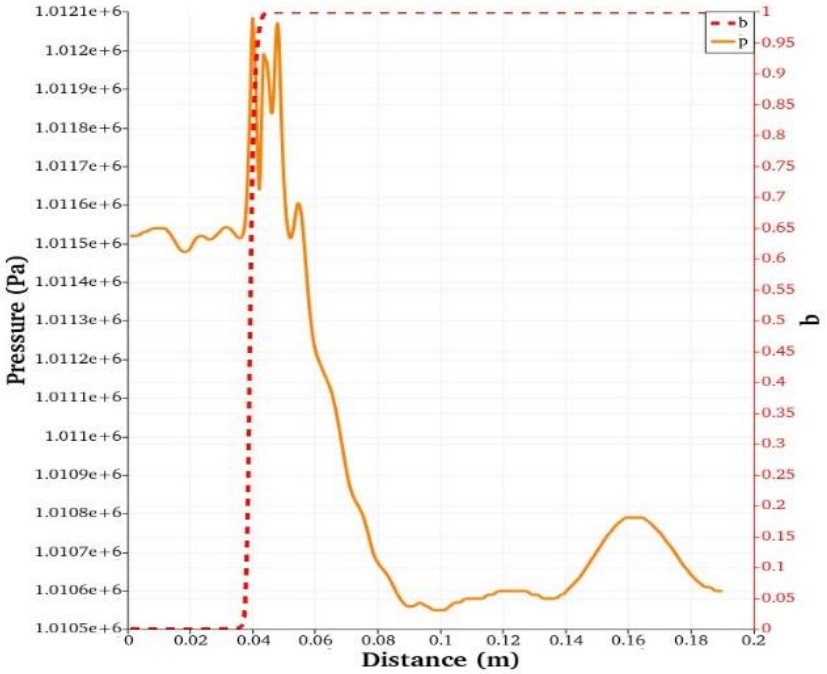

2.5 ms

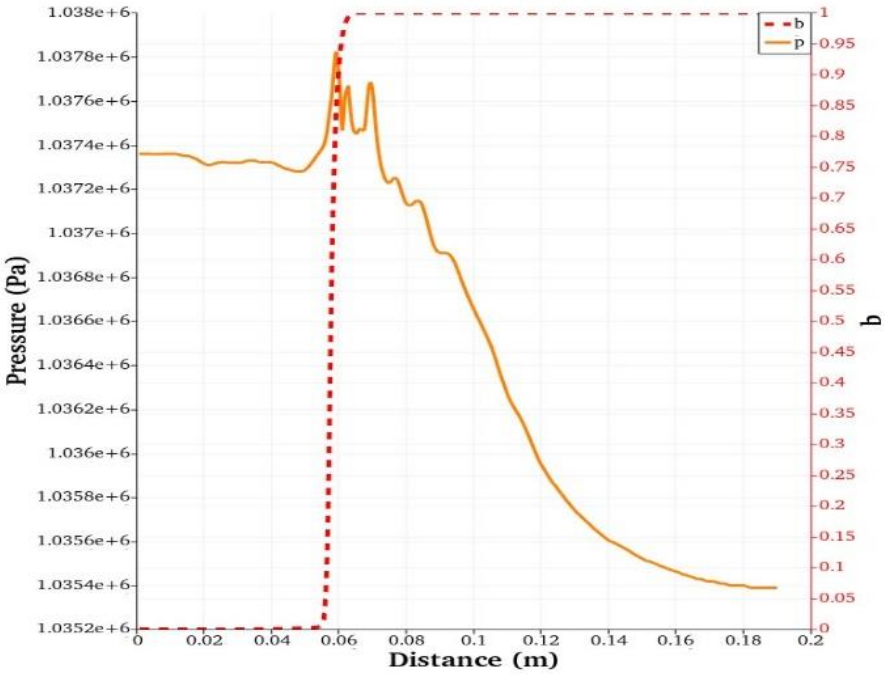

Figure 6.15: Pressure wave for a radial line at steps 1.5 and 2.5 ms (*P*=1 Mpa, *T*=360 K, ϕ=1 and *u'*= 2 ms^{-1}).

1.5 ms

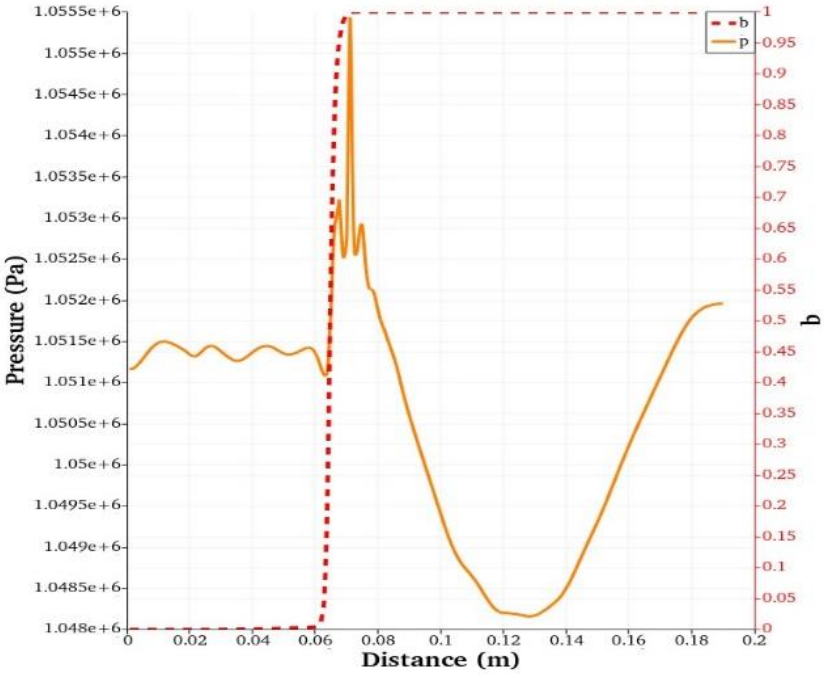

2.5 ms

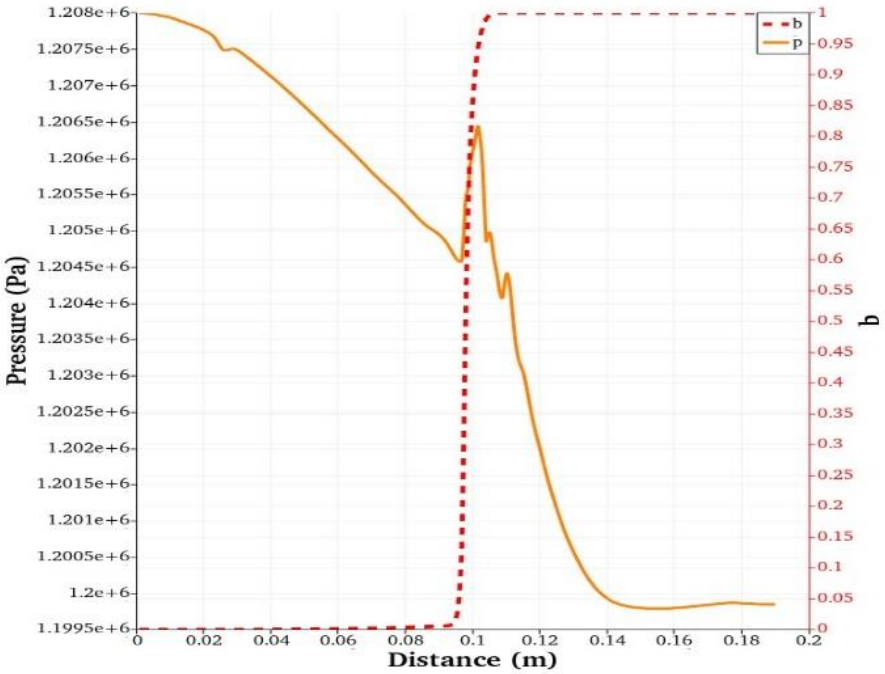

Figure 6.16: Pressure wave for a radial line at steps 1.5 and 2.5 ms (*P*=1 Mpa, *T*=360 K, ϕ=1 and *u*'= 6 ms^{-1}).

1.5 ms

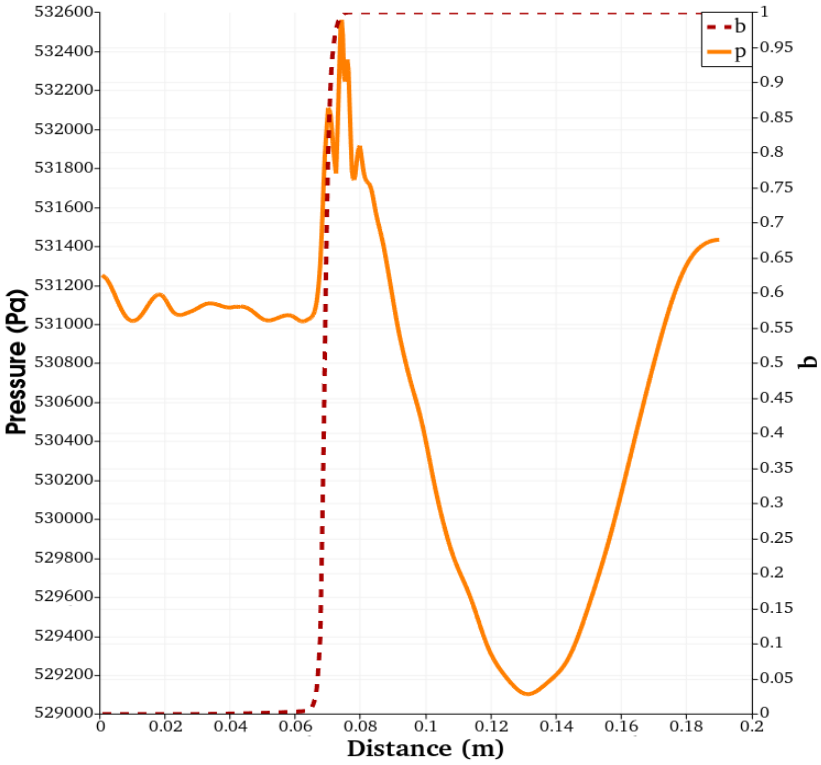

2.5 ms

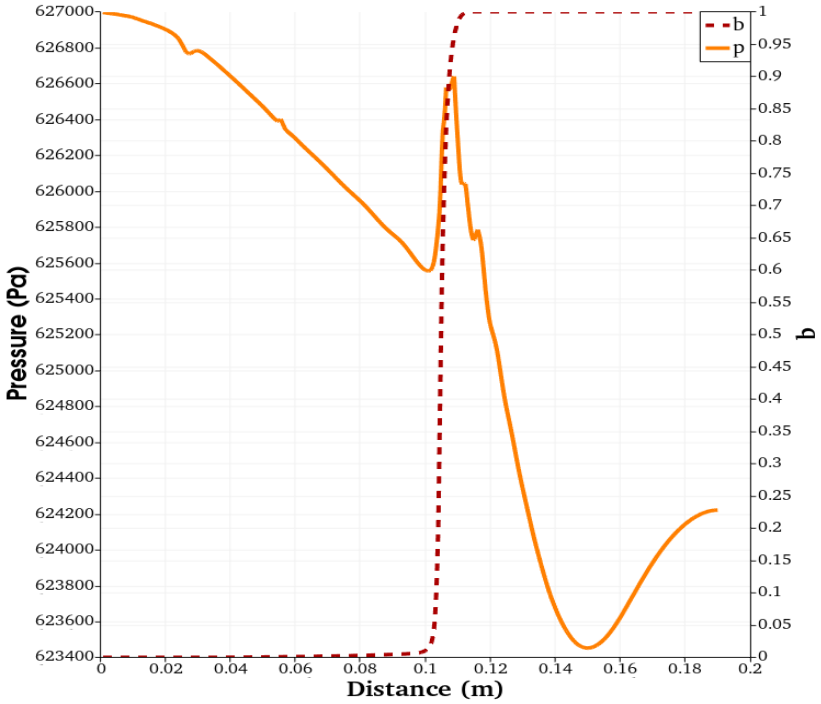

Figure 6.17: Pressure wave for a radial line at steps 1.5 and 2.5 ms (*P*=0.5 Mpa, *T*=360 K, ϕ=1 and *u*'= 6 ms^{-1}).

1.5 ms

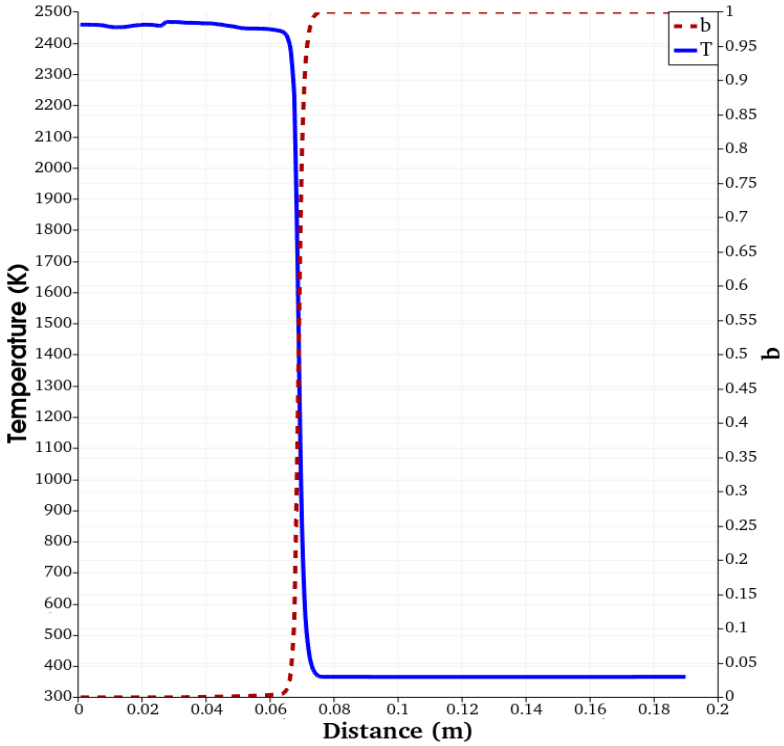

2.5 ms

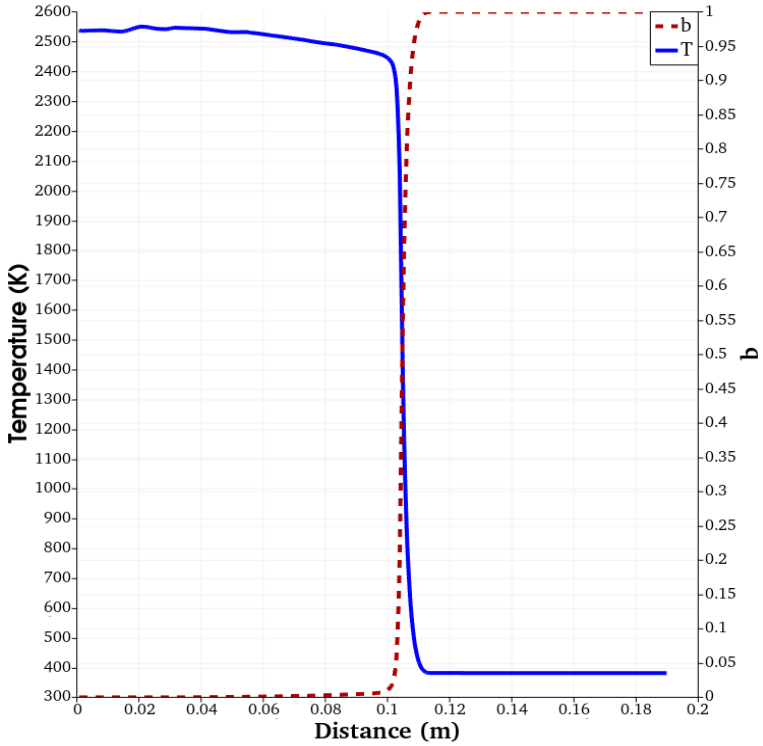

Figure 6.18: Temperature distribution for a radial line at steps 1.5 and 2.5 ms (*P*=0.5 Mpa, *T*=360 K, ϕ=1 and *u'*= 6 ms^{-1}).

6.6 Flame Wrinkling

Figures 6.19 and 6.20 present the flame isotherm-surface at 2000 K for different pressures and rms velocities. The turbulent eddies stretch the flame by generating flame surface wrinkles [186]. The turbulent flame wrinkling can be more significant in the following cases: (i) the increased pressure and u' result in lower Taylor length scales (λ), and (ii) the mixture with high laminar flame cellularity (lower *Le,* ϕ =0.5) has more turbulent flame wrinkling than the mixture with low laminar flame cellularity (higher *Le,* ϕ =1).

The effects of pressure and rms velocity are shown in the current simulation. At ϕ=1, the flame is slightly wrinkled at low pressure (0.1 MPa) and low u', while it is highly wrinkled at high pressure and high u'. Thus, the flame surface is more wrinkled for 6 ms^{-1} than 2 ms^{-1}. At 6 ms^{-1} Figure 6.19, the flame surface structure is finer with an initial pressure of 0.5 MPa than 0.1 MPa. As mentioned above, the increased pressure and rms velocity decrease the Taylor length scales, resulting in significant flame wrinkling.

The flame wrinkling evaluation is essential in practical applications as it enhances the burning and heat release rates. In the current model, the flame wrinkling is derived by the Ξ, calculated based on the turbulent burning velocity correlation. The flame wrinkling is not shown in the cases with ϕ=0.5 for all rms velocities and pressures (Figure 6.20) due to low Ξ, resulting from low turbulent burning velocity. The flame wrinkling factor (Ξ) is calculated using the experimental turbulent burning velocities (equations 3.36-41). Looking back to Figure 5.7, the turbulent burning velocities at u'= 6 ms^{-1} are almost double those at u'= 2 ms^{-1}, and those at ϕ=1 are double those at ϕ=0.5. In addition, the model does not show a considerable difference in flame structure between 0.5 and 1 MPa at u'= 6 ms^{-1} (Figure 6.19). This is because the turbulent burning velocity did not increase significantly as the pressure increased from 0.5 to 1 MPa (Figure 5.7).

Therefore, the flame brush thickness in the simulations depends on the turbulent burning velocity. If the model includes the increased u_t with flame size, the flame brush thickness will grow with the flame size; otherwise, when the model considers constant u_t with flame size, the flame brush will be steady.

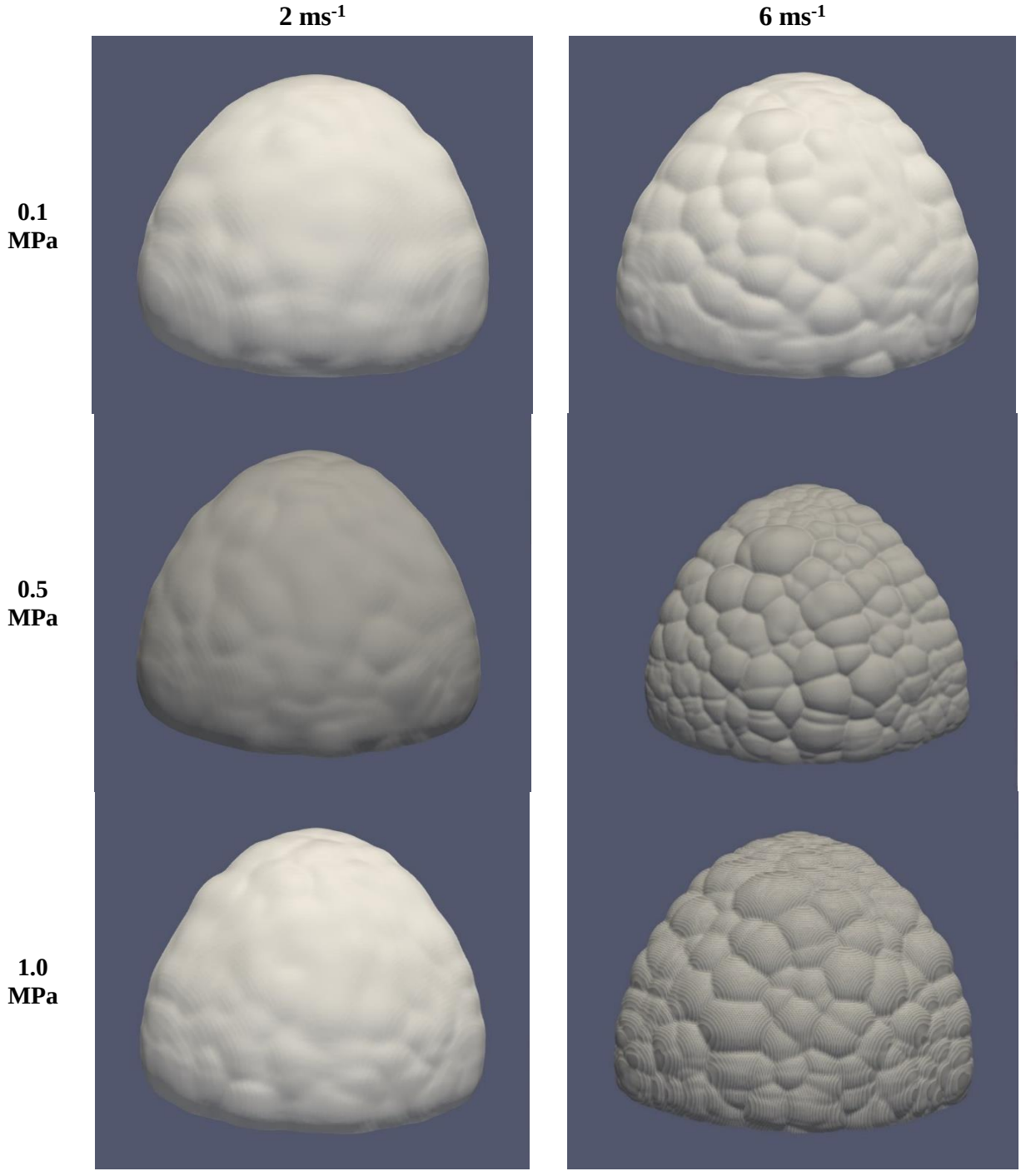

Figure 6.19: Flame isotherm-surface at 2000 K after 3ms of ignition for different pressures and rms velocities (ϕ=1).

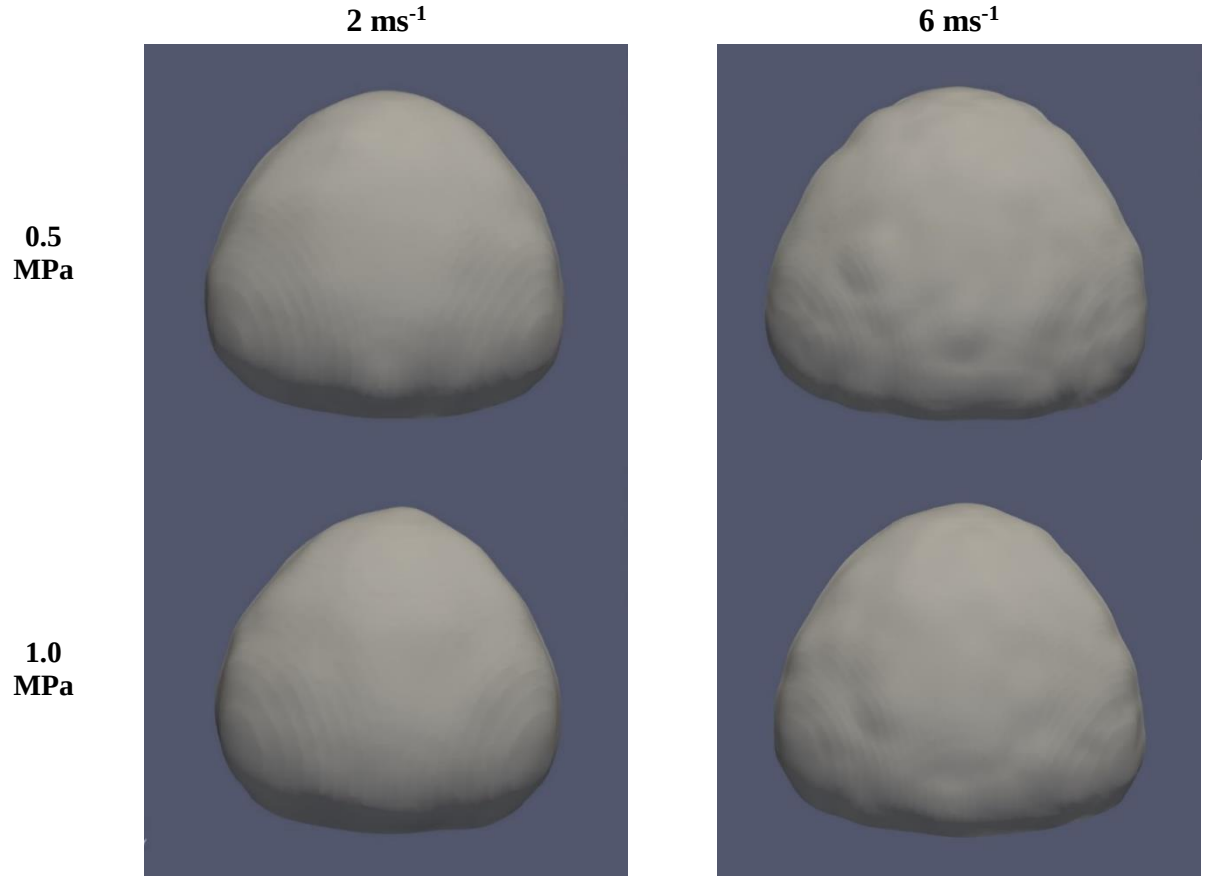

Figure 6.20: Flame isotherm-surface at 2000 K after 3ms of ignition for different pressures and rms velocities (ϕ=0.5).

6.7 Model Demonstration in a Simplified Gas Turbine-Like Configuration

This section aims to show the potential for practical application of the current model. This simulation does not attempt to replicate full gas turbine conditions. Rather, it illustrates the model's capacity to handle combustion scenarios relevant to gas turbine research, such as premixed hydrogen/air flames under constant pressure. The current model can predict the temperature distribution for premixed hydrogen/air flames at constant pressure conditions (suitable for gas turbine applications). Siemens Gas Turbine (SGT-100), Dry Low Emission (DLE) combustor, was selected as a model in the present study (figure 6.21) [187].

The reasons for choosing this model are that (i) the Siemens research group has extensively studied this combustor [188-190], (ii) they recently advanced this combustor and ran a gas turbine with hydrogen/air [190]. However, the actual dimension and experimental results of this novel combustor have not yet been published. The validation of this simulation will be postponed until the experimental results of the hydrogen/air gas turbine are published.

The present study numerically simulates the flame zone in the SGT-100-DLE combustor using OpenFoam software and takes the dimensions from [187] (Figure 6.21b). The following simplifications are applied to the model to reduce the computational cost: (i) the radial swirler air inlet (installed ahead of the combustor) is not modelled instead, the swirlFlowRateInletVelocity boundary condition is used, and the fuel/air inlet is assumed to be fully premixed, (ii) the transition outlet is not modelled, and (iii) the asymmetric geometry of the flame zone has been modelled (figure 6.22).

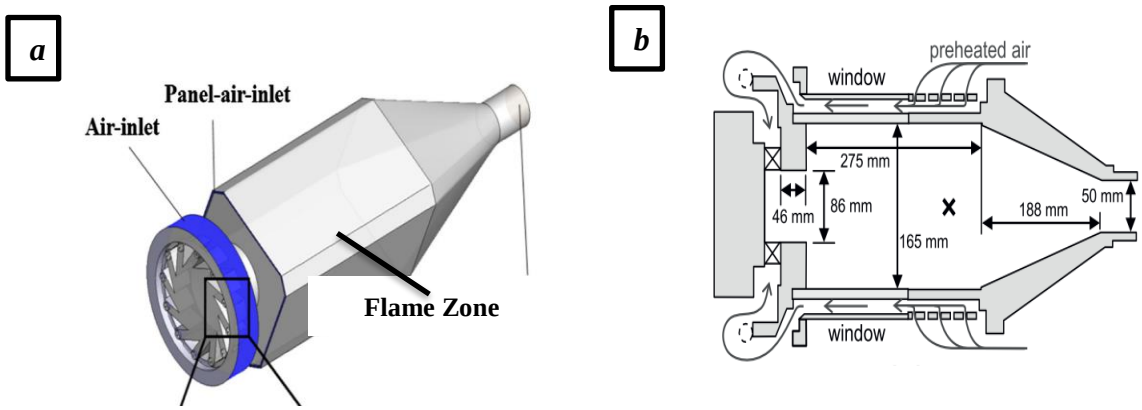

Figure 6.21: Siemens Energy SGT 100, DLE combustor [187], a) 3D combustor, and b) cross section combustor.

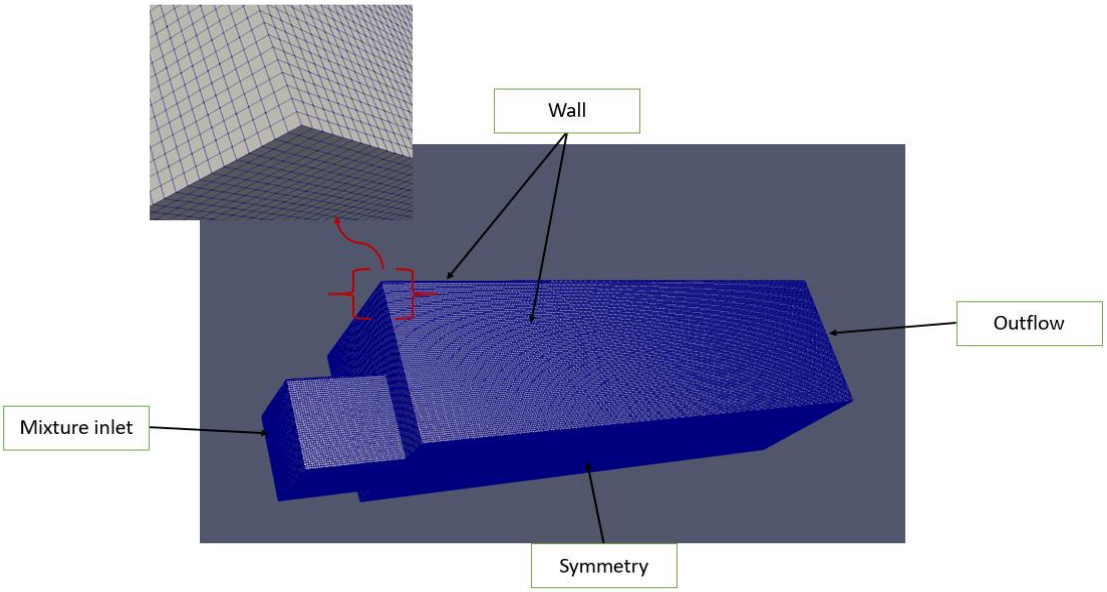

Figure 6.22: The modelled flame zone.

A global structured mesh of 1.956 million elements was generated for the calculation domain. The calculation domain includes only a premixing section (flame zone). The *k-ε* turbulence model associated with the flame wrinkling (Ξ) combustion model has been used. In the source term of the transport 'b' equation, the *U-K* correlation is used for the turbulent burning velocity, and $S_u = u_l$ for the laminar burning velocity. The stoichiometric hydrogen flame at 0.5 MPa, 360 K and $u' = 2$ m/s are adopted in this simulation. The gradient of any variable is zero on the symmetry plane. The initial mixture temperature is 360 K, the same as the wall's. Table 6.1 presents the boundary conditions for the current simulation.

Table 6-1: The initial and boundary conditions of the numerical simulation

Variable	Inlet	Wall	Symmetry	Outlet
Pressure	zeroGradient	zeroGradient	symmetrPlane	zeroGradient
Temperature	fixedValue; uniform 360;	zeroGradient	symmetrPlane	zeroGradient
Velocity U	swirlFlowRateInletVelocity; Flow rate constant 0.151;	fixedValue; uniform (0 0 0);	symmetrPlane	zeroGradient
k	Fixed value; Uuuniform 1;	kLowReWallllFunction; uniform 1;	symmetrPlane	zeroGradient
epsilon	terbulentInletKineticEnergyInlet; intensity 0.05; value uniform 1;	epsilonWallFunction; uniform 0.00754;	symmetrPlane	zeroGradient

The present model and correlation can provide the location of heat release, near-wall gas temperatures, combustion dynamic and exit temperature, which are essential for gas turbine designers. Figure 6.23 presents the temperature contours for the combustor at different time steps. Figure 6.24 illustrates the velocity (*U* ms-1) after 2 ms of the ignition. The velocity profile follows the temperature distribution profile, as discussed in the spherical flame (section 6.5).

From the initial results, the following steps need to be carried out in future work to get reliable numerical results:

1- The mesh dependency needs to be validated.

2- The turbulence is not fully developed, so the inlet needs to be extended to become fully developed and turbulent. This increases the computational cost and time.

3- The transition outlet needs to be added to the model.

4- The results need to be validated with experimental data for hydrogen/air combustors.

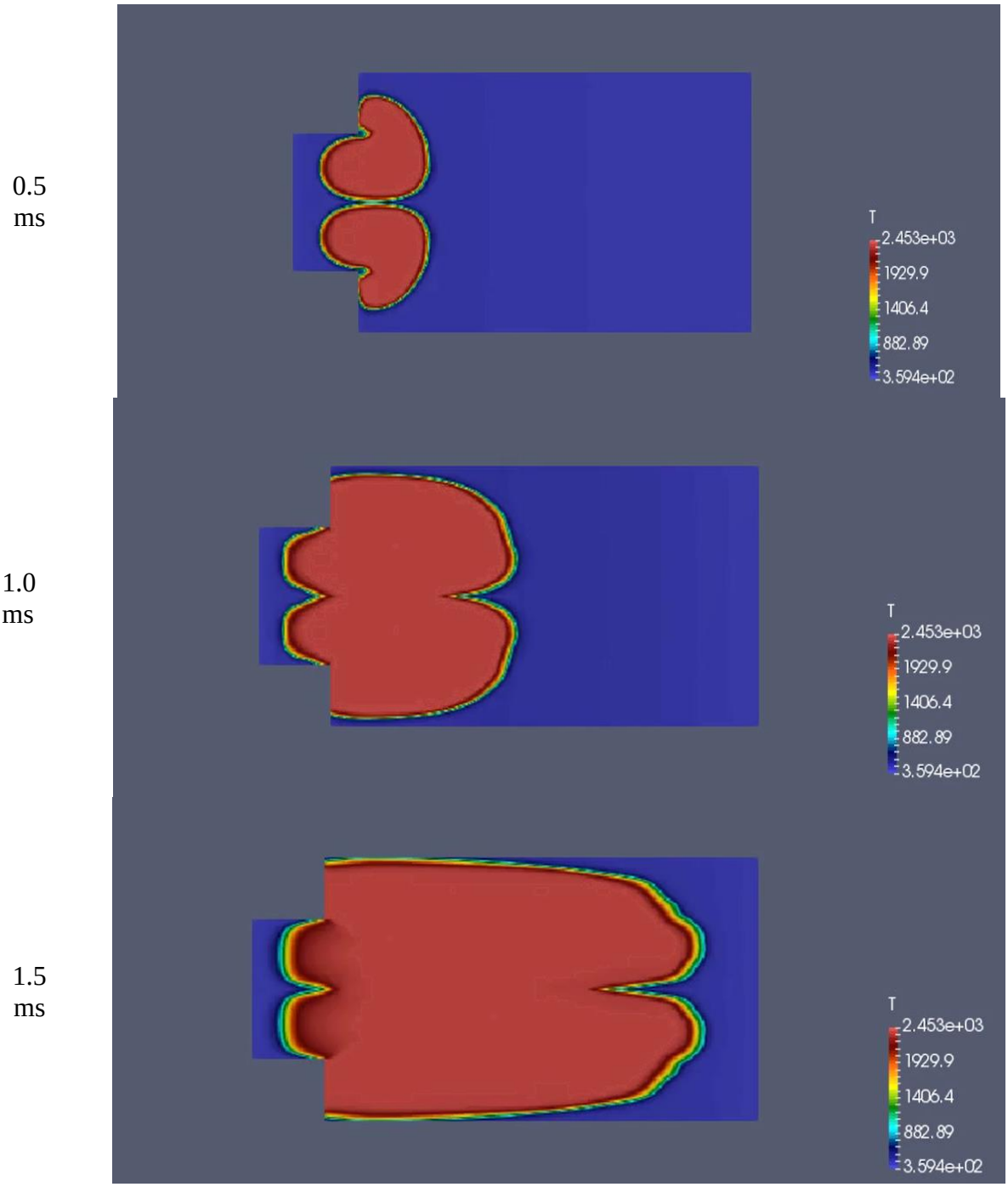
0.5 ms
T
2.453e+03
1929.9
1406.4
882.89
3.594e+02
1.0 ms
T
2.453e+03
1929.9
1406.4
882.89
3.594e+02
1.5 ms
T
2.453e+03
1929.9
1406.4
882.89
3.594e+02

2 ms

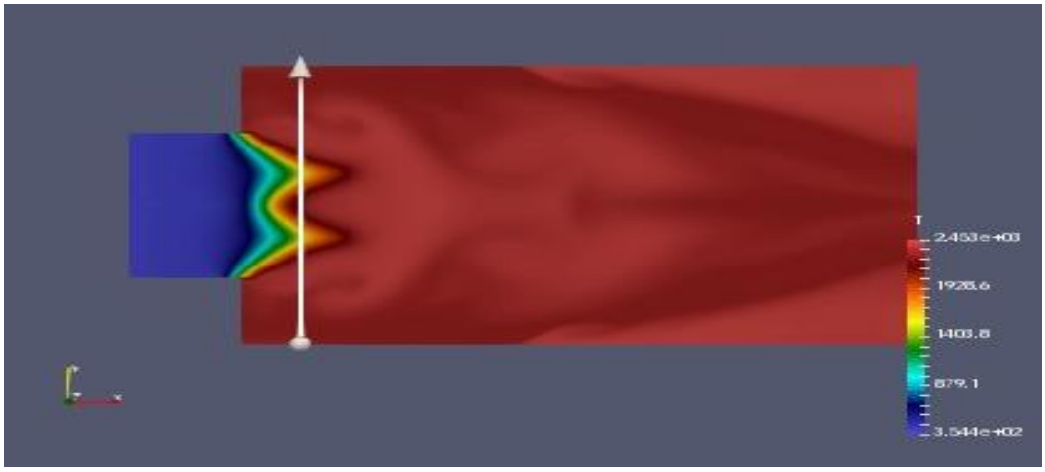

Figure 6.23: The temperature contours at different time steps for the stoichiometric hydrogen flame at 0.5 MPa, 360 K and *u'*= 2 ms^{-1}.

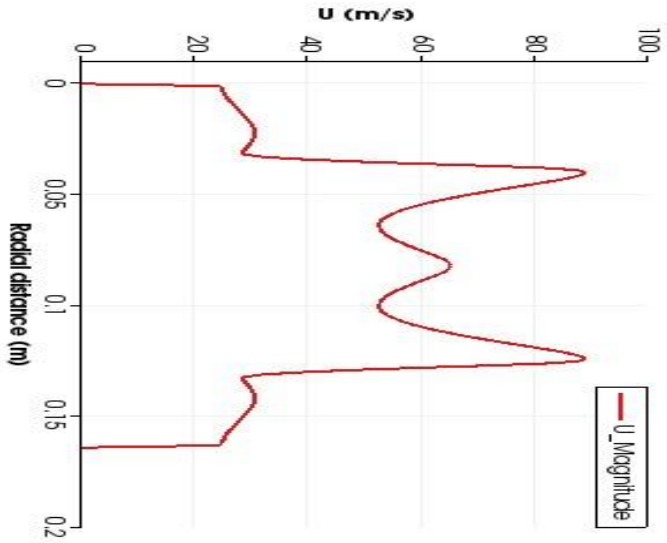

Figure 6.24: The velocity at 2 ms for the vertical line shown in Figure 6.23 at ms

6.8 Chapter Conclusion

The flame surface wrinkling combustion (Ξ) model has been used to simulate the turbulent spherical flame propagation of a hydrogen/air mixture. The experimental correlation for the turbulent burning velocity is used to calculate the source term in the transport equation for the density-weighted mean reaction regress variable 'b'. The different components of the numerical model (the laminar burning velocity, combustion and turbulence model, and the turbulent burning velocity correlation) have all been tested and validated. The following conclusions can be drawn:

1- Although the *k-ε* and LES models agree well with the experimental result, LES is preferred in the flame surface wrinkling investigations.

2- The LES simulation with the combustion model that uses the transport equation for S_u provides better agreement with the experiments than for constant laminar burning velocity.

3- The *k-ε* simulation with the combustion model that uses a constant laminar burning velocity provides better agreement with the experiments than the transport equation for S_u.

4- The *U-K* correlation agrees better with the experimental flame propagation than the *Da/Le* correlation.

5- From the flow field investigation, the maximum velocity was found at b=0.9. This velocity was associated with the pressure wave in the spherical flame propagation.

6- The maximum velocity increases as u' increases due to the increased turbulent kinetic energy. The peak value of pressure is more significant for higher turbulent kinetic energy.

7- The increased pressure and u' result in lower Taylor length scales (λ), leading to considerable flame wrinkling.

8- The flame wrinkling is associated with the high turbulent burning velocity. Therefore, the turbulent burning velocities control the flame wrinkling in the current model.

9- The current *k-ε* model associated with the wrinkling combustion model has been applied to simulate the flame zone in SGT-100. However, this simulation was not completed and left for future study due to the absence of experimental results.

Chapter 7: Conclusion

The present study has investigated laminar and turbulent premixed flames of methane-hydrogen-air mixtures at elevated initial pressures up to 1.0 MPa, at initial temperatures (303 K and 360 K), and over a wide range of equivalence ratios. Measurements were conducted in the Leeds fan-stirred spherical combustion vessel (MK-II). The laminar and turbulent measurements were used as inputs to a numerical model to simulate turbulent flame propagation. The conclusions of this work can be drawn as follows:

1- The laminar burning velocities for H_2/CH_4/air mixtures derived in previous studies [73, 75, 81, 85, 97] were limited to low initial pressure and a narrow range of H_2/CH_4/air mixtures. However, the present study includes a much wider range of H_2/CH_4/air mixtures at a high initial pressure. The pressure effect on the laminar burning velocity has been discussed in terms of the net reaction rate and the production of the active radical species (O, H, OH). Databases for laminar burning velocity, Markstein/length/-number, flame thickness and critical flame radius have been provided. The experimental data can serve as a valuable resource for kinetics researchers since the laminar burning velocity at high initial pressure is used to evaluate kinetic reaction mechanisms, which could be subsequently employed in the simulation of practical engineering applications. In addition, the laminar burning velocity can be used as input to a combustion model. The simulation results were compared against the experimentally derived laminar burning velocities. The experimentally derived laminar burning velocities agree with predictions based on recently developed H_2/CH_4 mechanisms within the San Diego, Konnov and Aramco2.0 models.

Although the agreement between numerical and experiment becomes poorer for rich-pure hydrogen explosions at high initial pressure, predictions remain within the limits of uncertainty in the experimental results.

2- An extensive database of turbulent burning velocities for hydrogen/air and hydrogen/methane/air has been presented. The turbulent burning velocity dependency on pressure, temperature, stretch rate and root mean square (rms) velocity have been quantified and discussed. This study is significant because the existing data on high-pressure turbulent flames, such as one may expect in a hydrogen-fuelled spark-ignition car engine or an industrial gas turbine, are scarce. In addition, the emphasis was put on the study of hydrogen-air flames, and this study is timely given the potential of hydrogen to replace hydrocarbons derived from natural gas and crude oil. Previous experimental studies [14, 80, 138, 146-148, 191] have limited focus on turbulent flame propagation for hydrogen/air and methane/hydrogen/air mixtures, particularly at high-pressure (10 bar) and high turbulence (u' = 10 ms^{-1}) conditions, which are most relevant to hydrogen-fueled ICEs and industrial gas turbines and burners. Moreover, this study revisited the previous *U/K* diagram [66, 135] and plotted new data. The latest data is situated in the regime considered unstable in Bradley's earlier studies. In addition, this study provided a new *U-K* correlation based on Ma_b instead of Ma_{sr}. Ma_{sr} is derived for mixtures with a unity Lewis number, which does not apply to the current fuel/air mixture. New correlations for turbulent burning velocity have been produced for a flame with a non-unity Lewis number, including all parameters that affect the turbulent burning velocity. These correlations have been used to simulate the hydrogen turbulent flame propagation.

The turbulent flame measurements have shown that the laminar burning velocity dominates over the turbulent eddy effects on u_t. Therefore, chemical reactivity precedes the effects of stretch and flame instability. In addition, the assertion that positive stretch (negative Ma_b) consistently increases turbulent burning velocity is not universally valid.

3- Computational Fluid Dynamic (CFD) tools have been used to obtain temperature, flow velocity, and flame wrinkling, which are difficult to measure for swift flame propagation. The laminar and turbulent measurements are used in the numerical simulation to achieve a combustion model that can capture the hydrogen/air turbulent flame propagation at high initial pressure. The numerical model was evaluated by simulating the spherical turbulent flame propagation using the flame wrinkling (Ξ) model. Different parameters have been tested to assess the numerical model (the laminar burning velocity, combustion and turbulence model, and the turbulent burning velocity correlation). In the LES simulation, the maximum predicted error in the flame radius is around 13% for the S_u = transport equation and 22% for $S_u = u_l$. However, the maximum predicted error in the flame radius is around 25% for the S_u = transport equation and 16% for $S_u = u_l$ in the k-ε simulation. Moreover, the maximum difference between the predicted flame radius and the experiments is 11% for the LES simulation using the *U-K* correlation and 24% for the *Da/Le* correlation. The *U-K* correlation agreed with the experiment better than the *Da/Le* correlation because the *U-K* correlation accounts for the flame wrinkling effect as a function of the flame kernel ($u'k$). Both k-ε and dynamic-K-equation LES models have agreed well with the experimental results. However, LES has provided more information about flame surface wrinkling.

The *U-K* correlation performed well when used to calculate the source term in combustion modelling. The current numerical model can be used to predict the field temperature and velocity for combustion systems at constant pressure conditions, such as gas turbines. Therefore, the present study has made recommendations, which are given below.

4- The findings of the present study have essisial implication for practical combustor design and pollutant control. The primary contribution of this work is the development of an experimentally derived turbulent burning velocity correlation under high-pressure and high-turbulence conditions relevant to modern engines. This correlation directly impacts the prediction of flame propagation speed, which is a key parameter in the design of premixed or partially premixed combustion systems such as gas turbines, internal combustion engines, and hydrogen-fueled burners. In practical terms, the ability to predict turbulent burning velocity with higher accuracy allows engineers to:

   a- minimizing flashback and blow-off risks in lean-premixed systems.

   b- design compact combustion chambers with controlled flame speed to reduce NOx formation.

   c- tune operating conditions (pressure, equivalence ratio, turbulence level) to strike a balance between efficiency and emissions.

5- Though detailed chemistry was not resolved in this work, flame speed correlates with the flame temperature and local equivalence ratio, both of which are tightly coupled to NOx formation, especially in hydrogen combustion. By improving the understanding of how turbulence influences flame speed under high-pressure conditions, this study indirectly informs strategies for NOx mitigation, such as operating in lean regimes with optimized flame stabilization. Furthermore, the empirical correlation developed here can be integrated into RANS or LES combustion models for combustor design, where computational cost prohibits the use of detailed chemistry. The flame speed model thus bridges the gap between fundamental flame dynamics and system-level combustion performance prediction.

7.1 Future work and recommendations

7.1.1 Experimental work

1- The laminar burning velocity for hydrogen/air mixtures at high initial pressure (1 MPa) cannot be derived in the present study due to the flame instabilities. This data is essential for kinetic validation. This could be done by deriving the laminar burning velocity at constant pressure or replacing the nitrogen with an inert gas (Argon or Helium) to suppress the flame instabilities. Therefore, the present study recommends this area for future research.

2- Post-processing of the Schlieren images will be performed to quantify the turbulent flame wrinkling under different initial conditions. With the advancement of artificial intelligence and neural networks, images can be analysed for accurate quantification of flame wrinkling.

3- Particle Image Velocimetry (PIV) and Planar Laser-Induced Fluorescence (PLIF) are proposed to further enhance the accuracy of flame measurements. PIV could be employed to obtain spatially resolved velocity fields, which would enable a more accurate quantification of turbulent intensity. However, the applicability of PIV is limited in the present study due to high operating pressures and rms velocity, which challenge seeding particle tracking, and image resolution. Additionally, PLIF provides an accurate determination of the reaction position. The Schlieren, PLIF, and PIV could be combined to improve the understanding of flame-turbulence interactions in future studies.

7.1.2 Numerical work

1- The simulation for Siemens Gas Turbine (SGT-100), Dry Low Emission (DLE) combustor can be finalized using LES and k-ε turbulence models.

2- The mesh dependency for k-ε needs to be validated. It must be noticed that around 25 million elements need to be developed to run for the current model size with the LES model. As a result, more computational time will be required to run the LES simulation.

3- The inlet boundary condition needs to be modified to obtain fully developed turbulence. This increases the computational cost and time.

5- The transition outlet must be added to the model.

6- The dimensions of the actual hydrogen/air gas turbine combustor can be sought, and the numerical results must be validated with experimental data on hydrogen/air combustors.

References

[1] *C. Klinlampu, N. Chimprang, and J. Sirisrisakulchai, "The sufficient level of growth in renewable energy generation for coal demand reduction," Energy Reports, vol. 9, pp. 843-849, 2023/10/01/ 2023.*

[2] *N. A. Al-Mufachi and N. Shah, "The role of hydrogen and fuel cell technology in providing security for the UK energy system," Energy Policy, vol. 171, p. 113286, 2022/12/01/ 2022.*

[3] *S. Machado Santos, J. Cabral Neto, and M. Mendonça Silva, "Forecasting model to assess the potential of secondary lead production from lead acid battery scrap," Environmental science and pollution research international, vol. 26, no. 6, pp. 5782-5793, 2019.*

[4] *J.-L. Chen, L. He, H. Yang, M. Ma, Q. Chen, S-J. Wu, Z-L. Xiao, "Empirical models for estimating monthly global solar radiation: A most comprehensive review and comparative case study in China," Renewable and Sustainable Energy Reviews, vol. 108, pp. 91-111, 2019/07/01/ 2019.*

[5] *Y. Koç, H. Yağlı, A. Görgülü, and A. Koç, "Analysing the performance, fuel cost and emission parameters of the 50 MW simple and recuperative gas turbine cycles using natural gas and hydrogen as fuel," International Journal of Hydrogen Energy, vol. 45, no. 41, pp. 22138-22147, 2020/08/21/ 2020.*

[6] *A. H. Schrotenboer, A. A. T. Veenstra, M. A. J. uit het Broek, and E. Ursavas, "A Green Hydrogen Energy System: Optimal control strategies for integrated hydrogen storage and power generation with wind energy," Renewable and Sustainable Energy Reviews, vol. 168, p. 112744, 2022/10/01/ 2022.*

[7] *M. S. Y. Ebaid, M. Hammad, and T. Alghamdi, "THERMO economic analysis OF PV and hydrogen gas turbine hybrid power plant of 100 MW power output," International Journal of Hydrogen Energy, vol. 40, no. 36, pp. 12120-12143, 2015/09/28/ 2015.*

[8] *S. Ravi, A. Morones, E. L. Petersen, and F. Güthe, "Effects of Hydrogen Addition on the Flame Speeds of Natural Gas Blends Under Uniform Turbulent Conditions," 2015. Available: https://doi.org/10.1115/GT2015-42903*

[9] *W. S. Chai, Y. Bao, P. Jin, G. Tang, L. J. R. Zhou, and S. E. Reviews, "A review on ammonia, ammonia-hydrogen and ammonia-methane fuels," vol. 147, p. 111254, 2021.*

[10] *A. Contreras, S. Yiğit, K. Özay, and T. N. Veziroğlu, "Hydrogen as aviation fuel: A comparison with hydrocarbon fuels," International journal of hydrogen energy, vol. 22, no. 10, pp. 1053-1060, 1997.*

[11] *E. J. K. Nilsson, A. van Sprang, J. Larfeldt, and A. A. Konnov, "The comparative and combined effects of hydrogen addition on the laminar burning velocities of methane and its blends with ethane and propane," Fuel, vol. 189, pp. 369-376, 2017/02/01/ 2017.*

[12] M. Al-Khafaji, J. Yang, AS. Tomlin, HM. Thompson, G. de Boer, K. Liu, ME. Morsy, "Laminar burning velocities and Markstein numbers for pure hydrogen and methane/hydrogen/air mixtures at elevated pressures," Fuel, vol. 354, p. 129331, 2023/12/15/ 2023.

[13] P. Chiesa , G. Lozza, and L. Mazzocchi, "Using Hydrogen as Gas Turbine Fuel," Journal of Engineering for Gas Turbines and Power, vol. 127, no. 1, pp. 73-80, 2005.

[14] M. Zhang, J. Wang, Y. Xie, W. Jin, Z. Wei, Z. Huang, H. Kobayashi, "Flame front structure and burning velocity of turbulent premixed CH4/H2/air flames," International Journal of Hydrogen Energy, vol. 38, no. 26, pp. 11421-11428, 2013/08/30/ 2013.

[15] G. S. Jackson, R. Sai, J. M. Plaia, C. M. Boggs, and K. T. Kiger, "Influence of H2 on the response of lean premixed CH4 flames to high strained flows," Combustion and flame, vol. 132, no. 3, pp. 503-511, 2003.

[16] E. Salzano, F. Cammarota, A. Di Benedetto, and V. Di Sarli, "Explosion behavior of hydrogen–methane/air mixtures," Journal of Loss Prevention in the Process Industries, vol. 25, no. 3, pp. 443-447, 2012/05/01/ 2012.

[17] R. Sankaran and H. G. Im, "EFFECTS OF HYDROGEN ADDITION ON THE MARKSTEIN LENGTH AND FLAMMABILITY LIMIT OF STRETCHED METHANE/AIR PREMIXED FLAMES," Combustion science and technology, vol. 178, no. 9, pp. 1585-1611, 2006.

[18] R. W. Schefer, D. M. Wicksall, and A. K. Agrawal, "Combustion of hydrogen-enriched methane in a lean premixed swirl-stabilized burner," Proceedings of the Combustion Institute, vol. 29, no. 1, pp. 843-851, 2002.

[19] Pitsch, "Carbon capture technology " in combustion webiner, ed. online, 2021.

[20] M. Ditaranto, T. Heggset, and D. Berstad, "Concept of hydrogen fired gas turbine cycle with exhaust gas recirculation: Assessment of process performance," Energy, vol. 192, p. 116646, 2020/02/01/ 2020.

[21] S. M. Candel, "Combustion instabilities coupled by pressure waves and their active control," Symposium, International, on Combustion, vol. 24, no. 1, pp. 1277-1296, 1992.

[22] E. L. Petersen, D. M. Kalitan, S. Simmons, G. Bourque, H. J. Curran, and J. M. Simmie, "Methane/propane oxidation at high pressures: Experimental and detailed chemical kinetic modeling," Proceedings of the Combustion Institute, vol. 31, no. 1, pp. 447-454, 2007.

[23] H. Kutkan and J. Guerrero, "Turbulent Premixed Flame Modeling Using the Algebraic Flame Surface Wrinkling Model: A Comparative Study between OpenFOAM and Ansys Fluent," vol. 6, no. 12, p. 462, 2021.

[24] H. Weller, "The development of a new flame area combustion model using conditional averaging- Thermo-fluids section report TF

" Imperial College of Science Technology and Medicine 1993, vol. 9307.

[25] H. G. Weller, G. Tabor, A. D. Gosman, and C. Fureby, "Application of a flame-wrinkling les combustion model to a turbulent mixing layer," Symposium (International) on Combustion, vol. 27, no. 1, pp. 899-907, 1998/01/01/ 1998.

[26] A. A. Konnov, A. Mohammad, V. R. Kishore, N. I. Kim, C. Prathap, and S. Kumar, "A comprehensive review of measurements and data analysis of laminar burning velocities for various fuel+air mixtures," Progress in energy and combustion science, vol. 68, pp. 197-267, 2018.

[27] C. K. Law, Combustion physics. Cambridge university press, 2010.

[28] B. Hopkinson, Containing Papers of a Mathematical and P. Character, "Explosions of coal-gas and air," vol. 77, no. 518, pp. 387-413, 1906.

[29] L. Flamm and H. Mache, Klasse IIa, "Die Verbrennung eines explosiven Gasgemisches in geschlossenem Gefäß," vol. 126, pp. 9-44, 1917.

[30] O. C. de Champfleur Ellis and R. V. Wheeler, "CVIII.—The movement of flame in closed vessels," Journal of the Chemical Society, Transactions, 10.1039/CT9252700764 vol. 127, no. 0, pp. 764-767, 1925.

[31] L. Bernard and v. E. Guenther, "Determination of the Speed of Flames and the Temperature Distribution in a Spherical Bomb from Time-Pressure Explosion Records," J. Chem. Phys., vol. 2, pp. 238-290, 1934.

[32] G.H. Markstien, "Experimental and theoretical studies of flame front stability.," J Aerosp Sci vol. 18, pp. 199–209, 1951.

[33] G. Dixon-Lewis, "Structure of laminar flames," Symposium (International) on Combustion, vol. 23, no. 1, pp. 305-324, 1991/01/01/ 1991.

[34] M. Matalon, "On Flame Stretch," Combustion science and technology, vol. 31, no. 3-4, pp. 169-181, 1983.

[35] J. H. Tien and M. Matalon, "On the burning velocity of stretched flames," Combustion and Flame, vol. 84, no. 3, pp. 238-248, 1991/04/01/ 1991.

[36] C. K. Wu and C. K. Law, "On the determination of laminar flame speeds from stretched flames," Symposium (International) on Combustion, vol. 20, no. 1, pp. 1941-1949, 1985/01/01/ 1985.

[37] K. N. C. Bray, "The challenge of turbulent combustion," Symposium (International) on Combustion, vol. 26, no. 1, pp. 1-26, 1996/01/01/ 1996.

[38] M. S. Mansour, "Fundamental study of premixed combustion rates at elevated pressure and temperature," Thesis (Ph.D.) -- University of Leeds (School of Mechanical Engineering), 2010., Leeds, 2010.

[39] M. Lawes, "Turbulent Burning," ed. university of leeds, 2002.

[40] R. Borghi, "On the Structure and Morphology of Turbulent Premixed Flames," in Recent Advances in the Aerospace Sciences: In Honor of Luigi Crocco on His Seventy-fifth Birthday, C. Casci and C. Bruno, Eds. Boston, MA: Springer US, 1985, pp. 117-138.

[41] N. Peters, "Laminar flamelet concepts in turbulent combustion," Symposium (International) on Combustion, vol. 21, no. 1, pp. 1231-1250, 1988/01/01/ 1988.

[42] T. Poinsot, D. Veynante, and S. Candel, "Quenching processes and premixed turbulent combustion diagrams," Journal of Fluid Mechanics, vol. 228, pp. 561-606, 1991.

[43] S. B. Pope, "Turbulent Premixed Flames," vol. 19, no. 1, pp. 237-270, 1987.

[44] S. Chaudhuri, F. Wu, and C. K. Law, "Scaling of turbulent flame speed for expanding flames with Markstein diffusion considerations," Physical Review E, vol. 88, no. 3, p. 033005, 09/09/ 2013.

[45] Y. Bo, Y. Li, and W. Gao, "Exploring the effects of turbulent field on propagation behaviors in confined hydrogen-air explosion using OpenFOAM," International Journal of Hydrogen Energy, vol. 50, pp. 912-927, 2024/01/02/ 2024.

[46] D. Veynante and L. Vervisch, "Turbulent combustion modeling," Progress in Energy and Combustion Science, vol. 28, no. 3, pp. 193-266, 2002/03/01/ 2002.

[47] J. Reveillon, E. Franquet, C. Langrée, G. Lecocq, B. Duret, and F. X. Demoulin, "CFD simulation of premixed flames propagating in an obstacles network," Fuel, vol. 329, p. 125266, 2022/12/01/ 2022.

[48] Santos, Guilherme Henrique, Dourado, and Wladimy, "Numerical Study of the b-Ξ Flame Wrinkling Combustion Model in Oracles Test Rig," Journal of Aerospace Technology and Management, vol. 7, pp. 1-10, 2015.

[49] E. Yasari, "Tutorial XiFoam," Chalmers University of Technology2010.

[50] D. B. Spalding, "Mixing and chemical reaction in steady confined turbulent flames," 1971.

[51] R. W. Bilger, S. B. Pope, K. N. C. Bray, and J. F. Driscoll, "Paradigms in turbulent combustion research," Proceedings of the Combustion Institute, vol. 30, no. 1, pp. 21-42, 2005/01/01/ 2005.

[52] J. Gaucherand, D. Laera, C. Schulze-Netzer, and T. Poinsot, "DNS of Turbulent Premixed Ammonia/Hydrogen Flames: The Impact of Thermo-Diffusive Effects," Flow, Turbulence and Combustion, vol. 112, no. 2, pp. 587-614, 2024/02/01 2024.

[53] T. L. Howarth and A. J. Aspden, "An empirical characteristic scaling model for freely-propagating lean premixed hydrogen flames," Combustion and flame, vol. 237, p. 111805, 2022.

[54] H. K. Versteeg, An introduction to computational fluid dynamics the finite volume method, 2/E. Pearson Education India, 2007.

[55] E. Mallard and H. L. Le Chatelier, "Recherche sur la Combusion des Mélanges Gazeux Explosives," eme serie, vol. 8, no. t IV, p. 274, 1883.

[56] N. N. Semenov, Chemical Kinetics and Chain Reaction. Oxford: The Clarendon press, 1935.

[57] C. N. Hinshelwood, The Kinetics of Chemical Change. Clarendon Press: Oxford, 1940.

[58] G. Dixon-Lewis and A. Williams, "Some observations on the structure of a slow burning flame supported by the reaction between hydrogen and oxygen at atmospheric pressure," Symposium (International) on Combustion, vol. 9, no. 1, pp. 576-586, 1963/01/01/ 1963.

[59] S. R. Turns, An introduction to combustion. New York: McGraw-Hill., 1996.

[60] M. E. Morsy, "Studies of Laminar and Turbulent Combustion Using Particle Image Velocimetry," University of Leeds, 2019.

[61] J. Göttgens, F. Mauss, and N. Peters, "Analytic approximations of burning velocities and flame thicknesses of lean hydrogen, methane, ethylene, ethane, acetylene, and propane flames," Symposium (International) on Combustion, vol. 24, no. 1, pp. 129-135, 1992/01/01/ 1992.

[62] F. A. Williams, Combustion theory : the fundamental theory of chemically reacting flow systems, Second edition. ed. (Combustion, science, and engineering series). Menlo Park, Calif: Benjamin/Cummings Pub. Co., 1985.

[63] A. S. Huzayyin, H. A. Moneib, M. S. Shehatta, and A. M. A. Attia, "Laminar burning velocity and explosion index of LPG–air and propane–air mixtures," Fuel, vol. 87, no. 1, pp. 39-57, 2008/01/01/ 2008.

[64] D. Bradley, M. Lawes, and M. E. Morsy, "Flame speed and particle image velocimetry measurements of laminar burning velocities and Markstein numbers of some hydrocarbons," 2019.

[65] D. Bradley, M. Lawes, and M. E. Morsy, "Combustion-induced turbulent flow fields in premixed flames," 2021.

[66] D. Bradley, M. Shehata, M. Lawes, and P. Ahmed, "Flame extinctions: Critical stretch rates and sizes," 2020.

[67] K. T. Aung, M. I. Hassan, and G. M. Faeth, "Flame stretch interactions of laminar premixed hydrogen/air flames at normal temperature and pressure," Combustion and Flame, vol. 109, no. 1, pp. 1-24, 1997/04/01/ 1997.

[68] D. Bradley, A. K. C. Lau, M. Lawes, and F. T. Smith, "Flame Stretch Rate as a Determinant of Turbulent Burning Velocity," Philosophical transactions of the Royal Society of London. Series A: Physical sciences and engineering, vol. 338, no. 1650, pp. 359-387, 1992.

[69] P. Ghanbari-Bavarsad, "Modeling stretched methane-air flame growth," 2008.

[70] B. Karlovitz, D. W. Denniston, D. H. Knapschaefer, and F. E. Wells, "Studies on Turbulent flames: A. Flame Propagation Across velocity gradients B. turbulence Measurement in flames," Symposium (International) on Combustion, vol. 4, no. 1, pp. 613-620, 1953/01/01/ 1953.

[71] D. Bradley, R. A. Hicks, M. Lawes, C. G. W. Sheppard, and R. Woolley, "The Measurement of Laminar Burning Velocities and Markstein Numbers for Iso-octane–Air and Iso-octane–n-Heptane–Air Mixtures at Elevated Temperatures and Pressures in an Explosion Bomb," Combustion and flame, vol. 115, no. 1, pp. 126-144, 1998.

[72] X. J. Gu, M. Z. Haq, M. Lawes, and R. Woolley, "Laminar burning velocity and Markstein lengths of methane–air mixtures," Combustion and flame, vol. 121, no. 1, pp. 41-58, 2000.

[73] E. Hu, Z. Huang, J. He, J. Zheng, and H. Miao, "Measurements of laminar burning velocities and onset of cellular instabilities of methane–hydrogen–air flames at elevated pressures and temperatures," International Journal of Hydrogen Energy, vol. 34, no. 13, pp. 5574-5584, 2009/07/01/ 2009.

[74] Z. Chen, "On the accuracy of laminar flame speeds measured from outwardly propagating spherical flames: Methane/air at normal temperature and pressure," Combustion and flame, vol. 162, no. 6, pp. 2442-2453, 2015.

[75] E. Hu, Z. Huang, J. He, C. Jin, and J. Zheng, "Experimental and numerical study on laminar burning characteristics of premixed methane–hydrogen–air flames," International Journal of Hydrogen Energy, vol. 34, no. 11, pp. 4876-4888, 2009/06/01/ 2009.

[76] F. Wu, W. Liang, Z. Chen, Y. Ju, and C. K. Law, "Uncertainty in stretch extrapolation of laminar flame speed from expanding spherical flames," Proceedings of the Combustion Institute, vol. 35, no. 1, pp. 663-670, 2015.

[77] S. Y. Liaoa, D. M. Jianga, J. Gaoa, Z. Huanga, and Q. Cheng-b, "Measurements of Markstein numbers and laminar burning velocities for liquefied petroleum gas–air mixtures," 2004.

[78] K. Takizawa, A. Takahashi, K. Tokuhashi, S. Kondo, and A. Sekiya, "Burning velocity measurement of fluorinated compounds by the spherical-vessel method," Combustion and Flame, vol. 141, no. 3, pp. 298-307, 2005/05/01/ 2005.

[79] D. Smith and J. T. Agnew, "The effect of pressure on the laminar burning velocity of methane-oxygen-nitrogen mixtures," Symposium (International) on Combustion, vol. 6, no. 1, pp. 83-88, 1957/01/01/ 1957.

[80] M. Fairweather, M. P. Ormsby, C. G. W. Sheppard, and R. Woolley, "Turbulent burning rates of methane and methane–hydrogen mixtures," Combustion and flame, vol. 156, no. 4, pp. 780-790, 2009.

[81] E. Hu, Z. Huang, J. Zheng, Q. Li, and J. He, "Numerical study on laminar burning velocity and NO formation of premixed methane–hydrogen–air flames," International Journal of Hydrogen Energy, vol. 34, no. 15, pp. 6545-6557, 2009/08/01/ 2009.

[82] C. J. Sung, Y. Huang, and J. A. Eng, "Effects of reformer gas addition on the laminar flame speeds and flammability limits of n-butane and iso-butane flames," Combustion and flame, vol. 126, no. 3, pp. 1699-1713, 2001.

[83] G. Yu, C. K. Law, and C. K. Wu, "Laminar flame speeds of hydrocarbon + air mixtures with hydrogen addition," Combustion and flame, vol. 63, no. 3, pp. 339-347, 1986.

[84] C. Mandilas, M. P. Ormsby, C. G. W. Sheppard, and R. Woolley, "Effects of hydrogen addition on laminar and turbulent premixed methane and iso-octane–air flames," Proceedings of the Combustion Institute, vol. 31, no. 1, pp. 1443-1450, 2007.

[85] E. C. Okafor, A. Hayakawa, Y. Nagano, and T. Kitagawa, "Effects of hydrogen concentration on premixed laminar flames of hydrogen–methane–air," International Journal of Hydrogen Energy, vol. 39, no. 5, pp. 2409-2417, 2014/02/04/ 2014.

[86] Q. Wang, X. H. Mei, Z. Y. Wei, C. Y. Zhao, and Y. Zhang, "Experimental investigation of transient ignition dynamics of hydrogen enriched methane diffusion impinging flames," Fuel, vol. 290, p. 120027, 2021/04/15/ 2021.

[87] D. Bradley, C. G. W. Sheppart, R. Woolley, D. A. Greenhalgh, and R. D. Lockett, "The development and structure of flame instabilities and cellularity at low Markstein numbers in explosions," Combustion and Flame, vol. 122, no. 1, pp. 195-209, 2000/07/01/ 2000.

[88] J. K. Bechtold and M. Matalon, "Hydrodynamic and diffusion effects on the stability of spherically expanding flames," Combustion and flame, vol. 67, no. 1, pp. 77-90, 1987.

[89] P. F. Ivashchenko and V. S. Rumyantsev, "Convective rise and propagation velocity of a large flame focus," Combustion, explosion, and shock waves, vol. 14, no. 3, pp. 338-341, 1978.

[90] G. Searby, "Experimental studies of instabilities of laminar premixed flames," 2006.

[91] N. Fogla, F. Creta, and M. Matalon, "Influence of the Darrieus-Landau instability on the propagation of planar turbulent flames," Proceedings of the Combustion Institute, vol. 34, no. 1, pp. 1509-1517, 2013/01/01/ 2013.

[92] L. Landau, Acta Physicochim. USSR, vol. 19, pp. 77-58, 1944.

[93] J. Huo, A. Saha, Z. Ren, and C. K. Law, "Self-acceleration and global pulsation in hydrodynamically unstable expanding laminar flames," Combustion and flame, vol. 194, pp. 419-425, 2018.

[94] M. E. Morsy and J. Yang, "The Instability of Laminar Methane/Hydrogen/Air Flames: Correlation between Small and Large-Scale Explosions," 2022.

[95] C. K. Law, G. Jomaas, and J. K. Bechtold, "Cellular instabilities of expanding hydrogen/propane spherical flames at elevated pressures: theory and experiment," Proceedings of the Combustion Institute, vol. 30, no. 1, pp. 159-167, 2005/01/01/ 2005.

[96] Y. Xie, M. Elsayed Morsy, J. Li, and J. Yang, "Intrinsic cellular instabilities of hydrogen laminar outwardly propagating spherical flames," Fuel (Guildford), vol. 327, 2022.

[97] D. Bradley, M. Lawes, K. Liu, S. Verhelst, and R. Woolley, "Laminar burning velocities of lean hydrogen–air mixtures at pressures up to 1.0 MPa," Combustion and flame, vol. 149, no. 1, pp. 162-172, 2007.

[98] D. Bradley, "Instabilities and flame speeds in large-scale premixed gaseous explosions," Philosophical transactions of the Royal Society of London. Series A: Mathematical, physical, and engineering sciences, vol. 357, no. 1764, pp. 3567-3581, 1999.

[99] H. Zhao, J. Wang, Z. Bian, X. Cai, X. Li, and Z. Huang, "Onset of cellular instability and self-acceleration propagation of syngas spherically expanding flames at elevated pressures," International journal of hydrogen energy, vol. 44, no. 51, pp. 27995-28006, 2019.

[100] F. N. Egolfopoulos, N. Hansen, Y. Ju, K. Kohse-Höinghaus, C. K. Law, and F. Qi, "Advances and challenges in laminar flame experiments and implications for combustion chemistry," Progress in Energy and Combustion Science, vol. 43, pp. 36-67, 2014/08/01/ 2014.

[101] M. P. Burke, M. Chaos, F. L. Dryer, and Y. Ju, "Negative pressure dependence of mass burning rates of H2/CO/O2/diluent flames at low flame temperatures," Combustion and Flame, vol. 157, no. 4, pp. 618-631, 2010/04/01/ 2010.

[102] Y. Wang and S. Verhelst, "Comparative analysis and optimisation of hydrogen combustion mechanism for laminar burning velocity calculation in combustion engine modelling," International Journal of Hydrogen Energy, vol. 56, pp. 880-893, 2024/02/22/ 2024.

[103] F. Wu, G. Jomaas, and C. K. Law, "An experimental investigation on self-acceleration of cellular spherical flames," Proceedings of the Combustion Institute, vol. 34, no. 1, pp. 937-945, 2013/01/01/ 2013.

[104] L. Gillespie, M. Lawes, C. G. W. Sheppard, and R. Woolley, "Aspects of Laminar and Turbulent Burning Velocity Relevant to SI Engines," SAE transactions, vol. 109, pp. 13-33, 2000.

[105] S. P. Ahmed, "Studies of turbulent burning rates and flame structures using 3D optical measurement techniques," University of Leeds, 2019.

[106] M. Lawes, G. J. Sharpe, N. Tripathi, and R. F. Cracknell, "Influence of spark ignition in the determination of Markstein lengths using spherically expanding flames," Fuel, vol. 186, pp. 579-586, 2016/12/15/ 2016.

[107] M. P. Burke, Z. Chen, Y. Ju, and F. L. Dryer, "Effect of cylindrical confinement on the determination of laminar flame speeds using outwardly propagating flames," Combustion and Flame, vol. 156, no. 4, pp. 771-779, 2009/04/01/ 2009.

[108] R. D. Mumby, "Experimental Characterisation of Fuel Blends," University of Leeds, 2016.

[109] D. R. Dowdy, D. B. Smith, S. C. Taylor, and A. Williams, "The use of expanding spherical flames to determine burning velocities and stretch effects in hydrogen/air mixtures," Symposium (International) on Combustion, vol. 23, no. 1, pp. 325-332, 1991/01/01/ 1991.

[110] A. P. Kelley and C. K. Law, "Nonlinear effects in the extraction of laminar flame speeds from expanding spherical flames," Combustion and Flame, vol. 156, no. 9, pp. 1844-1851, 2009/09/01/ 2009.

[111] M. I. Hassan, K. T. Aung, and G. M. Faeth, "Measured and predicted properties of laminar premixed methane/air flames at various pressures," Combustion and flame, vol. 115, no. 4, pp. 539-550, 1998.

[112] T. Iijima and T. Takeno, "Effects of temperature and pressure on burning velocity," Combustion and flame, vol. 65, no. 1, pp. 35-43, 1986.

[113] B. E. Milton and J. C. Keck, "Laminar burning velocities in stoichiometric hydrogen and hydrogen/hydrocarbon gas mixtures," Combustion and flame, vol. 58, no. 1, pp. 13-22, 1984.

[114] S. Verhelst, R. Woolley, M. Lawes, and R. Sierens, "Laminar and unstable burning velocities and Markstein lengths of hydrogen–air mixtures at engine-like conditions," Proceedings of the Combustion Institute, vol. 30, no. 1, pp. 209-216, 2005.

[115] P. Zhang, I. G. Zsély, M. Papp, T. Nagy, and T. Turányi, "Comparison of methane combustion mechanisms using laminar burning velocity measurements," Combustion and flame, vol. 238, p. 111867, 2022.

[116] Y. Zhang, J. Fu, J. Shu, M. Xie, and J. Liu, "A chemical kinetic investigation of laminar premixed burning characteristics for methane-hydrogen-air mixtures at elevated pressures," Journal of the Taiwan Institute of Chemical Engineers, vol. 111, pp. 141-154, 2020.

[117] ANSYS, ANSYS Chemkin Theory Manual 17.0 (15151), San Diego Reaction San Diego, 2015. [Online]. Available.

[118] Q. Yang, P. Zhao, and H. Ge, "reactingFoam-SCI: An open source CFD platform for reacting flow simulation," Computers & Fluids, vol. 190, pp. 114-127, 2019/08/15/ 2019.

[119] F.A. Williams, K. Seshadri, and R. Catolica. Available: http://web.eng.ucsd.edu/mae/groups/combustion/index.html

[120] W. E. Nichols, R. H. Cuenca, T. J. Schmugge, and J. R. Wang, "Pushbroom microwave radiometer results from HAPEX-MOBILHY," Remote Sensing of Environment, Article vol. 46, no. 2, pp. 119-128, 1993.

[121] A. M. Steinberg, C. M. Arndt, and W. Meier, "Parametric study of vortex structures and their dynamics in swirl-stabilized combustion," Proceedings of the Combustion Institute, vol. 34, no. 2, pp. 3117-3125, 2013/01/01/ 2013.

[122] U. Sen, T. Gangopadhyay, C. Bhattacharya, A. Mukhopadhyay, and S. Sen, "Dynamic Characterization of a Ducted Inverse Diffusion Flame Using Recurrence Analysis," Combustion science and technology, vol. 190, no. 1, pp. 32-56, 2018.

[123] S. Wang, A. M. Elbaz, G. Wang, Z. Wang, and W. L. Roberts, "Turbulent flame speed of NH3/CH4/H2/H2O/air-mixtures: Effects of elevated pressure and Lewis number," Combustion and Flame, vol. 247, p. 112488, 2023/01/01/ 2023.

[124] G. Damköhler, "The effect of turbulence on the flame velocity in gas mixtures," vol. 46, no. NACA-TM-1112, 1947.

[125] R. G. Abdel-Gayed, D. Bradley, and M. Lawes, "Turbulent Burning Velocities: A General Correlation in Terms of Straining Rates," Proceedings of the Royal Society of London. Series A, Mathematical and physical sciences, vol. 414, no. 1847, pp. 389-413, 1987.

[126] M. Lawes, M. P. Ormsby, C. G. W. Sheppard, and R. Woolley, "The turbulent burning velocity of iso-octane/air mixtures," Combustion and Flame, vol. 159, no. 5, pp. 1949-1959, 2012/05/01/ 2012.

[127] D. Bradley, M. Lawes, and M. S. Mansour, "Correlation of turbulent burning velocities of ethanol–air, measured in a fan-stirred bomb up to 1.2 MPa," Combustion and flame, vol. 158, no. 1, pp. 123-138, 2011.

[128] I. G. Shepherd and R. K. Cheng, "The burning rate of premixed flames in moderate and intense turbulence," Combustion and Flame, vol. 127, no. 3, pp. 2066-2075, 2001/11/01/ 2001.

[129] D. Bradley, M. Z. Haq, R. A. Hicks, T. Kitagawa, M. Lawes, C. G. W. Sheppard and R. Woolley , "Turbulent burning velocity, burned gas distribution, and associated flame surface definition," Combustion and flame, vol. 133, no. 4, pp. 415-430, 2003.

[130] S. A. Filatyev, J. F. Driscoll, C. D. Carter, and J. M. Donbar, "Measured properties of turbulent premixed flames for model assessment, including burning velocities, stretch rates, and surface densities," Combustion and flame, vol. 141, no. 1, pp. 1-21, 2005.

[131] A. Lipatnikov and J. Chomiak, "Turbulent flame speed and thickness: phenomenology, evaluation, and application in multi-dimensional simulations," vol. 28, no. 1, pp. 1-74, 2002.

[132] B. Bédat and R. K. Cheng, "Experimental study of premixed flames in intense isotropic turbulence," Combustion and Flame, vol. 100, no. 3, pp. 485-494, 1995/02/01/ 1995.

[133] M. Metghalchi and J. C. Keck, "Burning velocities of mixtures of air with methanol, isooctane, and indolene at high pressure and temperature," Combustion and flame, vol. 48, pp. 191-210, 1982.

[134] A. N. Lipatnikov and J. Chomiak, "Comment on "Turbulent burning velocity, burned gas distribution, and associated flame surface definition": D. Bradley, M.Z. Haq, R.A. Hicks, T. Kitagawa, M. Lawes, C.G.W. Sheppard, R. Woolley, Combust. Flame 133 (2003) 415," Combustion and flame, vol. 137, no. 1, pp. 261-263, 2004.

[135] D. Bradley, M. Lawes, K. Liu, and M. S. Mansour, "Measurements and correlations of turbulent burning velocities over wide ranges of fuels and elevated pressures," 2013.

[136] D. Bradley, M. Lawes, and M. S. Mansour, "Flame surface densities during spherical turbulent flame explosions," 2008.

[137] D. Bradley, M. Lawes, and M. E. Morsy, "Measurement of turbulence characteristics in a large scale fan-stirred spherical vessel," Journal of turbulence, vol. 20, no. 3, pp. 195-213, 2019.

[138] J. Goulier, A. Comandini, F. Halter, and N. Chaumeix, "Experimental study on turbulent expanding flames of lean hydrogen/air mixtures," Proceedings of the Combustion Institute, vol. 36, no. 2, pp. 2823-2832, 2017/01/01/ 2017.

[139] I. K. Nwagwe et al., "Measurements and large eddy simulations of turbulent premixed flame kernel growth," Proceedings of the Combustion Institute, vol. 28, no. 1, pp. 59-65, 2000.

[140] W. D. McComb, The Physics of Fluid Turbulence. Oxford University Press 1990.

[141] R. G. Abdel-Gayed, D. Bradley, M. N. Hamid, and M. Lawes, "Lewis number effects on turbulent burning velocity," Symposium (International) on Combustion, vol. 20, no. 1, pp. 505-512, 1985/01/01/ 1985.

[142] X. Cai, J. Wang, Z. Bian, H. Zhao, M. Zhang, and Z. Huang, "Self-similar propagation and turbulent burning velocity of CH4/H2/air expanding flames: Effect of Lewis number," Combustion and Flame, vol. 212, pp. 1-12, 2020/02/01/ 2020.

[143] Williams D and Bollinger L, "Effect of Reynolds Number in Turbulent Flow Range on Flame Speed of Bunsen Burner Flames," vol. 932, 1949.

[144] Z.-Y. Sun and G.-X. Li, "Turbulence influence on explosion characteristics of stoichiometric and rich hydrogen/air mixtures in a spherical closed vessel," Energy Conversion and Management, vol. 149, pp. 526-535, 2017/10/01/ 2017.

[145] A. Morones et al., "Laminar and Turbulent Flame Speeds for Natural Gas/Hydrogen Blends," in ASME Turbo Expo 2014: Turbine Technical Conference and Exposition, 2014, vol. Volume 4B: Combustion, Fuels and Emissions, V04BT04A039.

[146] M. Nakahara, T. Shirasuna, and J. Hashimoto, "Experimental Study on Local Flame Properties of Hydrogen Added Hydrocarbon Premixed Turbulent Flames," Journal of Thermal Science and Technology, vol. 4, no. 1, pp. 190-201, 2009.

[147] R. W. Schefer, "Hydrogen enrichment for improved lean flame stability," International Journal of Hydrogen Energy, vol. 28, no. 10, pp. 1131-1141, 2003/10/01/ 2003.

[148] P. Strakey, T. Sidwell, and J. Ontko, "Investigation of the effects of hydrogen addition on lean extinction in a swirl stabilized combustor," Proceedings of the Combustion Institute, vol. 31, no. 2, pp. 3173-3180, 2007/01/01/ 2007.

[149] N. N. Smirnov and V. F. Nikitin, "Modeling and simulation of hydrogen combustion in engines," International Journal of Hydrogen Energy, vol. 39, no. 2, pp. 1122-1136, 2014/01/13/ 2014.

[150] Marwaan Al-Khafaji, Junfeng Yang, Alison S. Tomlin, Harvey M. Thompson, Gregory de Boer, and Kexin Liu, "The Measurement of Turbulent Burning Velocities of Methane-Hydrogen-Air Mixtures at Elevated Pressures in a Spherical Vessel " Combustion and Flame, 2024.

[151] A. Lipatnikov, Fundamentals of premixed turbulent combustion. CRC Press, 2012.

[152] Marble FE and Broadwell JE, "The coherent flame model for turbulent chemical reactions," California instute of tecnology, Purdue university 1977.

[153] P. Siewert, " Flame Front Characteristics of Turbulent Lean Premixed Methane/Air Flames at High-Pressure.," PhD, Mechanical engineering Swiss Federal Institute of Technology Zurich (ETH Zurich) Zürich, Switzerland, 2006.

[154] D. Bradley, P. H. Gaskell, and X. J. Gu, "Burning velocities, markstein lengths, and flame quenching for spherical methane-air flames: A computational study," Combustion and Flame, vol. 104, no. 1, pp. 176-198, 1996/01/01/ 1996.

[155] E. S. Semenov, "Measurement of turbulence characteristics in a closed volume with artificial turbulence," Combustion, explosion, and shock waves, vol. 1, no. 2, pp. 57-62, 1965.

[156] M. M. A. O. Shehata, "New Fuels, Flame quenching and DDT," University of Leeds, 2019.

[157] C. Morley, "Gaseq: a chemical equilibrium program for Windows. ," ed, 2005.

[158] D. Bradley, M. Lawes, and M. S. Mansour, "The Problems of the Turbulent Burning Velocity: Computational Combustion Using High-Performance Computing," Flow, turbulence and combustion, vol. 87, no. 2-3, pp. 191-204, 2011.

[159] V. Sabelnikov and C. Fureby, "LES combustion modeling for high Re flames using a multi-phase analogy," Combustion and Flame, vol. 160, no. 1, pp. 83-96, 2013/01/01/ 2013.

[160] C. Fureby, "Large eddy simulation modelling of combustion for propulsion applications," Philosophical transactions of the Royal Society of London. Series A: Mathematical, physical, and engineering sciences, vol. 367, no. 1899, pp. 2957-2969, 2009.

[161] W.-W. Kim and S. Menon, "A new dynamic one-equation subgrid-scale model for large eddy simulations," 1995.

[162] N. Burali, S. Lapointe, B. Bobbitt, G. Blanquart, and Y. Xuan, "Assessment of the constant non-unity Lewis number assumption in chemically-reacting flows," Combustion Theory and Modelling, vol. 20, no. 4, pp. 632-657, 2016/07/03 2016.

[163] S. Ravi and E. L. Petersen, "Laminar flame speed correlations for pure-hydrogen and high-hydrogen content syngas blends with various diluents," International Journal of Hydrogen Energy, vol. 37, no. 24, pp. 19177-19189, 2012/12/01/ 2012.

[164] Z. Sheng, G. Yang, S. Li, Q. Shen, H. Sun, Z. Jiang, J. Liao, H. Wang, "Modeling of turbulent deflagration behaviors of premixed hydrogen-air in closed space with obstacles," Process Safety and Environmental Protection, vol. 161, pp. 506-519, 2022/05/01/ 2022.

[165] H. Jasak, "Numerical Modelling of Coupled Problems in Applied Physics

with OpenFOAM (16th ed.)," M. Al-Khafaji, Ed., ed. Cambridge, UK: University of Cambridge, 2023.

[166] D. Bradley, M. Lawes, R. Mumby, and P. Ahmed, "The stability of laminar explosion flames," 2019.

[167] D. Bradley, C. G. W. Sheppard, I. M. Suardjaja, and R. Woolley, "Fundamentals of high-energy spark ignition with lasers," Combustion and flame, vol. 138, no. 1, pp. 55-77, 2004.

[168] X. Qin, H. Kobayashi, and T. Niioka, "Laminar burning velocity of hydrogen–air premixed flames at elevated pressure," Experimental thermal and fluid science, vol. 21, no. 1, pp. 58-63, 2000.

[169] K. T. Aung, M. I. Hassan, and G. M. Faeth, "Effects of pressure and nitrogen dilution on flame/stretch interactions of laminar premixed H2/O2/N2 flames," Combustion and Flame, vol. 112, no. 1, pp. 1-15, 1998/01/01/ 1998.

[170] C. J. Sun, C. J. Sung, L. He, and C. K. Law, "Dynamics of weakly stretched flames: quantitative description and extraction of global flame parameters," Combustion and Flame, vol. 118, no. 1, pp. 108-128, 1999/07/01/ 1999.

[171] C. K. Law and C. J. Sung, "Structure, aerodynamics, and geometry of premixed flamelets," Progress in Energy and Combustion Science, vol. 26, no. 4, pp. 459-505, 2000/08/01/ 2000.

[172] E. Varea, J. Beeckmann, H. Pitsch, Z. Chen, and B. Renou, "Determination of burning velocities from spherically expanding H2/air flames," Proceedings of the Combustion Institute, vol. 35, no. 1, pp. 711-719, 2015/01/01/ 2015.

[173] F. Zhang, H. Bonart, T. Zirwes, P. Habisreuther, H. Bockhorn, and N. Zarzalis, "Direct Numerical Simulation of Chemically Reacting Flows with the Public Domain Code OpenFOAM," 2015, pp. 221-236.

[174] D. Bradley, P. H. Gaskell, X. J. Gu, and A. Sedaghat, "Premixed flamelet modelling: Factors influencing the turbulent heat release rate source term and the turbulent burning velocity," Combustion and flame, vol. 143, no. 3, pp. 227-245, 2005.

[175] K. N. C. Bray and R. S. Cant, "Some Applications of Kolmogorov's Turbulence Research in the Field of Combustion," Proceedings of the Royal Society. A, Mathematical and physical sciences, vol. 434, no. 1890, pp. 217-240, 1991.

[176] R. G. Abdel-Gayed and D. Bradley, "Dependence of turbulent burning velocity on turbulent reynolds number and ratio of flaminar burning velocity to R.M.S. turbulent velocity," Symposium (International) on Combustion, vol. 16, no. 1, pp. 1725-1735, 1977/01/01/ 1977.

[177] U. Ahmed, N. Chakraborty, and M. Klein, "Insights into the Bending Effect in Premixed Turbulent Combustion Using the Flame Surface Density Transport," Combustion science and technology, vol. 191, no. 5-6, pp. 898-920, 2019.

[178] D. Bradley, "Problems of predicting turbulent burning rates," Combustion theory and modelling, vol. 6, no. 2, pp. 361-382, 2002.

[179] A. R. Varma, U. Ahmed, M. Klein, and N. Chakraborty, "Effects of turbulent length scale on the bending effect of turbulent burning velocity in premixed turbulent combustion," Combustion and Flame, vol. 233, p. 111569, 2021/11/01/ 2021.

[180] R. Yu and A. N. Lipatnikov, "DNS study of dependence of bulk consumption velocity in a constant-density reacting flow on turbulence and mixture characteristics," Physics of fluids (1994), vol. 29, no. 6, p. 15, 2017.

[181] L. C. Allard M, "Recherches sur la combustion des mélanges gazeux

explosifs," J. Phys. Theor, pp. 59-84, 1985.

[182] *K. N. C. Bray, "Turbulent Combustion. By NORBERT PETERS. Cambridge University Press, 2000. 320 pp. ISBN 0521 60823.," Journal of Fluid Mechanics, vol. 426, pp. 407-409, 2001.*

[183] *H. Kobayashi, Y. Kawabata, and K. Maruta, "Experimental study on general correlation of turbulent burning velocity at high pressure," in Symposium (International) on Combustion, 1998, vol. 27, no. 1, pp. 941-948: Elsevier.*

[184] *T. Kitagawa, T. Nakahara, K. Maruyama, K. Kado, A. Hayakawa, and S. Kobayashi, "Turbulent burning velocity of hydrogen–air premixed propagating flames at elevated pressures," International Journal of Hydrogen Energy, vol. 33, no. 20, pp. 5842-5849, 2008/10/01/ 2008.*

[185] *V. A. Sabelnikov and A. N. Lipatnikov, "Bifractal nature of turbulent reaction waves at high Damköhler and Karlovitz numbers,," Physics of Fluids, vol. 32, no. 095118, 2020.*

[186] *A. M. Steinberg and J. F. Driscoll, "Straining and wrinkling processes during turbulence–premixed flame interaction measured using temporally-resolved diagnostics," Combustion and flame, vol. 156, no. 12, pp. 2285-2306, 2009.*

[187] *Z. Zhang, X. Liu, Y. Gong, Z. Li, J. Yang, and H. J. F. Zheng, "Investigation on flame characteristics of industrial gas turbine combustor with different mixing uniformities," vol. 259, p. 116297, 2020.*

[188] *L. McManus, S. Sadasivuni, K. Liu, and E. Munktell, "Numerical Study of the Effect of Fuel Heating Value Change on Combustion for Siemens Energy Dry Low Emission Combustor," in ASME Turbo Expo 2023: Turbomachinery Technical Conference and Exposition, 2023, vol. Volume 3A: Combustion, Fuels, and Emissions, V03AT04A052.*

[189] *K. Liu and S. Sadasivuni, "OPTIMISED PILOT BURNER WITH INTELLIGENT CONTROL TO ACHIEVE SUB 9 PPM EMISSIONS FOR SIEMENS ENERGY SGT-300-1S 7.9 MWe ENGINE," in ASME Turbo Expo 2023: Turbomachinery Technical Conference and Exposition GT2024, London, England, United Kingdom, 2024, vol. 2.*

[190] *J. May, "Demonstration of an Industrial Power-to-H2-to-Power Advanced Plant Concept with up to 100% H2 in an SGT400 Gas Turbine," presented at the Hydrogen Combustion Current and Future Research, Engineering Department, Cambridge University, 8th December 2023, 2023.*

[191] *A. Morones, M. A. Turner, V. León, K. Ruehle, and E. L. Petersen, "Validation of a New Turbulent Flame Speed Facility for the Study of Gas Turbine Fuel Blends at Elevated Pressure," 2019. Available: https://doi.org/10.1115/GT2019-90394*